frontiers | Research Topics

Ai-based energy storage systems

Edited by
Muhammad Khalid and Elżbieta Jasińska

Published in
Frontiers in Energy Research

ISSN 1664-8714
ISBN 978-2-8325-6511-7
DOI 10.3389/978-2-8325-6511-7

Generative AI statement
Any alternative text (Alt text) provided alongside figures in the articles in this ebook has been generated by Frontiers with the support of artificial intelligence and reasonable efforts have been made to ensure accuracy, including review by the authors wherever possible. If you identify any issues, please contact us.

About Frontiers

Frontiers is more than just an open access publisher of scholarly articles: it is a pioneering approach to the world of academia, radically improving the way scholarly research is managed. The grand vision of Frontiers is a world where all people have an equal opportunity to seek, share and generate knowledge. Frontiers provides immediate and permanent online open access to all its publications, but this alone is not enough to realize our grand goals.

Frontiers journal series

The Frontiers journal series is a multi-tier and interdisciplinary set of open-access, online journals, promising a paradigm shift from the current review, selection and dissemination processes in academic publishing. All Frontiers journals are driven by researchers for researchers; therefore, they constitute a service to the scholarly community. At the same time, the *Frontiers journal series* operates on a revolutionary invention, the tiered publishing system, initially addressing specific communities of scholars, and gradually climbing up to broader public understanding, thus serving the interests of the lay society, too.

Dedication to quality

Each Frontiers article is a landmark of the highest quality, thanks to genuinely collaborative interactions between authors and review editors, who include some of the world's best academicians. Research must be certified by peers before entering a stream of knowledge that may eventually reach the public - and shape society; therefore, Frontiers only applies the most rigorous and unbiased reviews. Frontiers revolutionizes research publishing by freely delivering the most outstanding research, evaluated with no bias from both the academic and social point of view. By applying the most advanced information technologies, Frontiers is catapulting scholarly publishing into a new generation.

What are Frontiers Research Topics?

Frontiers Research Topics are very popular trademarks of the *Frontiers journals series*: they are collections of at least ten articles, all centered on a particular subject. With their unique mix of varied contributions from Original Research to Review Articles, Frontiers Research Topics unify the most influential researchers, the latest key findings and historical advances in a hot research area.

Find out more on how to host your own Frontiers Research Topic or contribute to one as an author by contacting the Frontiers editorial office: frontiersin.org/about/contact

AI-based energy storage systems

Topic editors

Muhammad Khalid — King Fahd University of Petroleum and Minerals, Saudi Arabia

Elżbieta Jasińska — Wrocław University of Science and Technology, Poland

Citation

Khalid, M., Jasińska, E., eds. (2025). *AI-based energy storage systems*. Lausanne: Frontiers Media SA. doi: 10.3389/978-2-8325-6511-7

Table of contents

frontiers | Frontiers in Energy Research

TYPE Editorial
PUBLISHED 13 June 2025
DOI 10.3389/fenrg.2025.1626556

OPEN ACCESS

EDITED AND REVIEWED BY
ZhaoYang Dong,
City University of Hong Kong, Hong Kong SAR, China

*CORRESPONDENCE
Muhammad Khalid,
mkhalid@kfupm.edu.sa

RECEIVED 11 May 2025
ACCEPTED 12 May 2025
PUBLISHED 13 June 2025

CITATION
Khalid M and Jasińska E (2025) Editorial: AI-based energy storage systems. *Front. Energy Res.* 13:1626556. doi: 10.3389/fenrg.2025.1626556

Editorial: AI-based energy storage systems

Muhammad Khalid[1,2]* and Elżbieta Jasińska[3]

[1]Electrical Engineering Department, King Fahd University of Petroleum and Minerals (KFUPM), Dhahran, Saudi Arabia, [2]Interdisciplinary Research Center for Sustainable Energy Systems (IRC-SES), King Fahd University of Petroleum and Minerals (KFUPM), Dhahran, Saudi Arabia, [3]Wrocław University of Science and Technology, Wrocław, Poland

KEYWORDS

energy storage and conversion, artificial intelligence - AI, optimization, renewable energy, electric vehicles

Editorial on the Research Topic
AI-based energy storage systems

The global shift toward low-carbon energy infrastructure has accelerated innovations in energy storage systems (ESS), where Artificial Intelligence (AI) plays a critical role. The integration of AI into ESS enables real-time optimization, predictive maintenance, and smart grid coordination, which are indispensable for achieving sustainability goals and resilience in the face of increasing renewable penetration and distributed generation. This editorial integrates insights from ten high-impact studies to present a comprehensive outlook on how AI-driven methods are significantly transforming the future of energy storage within smart energy systems.

One key highlight of this progress relates to active power balancing across complex hybrid energy systems. Xiao et al. propose a Transfer Learning Double Deep Q-Network (TLDDQN) to handle active power in wind–photovoltaic–storage systems. This method decreases the requirement for thermal generation and effectively adapts to complex environments. Furthermore, it also implements adaptive entropy mechanisms, which can improve agent training, reduce convergence time, and enhance policy learning under inconsistent environments. Compared to particle swarm optimization, this AI-based approach not only accelerates training but also achieves higher accuracy in handling ESS dispatch. Complementing this, Awaji et al. develop a real-time energy management technique for DC microgrids integrating batteries and supercapacitors. Their energy management system (EMS) uses the Incremental Conductance algorithm for maximum power point tracking (MPPT). Furthermore, it effectively maintains grid stability during fault occurrences, which is also validated through OPAL-RT simulations. The study demonstrates the effectiveness of battery balancing, especially for systems that include PV generation and DC motor loads. Overall, the results show that robust control architectures powered by AI can significantly enhance grid flexibility and operational reliability.

In the broader context of intelligent MPPT systems, Alsulami et al. conduct a comparative analysis of traditional and AI-driven MPPT algorithms. Their work shows that Adaptive Neuro-Fuzzy Inference Systems (ANFIS) and Artificial Neural Networks (ANN) outperform conventional perturb-and-observe methods under fluctuating irradiance. However, they also point out that insufficient training data can impair performance in changing temperature conditions. Fuzzy Logic Control is noted for delivering the most balanced and reliable performance across solar and thermal variations, making it

particularly effective for embedded ESS in robotics and autonomous systems. These findings suggest that while deep learning holds promise, hybrid AI methods such as neuro-fuzzy systems may offer more consistent results under real-world uncertainties.

As electrification expands, especially with the growth of electric vehicles (EVs), demand-side management becomes essential. Almutairi et al. present a linear programming-based framework that optimizes EV charging in shared residential parking lots, accounting for transformer limits, charger availability, and user schedules. Their user satisfaction index demonstrates that even at 3%–6% EV penetration, satisfaction exceeds 75%–80% when infrastructure is optimized. Such modeling offers a user-centric approach to managing residential energy demand and reducing grid overload during peak hours. Further advancing this domain, Srihari et al. introduce an Improved Honey Badger Algorithm (IHBA) to manage Vehicle-to-Grid (V2G) and Grid-to-Vehicle (G2V) interactions. Their AI-based EMS integrates PV generation forecasts and user preferences, achieving high efficiency (over 98%), low power loss (0.197 kW), and low harmonic distortion (3.12%). This synergy between AI and EV-ESS coordination reflects a major shift in energy management paradigms, offering a scalable pathway toward intelligent transportation-energy convergence.

Battery health forecasting is another important area where AI adds notable value. Rammohan et al. simulate lithium-ion battery degradation in EVs using an Arrhenius-based mathematical framework. Their model indicates that raising the operating temperature from 25°C to 60°C decreases battery life from 6,000 to 3,000 h. These results quantitatively support the importance of thermal management and precise degradation forecasting. Including such models in AI-aided ESS systems could enable real-time lifecycle tracking and preventive adjustments to charging techniques, particularly in climate-sensitive or high-demand conditions.

Securing AI-powered grids is equally essential. Gupta et al. propose an AdaBoost ensemble model for detecting false data injection attacks in smart grids. Trained on real-world advanced metering infrastructure (AMI) data, the model achieves 85.2%–92.3% accuracy across five attack types, surpassing standard classifiers such as SVM and KNN. It dynamically adapts to misclassifications, making it resilient even with imbalanced datasets—a key factor in safeguarding AI-integrated ESS systems. As digitalization of the grid accelerates, such AI-based cybersecurity layers will become indispensable for ensuring uninterrupted and trustworthy energy services.

Long-term planning also benefits from AI integration. Altamimi presents a techno-economic sustainable planning (TESP) model for meshed microgrids, using voltage stability indices and load margin constraints to guide 10-year expansion strategies. These insights, when combined with AI forecasting tools, enable optimized asset allocation and ESS deployment under dynamic generation and load conditions. By simulating future scenarios and investment trade-offs, such frameworks help grid planners to anticipate challenges and improve resilience to volatility in renewable generation.

In the context of solar-ESS applications, Habib et al. analyze rooftop PV for commercial buildings using HelioScope simulation and field validation. Their system achieved inverter efficiencies of 98.83% and projected CO_2 savings of over 5 million metric tons across 25 years. Results show a levelized cost of energy (LCOE) of $0.0229/kWh and a payback period of 4.22 years. These findings show that a PV-ESS system is economically feasible if it is well-designed. Overall, the study emphasizes that accurate modeling and AI-informed configuration can drive both environmental and financial performance in building-scale deployments.

Lastly, for off-grid and remote applications, hybrid microgrids offer novel solutions. Raza et al. estimate the potential of integrating very small modular reactors (vSMRs) with PV, wind, and battery storage. Their simulations using MATLAB indicate that such systems effectively meet demand. They also generate internal rates of return of around 31%, with payback periods below 4 years. The inclusion of vSMRs ensures base-load support, while AI-managed renewable integration maximizes efficiency and availability. This showcases the potential of modular, AI-supervised energy systems in underserved areas, particularly where transmission infrastructure is weak or absent.

These studies emphasize a substantial transformation in energy systems toward intelligent, adaptive, and secure networks—moving beyond traditional passive infrastructure. AI-based energy storage systems are now central to achieving energy reliability, carbon mitigation, and user satisfaction. AI enables ESS to manage the growing complexities of decentralized energy generation and consumption. It does so through real-time energy dispatch, predictive maintenance, intelligent MPPT, cyber-secure grid interaction, and scalable microgrid design.

Altogether, the ten articles presented provide a forward-looking perspective on how AI can unlock new capabilities in energy storage and system optimization. They offer practical methodologies, validated frameworks, and scalable solutions that will inform the next-generation of sustainable energy design. As editor, I am confident that this body of work will serve as a catalyst for interdisciplinary innovation and play a meaningful role in advancing resilient, intelligent energy storage systems for the future.

Author contributions

MK: Writing – review and editing, Writing – original draft. EJ: Writing – review and editing.

Funding

The author(s) declare that no financial support was received for the research and/or publication of this article.

Conflict of interest

The authors declare that the research was conducted in the absence of any commercial or financial relationships that could be construed as a potential conflict of interest.

Generative AI statement

The author(s) declare that Generative AI was used in the creation of this manuscript. We acknowledge the use of Grammarly to enhance the language and grammar quality of this editorial.

Publisher's note

frontiers | Frontiers in Energy Research

TYPE Original Research
PUBLISHED 18 January 2024
DOI 10.3389/fenrg.2024.1353071

OPEN ACCESS

EDITED BY
Ch. Rami Reddy,
Chonnam National University, Republic of Korea

REVIEWED BY
Nagi Reddy B.,
Vignana Bharathi Institute of Technology, India
Balasubbareddy Mallala,
Chaitanya Bharathi Institute of Technology, India

*CORRESPONDENCE
Abdullah Altamimi,
a.altmimi@mu.edu.sa

RECEIVED 09 December 2023
ACCEPTED 03 January 2024
PUBLISHED 18 January 2024

CITATION
Altamimi A (2024), Techno-economic evaluation of meshed distribution network planning with load growth and expansion with multiple assets across multiple planning horizons.
Front. Energy Res. 12:1353071.
doi: 10.3389/fenrg.2024.1353071

Techno-economic evaluation of meshed distribution network planning with load growth and expansion with multiple assets across multiple planning horizons

Abdullah Altamimi[1,2]*

[1]Department of Electrical Engineering, College of Engineering, Majmaah University, Al-Majma'ah, Saudi Arabia, [2]Engineering and Applied Science Research Center, Majmaah University, Al-Majma'ah, Saudi Arabia

The smart grid paradigm has ushered in an era where modern distribution systems are expected to be both robust and interconnected in topology. This paper presents a techno-economic-based sustainable planning (TESP) strategy, which can be used as a planning framework for linked distribution systems, seeking to discover a realistic solution among competing criteria of diverse genres. In this comparative analysis-based study, three voltage stability assessment indices—VSA_A, VSA_B, and VSA_W—and a loss minimization condition (LMC)-based framework are used in the initial stage to achieve optimal distributed generation (DG)-based asset optimization for siting, followed by sizing. The respective techniques are evaluated across two variants of multiple load growth horizons spread across 10 years. The suggested TESP technique is tested on two variants of a mesh-configured microgrid (MCMG) with varied load growth scenarios. One variant considers a 65-bus MG with a fixed load growth of 2.7% across two load growth horizons. The other variant considers a 75-bus MG with varied load growth across four load growth horizons, encapsulating an expansion-based planning perspective. The numerical results of the suggested TESP approach in a comparative study demonstrate its effectiveness, and it can be used by researchers and planning engineers as a planning framework for interconnected distribution tools across multiple planning horizons. The proposed study would contribute to enhancing the robustness and interconnectivity of smart grid distribution systems. This dual focus could lead to more cost-effective and reliable power distribution systems.

KEYWORDS

power system, renewable energy, distributed generation, energy, energy consumption

1 Introduction

To keep up with the standards of modern societies, the global demand for power has skyrocketed. Distribution networks (DNs) are at the forefront of working at or near operational limits, which causes a variety of techno-economic issues (Evangelopoulos et al., 2016). Furthermore, in competitive deregulated markets, smartly addressed increasing demands must be subjected to acceptable voltage gradients and system losses. DNs were deterministically designed to retain unidirectional power flow with radial structure, allowing for ease of control and minimal protection requirements (Kazmi et al., 2017a).

Furthermore, distributed generation (DG) was not considered during the planning phase, and any future changes to the DN topology will be subjected to new planning tools and considerations. The limitations of traditional grid are being overcome with the advent of smart grids, which are expected to be reliable and provide a variety of feasible techno-economic solutions (Kazmi et al., 2017b). In addition, unlike radial-structured DN, the smart distribution network has given way to loop and meshed topology by closing certain normally open tie-switches (RDN). The incorporation of DG assets into interconnected topology provides a reliable and consistent alternative, helping transform RDN into an active DN (Mallala et al., 2023).

The optimal DG placements (ODGPs) in future smart distribution mechanisms have paved way for interconnected configured DNs and microgrids (MGs), which provides an appropriate opportunity for tightly inhabited urban centers subjected to existing infrastructure modernization (Mahmoud et al., 2017). The techno-economic objective attributed to ODGPs includes acceptable voltage gradients, low system losses and affordable power along with profitability, and overall saving incurred during operations across certain planning horizons (Alvarez-Herault et al., 2015). In various reported research works, researchers have made efforts to address concerned limitations in ODGP-based planning across various distribution mechanisms. Primarily, interconnected DNs have reviewed in terms of index-based optimization methods aimed at the attainment of techno-economic objectives. The prime assets considered are renewable and traditional DGs and reactive power compensation devices like capacitors and distribution static compensator (D-STATCOM). The loop or meshed DN infrastructure-based power system with ODGP-based optimization has considered tie-switches, and the respective impact on various load levels has been evaluated across various load growth horizons besides normal loading conditions. The index-based methodologies have been applied for ODGP in LDN aiming at achieving various technical objectives (Ali et al., 2019; Mallala and Dwivedi, 2022) under normal and load growth conditions for the attainment of techno-economic objectives (Arshad et al., 2018; Javaid et al., 2019).

The DN modernization under SG encompasses several aspects that necessitate the use of decision-making (DM) tools and techniques to reach Pareto optima by considering a multitude of constraints and objective functions. Furthermore, in addition to technical and economic standards, the geographical spread of a new tool necessitates an assessment of environmentally friendly and socially acceptable solutions. As a result, many potential alternative solutions must be assessed across various dimensions (objectives) in order to achieve Pareto optimal solution (Javaid et al., 2019).

Traditional asset optimization methods used in DN were aimed to observe the lowest cost solution. However, they may lack solutions that can be applied to all required rubrics. Furthermore, one of the distinguishing factors of traditional RDNs has been the radiality constraint (Das et al., 2017). According to the literature, DN-centric asset optimization within system restriction primarily intends to siting and sizing of individual assets (Al-Sharafi et al., 2017; Das et al., 2022). On the one hand, the technical side intends to reduce system active/reactive power losses, improve voltage profiles, and maximize DG-based renewable energy penetration, short circuit levels, system stability, acceptable bidirectional power flows, and overall power quality (Al-Sharafi et al., 2017; Das et al., 2022). On the other hand, it aims to improve monetary benefits tend to reduce system loses and costs through optimal allocation of resources and optimal plaining to minimize the maintenance cost.

According to the literature, there are many approaches to reach optimal solutions for the objectives discussed above. These approaches include traditional techniques, i.e., numerical methods, analytical methods, and deterministic methods, in addition to nature-inspired heuristic, meta-heuristic, and AI-inspired neural networks. However, in various scenarios and cases, such algorithms are subjected to achieve solutions which might lead to local optima (Kazmi et al., 2017a; Al-Sharafi et al., 2017; Kazmi et al., 2017b; Das et al., 2017; Javaid et al., 2019; Das et al., 2022; Mallala et al., 2023). However, the addition of further objectives or constraints can potentially increase the computational cost, and the results might not be the optimal result. This limitation is commonly associated with algorithms created by the hybridization of many algorithms which aim to achieve the global optima. Furthermore, multi-criteria optimization techniques are used to achieve Pareto optima amongst conflicting criteria/objectives (Kazmi et al., 2019; Mallala et al., 2023). While the literature acknowledges significant progress in the techno-economic optimization of DN under smart grid paradigms, ongoing research is required to address the complexities of such systems, especially considering the dynamic nature of load growth and system expansion.

The reviewed work from the perspective of voltage stability indices (VSIs) aiming at ODGPs has mostly focused on the RDN and fairly less for the loop of meshed configured DNs across various planning horizons (Kazmi et al., 2019; Paliwal, 2021). The limitation in all of them includes the fact that the load growth is usually considered constant across a certain large-scale horizon of 5 years, and expansion-based planning with an increased number of nodes are usually not catered, despite the reviewed works addressing the concerned issues partially (Modarresi et al., 2016; Kazmi et al., 2021). However, based on the search results, it can be inferred that techno-economic assessments are a common approach for evaluating distribution network planning (Gholami et al., 2022). Additionally, the use of power electronic transformers (PETs) has been proposed for economic dispatch in mixed AC/DC systems (Chen et al., 2021). Furthermore, optimal asset placement in interconnected and reliable modern distribution networks has been considered for smart grid modernization (Khan et al., 2022).

This paper aims to address the limitations in the existing literature by proposing a sustainable planning approach for meshed configured distribution networks (MDNs) with load growth and expansion across multiple planning horizons. The proposed approach, based on optimal distributed generation placement (ODGP) and voltage stability index (VSI), considers two constant load growth horizons and four variable load growth horizons. The approach evaluates techno-economic factors, rather than evaluating only technical or economic factors, and utilizes three VSIs, namely, VSI_A, VSI_B, and VSI_W, for ODGP, followed by loss minimization for the optimal sizing of DGs. The proposed approach is evaluated on an actual MDN-based campus microgrid and offers planning engineers and researchers an efficient and realistic solution for addressing load growth. The main contributions of this paper are as follows:

(i) Evaluating multiple DGs across various VSIs for siting and loss minimization condition (LMC) for sizing.
(ii) Assessing solutions based on techno-economic indices.
(iii) Evaluating solutions across multiple load growth horizons.
(iv) Including planning for both load growth and node expansion.
(v) Conducting numerical assessments on an actual mesh-configured microgrid (MCMG).

The remainder of the paper is organized as follows: Section 2 presents the proposed approach with mathematical terms and computation processes. The simulation arrangement and performance valuation-based indices are shown in Section 3. Section 4 illustrates the effectiveness of the approach across load growth and expansion of node-based planning horizons. The conclusions are reported in Section 5.

2 Proposed approach

The proposed method for optimal DG siting uses three voltage stability assessment indices, namely, *VSA_A*, *VSA_B*, and *VSA_D*, which are derived from literature sources (Kazmi et al., 2019; Paliwal, 2021; Das et al., 2022), aiming at achieving an optimal DG siting using load flow calculation. Load flow calculation is a numerical method used to analyze and calculate the steady-state behavior of an electrical power system. It determines the voltages, currents, and power flows in a power system under different operating conditions. VSA_A is calculated using Eq. 1, which measures the critical value of the sum of the fourth power of the voltage sensitivity index (V_seb) divided by the square of the total number of buses (k) minus a term involving the sum of squares of V_{seb} and a combination of coefficients (A_{AA}, B_{AA}, C_{AA}, and D_{AA}) related to the power flow solution. The critical value of VSA_A ranges from 0, indicating instability, to 1, indicating stability.

Similarly, VSA_B is calculated using Eq. 2, which measures the maximum value of the ratio of a term involving the sum of squares of V_{seb} and a combination of coefficients (E_{BB} and F_{BB}) related to the power flow solution divided by the sum of the fourth power of V_{seb}. The critical value of VSA_B ranges from 1, indicating instability, to 0, indicating stability. *VSA_D* in Eq. 3 shows the deviation, which is positive, pointing toward critical loading conditions of a bus in a distribution network that is close to voltage collapse.

$$VSA\_A = \sum_{i=1}^{k_l}\left(\frac{V_{seb}}{k}\right)^4 - \frac{4}{k}\sum_{i=1}^{k_l}\left(\frac{V_{seb}}{k}\right)^2\left[\left(\frac{A_{AA}}{C_{AA}}\right)+\left(\frac{B_{AA}}{D_{AA}}\right)\right] - \frac{4}{k^2}\left[\left(\frac{A_{AA}}{C_{AA}}\right)-\left(\frac{B_{AA}}{D_{AA}}\right)\right]^2 \geq 0, \quad (1)$$

where

$$A_{AA} = P_{2A}\left[\prod_{i=1}^{n} R_{nr}\right]\left[1-\left(\frac{X_{1x}X_{2x}}{R_{1r}R_{2r}}+\frac{X_{1x}X_{3x}}{R_{1r}R_{3r}}+\frac{X_{2x}X_{3x}}{R_{2r}R_{3r}}\right)\right] + Q_{2A}\left[\prod_{i=1}^{n} nx\right]\left[\left(\frac{R_{1r}R_{2r}}{X_{1x}X_{2x}}+\frac{R_{1r}R_{3r}}{X_{1x}X_{3x}}+\frac{R_{2r}R_{3r}}{X_{2x}X_{3x}}\right)-1\right];$$

$$B_{AA} = P_{2A}\left[\prod_{i=1}^{n} X_{nx}\right]\left[\left(\frac{R_{1r}R_{2r}}{X_{1x}X_{2x}}+\frac{R_{1r}R_{3r}}{X_{1x}X_{3x}}+\frac{R_{2r}R_{3r}}{X_{2x}X_{3x}}\right)-1\right] - Q_{2A}\left[\prod_{i=1}^{n} R_{nr}\right]\left[1-\left(\frac{X_{1x}X_{2x}}{R_{1r}R_{2r}}+\frac{X_{1x}X_{3x}}{R_{1r}R_{3r}}+\frac{X_{2x}X_{3x}}{R_{2r}R_{3r}}\right)\right];$$

$$C_{AA} = \left[abs\left\{\sum_{k\neq l}^{n} R_k R_l - \sum_{k\neq l}^{n} X_k X_l\right\} + 0.001\right];$$

$$D_{AA} = abs\left(R_1X_2 + R_2X_1 + R_1X_3 + R_3X_1 + R_2X_3 + R_3X_2\right) = abs\left[\sum_{k\neq l}^{n} R_k X_l\right].$$

$$VSA\_B = 4k^2\frac{\left[E_{BB}\sum_{i=1}^{k_l}\left(\frac{V_{seb}}{k}\right)^2 + \left(\frac{F_{BB}}{k}\right)^2\right]}{\sum_{i=1}^{k_l}\left(\frac{V_{sb}}{k}\right)^4} \leq 1, \quad (2)$$

where

$$E_{BB} = [abs\{(P_{2b}R_{1r} + P_{4b}R_{2r} + P_{6b}R_{3r}) + (Q_{2b}X_{1x} + Q_{4b}X_{2x} + Q_{6b}X_{3x})\} + 0.001];$$

$$F_{BB} = [abs\{(P_{2b}X_{1x} + P_{4b}X_{2x} + P_{6b}X_{3x}) - (Q_{2b}R_{1r} + Q_{4b}R_{2r} + Q_{6b}R_{3r})\} + 0.001].$$

$$VSA\_D = \sum_{i=1}^{k_l}(V_{seb} - V_{reb})^2 \geq 0, \quad (3)$$

where V_{seb} is the voltage value as a reference of substation voltage (sending end bus). V_{reb} represents the voltage value of the receiving end node/bus throughout the distribution network.

The weighted VSI factor is delegated as *VSI_W* and is based on weighted normalized values of *VSA_Aw*, *VSA_Bw*, and *VSA_Dw*, as shown in Eq. 4:

$$VSA_W = [(\omega_{Aw} \times VSI_{Aw}) + (\omega_{Bw} \times VSI_{Bw}) + (\omega_{Dw} \times VSI_{Dw})], \quad (4)$$

where $\omega_{Aw}, \omega_{Bw}, and\ \omega_{Dw}$ are the weight factors of each individual normalized values of VSI, and their addition should be 1.

The technique of loss minimization condition (LMC) remains the same as mentioned in Mahmoud et al. (2017). The expressions for LMC for P_{Loss} and Q_{Loss} subjected to zero loop currents are illustrated in Eqs 5, 6 as P_LMC and Q_LMC, respectively, as follows:

$$P_{LMC} = [(I_{2B})^2R_{2r} + (I_{1B})^2R_{1r} + (I_{3B})^2R_{3r}] \geq 0; \quad (5)$$

$$Q\_LMC = [(I_{2B})^2X_{2x} + (I_{1B})^2X_{1x} + (I_{3B})^2X_{3x}] \geq 0, \quad (6)$$

where $I_{1B}, I_{2B}, \text{and } I_{3B}$ are the individual line current across different feeders. $R_{1r}, R_{2r}, and\ R_{3r}$ are the individual line resistance across different feeders. $X_{1x}, X_{2x}, \text{and } X_{3x}$ are the individual line reactance across different feeders.

3 The simulation arrangement and performance valuation-based indices

Figure 1 shows the flow chart of the techno-economic-based sustainable planning (TESP) strategy for evaluating several load increase scenarios throughout DG placement planning periods. The

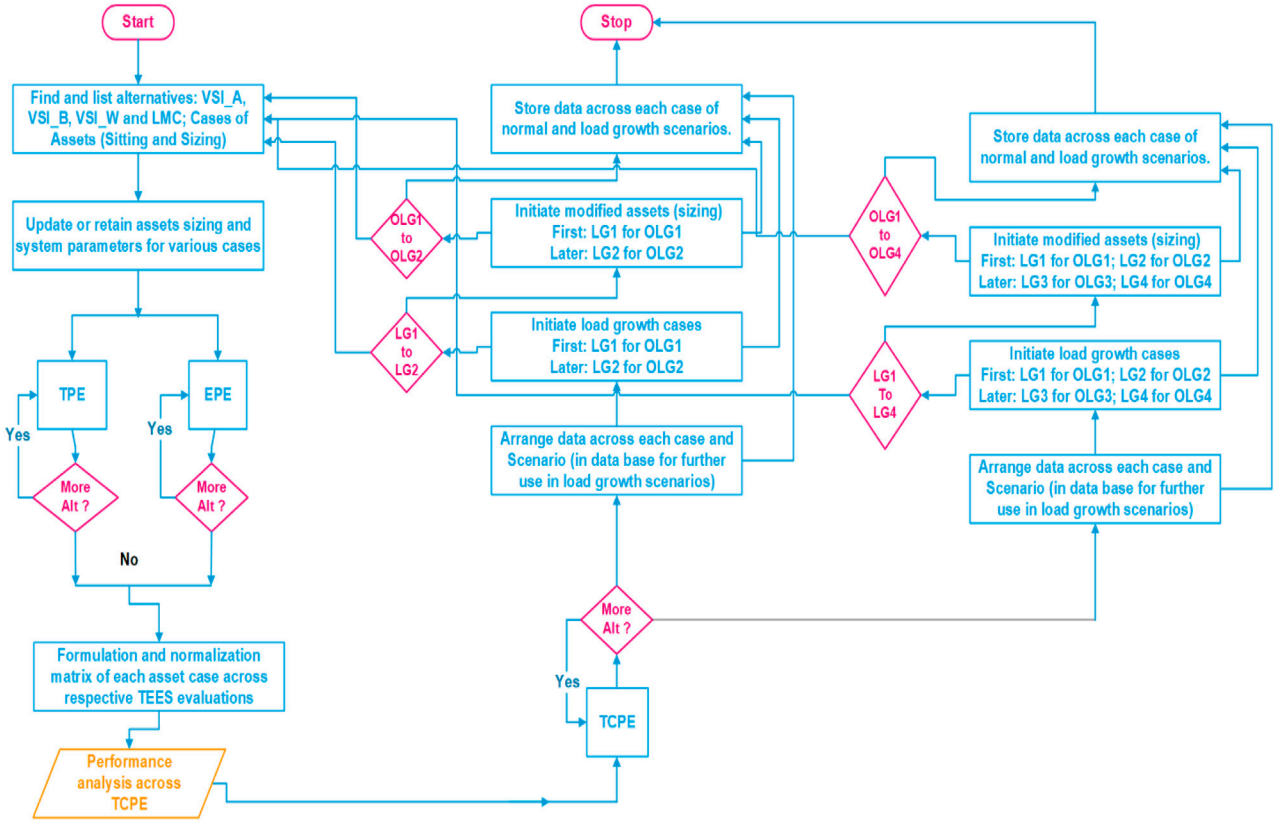

FIGURE 1
Flow chart of the proposed techno-economic-based sustainable planning (TESP) strategy across multiple planning horizons.

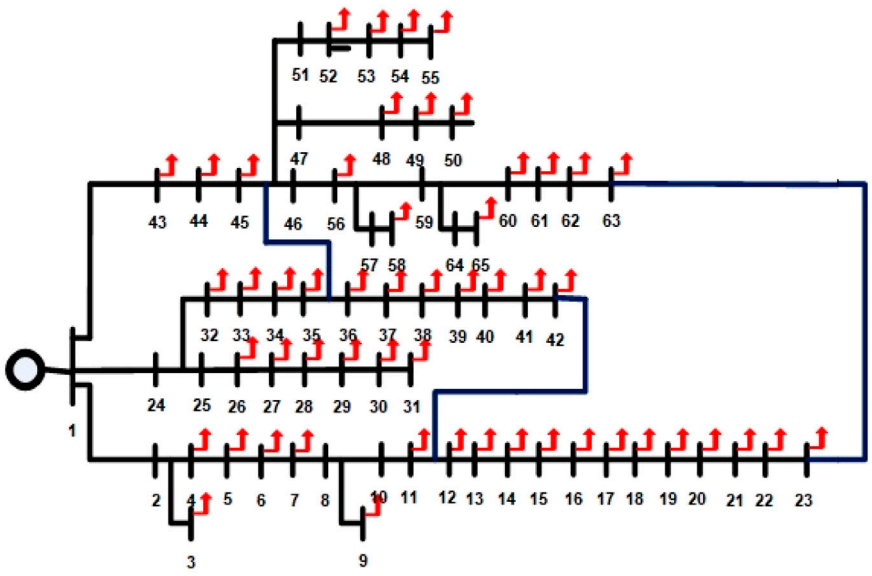

FIGURE 2
Sixty-five-bus microgrid meshed configured distribution network.

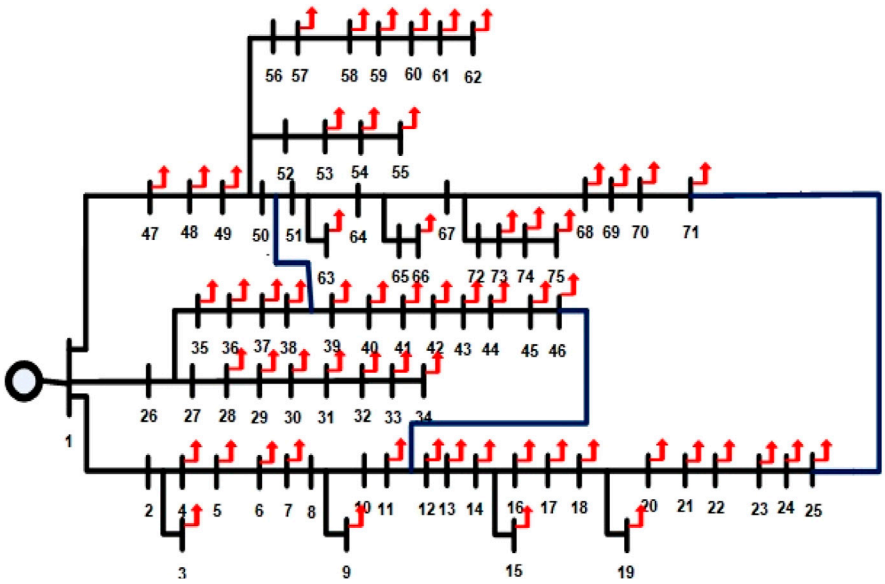

FIGURE 3
Seventy-five-bus expanded microgrid meshed configured distribution network.

TABLE 1 Technical performance evaluation parameters (Kazmi et al., 2021).

S. no.	Technical parameter	Designation	Relationship	Objective
1	Active power loss (P_{Loss}) (KW)	P_{Loss}	$\sum_{i=1}^{m_l-1} P_{Loss}{}^{TDS} + \sum P_{TB}$	Minimize
2	Reactive power loss (Q_{Loss}) (KVAR)	Q_{Loss}	$\sum_{i=1}^{m_l-1} Q_{Loss}{}^{TDS} + \sum Q_{TB}$	Minimize
3	Active power loss minimization (%)	P_{LossM}	$[\frac{P\_L_{No\_DG} - P\_L_{M\_DG}}{P\_L_{No\_DG}}] \times 100$	Maximize
4	Reactive power loss minimization (%)	Q_{LossM}	$[\frac{Q\_L_{No\_DG} - Q\_L_{M\_DG}}{Q\_L_{No\_DG}}] \times 100$	Maximize
5	Penetration of DG by percentage (%)	PDGP	$(\sum_{a=1}^{M} P_{DG} / \sum_{b=1}^{N} P_{LD}) \times 100$	Maximize
6	Voltage level (P.U.)	VL	V = 1.0 (reference voltage)	Maximize

research is carried out in two scenarios: one with two horizons of load expansion through a fixed node distribution network and the other with four horizons of expandable load development. A test system setup of a meshed configured microgrid is considered with two variants in this work: the first variant with a 65-bus system for fixed node evaluation, as shown in Figure 2, and the second variant with a 75-bus expanded system, as shown in Figure 3. The entire load horizon is 10 years, and both distribution network types are set up in a meshed topology. Without any DG in the meshed design, the normal active and reactive power loads in both networks are 3,950.505 KW and 1,913.317 KVAR, respectively, with losses of 60.51 KW and 34.63 KVAR. The load growth for 65-node MG is 2.7% in horizon 1 of 5 years (until 2025) and 2.7% in horizon 2 of 5 years (until 2030). The load growth for 75-node MG is 14.9% in horizon 1 of 3 years (until year 2023), 2.7% in horizon 2 of 2 years (until year 2025), 17.75% in horizon 3 of 3 years (until year 2028), and 2.7% in horizon 4 of 2 years (until year 2030). Table 1 and Table 2 show the technical and economic performance evaluation factors, respectively (Kazmi et al., 2021). Table 3 presents the load growth values for 65- and 75-bus meshed MGs in various planning horizons.

The base case mathematical model is created in MATLAB, and outcomes from the m-file are used to identify the weakest nodes according to the VSI. The outcome-based numericals were collected from the Simulink model setup and were used to perform the simulation The loop currents across TSs will be simulated until became nearly zero and voltages across the various buses became identical, which corresponded to the optimal sizing of assets based on 1% termination criteria. Finally, the obtained values from m-files are implemented in a MATLAB 2018a program, where the suggested multi-criteria sustainable planning technique is assessed using various matrices.

TABLE 2 Cost-economic performance assessment parameters (Kazmi et al., 2021).

S. no.	Technical parameter	Designation	Relationship	Objective
1	Cost of P_{Loss} in millions USD (M$)	CP_{Loss}	$[P\_L \times E_U \times T_Y\ (8760\,hrs)]$	Minimize
2	Savings of P_{Loss} in millions USD (M$)	SP_{Loss}	$\frac{PLC_{No\_DG} - PLC_{M\_DG}}{PLC_{No\_DG}} \times 100$	Maximize
3	Cost of active power for DG ($/MWh)	CDGP	$a \times P_{DG}^2 + b \times P_{DG} + c$, where a = 0, b = 20, and c = 0.25	Minimize
4	Cost of reactive power for DG ($/MVAR)	CDGQ	$[C(S_{DG\_M}) - C(\sqrt{(S_{DG\_M}^2 - P_{DG}^2)})] \times k$, where $S_{DG_M} = \frac{P_{DG_M}}{\cos\theta} = \frac{1.1 \times P_{DG}}{\cos\theta}; k = 0.5 - 1$	Minimize

TABLE 3 Load growth values across 65- and 75-bus meshed MGs.

Year	Active load (KW) 65 bus	Reactive load (KVAR) 65 bus	Apparent load (KVA) 65 bus	Load growth % 65 bus
2020	3949.77	1912.97	4388.64	-
2025	4512.56	2185.54	5013.96	2.7%
2030	5155.54	2496.95	5728.3813	2.7%
Year	Active load (KW) 75 bus	Reactive load (KVAR) 75 bus	Apparent load (KVA) 75 bus	Load growth % 75 bus
2020	3949.77	1912.97	4388.64	-
2023	5988.14	2899.97	6653.39	14.9
2025	6315.96	3058.84	7017.68	2.7
2028	10305.94	4991.11	11452.28	17.75
2030	10870	5264.24	10277.63	2.7

4 Results and discussion

4.1 Case 1 evaluation results

The cases with respective designations, in terms of nomenclature, are illustrated with case (C#) that have been evaluated across the following scenarios (C#/S#):

Case 1 (C1): DG placement in the 65-bus meshed configured microgrid.

Scenario 1 (C1/S1): evaluation across the radial network across two planning horizons of 5 years each of same load growth of 2.7%.

Scenario 2 (C1/S2): evaluation across the mesh network with VSA_A across two planning horizons of 5 years each of same load growth of 2.7%.

Scenario 3 (C1/S3): evaluation across the mesh network with VSA_B across two planning horizons of 5 years each of same load growth of 2.7%.

Scenario 4 (C1/S3): evaluation across the mesh network with VSA_W across two planning horizons of 5 years each of same load growth of 2.7%.

The two load growth horizons for C1 are shown with the following nomenclature:

Normal load:

- 2020
- 2020 optimal reinforcement (2020_O)

Load growth 1 across 5 years with a 2.7% growth rate:

- 2025
- 2025 optimal reinforcement (2025_O)

Load growth 1 across 5 years with a 2.7% growth rate:

- 2030
- 2030 optimal reinforcement (2030_O)

The DG placement and sizing at a 0.9 lagging power factor (LPF) in the 65-bus meshed configured MG evaluated across two planning horizons of 5 years each with a load growth of 2.7% increase per annum are illustrated in Tables 4–6. The 2.7% increment of power demand was chosen to simulate a realistic load growth scenario in the distribution system. This value was based on historical trends and future projections of population growth, urbanization, and industrialization in the area served by the distribution system. The DG siting and sizing based on VSA_A–LMC, VSA_B–LMC and VSA_W–LMC approaches across various parameters are shown in Tables 4–6, respectively. In all those tables, DG units with their capacities and an operating lagging power factor of 0.9 have been illustrated across abovementioned C1 scenarios. The 0.9 power factor was chosen as a typical value for the loads in the distribution system. This value is not necessarily regulated, but it is often used as a benchmark for power factor correction and improvement efforts in distribution systems. It is also a reasonable assumption for modeling and simulation purposes as it represents a moderate level of reactive power demand in the system.

TABLE 4 DG siting and sizing for a 65-bus meshed MG at 0.9 lagging power factor based on VSA_A and LMC approaches.

DG siting and sizing considering VSA_A- and LMC-based parameters	Normal case 2020	Optimal case 2020_O	5-year non-optimal case 2025	5-year optimal case 2025_O	10-year non-optimal case 2030	10-year optimal case 2030_O
Active/reactive load (KW + jKVAR)	3949.77 + j1912.97	3949.77 + j1912.97	4512.64 + j2185.82	4512.64 + j2185.82	5155.65 + j2497.17	5155.65 + j2497.17
Grid active/reactive power (KW + jKVAR)	4010.28 + j1947.6	1084.39 + j517.6	1650.54 + j7993.66	1389.52 + j666.94	2036.89 + j982.99	1550.84 + 746.78
DG1 bus and size (KW + j KVAR)	—	DG_5 @ 558 + j270.25	DG_5 @ 558 + j270.25	DG_5 @ 558 + j270.25	DG_5 @ 558 + j270.25	DG_5 @ 558 + j270.25
DG2 @ bus and size (KW + j KVAR)	—	DG_20 @ 441 + j213.59	DG_20 @ 441 + j213.59	DG_20 @ 630 + j305.12	DG_20 @ 630 + j305.12	DG_20 @ 720 + j348.71
DG3 @ bus and size (KW + j KVAR)	—	DG_40 @ 783 + j379.22	DG_40 @ 783 + j379.22	DG_40 @ 855 + j414.1	DG_40 @ 855 + j414.1	DG_40 @ 1170 + j566.66
DG4 @ bus and size (KW + j KVAR)	—	DG_52 @ 729 + j353.07	DG_52@ 729 + j353.07	DG_52 @ 729 + j353.07	DG_52 @ 729 + j353.07	DG_52 @ 810 + j392.3
DG5 @ bus and size (KW + j KVAR)	—	DG_62 @ 414 + j200.51	DG_62@ 414 + j200.51	DG_62 @ 414 + j200.51	DG_62 @ 414 + j200.51	DG_62 @ 414 + j200.51
Active power loss (KW)	60.51	59.62	62.90	62.88	67.24	67.19
Reactive power loss (KVAR)	34.63	21.27	24.48	24.17	28.87	28.04

TABLE 5 DG siting and sizing for a 65-bus meshed MG at 0.9 lagging power factor based on VSA_B and LMC approaches.

DG siting and sizing considering VSA_B- and LMC-based parameters	Normal case 2020	Optimal case 2020_O	5-year non-optimal case 2025	5-year optimal case 2025_O	10-year non-optimal case 2030	10-year optimal case 2030_O
Active/reactive load (KW + jKVAR)	3949.77 + j1912.97	3949.77 + j1912.97	4512.64 + j2185.82	4512.64 + j2185.82	5155.65 + j2497.17	5155.65 + j2497.17
Grid active/reactive power (KW + jKVAR)	4010.28 + j1947.6	922.45 + j440.09	1488.62 + j716.39	1200.61 + j576.59	1847.99 + j892.89	1442.97 + j696.25
DG1 bus and size (KW + jKVAR)	—	DG_5 @ 270 + j130.77	DG_5 @ 270 + j130.77	DG_5 @ 270 + j130.77	DG_5 @ 270 + j130.77	DG_5 @ 315 + j152.56
DG2 @ bus and size (KW + jKVAR)	—	DG_14 @ 630 + j305.12	DG_14 @ 630 + j305.12	DG_14 @ 720 + j348.71	DG_14 @ 720 + j348.71	DG_14 @ 810 + j392.3
DG3 @ bus and size (KW + jKVAR)	—	DG_17 @ 477 + j231.02	DG_17 @ 477 + j231.02	DG_17 @ 630 + j305.12	DG_17 @ 630 + j305.12	DG_17 @ 720 + j348.71
DG4 @ bus and size (KW + jKVAR)	—	DG_38 @ 855 + j414.1	DG_38 @ 855 + j414.1	DG_38 @ 900 + j435.89	DG_38 @ 900 + j435.89	DG_38 @ 1080 + j523.07
DG5 @ bus and size (KW + jKVAR)	—	DG_43 @ 855 + j414.1	DG_43 @ 855 + j414.1	DG_43 @ 855 + j414.1	DG_43 @ 855 + j414.1	DG_43 @ 855 + j414.1
Active power loss (KW)	60.51	59.68	62.98	62.97	67.34	67.32
Reactive power loss (KVAR)	34.63	22.23	25.68	25.36	30.31	29.82

For the VSA_A–LMC-based approach, the normal scenario in both cases is the same, such as the year 2020 scenario. Load has increased linearly at 2.7 percent per year in the actual model after 3 years, as well as due to the addition of new load programs. Because the load has changed and the DG capacity has remained the same as in scenario 2020, DG values for scenario 2023 will need to be adjusted for this model after 3 years. The DG capacity has been re-optimized to meet the model's current requirement. According to scenario 2020, weak nodes would remain the same.

Similarly, for VSA_B–LMC- and VSA_W–LMC-based approach variants, load has increased linearly at 2.7 percent per year in the actual model after 3 years, as well as due to the addition of new load programs. Because the load has changed and the DG capacity has remained the same as in scenario 2020, DG values for scenario 2023 will need to be optimized for this model after 3 years. The DG capacity has also been re-optimized to meet the model's current requirement. All three VSIs were performed according to their respective criteria in order to increase the voltage profile and maximize the model's technical characteristics.

TABLE 6 DG siting and sizing for a 65-bus meshed MG at 0.9 lagging power factor based on VSA_W and LMC approaches.

DG siting and sizing considering VSA_W-LMC-based parameters	Normal case 2020	Optimal case 2020_O	5-year non-optimal case 2025	5-year optimal case 2025_O	10-year non-optimal case 2030	10-year optimal case 2030_O
Active/reactive load (KW + jKVAR)	3949.77 + j1912.97	3949.77 + j1912.97	4512.64 + j2185.82	4512.64 + j2185.82	5155.65 + j2497.17	5155.65 + j2497.17
Grid active/reactive power (KW + jKVAR)	4010.28 + j1947.6	1534.42 + j736.06	2100.59 + j1012.34	1677.56 + j807	2324.93 + j1123.1	1856.9 + j895.88
DG1 bus and size (KW + jKVAR)	—	DG_5 @ 360 + j174.36	DG_5 @ 360 + j174.36	DG_5 @ 423 + j204.87	DG_5 @ 423 + 204.87	DG_5 @ 468 + 226.66
DG2 @ bus and size (KW + jKVAR)	—	DG_17 @ 270 + j130.77	DG_17 @ 270 + j130.77	DG_17 @ 405 + j196.15	DG_17 @ 405 + j196.15	DG_17 @ 423 + j204.87
DG3 @ bus and size (KW + jKVAR)	—	DG_38 @ 585 + j283.33	DG_38 @ 585 + j283.33	DG_38 @ 675 + j326.92	DG_38 @ 675 + j326.92	DG_38 @ 675 + j326.92
DG4 @ bus and size (KW + jKVAR)	—	DG_42 @ 630 + j305.12	DG_42 @ 630 + j305.12	DG_42 @ 675 + j326.92	DG_42 @ 675 + j326.92	DG_42 @ 720 + j348.71
DG5 @ bus and size (KW + jKVAR)	—	DG_62 @ 630 + j305.12	DG_62 @ 630 + j305.12	DG_62 @ 720 + j348.71	DG_62 @ 720 + j348.71	DG_62 @ 810 + j392.3
Active power loss (KW)	60.51	59.65	62.95	62.92	67.28	67.25
Reactive power loss (KVAR)	34.63	21.79	25.22	24.75	29.5	28.93

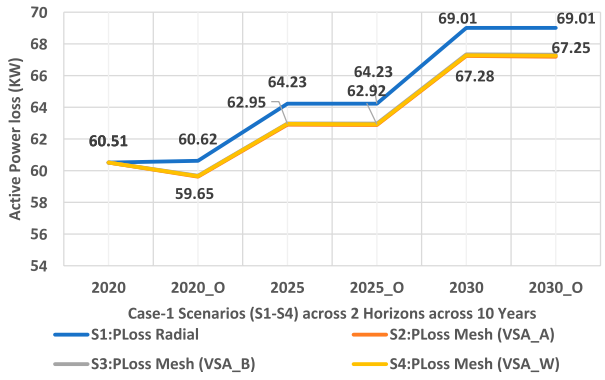

FIGURE 4
Active power loss trend across two planning horizons in the 65-bus meshed configured MG-based distribution network.

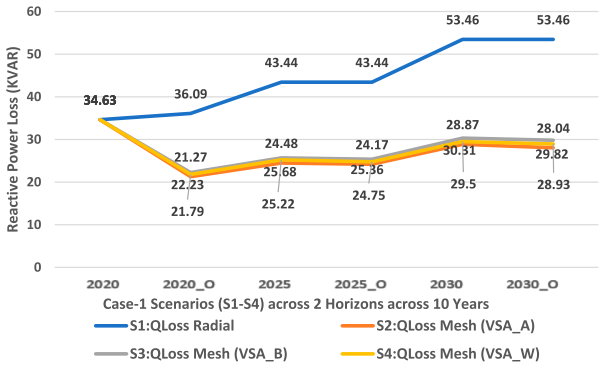

FIGURE 5
Reactive power loss trend across two planning horizons in the 65-bus meshed configured MG-based distribution network.

In Figure 4, case 1 shows an active power loss trend across two planning horizons (accumulatively 10 years) in the 65-bus meshed configured MG-based distribution network. It can be observed that the active power losses have reduced in meshed configured approaches in C1, scenarios 2–4 compared to the radial counterpart in scenario 1.

Figure 5 and Figure 6 show that a substantial improvement is active and prominent in reactive power loss minimization across all scenarios of C1. The reason being that reactive power loss is high because the distribution network is laid underground rather than overhead cables. Figure 7 shows that each VSI enhanced the voltage profile of the network according to its own specifications, and that all VSIs are significantly superior to a simple interconnected network. After maximizing the value of DG penetration in accordance with the policy, the voltage of each node is brought to unity. For this scenario, a new optimized model has been acquired. Figure 8 shows a phenomenal reduction in the cost of active power losses and an increase in savings.

4.2 Case 2 evaluation results

The cases with respective designations, in terms of nomenclature, are illustrated with case (C#) that have been evaluated across the following scenarios (C#/S#):

Case 2 (C2): DG placement in the 75-bus meshed configured microgrid.

Scenario 1 (C2/S1): evaluation across the radial network across four different planning horizons of 5 years each of various load growth levels.

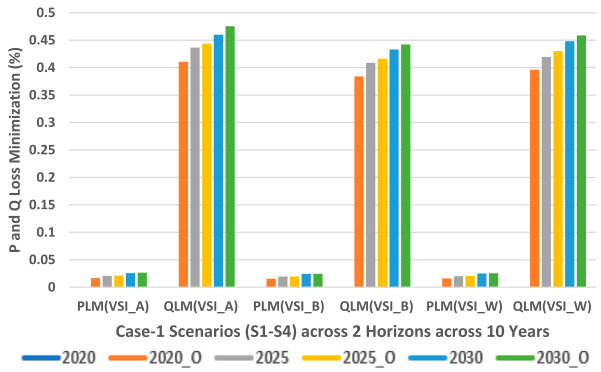

FIGURE 6
Active and reactive power loss minimization trends across two planning horizons in the 65-bus meshed configured MG-based distribution network.

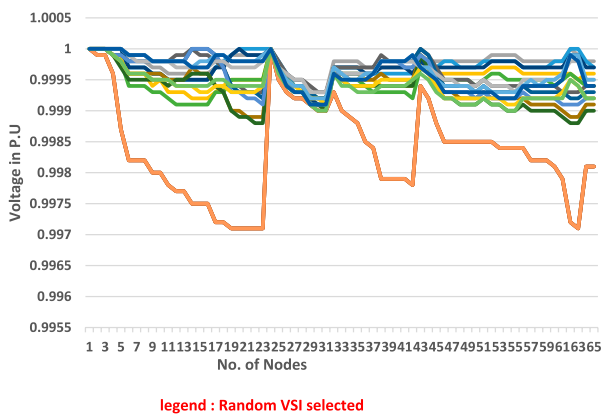

FIGURE 7
Voltage profile trend across two planning horizons in the 65-bus meshed configured MG-based distribution network.

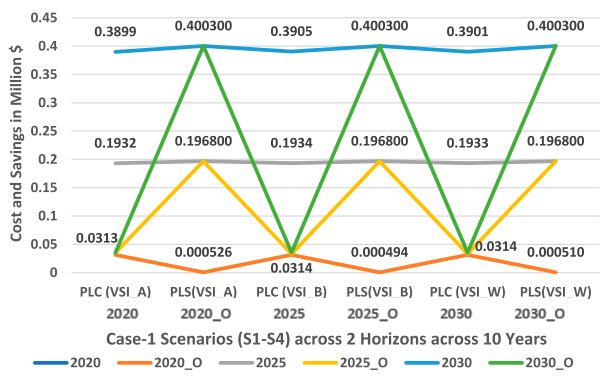

FIGURE 8
Cost of active power losses and savings trend across two planning horizons in the 65-bus meshed configured MG-based distribution network.

Scenario 2 (C2/S2): evaluation across the mesh network with VSA_A across four different planning horizons of various load growth levels.

Scenario 3 (C2/S3): evaluation across the mesh network with VSA_B across four different planning horizons of various load growth levels.

Scenario 4 (C2/S3): evaluation across the mesh network with VSA_W across four different planning horizons of various load growth levels.

The four load growth horizons for C2 are shown with the following nomenclature:

Normal load:

- 2020
- 2020 optimal reinforcement (2020_O)

Load growth 1 across 3 years with a 14.9% growth rate:

- 2023
- 2023 optimal reinforcement (2023_O)

Load growth 2 across 2 years with a 2.7% growth rate:

- 2025
- 2025 optimal reinforcement (2025_O)

Load growth 1 across 3 years with a 17.75% growth rate:

- 2028
- 2028 optimal reinforcement (2028_O)

Load growth 4 across 2 years with a 2.7% growth rate:

- 2030
- 2030 optimal reinforcement (2030_O)

The DG placement and sizing at 0.9 lagging power factor in the 75-bus meshed configured MG evaluated across four planning horizons of 2–3 years each with a variable expansion-based load growth increase per annum are illustrated in Tables 7–9. The DG siting and sizing based on VSA_A–LMC-, VSA_B–LMC-, and VSA_W–LMC approaches are illustrated across various parameters in Tables 7–9, respectively. In all those tables, DG units with their capacities and an operating lagging power factor (LPF) of approximately 0.9 have been illustrated across abovementioned C2 scenarios. All the data are provided in a self-explanatory manner.

In Figure 9, case 2 shows an active power loss trend across four planning horizons (accumulatively 10 years) in the 75-bus meshed configured MG-based distribution network. It can be observed that the active power losses have reduced in meshed configured approaches in C2, scenarios 2–4 compared to the radial counterpart in scenario 2.

Figure 10 and Figure 11 show that a substantial improvement is active and prominent in reactive power loss minimization across all scenarios of C2 and is quite greater than that in C1 and respective scenarios. The reason being that reactive power loss is high because the distribution network is laid underground rather than overhead

TABLE 7 DG siting and sizing for a 75-bus meshed MG at 0.9 lagging power factor based on VSA_A and LMC approaches.

DG place/size considering VSA_A–LMC-based parameters	Normal case 2020	Optimal case 2020_O	3-year non-optimal case 2023	3-year optimal case 2023_O	5-year non-optimal case 2025	5-year optimal case 2025_O	8-year non-optimal case 2028	8-year optimal case 2028_O	10-year non-optimal case 2030	10-year optimal case 2030_O
Active/reactive load (KW + jKVAR)	3949.77 + j1912.97	2196.99 + j1065.2	3151.17 KW + j1529.96 KVAR	2196.99 KW + j1065.18 KVAR	3221.19 KW + j1564.47 KVAR	2240.01 KW + j 1086.63 KVAR	7303.55 KW + j3773.83 KVAR	2521.24 KW + j1221.49 KVAR	7882.44 KW + j 4085.16 KVAR	2541.47 KW + j 1255.03 KVAR
Grid active/reactive power (KW + jKVAR)	4010.28 + j1947.6	5988.14 +j2899.97	5988.14 KW + j2899.97 KVAR	5988.14 KW + j2899.97 KVAR	6315.96 KW + j3058.84 KVAR	6315.96 KW + j 3058.84 KVAR	10305.94 KW + j4991.11 KVAR	10305.94 KW + j 4991.11 KVAR	10870 KW + j 5264.24 KVAR	10870 KW + j 5264.24 KVAR
DG1 bus and size (KW + jKVAR)	—	DG_5 @540 + j261.53	DG_5 = 558 KW + j270.25 KVAR	DG_5 = 540 KW + j261.53 KVAR	DG_5 = 558 KW + j270.25 KVAR	DG_5 = 540 KW + j261.53 KVAR	DG_5 @ 558 KW + j 270.25 KVAR	DG_5 @ 585 KW + j283.33 KVAR	DG_5 @ 558 KW + j 270.25 KVAR	DG_5 @ 630 KW + j305.12 KVAR
DG2 @ bus and size (KW + jKVAR)	—	DG_22 @ 990 + j479.48	DG_22 = 441 KW + j213.59 KVAR	DG_22 = 990 KW + j479.48 KVAR	DG_22 = 630 KW + j305.12 KVAR	DG_22 = 990 KW + j479.48 KVAR	DG_22 @ 630 KW + j305.12 KVAR	DG_22 @ 1350 KW + j653.84 KVAR	DG_22 @ 630 KW + j305.12 KVAR	DG_22 @ 1350 KW + j653.84 KVAR
DG3 @ bus and size (KW + jKVAR)	—	DG_44 @ 855 + j414.1	DG_44 = 783 KW + j379.22 KVAR	DG_44 = 855 KW + j414.1 KVAR	DG_44 = 855 KW + j414.1 KVAR	DG_44 = 1008 KW + j488.2 KVAR	DG_44 @ 855 KW + j414.1 KVAR	DG_44 @ 1620 KW + j784.6 KVAR	DG_44 @ 855 KW + j414.1 KVAR	DG_44 @ 1620 KW + j784.6 KVAR
DG4 @ bus and size (KW + jKVAR)	—	DG_57@ 1080 +j523.07	DG_57 = 729 KW + j353.07 KVAR	DG_57 = 1080 KW + j523.07 KVAR	DG_57 = 729 KW + j353.07 KVAR	DG_57 = 1215 KW + j588.45 KVAR	DG_57 @ 729 KW + j353.07 KVAR	DG_57 @ 3870 KW + j1874.3 KVAR	DG_57 @ 729 KW + j353.07 KVAR	DG_57 @ 4293 KW + j2079.2 KVAR
DG5 @ bus and size (KW + jKVAR)	—	DG_70 @ 414 + j200.51	DG_70 = 414 KW + j.51 KVAR	DG_70 = 414 KW + j200.51 KVAR	DG_70 = 414 KW + j200.51 KVAR	DG_70 = 414 KW + j200.51 KVAR	DG_70 @ 414 KW + j200.51 KVAR	DG_70 @ 540 KW + j261.53 KVAR	DG_70 @ 414 KW + j 200.51 KVAR	DG_70 @ 630 KW + j305.12 KVAR
Active power loss (KW)	60.51	87.85	88.03 KW	87.85 KW	91.23 KW	91.05 KW	183.61 KW	180.3 KW	198.44 KW	194.47 KW
Reactive power loss (KVAR)	34.63	43.9	46.63 KVAR	43.9 KVAR	48.68 KVAR	45.96 KVAR	325.77 KVAR	87.98 KVAR	363.97 KVAR	118.67 KVAR

10.3389/fenrg.2024.1353071

TABLE 8 DG siting and sizing for a 75-bus MG at 0.9 lagging power factor based on VSA_B and LMC approaches.

DG place/size considering VSA_A-LMC-based parameters	Normal case 2020	Optimal case 2020_O	3-year non-optimal case 2023	3-year optimal case 2023_O	5-year non-optimal case 2025	5-year optimal case 2025_O	8-year non-optimal case 2028	8-year optimal case 2028_O	10-year non-optimal case 2030	10-year optimal case 2030_O
Active/reactive load (KW + jKVAR)	3949.77 + j1912.97	2989.35 KW + j1454.05 KVAR	3320.48 KW + j1616.58 KVAR	2116.2 KW + j1028.77 KVAR	2447.26 KW + j1190.52 KVAR	2195.26 KW + j1068.28 KVAR	6277.59 KW + j3049.41 KVAR	2865.56 KW + j1613.34 KVAR	3444.16 KW + j1704.39 KVAR	2832.1 KW + j1401.92 KVAR
Grid active/reactive power (KW + jKVAR)	4010.28 + j1947.6	5988.14 KW + j2899.97 KVAR	6315.96 KW + j 3058.84 KVAR	5988.14 KW + j 2899.97 KVAR	6315.96 KW + j 3058.84 KVAR	6315.96 KW + j 3058.84 KVAR	10305.94 KW + j 4991.11 KVAR	10305.94 KW + j4991.11KVAR	10870 KW + j5264.24 KVAR	10870 KW + j5264.24 KVAR
DG1 bus and size (KW + jKVAR)	—	DG_5 = 270 KW + j130.77 KVAR	DG_5 = 270 KW + j130.77 KVAR	DG_5 = 270 KW + j130.77 KVAR	DG_5 = 270 KW + j130.77 KVAR	DG_5 = 270 KW + j 130.77 KVAR	DG_5 = 270 KW + j130.77 KVAR	DG_5 = 270 KW + j130.77 KVAR	DG_5 = 270 KW + j130.77 KVAR	DG_5 = 315 KW + j152.56 KVAR
DG2 @ bus and size (KW + jKVAR)	—	DG_14 = 630 KW + j305.12 KVAR	DG_14 = 630 KW + j 305.12 KVAR	DG_14 = 765 KW + j370.51 KVAR	DG_14 = 765 KW + j370.51 KVAR	DG_14 = 792 KW + j383.58 KVAR	DG_14 = 792 KW + j 383.58 KVAR	DG_14 = 783 KW + j 379.22 KVAR	DG_14 = 783 KW + j379.22 KVAR	DG_14 = 765 KW + j370.51 KVAR
DG3 @ bus and size (KW + jKVAR)	—	DG_18 = 477 KW + j231.02 KVAR	DG_18 = 477 KW + j231.02 KVAR	DG_18 = 1035 KW + j501.27 KVAR	DG_18 = 1035 KW + j501.27 KVAR	DG_18 = 1080 KW + j 523.07 KVAR	DG_18 = 1080 KW + j523.07 KVAR	DG_18 = 1800 KW + j871.78 KVAR	DG_18 = 1800 KW + j871.78 KVAR	DG_18 = 1890 KW + j915.37 KVAR
DG4 @ bus and size (KW + jKVAR)	—	DG_42 = 855 KW + j414.1 KVAR	DG_42 = 855 KW + j414.1 KVAR	DG_42 = 1035 KW + j501.27 KVAR	DG_42 = 1035 KW + j501.27 KVAR	DG_42 = 1080 KW + j 523.07 KVAR	DG_42 = 1080 KW + j523.07 KVAR	DG_42 = 2070 KW + j1002.5 KVAR	DG_42 = 2070 KW + j1002.5 KVAR	DG_42 = 2295 KW + j1111.5 KVAR
DG5 @ bus and size (KW + jKVAR)	—	DG_47 = 855 KW + j414.1 KVAR	DG_47 = 855 KW + j414.1 KVAR	DG_47 = 855 KW + j 414.1 KVAR	DG_47 = 855 KW + j414.1 KVAR	DG_47 = 990 KW + j 479.48 KVAR	DG_47 = 990 KW + j479.48 KVAR	DG_47 = 2700 KW + j1307.7 KVAR	DG_47 = 2700 KW + j1307.7 KVAR	DG_47 = 2970 KW + j1438.4 KVAR
Active power loss (KW)	60.51	88.21 KW	91.52 KW	88.06 KW	91.30 KW	91.30 KW	183.65 KW	182.62 KW	197.16 KW	197.10 KW
Reactive power loss (KVAR)	34.63	49.19 KVAR	52.85 KVAR	46.72 KVAR	49.60 KVAR	49.41 KVAR	98.27 KVAR	86.13 KVAR	132.12 KVAR	126.02 KVAR

10.3389/fenrg.2024.1353071

TABLE 9 DG siting and sizing for a 75-bus meshed MG at 0.9 lagging power factor based on VSA_W and LMC approaches.

DG place/size considering VSA_A–LMC-based parameters	Normal case 2020	Optimal case 2020_O	3-year non-optimal case 2023	3-year optimal case 2023_O	5-year non-optimal case 2025	5-year optimal case 2025_O	8-year non-optimal case 2028	8-year optimal case 2028_O	10-year non-optimal case 2030	10-year optimal case 2030_O
Active/reactive load (KW + jKVAR)	3949.77 + j1912.97	3601.33 KW + j1750.14 KVAR	3932.46 KW + j1912.67 KVAR	2566.13 KW + j 1245.93 KVAR	2897.19 KW + j1407.6 KVAR	2609.18 KW + j1267.92 KVAR	6691.28 KW + j3246.28 KVAR	4638.37 KW + j2273.25 KVAR	5216.95 KW + j2550.29 KVAR	4874.9 KW + j2384.33 KVAR
Grid active/reactive power (KW + jKVAR)	4010.28 + j1947.6	5988.14 KW + j2899.97 KVAR	6315.96 KW + j3058.84 KVAR	5988.14 KW + j2899.97 KVAR	6315.96 KW + j3058.84 KVAR	6315.96 KW + j3058.84 KVAR	10305.94 KW + j4991.11 KVAR	10305.94 KW + j4991.11 KVAR	10870 KW + j5264.24 KVAR	10870 KW + j5264.24 KVAR
DG1 bus and size (KW + jKVAR)	—	DG_5 = 360 KW + j174.36 KVAR	DG_5 = 360 KW + j174.36 KVAR	DG_5 = 423 KW + j204.87 KVAR	DG_5 = 423 KW + j204.87 KVAR	DG_5 = 423 KW + j204.87 KVAR	DG_5 = 423 KW + j204.87 KVAR	DG_5 = 405 KW + j196.15 KVAR	DG_5 = 405 KW + j196.15 KVAR	DG_5 = 387 KW + j187.43 KVAR
DG2 @ bus and size (KW + jKVAR)	—	DG_18 = 270 KW + j 130.77 KVAR	DG_18 = 270 KW + j130.77 KVAR	DG_18 = 540 KW + j261.53 KVAR	DG_18 = 540 KW + j 261.53 KVAR	DG_18 = 630 KW + j305.12 KVAR	DG_18 = 630 KW + j305.12 KVAR	DG_18 = 837 KW + j405.38 KVAR	DG_18 = 837 KW + j405.38 KVAR	DG_18 = 855 KW + j414.1 KVAR
DG3 @ bus and size (KW + jKVAR)	—	DG_42 = 585 KW + j283.33 KVAR	DG_42 = 585 KW + j283.33 KVAR	DG_42 = 882 KW + j427.17 KVAR	DG_42 = 882 KW + j427.17 KVAR	DG_42 = 945 KW + j457.68 KVAR	DG_42 = 945 KW + j457.68 KVAR	DG_42 = 1395 KW + j675.63 KVAR	DG_42 = 1395 KW + j675.63 KVAR	DG_42 = 1620 KW + j784.6 KVAR
DG4 @ bus and size (KW + jKVAR)	—	DG_46 = 630 KW + j305.12 KVAR	DG_46 = 630 KW + j305.12 KVAR	DG_46 = 720 KW + j348.71 KVAR	DG_46 = 720 KW + j348.71 KVAR	DG_46 = 810 KW + j392.3 KVAR	DG_46 = 810 KW + j392.3 KVAR	DG_46 = 1350 KW + j653.84 KVAR	DG_46 = 1350 KW + j653.84 KVAR	DG_46 = 1395 KW + j675.63 KVAR
DG5 @ bus and size (KW + jKVAR)	—	DG_70 = 630 KW + j305.12 KVAR	DG_70 = 630 KW + j305.12 KVAR	DG_70 = 945 KW + j 457.68 KVAR	DG_70 = 945 KW + j457.68 KVAR	DG_70 = 990 KW + j479.48 KVAR	DG_70 = 990 KW479.48 KVAR	DG_70 = 1863 KW + j902.29 KVAR	DG_70 = 1863 KW + j902.29 KVAR	DG_70 = 1935 KW + j937.16 KVAR
Active power loss (KW)	60.51	88.19 KW	91.50 KW	87.99 KW	91.23 KW	91.22 KW	183.34 KW	182.43 KW	196.95 KW	196.90 KW
Reactive power loss (KVAR)	34.63	48.87 KVAR	52.53 KVAR	45.92 KVAR	48.72 KVAR	48.53 KVAR	94.62 KVAR	85.02 KVAR	119.34 KVAR	119.01 KVAR

10.3389/fenrg.2024.1353071

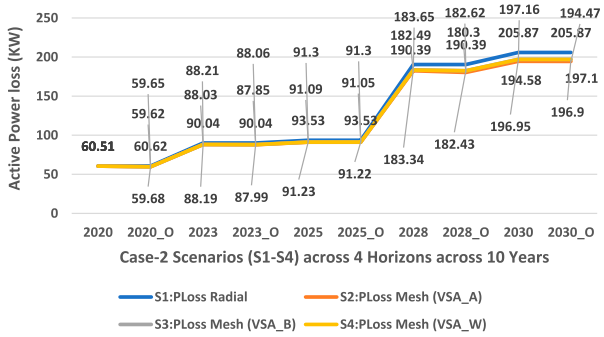

FIGURE 9
Active power loss trend across four planning horizons in the 75-bus meshed configured MG-based distribution network.

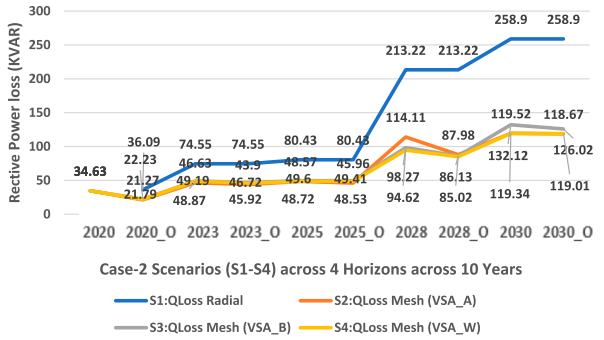

FIGURE 10
Reactive power loss trend across four planning horizons in the 75-bus meshed configured MG-based distribution network.

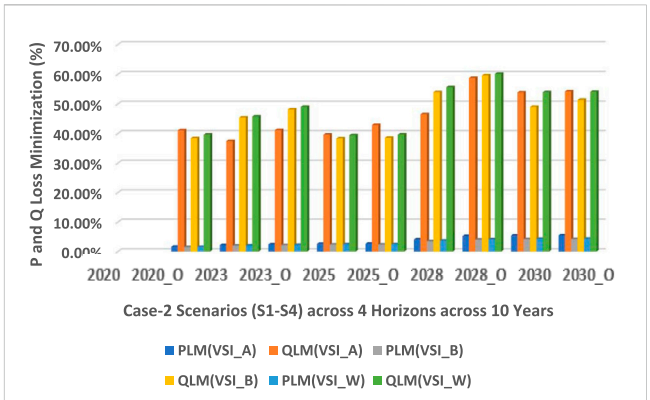

FIGURE 11
Active and reactive power loss minimization trends across four planning horizons in the 75-bus meshed configured MG-based distribution network.

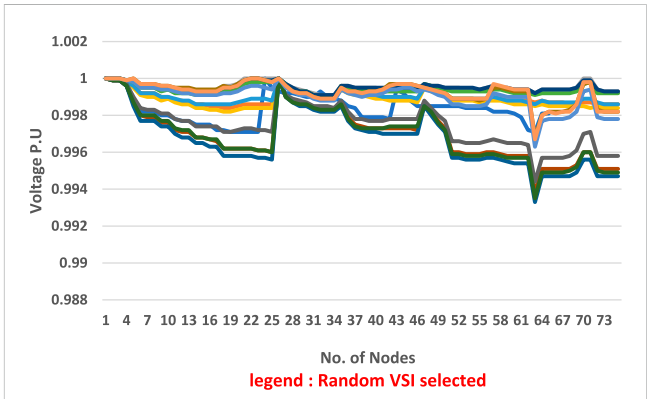

FIGURE 12
Voltage profile trend across four planning horizons in the 75-bus meshed configured MG-based distribution network.

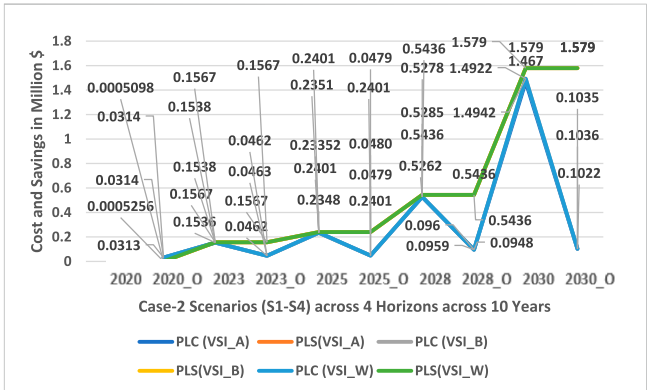

FIGURE 13
Cost of active power losses and savings trend across four planning horizons in the 75-bus meshed configured MG-based distribution network.

cables. Figure 12 shows that each VSI enhanced the voltage profile of the network according to its own specifications and all VSIs are significantly superior to a simple interconnected network. After maximizing the value of DG penetration in accordance with the policy, the voltage of each node is brought to unity. For scenario, a new optimized model has been acquired. Figure 13 shows a phenomenal reduction in the cost of active power losses and an increase in savings.

Further examination in Figure 10 and Figure 11 reveals that both active and reactive power losses are considerably minimized in C2 across all scenarios, surpassing the results of case 1 (C1). The higher reactive power loss in the baseline scenario is attributed to the network's underground cabling system. In Figure 12, the implementation of various voltage stability indices (VSIs) has been shown to significantly improve the voltage profile over a simple interconnected network, bringing each node's voltage closer to unity after the integration of maximum distributed generation (DG) penetration according to the set policy.

The obtained results in all situations were compared with the existing literature, and a close approximation was observed in the results, especially in evaluating contradictory criteria with cases of load increase over numerous planning horizons. It is also observed that fixed load growth by percentages does not capture the realistic pictures across medium horizons of 5 years, as evident from evaluated case 1. It is observed from evaluated case 2 that small planning horizons with variable load growth levels capture the requirements of expansion-based planning efficiently with the fixed counterpart.

5 Conclusion

Within the smart grid paradigm, current distribution networks aim to enhance reliability and interconnected topology while meeting diverse performance requirements. This study introduces a TESP (transmission expansion planning) strategy to address grid planning challenges. The proposed multi-stage comprehensive strategy employs voltage stability assessment indices (VSA_A, VSA_B, and VSA_W) and a load margin constraint (LMC) to assess and optimize the positioning and sizing of distributed generation (DG) assets. The evaluation of potential solutions considers technical and economic performance indicators across two load growth scenarios spanning 10 years. The TESP technique is tested on two variants of distribution grids (65-bus and 75-bus) with different load growth patterns. The results are compared with the existing literature, demonstrating close alignment, especially in assessing performance amid conflicting standards across various planning horizons. Notably, fixed load growth percentages may not accurately depict realistic scenarios over five-year planning horizons, as evident from case 1. Conversely, smaller planning horizons with variable load growth levels effectively address expansion-based planning needs, reducing assessment time and sensitivity analysis. Additionally, the TESP method offers a wide range of trade-off options for performance indicators, making it a valuable planning tool for academics and distribution system planners in interconnected distribution networks.

Data availability statement

The original contributions presented in the study are included in the article/Supplementary Material; further inquiries can be directed to the corresponding author.

Author contributions

AA: conceptualization, data curation, funding acquisition, resources, software, validation, writing–original draft, and writing–review and editing.

Funding

The author(s) declare financial support was received for the research, authorship, and/or publication of this article. The authors extend their appreciation to the Deanship of Scientific Research, Majmaah University, Saudi Arabia, for funding this research work through project number R-2023-192.

Conflict of interest

The author declares that the research was conducted in the absence of any commercial or financial relationships that could be construed as a potential conflict of interest.

Publisher's note

All claims expressed in this article are solely those of the authors and do not necessarily represent those of their affiliated organizations, or those of the publisher, the editors, and the reviewers. Any product that may be evaluated in this article, or claim that may be made by its manufacturer, is not guaranteed or endorsed by the publisher.

References

Ali, F., Nazir, Z., Inayat, U., and Ali, S. M. (2019). "Infrastructure of south Korean electric power system and potential barriers for the implementation of smart grid: a review," in International Conference on Innovative Computing (ICIC), Japan, August 29-31, 2023 (IEEE), 1–7.

Al-Sharafi, A., Sahin, A. Z., Ayar, T., and Yilbas, B. S. (2017). Techno-economic analysis and optimization of solar and wind energy systems for power generation and hydrogen production in Saudi Arabia. *Int. J. Renew. Sust. Ener Rev.* 69, 33–49. doi:10.1016/j.rser.2016.11.157

Alvarez-Herault, M.-C., N'Doye, N., Gandioli, C., Hadjsaid, N., and Tixador, P. (2015). Meshed distribution network vs reinforcement to increase the distributed generation connection. *Sustain. Energy, Grids Netw.* 1, 20–27. doi:10.1016/j.segan.2014.11.001

Arshad, M. A., Ahmad, S., Afzal, M. J., and Kazmi, S. A. A. (2018). "Scenario based performance evaluation of loop configured microgrid under load growth using multi-criteria decision analysis," in Proceedings of the 14th International Conference on Emerging Technologies (ICET), Islamabad, 21–22 Nov, 2018 (IEEE), 1–6.

Chen, L., Deng, X., Xia, F., Chen, H., Liu, C., Chen, Q., et al. (2021). A techno-economic sizing approach for medium-low voltage DC distribution system. *IEEE Trans. Appl. Supercond.* 31 (8), 1–6. doi:10.1109/tasc.2021.3101773

Das, B. K., Hoque, N., Mandal, S., Pal, T. K., and Raihan, M. A. (2017). A techno-economic feasibility of a stand-alone hybrid power generation for remote area application in Bangladesh. *Energy* 134 (1), 775–788. doi:10.1016/j.energy.2017.06.024

Das, S. K., Sarkar, S., and Das, D. (2022). Performance enhancement of grid-connected distribution networks with maximum penetration of optimally allocated distributed generation under annual load variation. *Arabian J. Sci. Eng.* 47 (11), 14809–14839. doi:10.1007/s13369-022-06951-x

Evangelopoulos, V. A., Georgilakis, P., and Hatziargyriou, N. D. (2016). Optimal operation of smart distribution networks: a review of models, methods and future research. *Electr. Power Syst. Res.* 140, 95–106. doi:10.1016/j.epsr.2016.06.035

Gholami, K., Islam, M. R., Rahman, M. M., Azizivahed, A., and Fekih, A. (2022). State-of-the-art technologies for volt-var control to support the penetration of renewable energy into the smart distribution grids. *Energy Rep.* 8, 8630–8651. doi:10.1016/j.egyr.2022.06.080

Javaid, B., Arshad, M. A., Ahmad, S., and Kazmi, S. A. A. (2019). "Comparison of different multi criteria decision analysis techniques for performance evaluation of loop configured Micro grid," in Proceedings of the 2019 2nd International Conference on Computing, Mathematics and Engineering Technologies (iCoMET), Sukkur, Pakistan, 30–31 January 2019 (IEEE), 1–7.

Kazmi, S. A. A., Ahmad, H. W., and Shin, D. R. (2019). A new improved voltage stability assessment index-centered integrated planning approach for multiple asset placement in mesh distribution systems. *Energies* 12, 3163. doi:10.3390/en12163163

Kazmi, S. A. A., Ameer Khan, U., Ahmad, W., Hassan, M., Ibupoto, F. A., Bukhari, S. B. A., et al. (2021). Multiple (TEES)-Criteria-Based sustainable planning approach for mesh-configured distribution mechanisms across multiple load growth horizons. *Energies* 14, 3128. doi:10.3390/en14113128

Kazmi, S. A. A., Shahzaad, M. K., and Shin, D. R. (2017b). Voltage stability index for distribution network connected in loop configuration. *IETE J. Res.* 63, 281–293. doi:10.1080/03772063.2016.1257376

Kazmi, S. A. A., Shahzad, M. K., and Shin, D. R. (2017a). Multi-objective planning techniques in distribution networks: a composite review. *Energies* 10, 208. doi:10.3390/en10020208

Khan, S. N., Kazmi, S. A. A., Altamimi, A., Khan, Z. A., and Alghassab, M. A. (2022). Smart distribution mechanisms—Part I: from the perspectives of planning. *Sustainability* 14 (23), 16308. doi:10.3390/su142316308

Mahmoud, P. H. A., Phung, D. H., and Vigna, K. R. (2017). A review of the optimal allocation of distributed generation: objectives, constraints, methods, and algorithms. *Renew. Sustain. Energy Rev.* 75, 293–312. doi:10.1016/j.rser.2016.10.071

Mallala, B., and Dwivedi, D. (2022). Salp swarm algorithm for solving optimal power flow problem with thyristor-controlled series capacitor. *J. Electron. Sci. Technol.* 20 (2), 100156. doi:10.1016/j.jnlest.2022.100156

Mallala, B., Venkata Prasad, P., and Palle, K. (2023). "Multi-objective optimization with practical constraints using AALOA," in International Conference on Information and Communication Technology for Intelligent Systems, Singapore, APRIL 4 – 5, 2024 (Springer Nature Singapore), 165–177.

Modarresi, J., Gholipour, E., and Khodabakhshian, A. (2016). A comprehensive review of the voltage stability indices. *Renew. Sustain Energy Rev.* 63, 1–12. doi:10.1016/j.rser.2016.05.010

Paliwal, P. (2021). Comprehensive analysis of distributed energy resource penetration and placement using probabilistic framework. *IET Renew. Power Gener.* 15 (4), 794–808. doi:10.1049/rpg2.12069

frontiers | Frontiers in Energy Research

TYPE Original Research
PUBLISHED 03 April 2024
DOI 10.3389/fenrg.2024.1359596

OPEN ACCESS

EDITED BY
Flah Aymen,
École Nationale d'Ingénieurs de Gabès, Tunisia

REVIEWED BY
Chuanyu Sun,
University of Padua, Italy
Rajeev Kumar,
KIET Group of Institutions, India

*CORRESPONDENCE
A. Rammohan,
rammohan.a@vit.ac.in
Kareem M. AboRas,
kareem.aboras@alexu.edu.eg
Amr Yousef,
a.yousef@ubt.edu.sa

RECEIVED 21 December 2023
ACCEPTED 18 March 2024
PUBLISHED 03 April 2024

CITATION
Rammohan A, Wang Y, Kannappan S S, Kumar P S, Ashok B, Kotb H, AboRas KM and Yousef A (2024), Service life estimation of electric vehicle lithium-ion battery pack using arrhenius mathematical model.
Front. Energy Res. 12:1359596.
doi: 10.3389/fenrg.2024.1359596

Service life estimation of electric vehicle lithium-ion battery pack using arrhenius mathematical model

A. Rammohan[1]*, Yong Wang[2], Subbu Kannappan S[3], Suresh Kumar P[1], Bragadeshwaran Ashok[4], Hossam Kotb[5], Kareem M. AboRas[5]* and Amr Yousef[6,7]*

[1]Automotive Research Centre, Vellore Institute of Technology, Vellore, India, [2]Systems Science and Industrial Engineering, Binghamton University, Binghamton, NY, United States, [3]Hyundai Motor India Limited, Sriperumbudur, India, [4]School of Mechanical Engineering, Vellore Institute of Technology, Vellore, Tamil Nadu, India, [5]Department of Electrical Power and Machines, Faculty of Engineering, Alexandria University, Alexandria, Egypt, [6]Electrical Engineering Department, University of Business and Technology, Jeddah, Saudi Arabia, [7]Engineering Mathematics and Physics Department, Faculty of Engineering, Alexandria University, Alexandria, Egypt

Durability is a desired characteristic for all battery packs in Electric Vehicles. In this study, the service life of the EV battery pack under real-world operating conditions is projected using an Arrhenius mathematical simulation model. The model comprises a 39.2 kWh EV Lithium-Ion battery pack integrated with a three-phase inverter to convert the battery pack's Direct Current output to Alternating Current. In addition, the Alternating Current output is coupled to a 100 kW permanent magnet synchronous motor, which is regarded as the load. A field-oriented controller provides pulse width-modulated output signals that are supplied back to the inverter to generate the correct driving current. Variable conditions of charge rate (C-rate: 1.25C – 4C), discharge rate (C-rate: 0.5C – 4C), temperature (25°C–60°C), and depth of discharge (30%–90%) are evaluated to determine the battery pack's service life. Under a 4C charge rate/0.5C discharge rate and 50% depth of discharge, the modeling results indicate the battery pack has a service life of approximately 6,000 h at low temperatures (25°C) and roughly 3,000 h at high temperatures (60°C). The model has been validated by comparing the results with experimental data from the literature.

KEYWORDS

energy storage, battery temperature, Li-ion battery, Arrhenius mathematical model, PMSM, service-life estimation, state of charge, durability

1 Introduction

Internal combustion (IC) engine-powered vehicles have been extensively used for transportation for over a century. The emissions from vehicles have significantly polluted the environment and thereby caused atmospheric changes. Also, the limited availability of petroleum resources, stringent emission norms, and ever-increasing prices have encouraged research into various clean and green energy transportation technologies. One such technology is Electric Vehicles (EVs), which have various advantages such as zero-emission and potential for energy-saving (Hill et al., 2019), less running cost (Weldon et al., 2018), and higher efficiency (Wang and Li, 2016; Somakettarin and Pichetjamroen,

2019; Somakettarin et al., 2023) as compared to IC engine vehicles. A 1% increase in the number of electric vehicles sold in a city can lower CO2 emissions by 0.096% locally and 0.087% in a neighboring city. Second, EVs have an indirect impact on CO2 emissions via substitution, energy consumption, and technological effects. Increasing renewable energy generation by 1% leads to a 0.036% reduction in EV carbon footprint (Wang et al., 2018). Lithium-ion batteries (LIBs) are compact compared to other battery technologies. LIBs also possess higher specific energy, high discharge current, low self-discharge rate, and long life. These characteristics help to achieve higher power efficiency because the cell can retain the charge for a longer time.

The LIB self-discharge rate is 0.5% monthly when not in use under normal conditions (Wang et al., 2018). Recent EVs have a battery service contract that promises the battery for a particular duration, typically 5–8 years, or a distance such as nearly 100,000 km. When driving, an EV generally consumes one kWh of energy to travel about 4.5–6.5 km (3–four miles). In adverse conditions, the performance of the battery is greatly affected due to its temperature and depth of discharge (DOD), and the service life is reduced (Tufail et al., 2023). The service life of the battery can be estimated through electrical equivalent circuit modeling, which helps to determine the open-circuit voltage, terminal voltage, current, State of Health (SOH), and State of Charge (SOC). Among these parameters, SOC is an important factor being investigated to determine the amount of energy inside a battery to drive an EV. The other prominent models in the involved literature are the electrochemical model (Rahman et al., 2016; Wang et al., 2023), the equivalent circuit model (Kunwar et al., 2023), and the data-driven model (Li et al., 2020; Zhang R. et al., 2023).

Many research works on battery life estimation focus only on electrochemical mathematical models, thermal models, and a few data-driven models (Zhang X. et al., 2023). For example, Rahman *et al.* (Rahman et al., 2016) utilized particle swarm optimization (PSO) to identify electrochemical model parameters such as solid-phase diffusion coefficient at the positive and negative electrodes and intercalation/de-intercalation at the anode and the cathode. According to Sung's experimental results, the battery model developed considering these parameters was reasonably accurate. Wang *et al.* (Wang et al., 2023) demonstrated the high-accuracy prediction of the electrochemical model, but the simulation of the model required substantial computational effort. The reason behind preferring the electrochemical model is its ability to obtain an accurate evaluation within LIB. Still, it is difficult to identify the parameters of battery electrochemistry in real-time applications. Besides these models, the equivalent circuit model has been adopted extensively in real-time applications due to its highly simplified structure and relatively fewer model parameters (Zhang et al., 2021). The typical framework of the equivalent circuit model consists of several resistor-capacitor networks where the number of networks is the order of the model. The key is whether the electric energy used to charge the EV battery is produced using renewable energy. If the battery is charged using typical thermal power generation, EVs do not significantly contribute to carbon emission reductions. However, most renewable energy sources are intermittent, creating spatial and temporal gaps between energy availability and use by end users (Lu et al., 2022). To address these difficulties, adequate energy storage devices, such as batteries for the power grid, and full usage of renewable energy are required (Sun et al., 2019). In comparison to these models, data-driven models, such as support vector machines (Chen et al., 2019) and neural networks (Wang et al., 2017), describe the electrical behavior of the LIB without prior knowledge. However, the performance of the data-driven models depends on the possibility of capturing the data for the entire operational range of the battery (Sha et al., 2024).

As there is a considerable possibility of LIBs being subjected to fast charging and discharging at extreme cycling conditions more often, the study of thermal behaviour becomes crucial because it has a direct effect on performance and service life. Also, it is seen that the heat generation in the battery pack has a notable impact on the fading of the capacity (Richter et al., 2017). Charging the LIB at 0–45°C and discharge at 0–55°C is generally safe. Numerous models such as heat transfer, data-driven, and heat generation models have been investigated and established for capturing thermal behaviour for service life estimation (Shen et al., 2024). Guo *et al.* (Wali et al., 2021) developed a multi-physics heat transfer model capable of accurately predicting electrical and thermal behaviour. The model is also flexible enough to be coupled with other multi-physics equations to carry out system analysis effectively. Also, the three-dimensional heat transfer models can effectively obtain the distribution of the temperature inside the LIB, which helps to detect hot spots. The developed heat generation model uses the internal resistance of the battery and heat generation as a result of Joule's heating and entropy change (Liu et al., 2019).

The various studies show that the electrical and thermal effects significantly affect the LIB. The electrical and thermal behaviour are coupled as electro-thermal models to capture the above-said variations efficiently and simultaneously (Zhang et al., 2016). Yang *et al.* proposed an electro-thermal model that considers the relationship between the electrochemical and thermal behaviour of the cell to predict the behaviour of the battery under different drive cycles (Yang et al., 2019). While battery technologies are constantly improving to increase reliability and efficiency, the estimation of the actual SOC and SOH is extremely crucial. Li-ion cells degrade over time due to the growth of solid electrolyte interface and electrolyte decomposition (Wang et al., 2017). The SOC and SOH degradation of the cell is affected directly (Li et al., 2022; Xu et al., 2023).

LIB SOH is estimated using its voltage, current, and discharge-charge cycles to indicate its lifespan. Although all these parameters indicate the SOH, capacity is used for simplicity to estimate the lifetime under different cycling conditions (Marques et al., 2019). However, because the capacity cannot be directly measured online, there is a requirement to establish a quantitative relation between various measurable parameters of the battery and the capacity for SOH estimation (Li et al., 2019). It was found in the literature that the resistances (ohmic and polarization resistance) are the major contributing factors to capacity loss and can be useful in predicting battery life (Zhu et al., 2023).

The real-time life estimation of solid-state electronics based on the Arrhenius model is used to detect the failure of any device that is experimented with and projected to estimate the lifetime in hours concerning the change in temperature at its junction (R et al., 2021), which is an intuitive idea for this research. The accuracy of the battery lifetime estimation greatly depends on aging effects and capacity fade. Ashwin *et al.* (Ashwin et al., 2016) developed a P2D

model that considers electrochemical processes to study the aging of the batteries under repeated loading conditions. This model integrates all the essential electrical and chemical processes under a valuable algorithm for the battery monitoring system (Huang et al., 2022).

Yonemoto *et al.* (Yonemoto YKTIKO, 2020) invented a capacity prognostic device that determines a prediction function coefficient using capacity degradation of the battery (capacity fade). Also, García *et al.* (García et al., 2023) proposed a novel test methodology that is useful for predicting the remaining capacity of the cell after every cycle of discharge and charge. The parameters are considered for investigating the battery charge and discharge cycling effect due to the varying DOD between 20% and 100% DOD, discharge rates, charge rates, and operating temperatures −18°C to 40°C. The results indicate that the negative effect of higher temperatures can affect lifetime and performance. Wang *et al.* (Wang et al., 2011) indicated the effect of cycling on the capacity fade of LiFePO4 cells. The test conditions include the DOD that varies from 90% to 10%, operating temperature ranging from −30°C to 60°C, and discharge current varying from 1 A to 20 A. The experimental results indicate a larger impact of temperature and time on capacity loss than the DOD (Zhou et al., 2024).

While determining battery health is vital, it is equally important to predict the end of life for LIB, as it helps to take preventive and corrective measures to avoid unintended problems (Zhang et al., 2022). Berecibar (Berecibar et al., 2016) discussed the testing procedures and developed an estimation model for the SOH of the battery, which is useful for forecasting its life. The cells were subjected to extensive cycling and operating conditions such as operating temperatures, discharge-charge rate, and DOD, with results indicating the greater accuracy of the proposed model. Hoyul *et al.* (Yul Yongin-si et al., 2013) patented a prediction system that comprises a learning data input unit, target data input, and machine learning to assign the weights to battery factors in data input. The prediction system consists of a lifetime prediction unit for indicating the lifetime of a battery cell. Energy Storage Systems (ESS) are subdivided into four major categories such as chemical, mechanical, thermal, and electromechanical systems (Hannan et al., 2021). Hossain Lipu *et al.* stated that SOC assessment under hundreds of lithium-ion battery cells in EV operation remains unresolved (Hossain Lipu et al., 2020). Yu *et al.* estimated SOC for a series-parallel LIB equivalent circuit through an OCV-SOC-temperature relationship (Yu et al., 2023).

Table 1 shows the types of batteries considered for investigation and its algorithm and research outcome in a nutshell related to battery lifetime estimation along with the current proposed work. Considering various models discussed in this section, our method has the advantage of using PMSM as load whereas other models considered only RC or RLC load. Another advantage of our method is that it considers all critical parameters of the battery pack such as temperature, charge-discharge rate, and DOD which estimates the lifetime precisely (Mu et al., 2021). The novelty or contribution of the current proposed work is summarized as follows. The study of the existing literature indicates that most of the work regarding the modeling and estimation of the SOH was carried out on the Li-ion cells. It has been observed from the various models discussed in the literature that real-time pack-level battery capacity models were absent for EVs. In addition, a literature gap was found, indicating that no model considered the PMSM load. Most of the authors considered resistive load or RLC load in their simulation work. It was also found from the literature that parameters such as temperature, discharge rate, or DOD have been considered individually in the previous work (Lü et al., 2024). Considering the research gaps, the contribution or novelty of this proposed work uses a mathematical model of PMSM drive that comprises a LIB battery-pack and PMSM in MATLAB-Simulink environment for the lifetime estimation of the pack considered, which considers various operating working conditions such as operating temperature, discharge–charge rates, and DOD. It is assumed that the internal resistance of the battery cell is constant during the charging and discharging cycle and will not change with the current. In this paper, for example, 4C/4C, which is intended as the discharge/charge rate, is considered.

This work considers the battery pack voltage of 327 V and the current of 119.87 Ah. The entire battery pack is charged at rates of 1.25C, 2C, 3C, and 4C and discharged at 0.5C, 1C, 2C, and 4C, respectively. During the operation, the temperature, SOC, and depth of charge are considered inputs to the model. The battery pack is cycled continuously at various charge-discharge rates that depend on the required motor power. The complete system is controlled by a field-oriented controller that uses pulse width modulation to control the motor voltage. Finally, the capacity degradation of the entire pack is analyzed using the data obtained through simulation to predict the useful lifetime.

The rest of this paper is organized as follows: Section 2 describes a model-based design for PMSM along with a battery pack, inverter and discharge model. It is followed by Section 3, which deals with the overall model along with results and discusses the proposed system. Finally, Section 4 concludes the work.

2 Model-based design for PMSM drive in EV

The lifetime estimation model proposed in this work primarily consists of a battery pack, a three-phase inverter, a Permanent Magnet Synchronous Motor (PMSM), and a field-oriented controller (FOC) along with position sensors. The specifications are similar to the commercially available EV battery pack as given in Table 2 and are taken as a benchmark to model the PMSM Drive shown in Figure 1.

The LIB pack generates power to the PMSM (acts as the load) through a three-phase inverter that converts the DC voltage to a three-phase AC supply. The voltage and current are monitored by voltage and current sensors, respectively. The field-oriented controller is used to control and drive the motor using a sensor feedback loop to produce gate pulses. The primary function of a field-oriented control algorithm is to take a user-defined voltage uq and, by continually reading the relative position of the motor rotor, determine the proper phase voltages ua, ub, and uc. The FOC algorithm generates phase voltages that form a magnetic field in the motor's stator that is 90° "behind" the permanent magnets of the rotor, resulting in a pushing effect. The Rotor Position Sensor is used to determine the rotating angle of any rotary application, especially PMSM. Rotor position sensors are mandatory for effective and trustworthy control of PMSM (Bhardwaj, 2013).

TABLE 1 Summary of representative battery life estimation models.

References	Model/Method	Battery Type	Description	Results
Marques *et al.* (Marques et al., 2019)	Semi-empirical model - Power-law relation with time (capacity loss), Arrhenius correlation (temperature effect)	Lithium manganese oxide (LiMn2O4), Lithium-ion phosphate (LiFePO4)	Comparative life cycle assessment of LiMn2O4 and LiFePO4 for addressing capacity fade	The aging of LiFePo4 had almost four times higher effect than LiMn2O4
Li *et al.* (Li et al., 2019)	Experimental, 2nd equivalent circuit model (ECM)	Lithium-ion	Establishment of the relation between capacity loss and measurable parameters	The capacity available decreases with the increase in ohmic resistance
Ashwin (Ashwin et al., 2016)	Modified Newman model	Lithium-ion	Study of the capacity fade of the battery under cyclic loading conditions	Battery life is found to be significantly affected by the convective heat transfer coefficient
García *et al.* (García et al., 2023)	Electrical model	Lithium iron phosphate (LiFePO4)	Development of a life cycle model that investigates the battery life and effect of fast charging	The cycle life of the battery degrades with an increase in charge current rates
Wang *et al.* (Wang et al., 2011)	Power law equation for capacity loss, Arrhenius correlation for temperature effect	Lithium iron phosphate (LiFePO4)	Development of a semi-empirical life model	The power-law relationship can represent life cycle data
Berecibar *et al.* (Berecibar et al., 2016)	Electrical model	Lithium iron phosphate (LiFePO4)	Prediction of SOH using capacity estimation	The model has an average error of 1.5% at the pack level
Deng *et al.* (Deng et al., 2020)	Gaussian process regression	Lithium-ion	Predict the SOC of the battery pack	Estimation error under different temperatures is lower than 3.9%
Deng *et al.* (Deng et al., 2021)	Data-driven methods	Three types of Lithium batteries	Predict battery SOH	RMSE is lower than 1.3%
Che *et al.* (Che et al., 2021)	Gaussian process regression	Transfer learning and recurrent neural network	Predict remaining useful life based on the optimized health indicators	Error less than five cycles
Proposed work	Arrhenius correlation included in charging/discharging along with DoD	Lithium-ion (Nickel Manganese Cobalt)	Predict the lifetime of the battery pack in hours	At 4C/4C lifetime decreases by 32.8%

TABLE 2 Model specifications.

Battery pack - lithium-ion	Voltage - 327 V
	Power capacity - 39.2 kWh
Three-Phase Inverter	180° Conduction Mode
PMSM Motor	Power - 100 kW
	Torque - 395 Nm
PMSM Controller	FOC

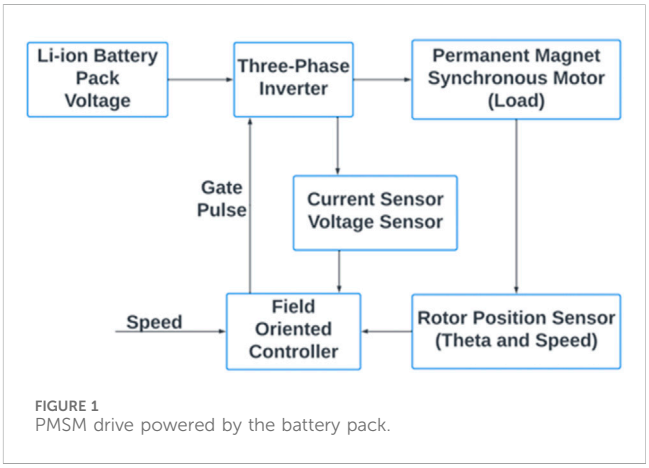

FIGURE 1
PMSM drive powered by the battery pack.

The elaborate model of Figure 1 block diagram is shown in Figure 4.

2.1 LIB pack model

The LIB pack model developed using MATLAB SIMULINK is shown in Figure 2. The battery pack is subdivided into sub-battery packs, and each pack is connected into a series of parallel combinations. The full battery pack is attached to the main model, as shown in Figure 4. The phosphate LIB is considered a potential battery technology that could be utilized in automotive applications due to its thermal and electrical stability. This battery type also offers good electrical performance with low resistance.

The capacity of the modeled battery pack is 39.2 kWh. The cells are LFP - A123 ANR 26650. More specifications of the battery cell are given in Table 3.

The number of cells calculated using Eq. 1 and 2 (Buchmann, 2017) indicates approximately 102 cells in series combination as a single pack, and a 53 - single pack is connected in parallel combinations to deliver 39.2 kWh. Overall, the battery pack consists of 5,406 cells with a weight of approximately 389.2 kg.

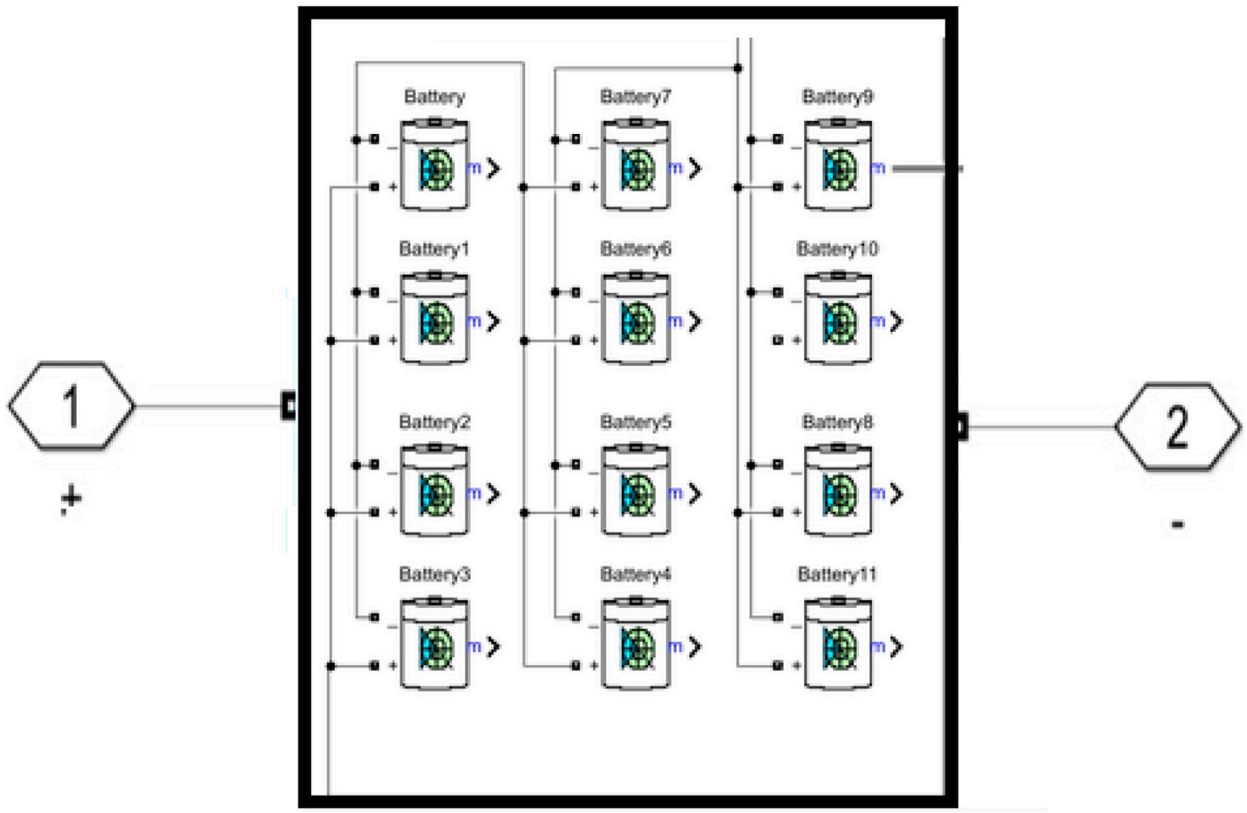

FIGURE 2
Battery pack model.

TABLE 3 Specifications of the battery cell.

Parameter	Ratings
Nominal Voltage	3.3 V
Nominal Capacity	2.3 Ah
Standard Charge	3A to 3.6V CCCV, 45 min
Rapid Charge	10 A to 3.6V CCCV, 15 min
Nominal Discharge Current	2.3 A
Internal Resistance	10 mΩ
Discharge Cut-off Voltage	2.40 V
Cell Weight	72 g
Cell Dimensions	ø 26 × 55 mm

$$\text{Number of cells (series)} = \frac{\text{Battery pack voltage, V}}{\text{Cell voltage, V}} \quad (1)$$

$$\text{Number of cells (parallel)} = \frac{\text{Battery pack capacity, Ah}}{\text{Cell capacity, Ah}} \quad (2)$$

A modified Shepherd's model is used to describe the voltage dynamics of the Li-ion battery pack (Wang et al., 2023). The equivalent discharge-charge model of the Li-ion battery shown in Figure 3 consists of an internal resistance of approximately 10 mΩ,

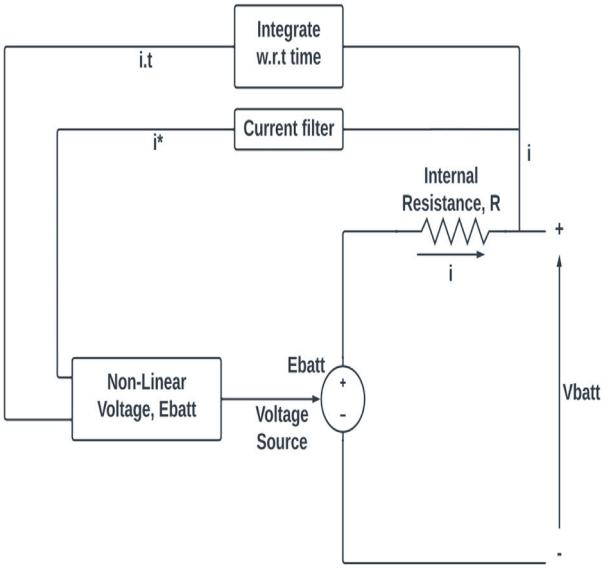

FIGURE 3
Discharge-charge battery model.

which leads to a voltage drop based on the battery chemistry. The temperature is an important factor that affects the performance of the LIB in terms of pack voltage, discharge capacity, charge-discharge

characteristics, and power capability. The variation in the battery voltage that considers the impact of temperature in the case of discharge and charge conditions is represented by Eq. 3 and 4, respectively. It is assumed that the internal resistance, R, is dependent on the operating temperature of the battery (An et al., 2023). The remaining useful time 't' in hours in the Arrhenius model included in the charging and discharging Eq. 3 and 4 is acquired through the SIMULINK model for each second.

$$V_{batt\,(di)} = E_0\,(T) - R\,(T)\cdot I - K\,(T)\cdot I^{*}\frac{Q(T_a)}{Q(T_a) - it} - K\left(\frac{Q(T_a)}{Q(T_a) - It}\right)It + Ae^{-B\cdot It} \quad (3)$$

$$V_{batt\,(ch)} = E_0\,(T) - R\,(T)\cdot I - K\,(T)\cdot I^{*}\frac{Q(T_a)}{it + 0.1Q(T_a)} - K\left(\frac{Q(T_a)}{Q(T_a) - It}\right)\cdot It + Ae^{-B\cdot It} \quad (4)$$

In Eq. 3 and 4, the terms are $E_0\,(T)$ – constant voltage, K(T) – polarisation constant, Q (T_a)–capacity, R(T) – internal resistance (An et al., 2023).

$$E_0\,(T) = E_0|_{Tref} + \frac{\partial E}{\partial T}\,(T - Tref) \quad (5)$$

$$K\,(T) = K\,(T)|_{Tref}\cdot e^{\alpha\left(\frac{1}{T} - \frac{1}{Tref}\right)} \quad (6)$$

$$Q\,(T_a) = Q|_{T_a} + \frac{\Delta Q}{\Delta T}\,(T_a - Tref) \quad (7)$$

$$R\,(T) = R|_{Tref}\cdot e^{\beta\left(\frac{1}{T} - \frac{1}{Tref}\right)} \quad (8)$$

The overall heat generated PL during the process of discharging and charging is expressed with the help of Eq. 9 (An et al., 2023).

$$P_L = [E_o\,(T) - V_{batt}\,(T)]\cdot I + \frac{\partial E}{\partial T}\cdot I + I\cdot T \quad (9)$$

The aging of the battery pack is one of the major issues in EV technology and has considerable effects, such as an increase in charging losses, which results in reduced efficiency, a decrease in driving range, and a reduction in acceleration. The available energy inside the pack is lost gradually as the active material inside transforms into an inactive phase. This energy reduction is represented by a factor called the aging factor that is dependent on the percentage of the battery that has been discharged (DOD) as defined in Eq. 10. The impact of the constant discharging and charging process on the battery capacity is indicated by Eq. 11 (An et al., 2023).

$$\lambda\,(n) = \lambda\,(n-1) + \left(\left(\frac{1}{2N\,(n-1)}\right)\cdot\left(1 - \frac{DOD\,(n-2)}{DOD\,(n-1)}\right)\right) + \left(\left(\frac{1}{2N\,(n-1)}\right)\cdot\left(1 - \frac{DOD\,(n)}{DOD\,(n-1)}\right)\right) \quad (10)$$

$$(n) = C_{BOL}\,(1 - \lambda\,(n)) - \lambda\,(n)\cdot C_{EOL} \quad (11)$$

Here, $n = k\cdot T_h$ (k = 1, 2, 3, . . . , ∞).

2.2 Three-phase inverter model

The three-phase inverter is used to convert direct current from LIB (327 V and 39.2 kWh) into AC for powering variable speed PMSM that acts as the load. The model developed is a 180° conduction mode type in which three switches are 'on' at any instant and the gate pulses switch the device to an 'on' or 'off' position based on the signals from the motor controller. Table 4 indicates the PMSM phase voltages Va, Vb, and Vc based on the variation of the load. A capacitor is connected in parallel to the RL circuit (equivalent stator winding circuit) to reduce voltage fluctuations. This ensures that sinusoidal current is generated from the inverter, as explained in Eq. 12 is generated from the inverter (Buchmann, 2017).

TABLE 4 Phase Voltages of the Three-Phase Inverter (1 indicates ON and 0 indicates OFF).

Switch						Phase Voltage		
S_1	S_3	S_5	S_2	S_4	S_6	V_a	V_b	V_c
0	0	0	1	1	1	0	0	0
1	0	0	0	1	1	$2V_{dc}/3$	$-V_{dc}/3$	$-V_{dc}/3$
1	1	0	0	0	1	$V_{dc}/3$	$V_{dc}/3$	$-2V_{dc}/3$
0	1	0	1	0	1	$-V_{dc}/3$	$2V_{dc}/3$	$-V_{dc}/3$
0	1	1	1	0	0	$-2V_{dc}/3$	$V_{dc}/3$	$V_{dc}/3$
0	0	1	1	1	0	$-V_{dc}/3$	$-V_{dc}/3$	$2V_{dc}/3$
1	0	1	0	1	0	$V_{dc}/3$	$-2V_{dc}/3$	$V_{dc}/3$
1	1	1	0	0	0	0	0	0

$$i_L = \int \frac{1}{L_s}\,(V - i_L R_s) \quad (12)$$

2.3 Permanent magnet synchronous motor and EV drive model

A permanent magnet synchronous motor (PMSM) is modeled and integrated with the drive system as a load that acts on the battery pack. It consists of three-phase windings in the stator and permanent magnets in the rotor. Each stator winding consists of inductance and resistance connected in series with the input being the voltage applied to the armature of the motor and the output is the angular motion (position) of the shaft. The electromagnetic current flowing across each of the stator windings (i_A, i_B, i_C) is calculated using Eq. 13, which considers the back emf and the motor torque constant (Buchmann, 2017).

$$i_L = \int \frac{1}{L_s}\left(-i_L R_s + V - K_b\frac{d\phi}{dt}\right) \quad (13)$$

The angular acceleration of the shaft and the speed during rotation are found using Eq. 14 and 15 (Krishnan, 2017).

$$J\cdot\frac{d^2\phi}{dt^2} = T_{em} - b\frac{d\phi}{dt} \quad (14)$$

$$w = \frac{d\phi}{dt} \quad (15)$$

In a balanced three-phase machine, the summation of the three-phase currents is zero as given by Eq. 16. However, this equation does not hold if there is an imbalance in voltage or current.

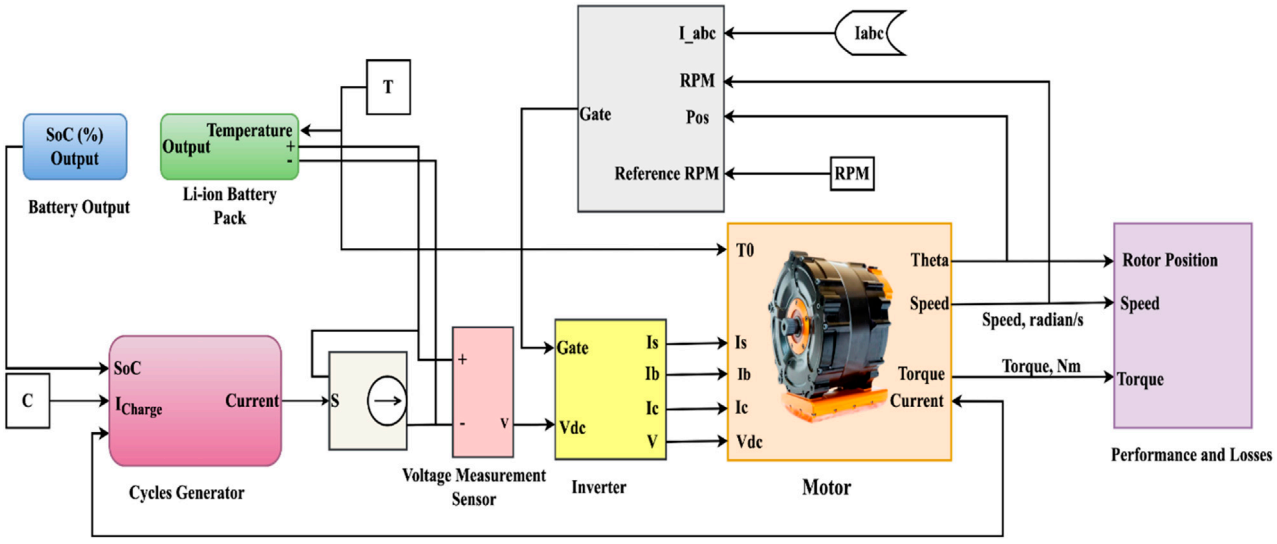

FIGURE 4
EV drive system.

$$i_A + i_B + i_C = 0 \quad (16)$$

To calculate torque, Park's transform is used, which transforms the stator winding currents to $i_{d'}$, $i_{q'}$, $i_{0'}$ frame (independent of rotor angle) as represented in Eq. (17)-19) (Krishnan, 2017).

$$i_{d'} = \frac{2}{3}\left(i_A \cos\phi_e + i_B \cos\left(\phi_e - 2\pi/3\right) + i_C \cos\left(\phi_e + 2\pi/3\right)\right) \quad (17)$$

$$i_{q'} = -\frac{2}{3}\left(i_A \sin\phi_e + i_B \sin\left(\phi_e - 2\pi/3\right) + i_C \sin\left(\phi_e + 2\pi/3\right)\right) \quad (18)$$

$$i_{0'} = \frac{2}{3}\left(0.5i_A + 0.5i_B + 0.5i_C\right) \quad (19)$$

where, $\phi_e = n\ \phi$

The current i_0 represents the imbalance in A, B, and C phase currents and can be taken as the zero-sequence component of the current. The mathematical models of the Li-ion battery pack, inverter and the developed PMSM are integrated with a Field Oriented Controller to construct an electric drive system, which is shown in Figure 4. Based on battery configuration the total voltage is 327 V and the current is 119.87 Ah, which is considered for vehicle operation. The entire battery pack is charged at charge rates of 1.25C, 2C, 3C, 4C and discharged at 0.5C, 1C, 2C, 4C, respectively. During the operation, the temperature, SOC, and depth of charge are considered as input to the model. Based on these inputs, the pack is cycled continuously at various charge-discharge rates that depend on the power required by the motor. The entire drive system is controlled by a field-oriented controller, which uses pulse width modulation to control the load voltage. Finally, the capacity degradation of the entire pack is analyzed to predict the useful lifetime.

3 Results and discussions

The drive model shown in Figure 4 is developed using MATLAB-Simulink (R2019a) with mathematical equations to carry out cycling of the battery pack under varying conditions of discharge rate (0.5C, 1C, 2C, 4C) and charge rate (1.25C, 2C, 3C, 4C).

Here, C indicates the charge capacity of the pack. For example, if the capacity of the battery is 2.3Ah for a cell, then 0.5C denotes 1.15A. The battery temperature considered in this work is 25°C, 40°C, 50°C and 60°C with the DOD as 80%, 70%, 60%, 50%, 40%, and 30%, respectively. In addition, the pack is considered to have reached its end of life when the available capacity reduces to 80% of the actual capacity. The methodological validation of the proposed model is compared with Wang *et al.* experimental results. As shown in Figures 5A,B, the capacity loss results of a cell model are validated for a 0.5C discharge rate at a battery temperature of 60°C. The analysis of the results obtained in Figure 5A indicates a maximum variation of approximately 9.7% at 0.5C discharge rate, operating temperature of 60°C and 80% DOD, whereas a variation of 6.5% is observed at 50% DOD (Figure 5B) with the rest of the conditions remaining the same. Therefore, the mathematical model developed to estimate lifetime produces results that are closer to the experimental outcome (Wang et al., 2011). The battery pack, which is modeled using the validated $LiFePO_4$ cell, is tested under varying conditions of C-rate, operating temperature, and DOD as described earlier, with the PMSM acting as the load. The life of a battery pack can be estimated using various methods and parameters. In this work, the lifetime of battery packs is estimated in hours using Eq. 3 and 4, which involve battery pack capacity, charging, discharging, and battery temperature.

Figure 6A indicates the degradation of battery pack capacity when it is subjected to varying C-rates (both discharging and charging) at the conditions of 40% DOD and the battery operating temperature at 25°C. From the analysis that considers the 4C constant discharge rate, it is seen that the lifetime reduces from 1,463 h–867 h as the charge rate increases from 1.25C to 4C. Similarly, when the charging rate is kept constant at 4C, the lifetime is seen to reduce drastically from 6,675 h–867 h as the discharge rate

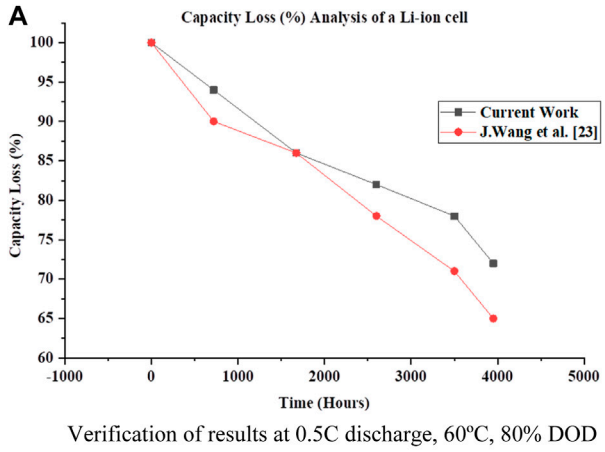

FIGURE 5
Capacity loss comparison at 50% and 80% DOD. **(A)**: Verification of results at 0.5C discharge, 60°C, 80% DOD. **(B)**: Verification of results at 0.5C discharge, 60°C, 50% DOD.

increases to 4C. As the battery operating temperature is increased to 40°C (Figure 6B) at a discharge rate of 4C, it is seen that lifetime reduces from 1,093 h–648 h as the charge rate increases from 1.25C to 4C. Similarly, when the charging rate is kept constant at 4C, the lifetime is seen to reduce drastically from 4,988 h–648 h as the discharge rate increases to 4C. In the case of 50°C (Figure 6C) with the same conditions, at a 4C constant discharge rate, the lifetime is seen to drop from 913 h to 542 h as the charge varies from 1.25C to 4C; at the 4C constant charge rate, the lifetime drops from 4,169 h–542 h as the discharge rate increases to 4C.

Correspondingly, at 60°C (Figure 6D), the lifetime is observed to drop from 772 h to 458 h as the charge rate varies from 1.25C to 4C at a discharge rate of 4C and from 3,522 h–458 h as the discharge rate increases to 4C that considers 4C charge rate. Also, it is noticed that with the increase in temperature to 60°C at constant discharge and charge rate of 0.5C/1.25C, the lifetime reduces from 6,786 h (at 25°C) to 3,580 h (at 60°C). At the same time, at a constant discharge and charge rate of 4C/4C, the lifetime is reduced from 867 h (at 25°C) to 458 h (at 60°C).

On carrying out the analysis at 80% DOD (Figure 7) under the same conditions of discharge-charge rates and operating temperatures, the trend remains the same. However, with the rise in DOD, the lifetime is seen to be reduced significantly. Considering the 4C discharge rate at 25°C (Figure 7A), the lifetime of the pack reduces from 1,094 h–583 h as the charge rate increases to 4C, whereas, at 4C charge rates, there is a drastic reduction from 4,253 h–583 h as the discharge rate increases. As the battery operating temperature is increased to 40°C (Figure 7B) at a discharge rate of 4C, it is seen that lifetime reduces from 817 h to 435 h as the charge rate increases from 1.25C to 4C. Similarly, when the charging rate is kept constant at 4C, the lifetime is seen to reduce drastically from 3,178 h–583 h as the discharge rate increases to 4C. In the case of 50°C (Figure 7C) with the same conditions, at the 4C constant discharge rate, the lifetime is seen to drop from 683 h to 364 h as the charge varies from 1.25C to 4C; at the 4C constant charge rate, the lifetime drops from 2,655 h–364 h as the discharge rate increases to 4C. Correspondingly, at 60°C (Figure 7D), the lifetime is observed to drop from 577 h to 307 h as the charge rate varies from 1.25C to 4C at a discharge rate of 4C and from 2,244 h–307 h as the discharge rate increases to 4C that considers 4C charge rate. However, it is noticed that with the increase in temperature to 60°C at a constant discharge and charge rate of 0.5C/1.25C, the lifetime is reduced from 4,865 h (at 25°C) to 2,567 h (at 60°C). At the same time, at a constant discharge and charge rate of 4C/4C, the lifetime is reduced from 583 h (at 25°C) to 307 h (at 60°C).

At a given discharge-charge rate, the battery pack cycled at DOD greater than 50% was observed to reach the end of life early as compared to 40% of DOD. Also, as the operating temperature and DOD increase, the estimated lifetime of the pack decreases due to the degradation in capacity. For instance, considering the 2C discharge and 4C charge rate, the remaining life is approximately 2,000 h at the operating temperature of 25°C and 30% DOD. However, as the temperature increases to 60°C, which keeps the DOD at 30%, the remaining life drops to 1,056 h. Because the battery is continuously cycled at the represented charge-discharge rates, the life (in hours) is low. Here, the remaining life is analyzed for the 4C charge rate condition because this analysis indicates the worst-case scenario clearly as compared to lower charge rates. The results are tabulated in Table 5, which indicates the best case and worst case for the operation of the battery pack, along with the travel range in kilometers (km). With a 1C discharge rate, the optimum distance range is 205,010 km, and the worst condition is 65,105 km. The kilometer range is calculated by multiplying the life (hours) with the average economy speed of the EV, 50 km/h (Iclodean et al., 2017).

The numerical calculation of the kilometer travelled at 1C discharge rate, which is calculated by Eq. (19).

$$Kilometers\ (km) = Speed \times Time$$

205,010 km = 50 × 4,100.2 h.

At a particular C-rate, it is observed that the pack cycled at greater DOD reaches the 80% end-of-life condition sooner as compared to the condition at lower DOD. This observation is clearly shown in Figure 8 using two cases: 0.5C discharge/1.25C charge rate and 4C discharge/4C charge rate to show the effect at lower C-rate and higher C-rate conditions. Also, it is evident that with the rise in operating temperature, the expected lifetime decreases drastically in both cases. Therefore, the graph in Figure 8 shows the range within which the lifetime (in hours) of the pack may vary due to changes in the operating conditions.

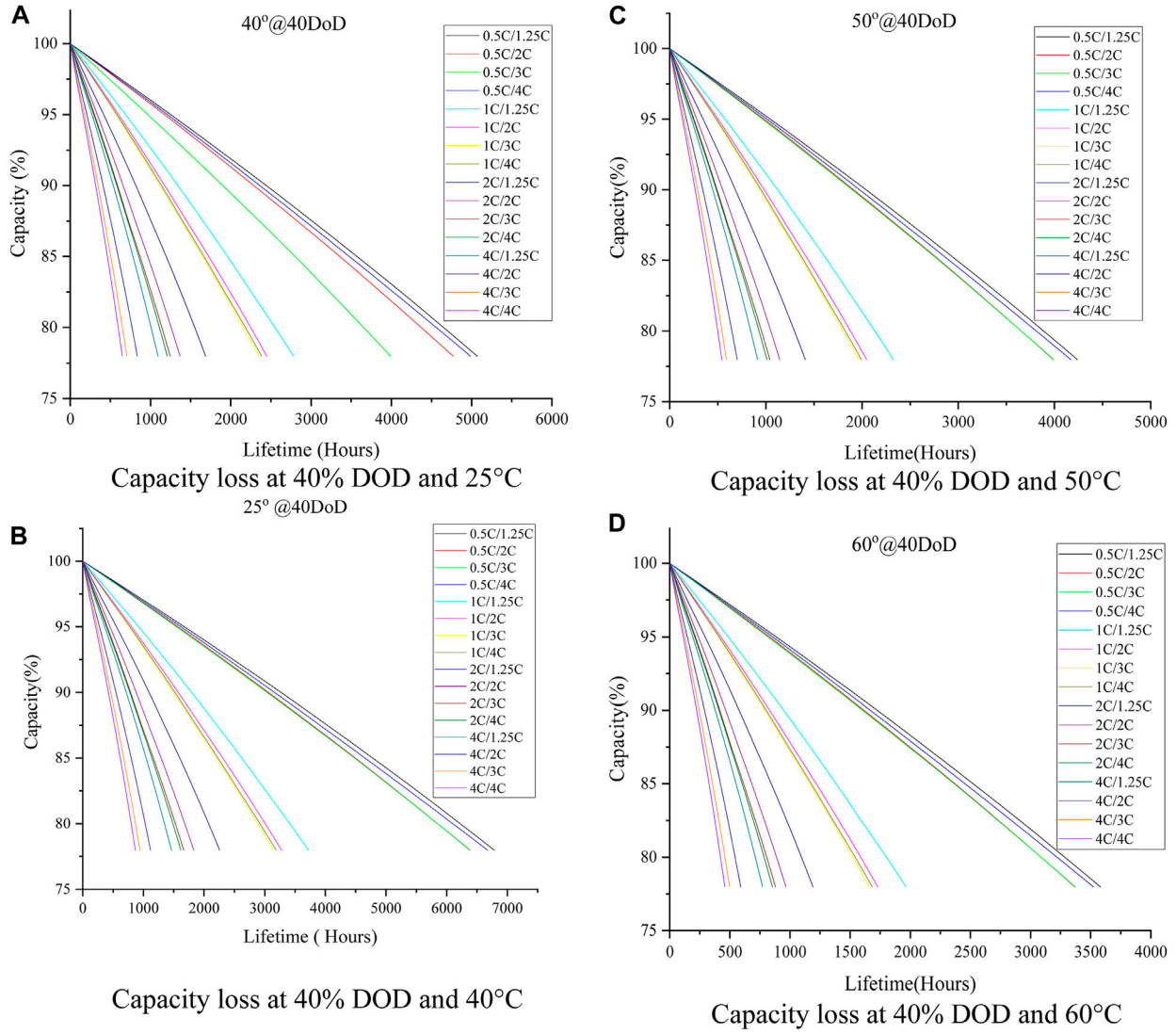

FIGURE 6
Capacity loss at 40% DOD. **(A)**: Capacity loss at 40% DOD and 25°C **(B)**: Capacity loss at 40% DOD and 40°C **(C)**: Capacity loss at 40% DOD and 50°C **(D)**: Capacity loss at 40% DOD and 60°C.

4 Conclusion

The remaining useful life of the battery pack in the Permanent magnet synchronous motor drive is analyzed through mathematical modeling of the Lithium ion pack, three-phase inverter, and Permanent magnet synchronous motor. A 327 V, 119.87 Ah battery pack, 180° conduction mode inverter, and 100 kW, 395 Nm permanent magnet synchronous motor available in the market are considered. The battery is modeled considering the operating temperature and aging effects (cycling). The effect of the parameters -- discharge-charge rate, operating temperature, and Depth of Discharge on the battery pack is investigated considering the Permanent magnet synchronous motor as the current drawing load. The results indicate that the lifetime of the Li-ion battery pack is largely dependent on the discharge rate and operating temperature, and the effect of the charge rate and the Depth of Discharge is comparatively less.

The self-discharge phenomenon that affects calendar aging is not considered for this modeling. Consideration of these parameters for estimating the lifetime of the Li-ion battery pack that powers the Permanent magnet synchronous motor drive will yield more accurate results in comparison. However, the results obtained from the work attempt to estimate the lifetime under critical conditions that the battery pack may be subjected to during its service life. The results of the proposed work are summarised as follows:

- At 40% Depth of Discharge, as the operating temperature of the pack is maintained at 25°C, the lifetime predicted is in the range of 6,786 h–867 h. However, when its operating temperature reaches 60°C, the predicted lifetime is in the range of 3,580 h–458 h.
- At severe conditions, about 80% Depth of Discharge when the operating temperature is maintained at 25°C, the lifetime is in

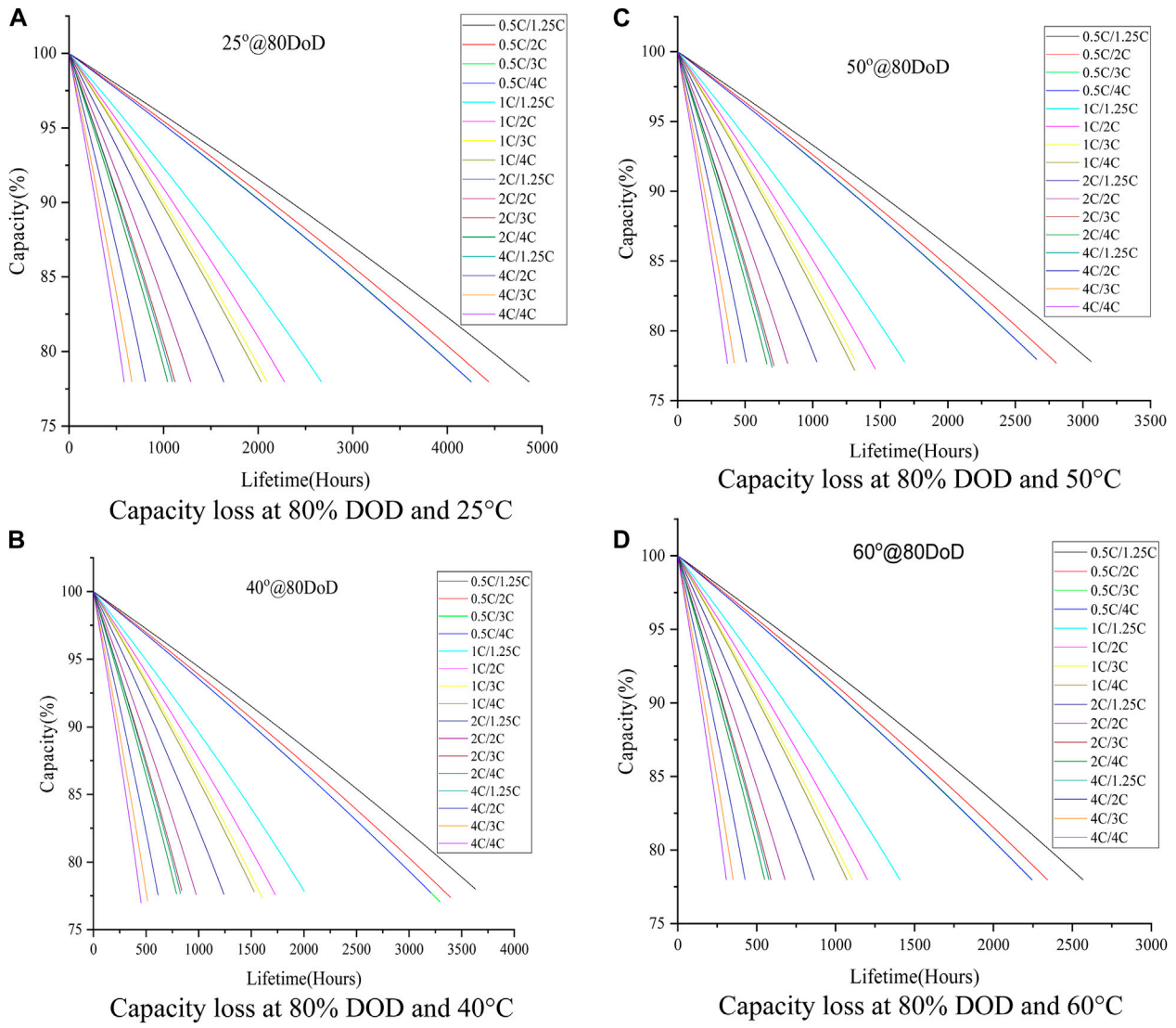

FIGURE 7
Capacity loss at 80% DOD. **(A)**: Capacity loss at 80% DOD and 25°C **(B)**: Capacity loss at 80% DOD and 40°C **(C)**: Capacity loss at 80% DOD and 50°C **(D)**: Capacity loss at 80% DOD and 60°C.

TABLE 5 Effect of temperature and DOD on life (in hours) at 4C rate.

Discharge Rate (C)	*Operating Condition*	*Battery Temperature (°C)*	*DOD (%)*	*Life (hours)*	*Kilometers (km)*
0.5	Optimum	40	30	6,326.5 h	316,325
	Worst	60	80	2,244.8 h	112,240
1	Optimum	25	30	4,100.2 h	205,010
	Worst	60	80	1,302.1 h	65,105
2	Optimum	25	30	2,002 h	100,100
	Worst	60	80	651.8 h	32,590
4	Optimum	40	30	772.6 h	38,630
	Worst	60	80	307.8 h	15,390

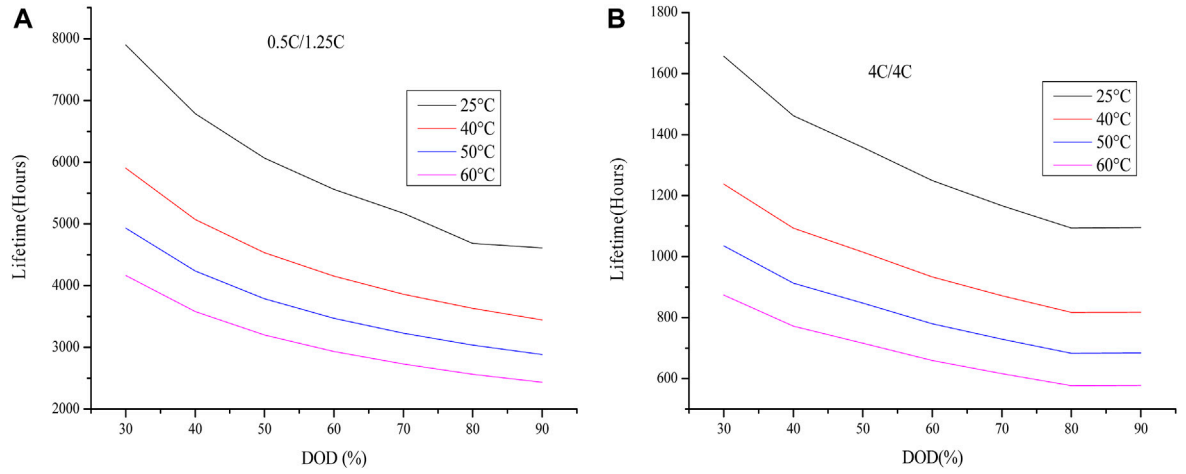

FIGURE 8
Capacity loss at different C-rate. **(A)** Lifetime loss at 0.5 C/1.25 C **(B)** Lifetime loss at 4C.

the range of 4,865 h–583 h. As the operating temperature is close to 60°C, the lifetime is expected to range from 2,567 h–307 h.

- Upon analysis of the effect on lifetime predicted by the increase in DOD from 40% to 80%: At a 0.5C/1.25C rate, it is seen that the lifetime decreases by 28.3%. At the 4C/4C rate, it is seen that the lifetime decreases by 32.8%

The results obtained can be used along with machine learning algorithms to predict the lifetime for additional conditions. Also, the real-time experimental work leads to accurate data that is helpful for precise battery life estimation. However, the cost of the battery pack is too high to carry out the experimental work.

Data availability statement

The original contributions presented in the study are included in the article/Supplementary Material, further inquiries can be directed to the corresponding authors.

Author contributions

RA: Conceptualization, Data curation, Formal Analysis, Funding acquisition, Investigation, Methodology, Project administration, Resources, Software, Supervision, Validation, Visualization, Writing–original draft, Writing–review and editing. YW: Conceptualization, Data curation, Formal Analysis, Funding acquisition, Investigation, Methodology, Project administration, Resources, Software, Supervision, Validation, Visualization, Writing–original draft, Writing–review and editing. SK: Conceptualization, Data curation, Formal Analysis, Funding acquisition, Investigation, Methodology, Project administration, Resources, Software, Supervision, Validation, Visualization, Writing–original draft, Writing–review and editing. SK: Project administration, Resources, Software, Supervision, Validation, Visualization, Writing–original draft, Writing–review and editing, Conceptualization, Data curation, Formal Analysis, Funding acquisition, Investigation, Methodology. BA: Conceptualization, Data curation, Formal Analysis, Funding acquisition, Investigation, Methodology, Project administration, Resources, Software, Supervision, Validation, Visualization, Writing–original draft, Writing–review and editing. HK: Conceptualization, Data curation, Formal Analysis, Funding acquisition, Investigation, Methodology, Project administration, Resources, Software, Supervision, Validation, Visualization, Writing–original draft, Writing–review and editing. KA: Conceptualization, Data curation, Formal Analysis, Funding acquisition, Investigation, Methodology, Project administration, Resources, Software, Supervision, Validation, Visualization, Writing–original draft, Writing–review and editing. AY: Conceptualization, Data curation, Formal Analysis, Funding acquisition, Investigation, Methodology, Project administration, Resources, Software, Supervision, Validation, Visualization, Writing–original draft, Writing–review and editing.

Funding

The author(s) declare that no financial support was received for the research, authorship, and/or publication of this article.

Acknowledgments

We thank the Vellore Institute of Technology (VIT) and State University of New York (SUNY)-Binghamton University for providing licensed tools for this research.

Conflict of interest

Author SK was employed by Hyundai Motor India Limited.

The remaining authors declare that the research was conducted in the absence of any commercial or financial relationships that could be construed as a potential conflict of interest.

Publisher's note

References

An, Z., Zhao, Y., Du, X., Shi, T., and Zhang, D. (2023). Experimental research on thermal-electrical behavior and mechanism during external short circuit for LiFePO4 Li-ion battery. *Appl. Energy* 332, 120519. doi:10.1016/j.apenergy.2022.120519

Ashwin, T. R., Chung, Y. M., and Wang, J. (2016). Capacity fade modelling of lithium-ion battery under cyclic loading conditions. *J. Power Sources* 328, 586–598. doi:10.1016/j.jpowsour.2016.08.054

Berecibar, M., Garmendia, M., Gandiaga, I., Crego, J., and Villarreal, I. (2016). State of health estimation algorithm of LiFePO4 battery packs based on differential voltage curves for battery management system application. *Energy* 103, 784–796. doi:10.1016/j.energy.2016.02.163

Bhardwaj, M. (2013). *Application report sensored field oriented control of 3-phase permanent magnet synchronous motors*.

Buchmann, I. (2017). *Batteries in a portable world - a handbook on rechargeable batteries for non-engineers*. 4th. Richmond, Canada: Cadex Electronics.

Che, Y., Deng, Z., Lin, X., Hu, L., and Hu, X. (2021). Predictive battery health management with transfer learning and online model correction. *IEEE Trans. Veh. Technol.* 70, 1269–1277. doi:10.1109/TVT.2021.3055811

Chen, X., Lei, H., Xiong, R., Shen, W., and Yang, R. (2019). A novel approach to reconstruct open circuit voltage for state of charge estimation of lithium ion batteries in electric vehicles. *Appl. Energy* 255, 113758. doi:10.1016/j.apenergy.2019.113758

Deng, Z., Hu, X., Lin, X., Che, Y., Xu, L., and Guo, W. (2020). Data-driven state of charge estimation for lithium-ion battery packs based on Gaussian process regression. *Energy* 205, 118000. doi:10.1016/j.energy.2020.118000

Deng, Z., Hu, X., Lin, X., Xu, L., Che, Y., and Hu, L. (2021). General discharge voltage information enabled health evaluation for lithium-ion batteries. *IEEE/ASME Trans. Mechatronics* 26, 1295–1306. doi:10.1109/TMECH.2020.3040010

García, A., Monsalve-Serrano, J., Martinez-Boggio, S., and Golke, D. (2023). Energy assessment of the ageing phenomenon in Li-Ion batteries and its impact on the vehicle range efficiency. *Energy Convers. Manag.* 276, 116530. doi:10.1016/j.enconman.2022.116530

Hannan, M. A., Wali, S. B., Ker, P. J., Rahman, M. A., Mansor, M., Ramachandaramurthy, V., et al. (2021). Battery energy-storage system: a review of technologies, optimization objectives, constraints, approaches, and outstanding issues. *J. Energy Storage* 42, 103023. doi:10.1016/j.est.2021.103023

Hill, G., Heidrich, O., Creutzig, F., and Blythe, P. (2019). The role of electric vehicles in near-term mitigation pathways and achieving the UK's carbon budget. *Appl. Energy* 251, 113111. doi:10.1016/j.apenergy.2019.04.107

Hossain Lipu, M. S., Hannan, M. A., Hussain, A., Ayob, A., Saad, M. H., Karim, T. F., et al. (2020). Data-driven state of charge estimation of lithium-ion batteries: algorithms, implementation factors, limitations and future trends. *J. Clean. Prod.* 277, 124110. doi:10.1016/j.jclepro.2020.124110

Huang, Z., Luo, P., Jia, S., Zheng, H., and Lyu, Z. (2022). A sulfur-doped carbon-enhanced Na3V2(PO4)3 nanocomposite for sodium-ion storage. *J. Phys. Chem. Solids* 167, 110746. doi:10.1016/j.jpcs.2022.110746

Iclodean, C., Varga, B., Burnete, N., Cimerdean, D., and Jurchiș, B. (2017). Comparison of different battery types for electric vehicles. *IOP Conf. Ser. Mater Sci. Eng.* 252, 012058. doi:10.1088/1757-899X/252/1/012058

Krishnan, R. (2017). *Permanent magnet synchronous and brushless DC motor drives*. Boca Raton, FL, USA: CRC Press.

Kunwar, R., Pal, B., Izwan, M. I., Daniyal, H., Zabihi, F., Yang, S., et al. (2023). Characterization of electrochemical double layer capacitor electrode using self-discharge measurements and modeling. *Appl. Energy* 334, 120658. doi:10.1016/j.apenergy.2023.120658

Li, S., He, H., Su, C., and Zhao, P. (2020). Data driven battery modeling and management method with aging phenomenon considered. *Appl. Energy* 275, 115340. doi:10.1016/j.apenergy.2020.115340

Li, X., Wang, Q., Yang, Y., and Kang, J. (2019). Correlation between capacity loss and measurable parameters of lithium-ion batteries. *Int. J. Electr. Power and Energy Syst.* 110, 819–826. doi:10.1016/j.ijepes.2019.03.046

Li, Y., Li, K., Liu, X., Li, X., Zhang, L., Rente, B., et al. (2022). A hybrid machine learning framework for joint SOC and SOH estimation of lithium-ion batteries assisted with fiber sensor measurements. *Appl. Energy* 325, 119787. doi:10.1016/j.apenergy.2022.119787

Liu, K., Li, K., Peng, Q., and Zhang, C. (2019). A brief review on key technologies in the battery management system of electric vehicles. *Front. Mech. Eng.* 14, 47–64. doi:10.1007/s11465-018-0516-8

Lü, H., Chen, X., Sun, Q., Zhao, N., and Guo, X. (2024). Uniform garnet nanoparticle dispersion in composite polymer electrolytes. *Wuli Huaxue Xuebao/Acta Phys. - Chim. Sin.* 40, 2305016. doi:10.3866/PKU.WHXB202305016

Lu, Y., Tan, C., Ge, W., Zhao, Y., and Wang, G. (2022). Adaptive disturbance observer-based improved super-twisting sliding mode control for electromagnetic direct-drive pump. *Smart Mater Struct.* 32, 017001. doi:10.1088/1361-665X/aca84e

Marques, P., Garcia, R., Kulay, L., and Freire, F. (2019). Comparative life cycle assessment of lithium-ion batteries for electric vehicles addressing capacity fade. *J. Clean. Prod.* 229, 787–794. doi:10.1016/j.jclepro.2019.05.026

Mu, S., Liu, Q., Kidkhunthod, P., Zhou, X., Wang, W., and Tang, Y. (2021). Molecular grafting towards high-fraction active nanodots implanted in N-doped carbon for sodium dual-ion batteries. *Natl. Sci. Rev.* 8, nwaa178. doi:10.1093/nsr/nwaa178

R, A., Rk, C., and Vp, C. (2021). Experimental analysis on estimating junction temperature and service life of high power LED array. *Microelectron. Reliab.* 120, 114121. doi:10.1016/j.microrel.2021.114121

Rahman, M. A., Anwar, S., and Izadian, A. (2016). Electrochemical model parameter identification of a lithium-ion battery using particle swarm optimization method. *J. Power Sources* 307, 86–97. doi:10.1016/j.jpowsour.2015.12.083

Richter, F., Kjelstrup, S., Vie, P. J. S., and Burheim, O. S. (2017). Thermal conductivity and internal temperature profiles of Li-ion secondary batteries. *J. Power Sources* 359, 592–600. doi:10.1016/j.jpowsour.2017.05.045

Sha, L., Sui, B.-B., Wang, P.-F., Gong, Z., Zhang, Y. H., Wu, Y. H., et al. (2024). 3D network of zinc powder woven into fibre filaments for dendrite-free zinc battery anodes. *Chem. Eng. J.* 481, 148393. doi:10.1016/j.cej.2023.148393

Shen, Y., Xie, J., He, T., Yao, L., and Xiao, Y. (2024). CEEMD-fuzzy control energy management of hybrid energy storage systems in electric vehicles. *IEEE Trans. Energy Convers.* 39, 555–566. doi:10.1109/TEC.2023.3306804

Somakettarin, N., and Pichetjamroen, A. (2019). Characterization of a practical-based ohmic series resistance model under life-cycle changes for a lithium-ion battery. *Energies (Basel)* 12, 3888. doi:10.3390/en12203888

Somakettarin, N., Pichetjamroen, A., Teerakawanich, N., Chindamanee, P., Chupong, C., and Suppitaksakul, C. (2023). An evaluation of battery energy efficiency with multi-step sampling rate recording for DC data loggers. *Energy Rep.* 9, 866–872. doi:10.1016/j.egyr.2022.11.103

Sun, C., Negro, E., Vezzù, K., Pagot, G., Cavinato, G., Nale, A., et al. (2019). Hybrid inorganic-organic proton-conducting membranes based on SPEEK doped with WO3 nanoparticles for application in vanadium redox flow batteries. *Electrochim Acta* 309, 311–325. doi:10.1016/j.electacta.2019.03.056

Tufail, M. K., Zhai, P., Jia, M., Zhao, N., and Guo, X. (2023). Design of solid electrolytes with fast ion transport: computation-driven and practical approaches. *Energy Mater. Adv.* 4, 15. doi:10.34133/energymatadv.0015

Wali, S. B., Hannan, M. A., Reza, M. S., Ker, P. J., Begum, R., Rahman, M. A., et al. (2021). Battery storage systems integrated renewable energy sources: a biblio metric analysis towards future directions. *J. Energy Storage* 35, 102296. doi:10.1016/j.est.2021.102296

Wang, J., Liu, P., Hicks-Garner, J., Sherman, E., Soukiazian, S., Verbrugge, M., et al. (2011). Cycle-life model for graphite-LiFePO4 cells. *J. Power Sources* 196, 3942–3948. doi:10.1016/j.jpowsour.2010.11.134

Wang, L., Zhao, X., Deng, Z., and Yang, L. (2023). Application of electrochemical impedance spectroscopy in battery management system: state of charge estimation for aging batteries. *J. Energy Storage* 57, 106275. doi:10.1016/j.est.2022.106275

Wang, M., Jiang, C., Zhang, S., Song, X., Tang, Y., and Cheng, H. M. (2018). Reversible calcium alloying enables a practical room-temperature rechargeable calcium-ion battery with a high discharge voltage. *Nat. Chem.* 10, 667–672. doi:10.1038/s41557-018-0045-4

Wang, Q.-K., He, Y.-J., Shen, J.-N., Ma, Z. F., and Zhong, G. B. (2017). A unified modeling framework for lithium-ion batteries: an artificial neural network based thermal coupled equivalent circuit model approach. *Energy* 138, 118–132. doi:10.1016/j.energy.2017.07.035

Wang, Y., and Li, L. (2016). Li-ion battery dynamics model parameter estimation using datasheets and particle swarm optimization. *Int. J. Energy Res.* 40, 1050–1061. doi:10.1002/er.3497

Weldon, P., Morrissey, P., and O'Mahony, M. (2018). Long-term cost of ownership comparative analysis between electric vehicles and internal combustion engine vehicles. *Sustain Cities Soc.* 39, 578–591. doi:10.1016/j.scs.2018.02.024

Xu, J., Sun, C., Ni, Y., Lyu, C., Wu, C., Zhang, H., et al. (2023). Fast identification of micro-health parameters for retired batteries based on a simplified P2D model by using padé approximation. *Batteries* 9, 64. doi:10.3390/batteries9010064

Yang, Z., Patil, D., and Fahimi, B. (2019). Electrothermal modeling of lithium-ion batteries for electric vehicles. *IEEE Trans. Veh. Technol.* 68, 170–179. doi:10.1109/TVT.2018.2880138

Yonemoto Yktiko, M. (2020). *Secondary-battery monitoring device and prediction method of battery capacity of secondary battery*.

Yu, Q., Huang, Y., Tang, A., Wang, C., and Shen, W. (2023). OCV-SOC-temperature relationship construction and state of charge estimation for a series– parallel lithium-ion battery pack. *IEEE Trans. Intelligent Transp. Syst.* 24, 6362–6371. doi:10.1109/TITS.2023.3252164

Yul Yongin-si, H., Yongin-si, J., Ho Yongin-si, C., Yongin-si, H., Yongin-si, Y., Bum Yongin-si, S., et al. (2013). *System for predicting lifetime of battery*.

Zhang, R., Li, X., Sun, C., Yang, S., Tian, Y., and Tian, J. (2023a). State of charge and temperature joint estimation based on ultrasonic reflection waves for lithium-ion battery applications. *Batteries* 9, 335. doi:10.3390/batteries9060335

Zhang, X., Lu, Z., Yuan, X., Wang, Y., and Shen, X. (2021). L2-Gain adaptive robust control for hybrid energy storage system in electric vehicles. *IEEE Trans. Power Electron* 36, 7319–7332. doi:10.1109/TPEL.2020.3041653

Zhang, X., Tang, Y., Zhang, F., and Lee, C.-S. (2016). A novel aluminum–graphite dual-ion battery. *Adv. Energy Mater* 6, 1502588. doi:10.1002/aenm.201502588

Zhang, X., Wang, Y., Yuan, X., Shen, Y., and Lu, Z. (2023b). Adaptive dynamic surface control with disturbance observers for battery/supercapacitor-based hybrid energy sources in electric vehicles. *IEEE Trans. Transp. Electrification* 9, 5165–5181. doi:10.1109/TTE.2022.3194034

Zhang, X., Wang, Z., and Lu, Z. (2022). Multi-objective load dispatch for microgrid with electric vehicles using modified gravitational search and particle swarm optimization algorithm. *Appl. Energy* 306, 118018. doi:10.1016/j.apenergy.2021.118018

Zhou, Y., Wang, B., Ling, Z., Liu, Q., Fu, X., Zhang, Y., et al. (2024). Advances in ionogels for proton-exchange membranes. *Sci. Total Environ.* 921, 171099. doi:10.1016/j.scitotenv.2024.171099

Zhu, L., Li, Z., and Hou, K. (2023). Effect of radical scavenger on electrical tree in cross-linked polyethylene with large harmonic superimposed DC voltage. *High. Volt.* 8, 739–748. doi:10.1049/hve2.12302

Nomenclature

AC	Alternating current
C-rate	Charge and Discharge rate
LIB	Lithium-ion batteries
DOD	Depth of Discharge
ESS	Energy storage system
OCV	Open circuit voltage
RC	Resistor–capacitor circuit
RLC	Resistor capacitor inductor circuit
ECM	Equivalent circuit model
Ebatt	Non-linear Voltage, V
E_o	Constant Voltage, V
exp	exponential
EV	Electric Vehicle
FOC	Field-Oriented Control
I	Battery current (A)
IC	Internal combustion
K	Polarization Constant
iA, iB, iC	Three phase currents, A
iL	Current across the inductor, A
$i_{d'}$, $i_{q'}$, $i_{0'}$	d'q'0′frame currents
$LiFePO_4$	Lithium Iron Phosphate
Li-ion	Lithium Ion
N	Maximum number of cycles
P_L	Heat generated during the charge-discharge cycle, W
P2D	Pseudo-Two-Dimensional
PMSM	Permanent Magnet Synchronous Motor
q-axis	Quadrature Axis
R	Internal resistance
SOC	State of Charge
SOH	State of Health
Ta	Ambient Temperature, K
t	Lifetime, h
V_{batt}	Battery voltage, V
ΔQ/ΔT	Maximum capacity temperature coefficient, Ah/K
λ	Battery Aging Factor
ζ	Arrhenius rate constant for internal resistance, Ω

frontiers | Frontiers in Energy Research

TYPE Original Research
PUBLISHED 10 April 2024
DOI 10.3389/fenrg.2024.1357863

OPEN ACCESS

EDITED BY
Flah Aymen,
École Nationale d'Ingénieurs de Gabès, Tunisia

REVIEWED BY
José Baptista,
University of Trás-os-Montes and Alto Douro, Portugal
Ramesh G. P.,
St Peter's Institute of Higher Education and Research, India
Mohammed Rashad Baker,
University of Kirkuk, Iraq

*CORRESPONDENCE
Przemysław Falkowski-Gilski,
przemyslaw.falkowski@eti.pg.edu.pl
Parameshachari Bidare Divakarachari,
paramesh@nmit.ac.in

RECEIVED 18 December 2023
ACCEPTED 13 March 2024
PUBLISHED 10 April 2024

CITATION
Srihari G, Krishnam Naidu RSR, Falkowski-Gilski P, Bidare Divakarachari P and Kiran Varma Penmatsa R (2024), Integration of electric vehicle into smart grid: a meta heuristic algorithm for energy management between V2G and G2V.
Front. Energy Res. 12:1357863.
doi: 10.3389/fenrg.2024.1357863

Integration of electric vehicle into smart grid: a meta heuristic algorithm for energy management between V2G and G2V

G. Srihari[1], R. S. R. Krishnam Naidu[2], Przemysław Falkowski-Gilski[3]*, Parameshachari Bidare Divakarachari[4]* and Ravi Kiran Varma Penmatsa[5]

[1]School of Technology, The Apollo University, Chittoor, India, [2]Department of Electrical and Electronics Engineering, Nadimpalli Satyanarayana Raju Institute of Technology, Visakhapatnam, India, [3]Faculty of Electronics, Telecommunications and Informatics, Gdansk University of Technology, Gdansk, Poland, [4]Department of Electronics and Communication Engineering, Nitte Meenakshi Institute of Technology, Bengaluru, India, [5]Department of CSE, Sagi Rama Krishnam Raju Engineering College, Bhimavaram, India

Recently, Electric Vehicles (EV) have been providing fast response and substantial progress in the power generation model. Further, EVs are exploited as adaptable Energy Storage Systems (ESSs) and show a promising performance in ancillary service markets to increase the demand of Smart Grid (SG) integration. The expansion of Vehicle-to-Grid concept has created an extra power source when renewable energy sources are not available. Yet, numerous operational problems still are required to be considered for EV implementation to turn out to be extensive. Even the development of Photo-Voltaic (PV) technology creates a problem in SGs when used for EV charging. Because of this, the Energy Management System (EMS) is required to handle charging requirements and deal with the intermittent generation. Here, in this research, an Improved Honey Badger algorithm (IHBA) is proposed for integrating SGs with EV parking lot, solar panels, and dynamic loads at the Point of Common Coupling (PCC). The proposed IHBA uses a dynamic programming method to optimize the charging Grid-to-Vehicle (G2V) or discharging Vehicle-to-Grid (V2G) profiles of the EVs using the forecasts of PV generation. This algorithm considers user preferences while also lowering reliance on the grid and maximizing SG effectiveness. The study's findings show that the Honey Badger method is efficient in resolving issues involving large search spaces. The developed method is used to optimize charging and discharging of EV which is tested in MATLAB to obtain a stable load profile. From the evaluation of obtained results, it is evident that the IHBA controller outperforms the WOA and EHO controllers in terms of total harmonic distortion voltage (3.12%), power loss (0.197 kW) and efficiency (98.47%).

KEYWORDS

electric vehicle, energy management system, energy storage systems, improved honey badger algorithm, smart grid, photo-voltaic

1 Introduction

In recent days, one of the electric industry's areas of expanding interest is the smart grid (SG). An integrated communication and power system known as SG enables a robust, bi-directional communication infrastructure with distributed computers. Additionally, enhanced control, stability, and optimized power delivery are made possible by this system (Makeen et al., 2023). In cities where Plug-in Electric Vehicles (PEVs) are widely available, parking lots should consider implementing smart management and scheduling options. The rapid advancement of Electric Vehicle (EVs) has resulted in a considerable burden on the power grid system for the implementation of an effective control framework (ur and Rehman, 2022). The process of charging EVs imposes an excessive strain on the power grid, leading to voltage fluctuations and supply shortages. As PEVs continue to increase, they are emerging as the most probable alternative to combustion engine vehicles (Spanoudakis et al., 2023). In comparison to other new energy vehicles like Hybrid EVs (PHEVs), PEVs possess larger storage batteries, making them well-suited for participating in Grid-to-Vehicle (G2V) or Vehicle-to-Grid (V2G) energy supervision (Grasel et al., 2023). Grid operators and vehicle owners are showing interest in V2G because it presents a potential backup for renewable energy sources like solar and wind power. Additionally, they enhance the grid's technical performance in respect to efficiency, stability, dependability, and generation dispatch. Since many EVs are useable as both a load and an ESS to assist the grid, a new emerging technology called V2G has emerged. Nonetheless, the disorganized EV charging demonstrates a significant influence on the power system. Therefore, optimal V2G system coordination is required (Zhang et al., 2023a). There are many different types of business models and information system architectures related to smart grids that are suggested until today, but none of them are consistent with specific standards (Ismail et al., 2023). Effective management of electric vehicles has the potential to enhance the reliability and stability of power grids. Furthermore, they facilitate the integration of renewable sources and improve the overall efficiency of the system (Kumari et al., 2022). Energy Management Systems (EMS) enables the operation and supervision of Battery Energy Storage Systems (BESS) in standalone power systems (Thirugnanam et al., 2023).

Generally, the vehicle utilizes both the internal combustion engine as well as battery-powered motor powertrain. The petrol engine is exploited to operate and charge the vehicle once the battery gets drained. Some model-free methodologies have lately demonstrated their efficacy in a variety of decision-making applications, including e-healthcare and Intelligent Transportation Systems (ITS) (Zhang et al., 2023b). Reinforcement learning does not require prior system knowledge, it learns a sound control strategy and acts appropriately to attain desired goals. Rarely documented are EV batteries as storage with a bidirectional converter (Kumar et al., 2022). It is advised to employ high power quick charging when using EVs as energy storage systems. The early stages of V2G progress within a smart grid facility aimed at facilitating power generation from unpredictable renewable energy sources. Additionally, a majority of reported studies employ Level 1 and 2 charging for V2G technology (Sureshkumar et al., 2022). V2G technology, also referred to as Vehicle-Grid Integration (VGI), enables the transfer of surplus power from electric vehicles to the smart grid. This innovative approach aids in meeting electricity demands during the high usage periods, and serves as an additional energy source when weather-dependent renewable sources are inaccessible (Egbue et al., 2022). The system power quality is impacted by EV charging which affects different sections of the distribution grid. Unplanned and undesirable peaks in the grid demand are caused by the uncoordinated charging of electric vehicles. Furthermore, fast charging and the presence of non-linear components in the charging infrastructure cause harmonic content to be introduced into the grid voltage (İnci et al., 2022). In addition, this causes power outages, voltage instability, transformer overloading, and a decline in reliability indices. Moreover, when EVs are charged using pre-existing connections, voltage instability occurs in the host facilities. The battery storage capacity of a single PHEV is minimal when compared to the grids (Liu et al., 2023). Because EVs require a lot of power to recharge their batteries, using them has an undesirable influence on the power quality. Transformer life cycle decreases when EV interference in the system increases. Even so, by grouping PHEVs as storage devices, an improved coordination and dependability is attained in a smart grid (Tirunagari et al., 2022). Therefore, a distribution and transmission system operator, the electrical market and PHEV owners, all work together effectively with the help of an aggregator which is useable as a communication/controller device or algorithm.

The main contributions of this research are as follows.

- This article use an EMS named Improved Honey Badger Algorithm (IHBA) which is deployed to suggest how energy is distributed among ESS, PV, and EV.
- The IHBA method of controlling the converter current and DC bus voltage is provided. Implementing a control method allows for the stabilization of the DC bus voltage.
- A review of different topologies is used to connect the batteries and the load. This analysis, which outlines the merits and downsides of each structure, is displayed using a variety of models.

The manuscript is structured as follows: the existing researches based on EMS in EV are described in Section 2. The suggested IHBA is described in Section 3, while the explanation of outcomes are presented in Section 4. At last, the conclusions are detailed in Section 5.

2 Literature review

A wide-ranging Switched Reluctance Motor (SRM) for plug-in EVs was developed by Cheng et al. (Cheng et al., 2020) based on a variety of driving and charging measurements. The motor driving mode had four essential activities that were to be performed in order to accurately analyze the decelerating actions. There were three ways to charge batteries that did not require extra battery points. For the objective of recharging the drive battery, a three-channel periodic boost converter featuring PF control characteristics was executed by SRM windings and associated converters. An incorporated half-

bridge converter was used to power the additional batteries from the engine. However, it had a huge loss.

Liu et al. (Liu et al., 2020) demonstrated a new method called Hierarchical V2G/G2V EMS for rechargeable drive reassembled through onboard circuit along with a converter. A V2G energy management system containing an Electric Drive Range-Extended On-Board Charger (EDROC) was suggested. In the V2G/G2V, the suggested EDROC employed a synchronous motor as a charging inductance, eliminating the need for extra equipment. Additionally, this research presented a classified V2G/G2V EMS along with a control approach that contained EDROC which reduced the dispersion of PEV State of Charge (SOC).

He et al. (He et al., 2021) presented a new technique named Four-Quadrant Operation of Bidirectional charges for EV in parking lots. This research presented to achieve the objective of maintaining a constant current during the charging and discharging processes of EV on the load side. By employing the Model Predictive Control (MPC) strategy, EV chargers efficiently transferred both active and reactive powers among EV batteries, as well as the grid. In the exchange of active power, a new mode called V2G was presented. But the system required approximately three grid cycles, equivalent to 60 milliseconds, in order to respond to a fresh command.

Justin et al. (Justin et al., 2022) presented a new method named V2G by means of fast charging stations. EV batteries having the potential to serve as energy storage units in smart grids, contributed to the energy in small power networks. They stored excess energy from the grid to provide energy back to the grid when there was a need for it. A test system for a smart grid was designed, and included a DC fast charging station to connect with the EV. An appreciable total harmonic distortion was attained by sensible design of the LCL filter. Nonetheless, according to IEEE standards, the harmonic current distortion was low and limited in this research.

Dhasharatha et al. (Rahman et al., 2018) represented a new technique of simulation and analysis of V2G and G2V technology in electric vehicles. This paper presented a design for executing V2G-G2V system within a smart grid, specifically utilizing Level 3 fast charging for EVs. The architecture included a modeled smart grid test system that incorporated a fast-charging place for connecting with EVs. Simulation studies were conducted to display the energy transfer capabilities of V2G-G2V within the system. Harmonic distortion was limited and underneath on power systems standards.

An innovative method known as Smart EMS for electrical grids driven by heterogeneous renewable energy sources and EV storage was presented by Madhavaram and Manimozhi (Madhavaram and Manimozhi, 2022). The method offered an innovative EMS for SGs that made use of EV storage and unconventional energy sources. While several studies explored MG EMSs with energy storage, their implementation in real-time scenarios was often hindered by various factors. Nevertheless, there was room for the development of more advanced and intelligent decision-making strategies, specifically tailored for Electric Vehicle Systems (EVSs).

Al-Abri and Albadi (Al-Abri and Albadi, 2022) implemented an effect of vehicles on the planning and operation of the distribution method. This research described the capability of services offered by EVs and found the potential effect. At the distribution system level, EVs offered ancillary works based on local operational problems, and furthermore, the categorization was variant from market to market as well as from need of individual country's laws. While utilizing this method to reduce the negative effects, choosing the optimal sizing and spot of EVs charging values was essential to manage the power quality and trust ability. Yet, it further required to consider the potential effect of EVs on reactive power market architecture and the economy.

Hybrid storage was demonstrated by Guentri et al. (Guentri et al., 2021) as a means of controlling and managing PV array energy. The goal of this study was to modify the energy sources' voltage regulation architecture in accordance with these reliable control ideas. The performance metrics and dependability of these methods were also evaluated. Efficiency was increased by using the Genetic Algorithm (GA) optimization technique, which significantly reduced peak overshoot and settling time. The GA-based Proportional Integral Derivative (PID) controller architecture only caused problems for the machine after 67% of it was reached.

An EMS for grid-EV and renewable power was successfully developed by Al-Dhaifallah et al. (Al-Dhaifallah et al., 2021). Three different charging techniques were taken into consideration in order to evaluate the behavior of EVs: supervised, unsupervised, and smart charging methods. Through the utilization of the Modified Harmony Search (MHS) method, micro grid optimization planning was handled. Although it was a crucial issue, the MG's Day-ahead planning merits more thought. However, a number of problems, such as their short battery life, poor start-up performance, and limited driving range were preventing them from developing further.

By controlling the PFC and DC voltage with a Resettable Integrator (RI) control technique, Kanimozhi et al. (Kanimozhi et al., 2022) presented an effective two-stage charger system. The regulator handled a nonlinear switching converter with a quicker dynamic response and enhanced its robustness. The rectifier diodes and inverter switches were used in the following phase to help them achieve ZVS/ZCS. However, the switching loss increased in proportion to the power that was shielded from the diode's presence when the diode delay was considered.

Using an Artificial Neural Network (ANN) in conjunction with the Particle Swarm Optimization (PSO) method for battery Electric Vehicle (EV), Nouri et al. (Nouri et al., 2024) presented a V2G system with intelligent management to guarantee precise and steady energy extraction from the solar power system, even under varying sunlight situations. While combined with the Constant Voltage/ Constant Current method, the fuzzy logic system ensures that the electric vehicle batteries are charged and discharged in compliance with exact pre-established circumstances. But when EVs do not take part in energy management, the energy efficiency value drops, emphasizing how important V2G operation is. In these situations, the grid makes up for the energy shortage, which was ineffective from a commercial perspective.

2.1 Review

This study examined a number of V2G technology-related topics, including advantages and disadvantages. Research indicates that the automotive and electric power sectors are mutually beneficial, and bolstering one through the other is advantageous for both. Regarding renewable energy, low emissions, energy economy, and power system dependability,

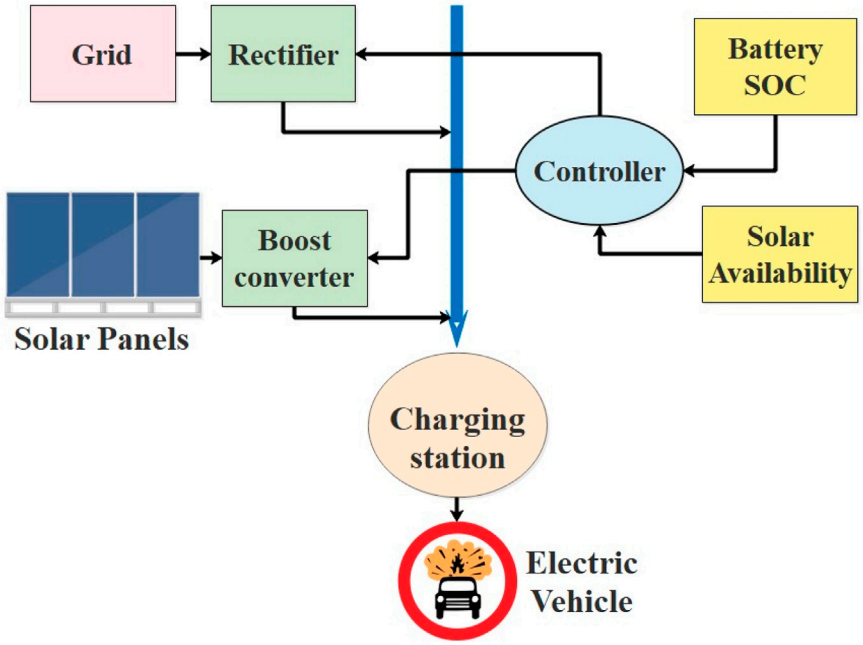

FIGURE 1
Overall workflow of the proposed method.

V2G technology is very promising. This technology offers ancillary services in addition to making it simple to integrate renewable resources into the utility. The power sector is made more dependable and stable by having a sufficient number of EVs with V2G capability on the road and an effective power management and control strategy. But there are many obstacles to EV grid integration, particularly in developing nations. Range anxiety, a lack of consumer awareness, high ownership costs, and inadequate charging infrastructure are the main issues impeding the widespread adoption of electric vehicles. Understanding the change in interest in the automotive and power markets is crucial in this regard. This essay addresses the numerous ideas surrounding EVs, the potential provided by V2G, the challenges associated with implementation, and possible solutions.

3 Proposed methodology

A hybrid system consisting of Photo-Voltaic (PV) cells and batteries is recommended as a resolution for various problems. A continuous charging of EVs is presently not viable, conferring to the grid overload. Users are unsure because of the charging disruptions. Hence, combining grid-connected charging with battery and PV charging is suggested to tackle the issue of car charging. The proposed method works well for providing EV charging without any delays. The main benefit of the proposed system is its capacity to promptly meet the charging requirements of all EVs, while also minimizing the increased grid burden. Many optimization methods are used to develop this control algorithm. Figure 1 shows a summary of the proposed method.

The generation and consumption of power varies over time and space with distributed energy sources. The traditional power grid's energy management is now more difficult and complex as a result. With the expansion of SG, power distribution has become more adaptable, effective, dependable, and secure. Smart energy metering, improved control, and advanced communication technologies are all included in the smart grid.

In smart grids, EV batteries are exploited as potential storage devices which assist in EMS by saving energy once it is surplus (G2V), and then returning it to grid (V2G) as soon as needed. The development of appropriate control systems and infrastructure is necessary to make this idea a reality. This article provides the design for integrating EV fast charging into a smart grid for a V2G-G2V system. An EV interface is provided by a dc fast charging station in a simulated smart-grid test system. V2G-G2V power transfer is established over modelling studies where the regulator delivers better dynamic results based on voltage stability, while the charging station strategy guarantees limited THD of the grid injected current.

3.1 Energy management system

The goal of power distribution networks is to run smoothly in order to provide more efficient and reliable electricity to local consumers. But when more EVs are adopted, the demand profile for each distribution network is significantly increased, which further puts pressure on the network's stability and structural integrity. When modelling grid stability, the different contributing factors that affect the EV charging load are crucial. The random travel habits of multiple EV users lead to intermittent charging patterns, which cause load fluctuations and imbalances in the grid's component parts. A specialized block uninterruptedly gathers power data from various sources, such as EV charging

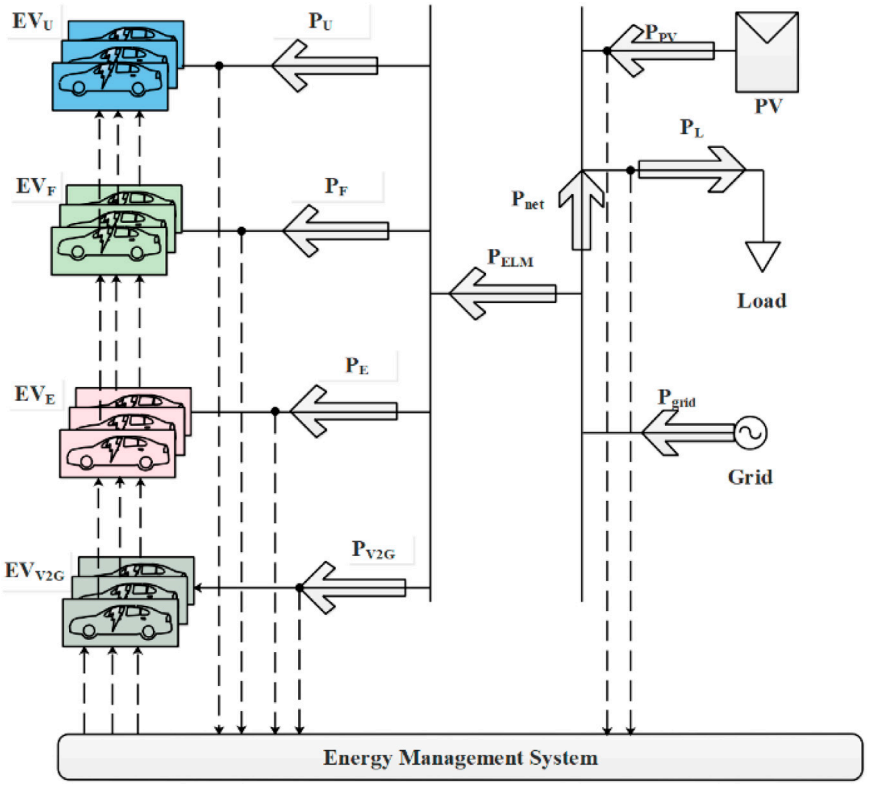

FIGURE 2
Simplified arrangement of the proposed smart grid.

stations, PV systems, and smart grids (Bot et al., 2022), for use in the EMS that is provided. The EMS makes excellent use of this information to organize EV charging (Karoń, 2022). Additionally, the EMS also gathers unique EV charging profiles supplied by the EV user when they arrive at the parking lot in order to optimize the operation of SG. The EV data profile is structured as $EV_{i,j}$ {struct}, where i refers to the charger group and j refers to the charger's outlet. The data structure contains several key parameters, including user/vehicle identifier (ID), the chosen charging mode ($Mode$), connection time (t_0), expected disconnection time (t_f), current state of charge (SOC_c), desired final stage of charge (SOC_f), maximum battery capacity (E_{bat}), and nominal charging power (P_{nom}). These parameters are crucial for effective management and optimization of EV charging within the smart grid.

EVs are arranged in a suggested simplified configuration of the SG illustration (P_{EV_v}), as shown in Figure 2. P_{PV} and P_L stand for power produced by PV panels and power used through loads. Additionally, the energy management happens from the power system which employs optimization to find the precise charging instruction (P_{EV_v}) for all the charging apparatuses. The suggested EMS presents a collection $\mathcal{M} = \{EV_u, EV_F, EV_E, EV_{V2G,}\}$ consisting of four distinct modes for EV charging: ULTRA, FAST, ECO, and V2G.

The complete power flow connected with each vehicle working in every charging mode is characterized by P_u, P_F, P_E, and P_{V2G}, consistently. In this research, reactive power values are not taken into consideration as they have focused only on active power which have been taken into an account for optimization process. Similarly, distribution impedance is not to be taken into account; instead, all converters' efficiency is evaluated. In order to use the same station for multiple charging modes, EV users choose charging mode at any place. Grid loads are typically divided into two categories, dynamic and static. The generation of PV is exploited to characterize the various climate environments, and it is assumed that this paper represents a characteristic demand outline of a profitable formation. From Figure 3, it is seen that the power flow constraints of the suggested scheme configuration is characterized by $P_{grid} = P_{net} + P_{EV_M}$, where $P_{net} = P_L - P_{p_v}$. The balance between electricity demand and generation is represented by the above equation. The reasonable layout of EMS block that comprises of the four efficient components: acquisition, supervision, optimization, and prediction is shown in Figure 3.

3.2 EMS operation

Driver behavior which is dependent on a number of factors including weather, traffic density, acceleration rate, and keeping a minimum safe space between following vehicles, is a major influence in determining how much energy an electric vehicle uses. Multiple EVs charging at once, have a negative impact on the power system because fast charging stations are under a lot of strain. One of the main concerns for power systems is the possibility of a quick adoption of EVs, and a move toward electric transportation networks. Optimizing charging techniques to reduce peak demand is a crucial step in preventing the electrical system from

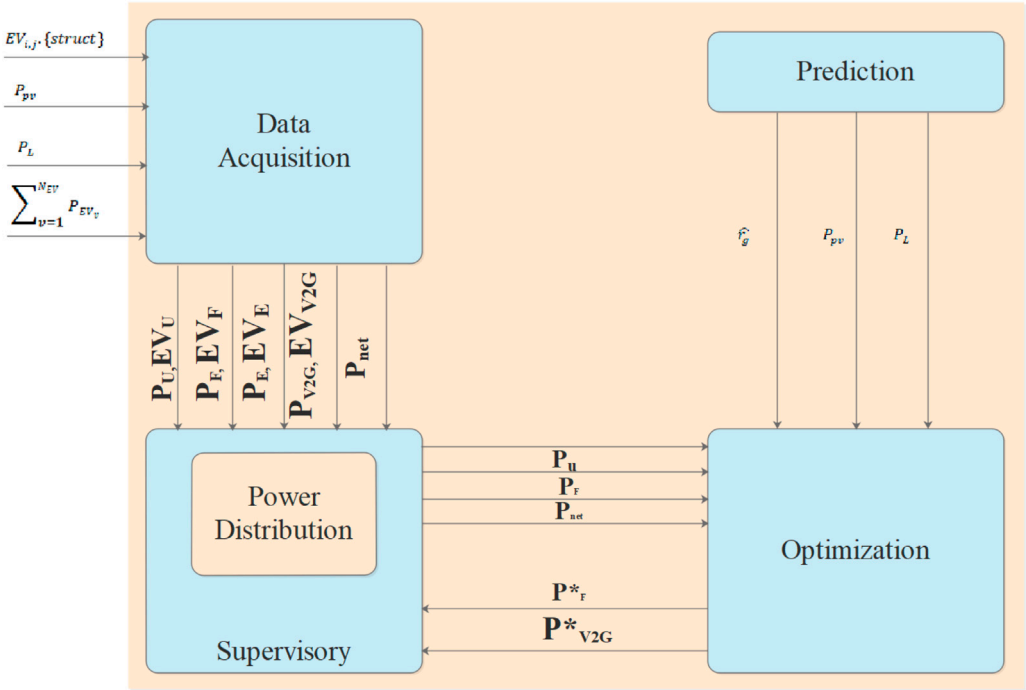

FIGURE 3
Overview of the proposed architecture.

being overloaded. The EV user chooses the anticipated charging outline when a car is plugged into a charging station, while the acquisition model collects and organizes data from the EV user. In addition, there is an ongoing load demand and PV generation acquisition. Real-time tasks inside the system are managed by the supervisor module (Raju et al., 2023). Data from the acquisition module is used to determine whether an optimization procedure is required. The supervisor component separates and guides the outcomes to inverter after updating the power references for the ULTRA and FAST charging modes at the end of every calculation step. An optimization procedure is also started by the supervisor module when the ECO and V2G modes are chosen. A dynamic programming is utilized in this scenario to determine power references for EV charging during the course of the connection period. Dynamic programming is used in the optimization process to obtain the ideal charging progression throughout the day. By giving predicted data, the prediction module helps with optimization of energy price ($\widehat{r_g}$), PV generation forecast ($\widehat{P_{pv}}$), and load demand ($\widehat{P_L}$).

3.3 EV functional mode

To establish each vehicle's state of charge (SOC) behavior, and to update the investigation, a battery is used (Mojumder et al., 2022; Gan et al., 2024). Eqs 1, 2 mathematically represent the SOC.

$$\boldsymbol{SOC_v[n+1] = SOC_v[n] + \eta EV \frac{P_{EV_v}[n]\Delta t}{E_{bat_v}}} \tag{1}$$

The equation for SOC behavior of each vehicle based on a linear battery model is as follows.

- $SOC_v[n+1]$ characterizes the resultant battery proportion of one sample gain (at sample n+1) for vehicle v.
- $SOC_v[n]$ represents the current battery percentage for vehicle v at sample n.
- ηEV denotes the charging/discharging efficiency.
- $P_{EV_v}[n]$ represents the charging power available for vehicle v at the current sample n.
- E_{bat_v} denotes the total battery capacity for vehicle v.

$$\boldsymbol{0 \le SOC_v[n+1] \le 1}, \tag{2}$$

Which restricts the control performance and provides the charging electric vehicle PEV_v as given in Eq. 3:

$$\boldsymbol{PEV_v = \begin{cases} P_{EV_v}, & if\ 0 \le SOC_v[n+1] \le 1, \\ 0, & otherwise \end{cases}} \tag{3}$$

The EV integration position is demarcated as shown in Eq. 4:

$$\boldsymbol{EV_{conn} = \begin{cases} 1, if\ EV_{i,j}.\{t_0\} \le EV_v(t_m) \le EV_{i,j}.\{t_f\}, \\ 1, if\ SOC_v[n+1] \le 1, \\ 0, otherwise \end{cases}} \tag{4}$$

In Eqs 2, 3, $\{EV_{i,j}.\{t_f\}$ and $\{EV_{i,j}.\{t_f\}$ are parameters of EV acquisition framework and refer to the initial and final charging times, correspondingly. The parameter t_m signifies the current time within the time period $[t_i, t_f]$. Originally, the rate of t_i is quantified as t_0.

3.4 Supervisory and optimization algorithm based on honey badger algorithm

Optimization issues like optimal power flow and electrical vehicle charged orderly planning are addressed by IHBA. Therefore, the benefits of applying IHBA to optimization problems include superiority based on convergence speed and a balance among exploration and exploitation. The clear explanation about IHBA is explained in the following section.

3.4.1 General biology

Honey Badgers (HB) have fluffy black and white fur and are known for their fearlessness. They are about the size of a dog, with a body length of 60–70 cm, and a weight range of 7–13 kg, but hunt and prey fearlessly on about 60 different species including poisonous snakes. These critters are intelligent and enjoy feeding on honey, as well as using tools. They normally live alone in self-dug burrows and cooperate with remaining badgers during the mating season. The HBs have 12 recognized subspecies. They do not have a particular breeding season, and cubs are born all year long. Whenever larger predators are unable to flee, honey badgers are brave, and do not hesitate to attack them. These animals also reach out to bird nests and beehives for food, thanks to their exceptional climbing abilities (Hashim et al., 2022).

In order to find its prey, the honey badger uses its anticipation of smell and sluggish, continuous pacing. It uses a persistent search and digging method to locate its target's general position before capturing it. In search of food, the honey badger excavates up to fifty holes in a day throughout a 40-km or even greater radius. Although honey is a HB's favorite delicacy, they are not very good at discovering beehives. On the other hand, the honeyguide bird detects beehives skillfully, but lacks the tools to get to the honey inside. So, this bird acts as a guide and directs the badger to the swarm, aids and exposes the beehives with its long claws, setting the stage for a mutually advantageous link or connection among the two creatures. As a consequence, both creatures benefit from their collaboration and share in the spoils (Chen et al., 2022).

3.4.2 Inspiration

The HBA reproduces the foraging performance of this creature, consisting of two approaches for finding food; smelling and burrowing, or using a honey guidance mode. The first approach is recognized as the digging, and its subsequent process is acknowledged as honey. Honey badger utilizes its sense of smell to find its prey while it is in the digging mode. Once it has reached the general region, it investigates the surroundings, encircling the prey to discover the best site for digging and apprehending it. It follows the honey route which is guided by the bird that facilitates direct communication among the honeyguide bird and the beehives.

3.4.3 Steps for algorithm

HBA is a global approach which subsequently takes into account both the exploration and exploitation phases (Düzenli et al., 2022). To begin with, the initial population with a uniform distribution is created. It determines the fitness function and generates the EV parameters at random after the initialization process (Fathy et al., 2023). The population of probable results in the HBA are indicated with mathematical formulas in Eq. 5.

$$\textbf{Population of candidate solution} = \begin{bmatrix} x_{11} & x_{12} & x_{13} & \cdots & x_{1D} \\ x_{21} & x_{22} & x_{23} & \cdots & x_{2D} \\ \cdots & \cdots & \cdots & \cdots & \cdots \\ x_{n1} & x_{n2} & x_{n3} & \cdots & x_{nD} \end{bmatrix}$$
$$\textbf{ith position of honey badger } x_i = \left[X_i^1,\ X_i^2, \ldots ..\ X_i^D \right] \tag{5}$$

Step 1: Initialization stage.

Eq. 6 computes the population size N and preliminary positions.

$$x_i = lb_i + r_1 \times (ub_i - lb_i), r_1 \textit{ is a random number between } 0 \textit{ and } 1 \tag{6}$$

Here, i_{th} badger signifies one probable resolution at location x_i, while lower bound is denoted as lb_i and upper bound is denoted as ub_i.

Step 2: Intensity

The intensity of the prey denotes their separation and connection with each other. I_i refers to the target of the trace strength as displayed in Eq. 7. In case of a strong smell, movement is quick.

$$I_i = r_2 \times \frac{S}{4\pi d_i^2}, r_2 \textbf{ is a random number between } 0 \textbf{ and } 1 \tag{7}$$

In Eq. 8, S refers to the source of honey which corresponds to the prey's position. The distance among prey and i_{th} badger is indicated as d_i which is referred in Eq. 9.

$$S = (x_i - x_{i+1})^2 \tag{8}$$
$$d_i = x_{prey} - x_i \tag{9}$$

Step 3: Update density factor

In order to provide a unified conversion from exploration to exploitation in the method, the density factor designated as α introduces time-varying randomization. Iterative updates are made to the value of α, which gets smaller over time. Eq. 10 is used to calculate this decreasing factor that lowers the level of randomization, as supplementary iterations are performed.

$$\alpha = C \times exp\left(\frac{-t}{t_{max}}\right), t_{max} = \textbf{maximum number of iteration} \tag{10}$$

C refers constant $\geq$ 1.

Step 4: Avoidance from local best

To get around local optima areas, this step is used combine with the previous ones. The proposed algorithm includes a flag F that regulates the exploration route to address this. The algorithm allows the agents to search the space completely through direction change, which increases likelihood of finding excellent solutions.

Step 5: Modifying agent's position

The update of the IHBA position (x_{new}), as formerly defined, involves two individual stages recognized as "digging" and "honey". The following steps provide a thorough justification.

Step 5-1 Digging stage

A badger makes signals that mirror the shape of cardioid during the digging phase. The mathematical representation shown in Eq. 11 is used to model the motion of the cardioid.

$$x_{new} = x_{prey} + F \times \beta \times I \times x_{prey} + F \times r_3 \times \alpha \times di \times |cos(2\pi r_4) \times [1 - cos(2\pi r5)]| \quad (11)$$

Here, x_{prey} signifies prey position, and $\beta \geq 1$ indicates the badger's ability to obtain food. Whereas, r_3, r_4, and r_5 represent three random values between 0 and 1. F operates as a flag that adjusts the search route which is defined by Eq. 12.

$$F = \begin{cases} 1 & if\ r_6 \leq 0.5 \\ -1 & else, \end{cases} \quad r_6\ works\ among\ 0\ \&\ 1 \quad (12)$$

The behavior of the HB is significantly impacted by a number of elements during the digging period. These include the time-varying search influence factor α. Moreover, the badger comes across F-designated disruptions while engaging in digging activities that enable it to choose a prey spot which is even more advantageous.

Step 5-2 Honey phase

x_{new} signifies a new position, whereas x_{prey} characterizes the prey position. Eq. 13 displays the process of x_{new},

$$x_{new} = x_{prey} + F \times r7 \times \alpha \times d_i, r_7\ works\ among\ 0\ \&\ 1 \quad (13)$$

Distance is referred as d_i. In this step, the research behavior is influenced by the variable α, which is a measure of how search habits have changed over time. The honey badger also has disruptions identified as F.

3.5 Improved Honey Badger Algorithm

Ultimately, the suggested method controls the energy in the EV system by calculating the best fitting values for the EV parameters, including battery SOC, engine torque, speed, and battery power. Reducing power loss while maintaining optimal energy management is the main goal of the suggested system. In addition, this article explores the cooperative assessment of EMS operation with various considerations during the suggested implementation of energy management according to IHBA, including the consequences of V2G/G2V uncertainty in EMS operation and trading features of EV arrival time in driving schedule of an EV. The badger's exploration phase in the initial HBA (Bishla and Khosla, 2023) begins with a local search in the methodology. The heart-shaped updating process causes this local search capability to be underwhelming. The update mode of HBA (Thumati et al., 2023) that is modulated by a random parameter R, is thereby strengthened by the introduction of a spiral motion mechanism. If $R < 0.3$, it is updated near the current location. Alternatively, as stated in Eq. 14, it is also updated towards the global optimal location.

$$X_{updated} = \begin{cases} d_j.e^{bt}.cos(2\pi l) + X_i & R < 0.3 \\ d_j.e^{bt}.cos(2\pi l) + X_b & R \geq 0.3 \end{cases} \quad (14)$$

Where d_j refers the distance among the j^{th} badger and prey, b refers the logarithmic spiral shape constant, t refers the value between [−1, 1], $X_{updated}$ refers to the updated location of the honey badger, X_i and X_b describe the current and global optimal locations of the prey, respectively. The initial energy of the electric vehicle must be somewhat near to the final energies of the vehicle at the conclusion of the control horizon. When applying the optimal energy schedule repeatedly, this restriction is taken into account. Figure 4 shows the flowchart of IHBA model.

In this work, the load variance decrement is regarded as an objective function which is signified as Eq. 15.

$$Minimize, Load\ Varaince\ (J) = \sum_{t=1}^{T} \frac{1}{T} (Loads\ (t) - mean\ (Loads))^2 \quad (15)$$

The arithmetic formulations for power and charge balance are specified in Eqs 16, 17, correspondingly.

$$P_{g,t} - P_{c,t} + P_{d,t} = P_{L,t} \quad (16)$$

Where, $P_{L,t}$ is referred to as load demand, the load requirement from the grid at time t is denoted as $P_{g,t}$, whereas $P_{c,t}, P_{d,t}$ correspondingly refer to the charging and discharging power.

$$SOC_t = SOC_{t-1} + \frac{P_{c,t}\Delta t\eta}{Q_{EV}} - \frac{P_{d,t}\Delta t\eta}{Q_{EV}\eta} \quad (17)$$

Where, Q_{EV} stands for the battery capacity of EV, time interval is represented as Δt, whereas the efficiency of the storage charger is stated as η.

The pseudo-code of the recommended algorithm comprises population initialization, evaluation, and constraint updates which are provided in Algorithm 1.

3.5.1 Algorithm 1: pseudocode of IHBA

Set parameter $t_{max}, \mathcal{N}, \beta, C$.
Initialize the population with positions.
Evaluate the fitness of each honey badger position x_i using objective function and assign to $f_i, i \in [1, 2, \ldots, N]$.
Save best position x_{prey} and assign fitness to f_{prey}.
while t ≤ t_{max} do
  Update the decreasing factor α.
  for i = 1 to N do
    Calculate the intensity I_i.
    if r < 0.5 then ▷ r is random number between 0 and 1
      Update the position x_{new}.
    else
      Update the position x_{new}.
    end if
    Evaluate new position and assign to f_{new}.
    if $f_{new} \leq$ fi then
      Set xi = x_{new} and fi = f_{new}.
    end if
    if $f_{new} \leq f_{prey}$ then
      Set $x_{prey} = x_{new}$ and $f_{prey} = f_{new}$.
    end if
  end for
end while Stop criteria satisfied.
Return x_{prey}

4 Result and discussion

In this study, experimental results are confirmed using MATLAB R2022b. The PV-EV grid evaluation is built and evaluated using a PC laboratory stand with Windows 11 and an

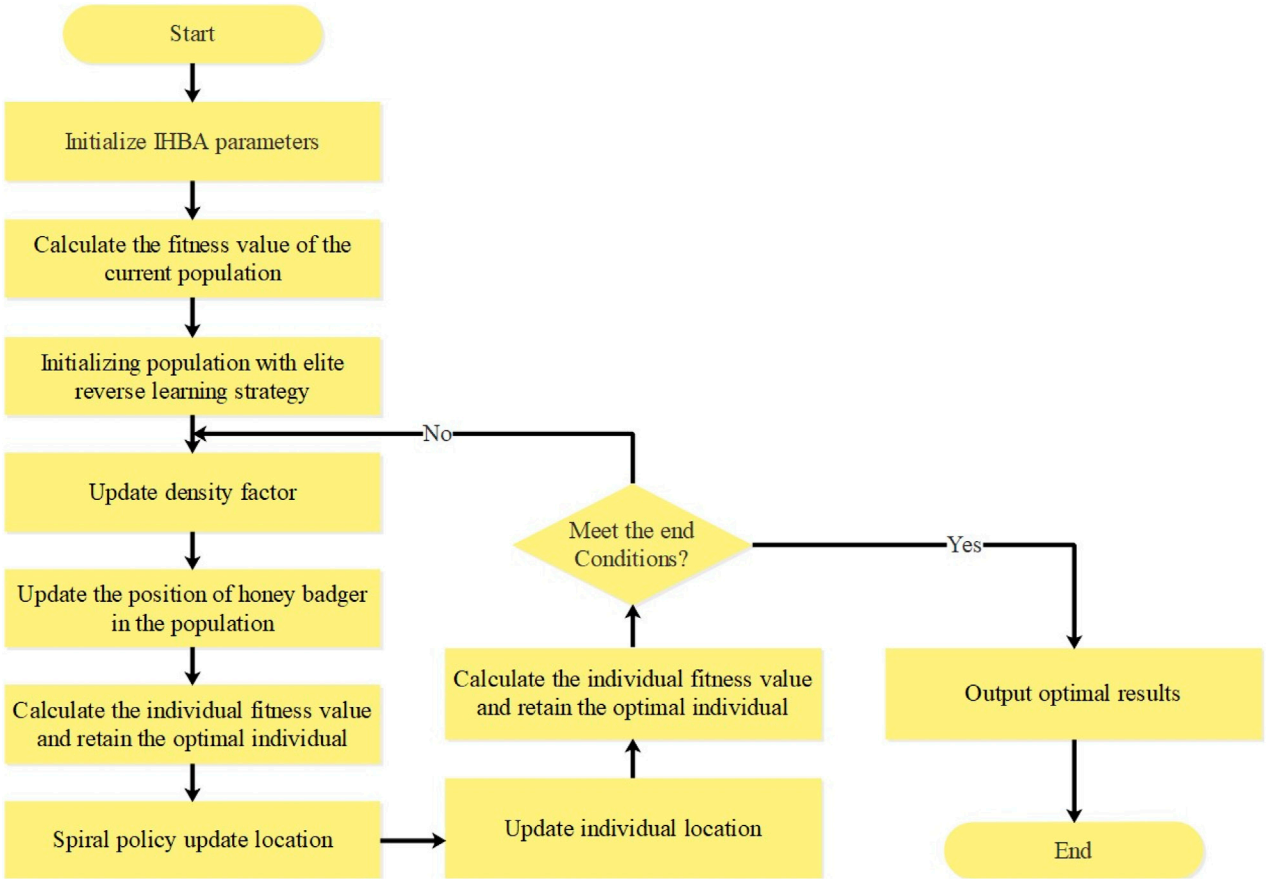

FIGURE 4
Flowchart for IHBA model.

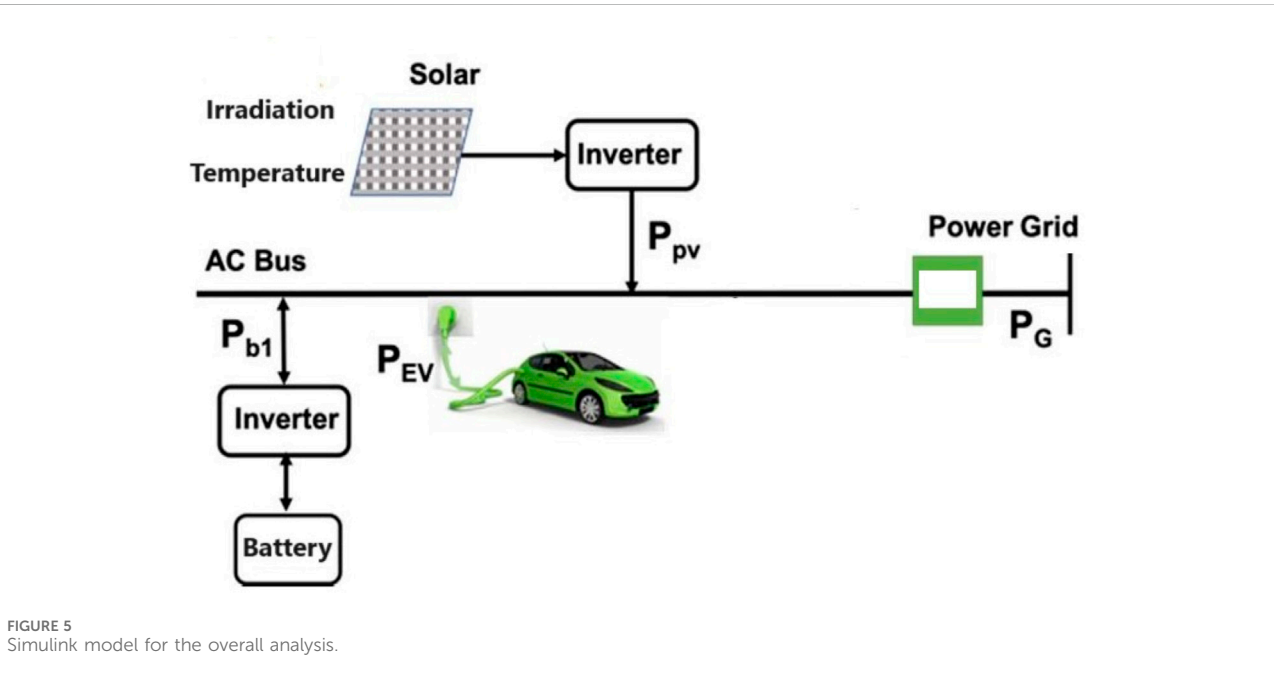

FIGURE 5
Simulink model for the overall analysis.

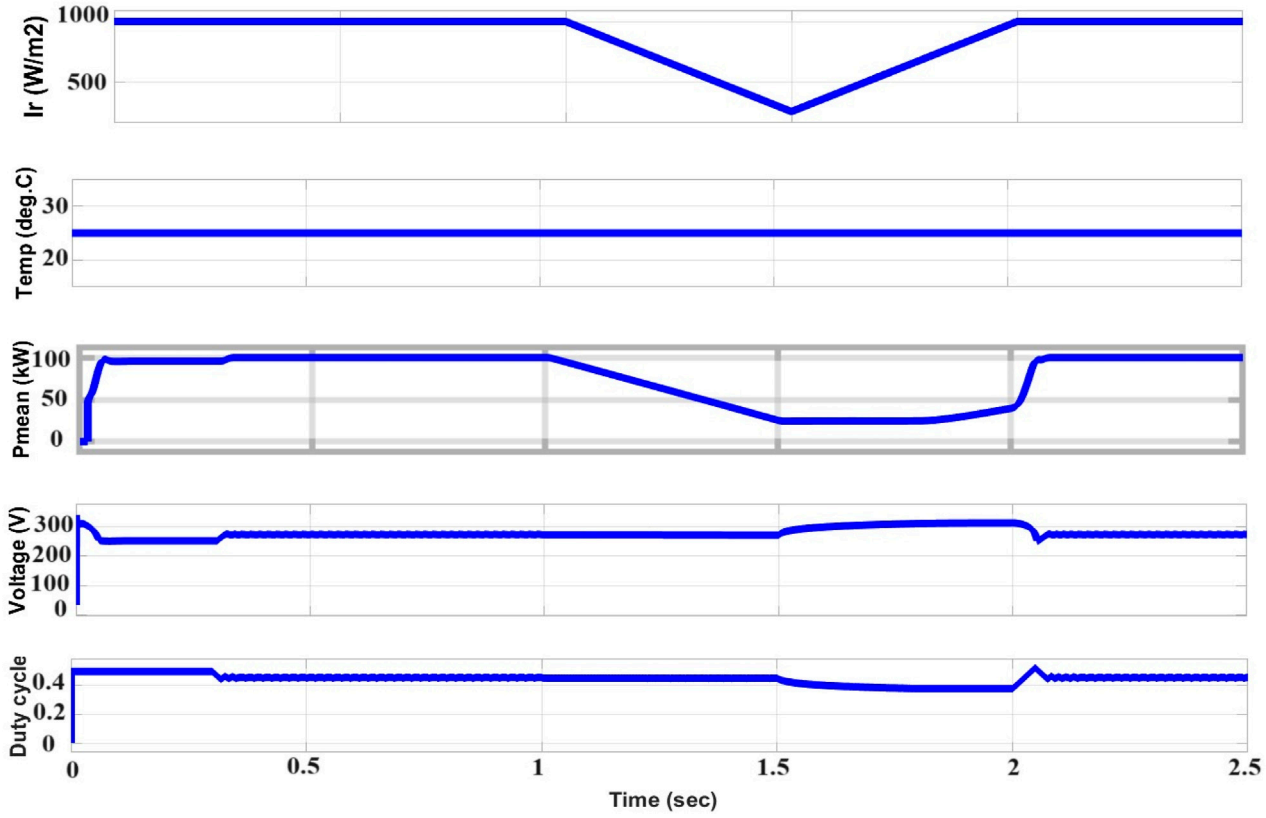

FIGURE 6
Extracted power flow using IHBA controller for PV array.

TABLE 1 Performance comparison of PV with different optimization methods.

Optimization methods	Generated power (kW)	MPP power (kW)	Precision (%)
WOA	81.64	83.46	91.13
EHO	84.46	86.72	95.47
IHBA	93.27	96.57	98.48

Intel Core i9 CPU as well as 32 GB of RAM. In this paper, various strategies for employing a charging station are created on smart grid conjunction to charge EVs throughout the day are described. IHBA is exploited to accomplish optimal design related with customary parameters included in the algorithm process. The recommended IHBA method is operated with constant value as 2, beta as 7, 50 collecting agents, 500 maximum iterations, 30-dimension, 30 population size, and EV consuming 15 kw/h for every 100 km to help the charging station provide continuous charge. The results show EV charging by employing the stated combination, and the recommended approach remains continuous during the charging phase, in contrast to the traditional grid-alone charging. The simulation depiction of entire analysis is revealed in Figure 5.

The findings demonstrate the necessity of utilizing smart technology to manage the charging of PHEVs for increasing the

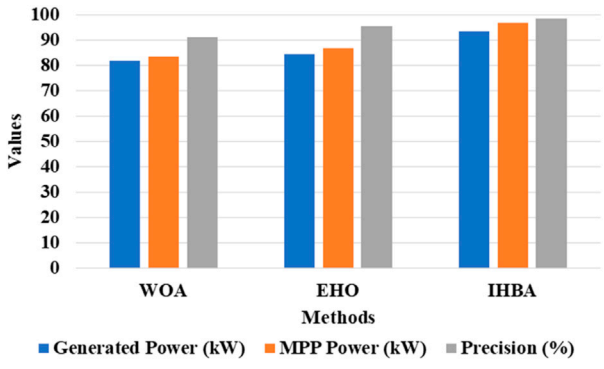

FIGURE 7
Graphical analysis of PV performances.

TABLE 2 Performance comparison of EV with different optimization methods.

Optimization methods	V_THD (%)	Efficiency (%)	Power loss (KW)
WOA	3.79	94.48	0.238
EHO	3.48	96.19	0.219
IHBA	3.12	98.47	0.197

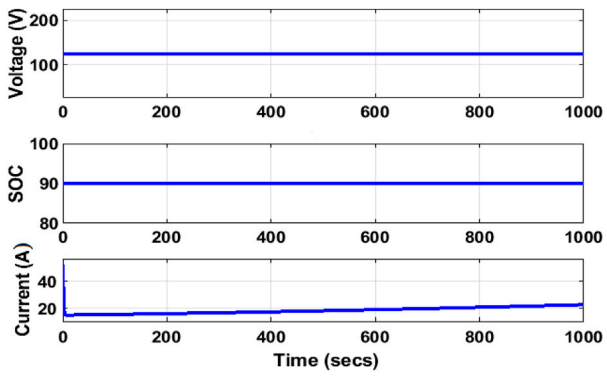

FIGURE 8
Performance of EV in terms of current, SOC and voltage.

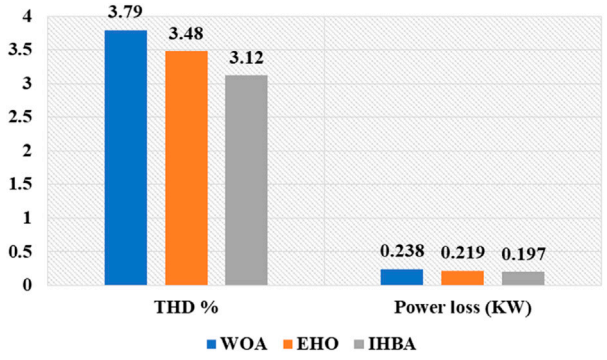

FIGURE 9
Study of THD and Power loss.

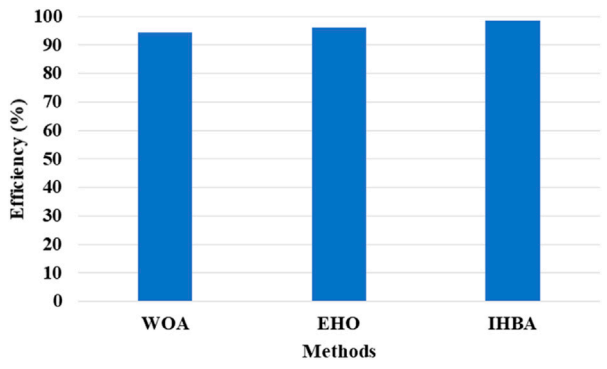

FIGURE 10
Performance of efficiency.

superiority of electrical energy delivery. The power flow with respect to that PV array is extracted with the assistance of IHBA controllers which is shown in Figure 6. Additional performance metrics including voltage and duty cycle numbers are also shown in respective Figure 6.

By altering converter's duty cycle to match necessary load at continuous output voltage, MPPT is employed to monitor MPP of PV panels. Consequently, a converter is used to rise the voltage which results in a new duty cycle value and drives PV to the peak MPPT level. The connected load will therefore affect how the MPPT value changes. Table 1 displays the MPPT precision and power results. It clearly shows that the suggested IHBA achieves an increased precision of 98.48%, which is better than traditional techniques, namely, Whale Optimization Algorithm (WOA) with 91.13% precision, and Elephant Herding Optimization (EHO) with 95.47% precision. Figure 7 shows the graphical analysis of PV performances.

According to the results from Table 1 and Figure 7, the IHBA controller outperforms the WOA and EHO controllers by achieving 96.57 kW MPP power. While EHO obtains the maximum power of 86.72 kW, the WOA controller obtains the maximum power of 83.46 kW.

To enhance this setup, the voltage source inverter must have a number of characteristics such as active power filtering and power factor change. Current harmonics produced by nonlinear loads interconnected to the grid degrade the efficiency of the power. To account for these armature currents, active power filters are used. Voltage regulation issues arise once PV is linked to the grid. The performance analysis through the waveform assessment of the voltage, SOC and current for EV is shown in Figure 8.

The converters must produce reliable, high-quality voltage in order to keep the voltage controlling apparatus from deteriorating. The computational method described in this paper that predicts a large number of inverter designs is used to identify the best battery presence organization. The SOC calculation protects the batteries from unexpected disruptions and prevents them from being overcharged, which possibly harms their interior predetermination.

Nodal voltages above the lower voltage limit results from a sudden decrease in PV output power. The utilization of renewable sources as well as the stability of distribution networks is severely impacted by nodal voltage fluctuations. As a result, there is growing interest in investigating advanced techniques for voltage regulation in distribution networks that contain large amounts of photovoltaic power. The benefit of the suggested voltage regulation method over the reference centralized techniques is that it accomplishes the same voltage control effect, while causing less distribution network loss. They are not required to alter their reactive outputs in order to use the suggested voltage regulation method. Table 2 compares the

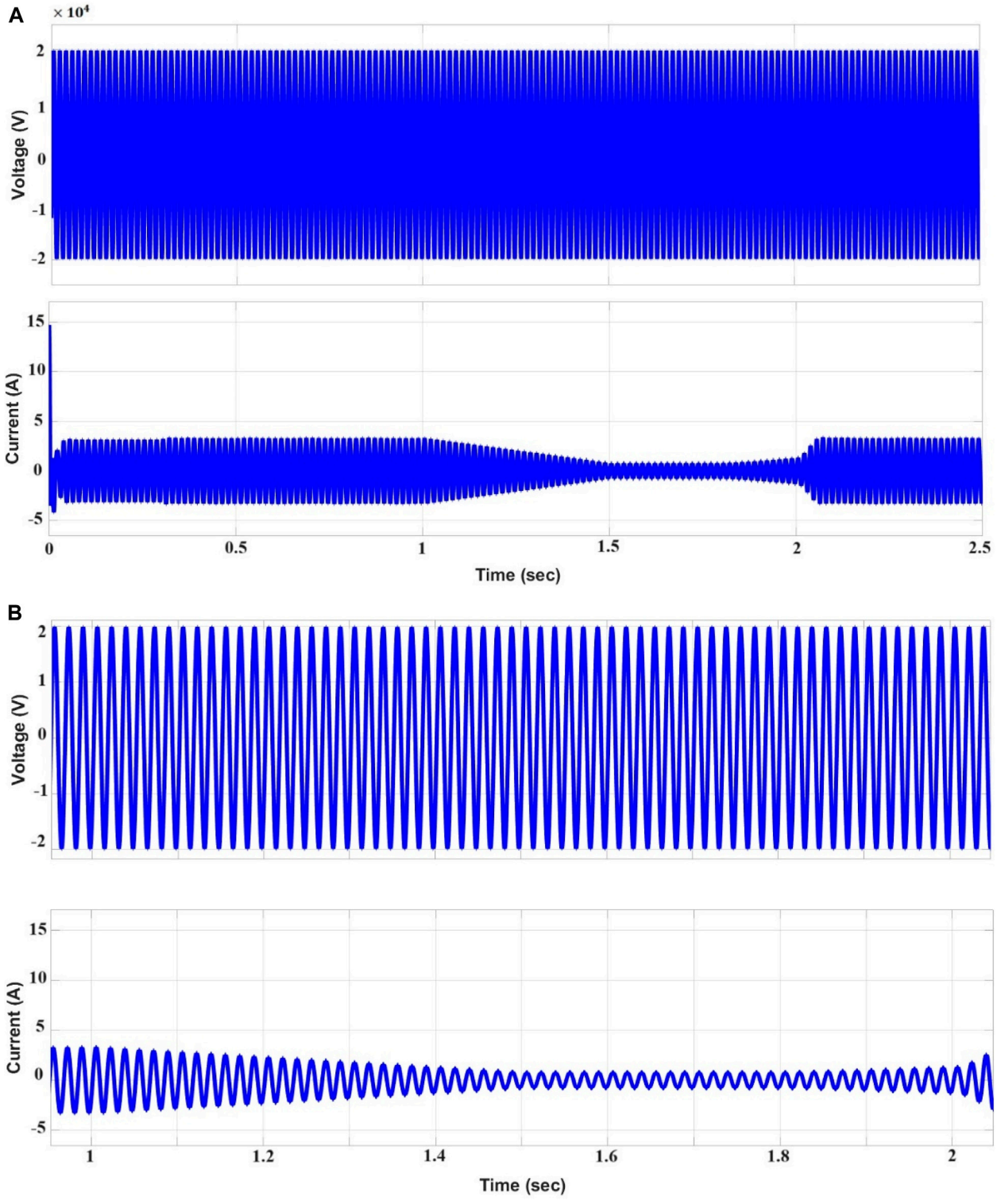

FIGURE 11
(A) Grid constraints **(B)** Zoom View of voltage and current.

efficiency, power loss and THD voltage (V_THD) results of various optimization techniques. Additionally, it provides more services on load with suitable charging conditions and a reduced voltage profile. Figure 9 displays the THD and power loss of the optimization methods, while Figure 10 displays the efficiency of proposed IHBA.

The voltage at DC-link does not have to be amplified throughout the design process above the input voltage. The recommended charger configuration offers an unusually broad output voltage spectrum while maintaining efficiency throughout the second phase. An internal parameter is used to indicate the concurrent power dissipation of all

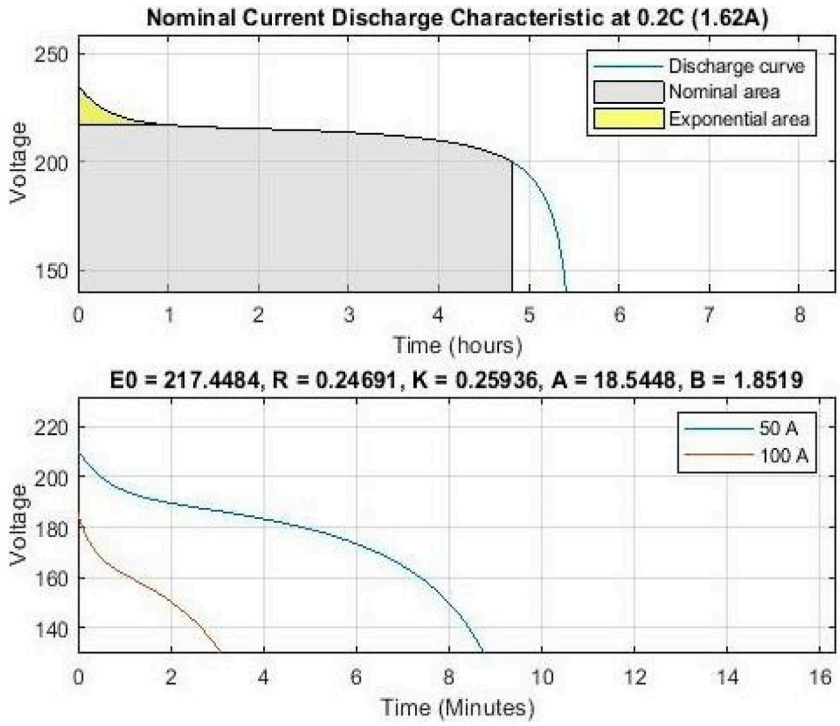

FIGURE 12
Characteristics of discharge current.

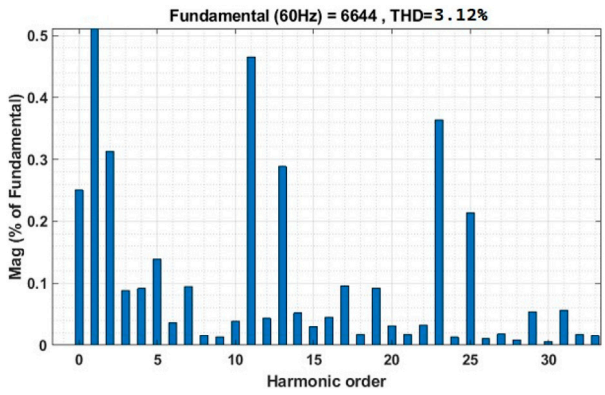

FIGURE 13
V_THD performance of IHBA.

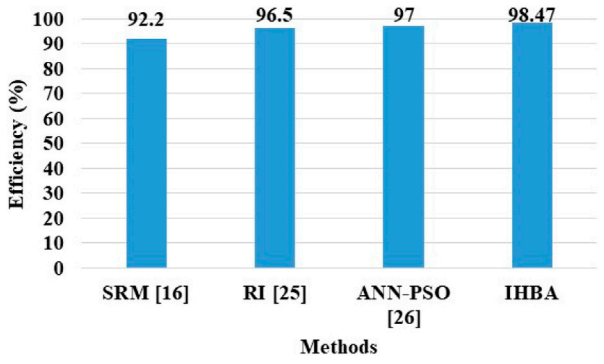

FIGURE 14
Graphical illustration of Efficiency performance.

of the semiconductor devices in the framework. The power that is quickly lost, only encompasses the potential power that the block releases. The values using a logarithmic model reflect the amount of power used by the component over time. This Efficiency function controls because the losses for elements through a particular power consumption value are recognized.

Figure 11A details the grid voltage and current limitations, whereas Figure 11B displays the grid parameters with zoomed-in detail. Under different lighting conditions, the device produces extreme amounts of energy by increasing grid current/voltage. MPPT initially chooses MPP to use a variety of controllers. Also, how the controller is used to manage peak loads in the grid side using the projected RES is explained here. The architecture that arises is largely composed of accurate, thorough simulations of the outcomes of testing that are both challenging and secure. The approach has also been used to look at how Hybrid Renewable Energy Sources (HRES) changes behavior when there is an active shift in behavior. Figure 12 displays the battery's nominal current and discharge statistics.

In order to describe the nonlinear relationship between the State of Charge (SOC) and the voltage at the energy storage system's terminals, the graphical model (Figure 12) was created using Shepherd's equation. Figure 12 shows the discharge curve of a 1.62 Ah, 220 V nominal voltage battery from an initial fully charged condition to a final completely discharged state which

TABLE 3 Comparative study of various performances.

Performances	SRM (Cheng et al., 2020)	RI (Kanimozhi et al., 2022)	ANN-PSO (Nouri et al., 2024)	IHBA
Efficiency (%)	92.2	96.5	97	98.47
V_THD (%)	4.95	-	-	3.12

TABLE 4 Comparison of speed performance.

Performance	GA-PID (Guentri et al., 2021)	MHS (Al-Dhaifallah et al., 2021)	IHBA
Speed (km/hr.)	84	87	91

has a polynomial-shaped curve that represents the voltage time relationship. There are three main processes that occur in the voltage curve of a battery during charging/discharging, an exponential drop from full charge as the battery starts to discharge, a linear section about the rated voltage where the battery is typically operated, and a nonlinear section as the battery approaches its completely discharged state which are illustrated in Figure 12. Every portion that is highlighted is significant in conveying the features of the development of the energy storage system model. The impact of PHEVs on the power grid are reduced with the use of an appropriate controller, a smart charging system, and an effective management to transfer loads and avoid peaks. Each restriction in this case has a prior description in the anticipated section.

4.1 Comparative analysis

Furthermore, it is necessary to add extra parts such as converters or diode bridge rectifiers to the existing SRM (Cheng et al., 2020). The converter and rectifier are the two most crucial elements of the charger design. The current charger architecture does not include any new parts because it is more compact, less expensive, and better than other battery chargers. The architecture in (Cheng et al., 2020) is completely dependent on nonlinear equipment and needs to be put into separate engine coil plugs. Unlike other controllers, this one effectively accounts for the power loss of the traction machine. Figure 13 displays the V_THD evaluation for the IHBA controller. Table 3 gives a clear evaluation of the proposed IHBA by comparing with the existing approaches such as SRM (Cheng et al., 2020), RI (Kanimozhi et al., 2022) and ANN-PSO (Nouri et al., 2024).

Figure 14 shows the graphical illustration of efficiency of the proposed method with existing methods such as SRM (Cheng et al., 2020), RI (Kanimozhi et al., 2022) and ANN-PSO (Nouri et al., 2024). From the Figure 14, it is evident that the existing SRM (Cheng et al., 2020), RI (Kanimozhi et al., 2022) and ANN-PSO (Nouri et al., 2024) obtain an efficiency of 92.2%, 96.5% and 97% respectively. The electrodynamic connection of multiphase equipment has an effect on PF, aside from the possible benefits of several methods that are greater than real SRM design (Cheng et al., 2020). The proposed methods have a lower THD than the existing methods. Although the motor impedance locations for distinct units differ, the integrated equipment retains the identical recharging aspect when using the proposed control strategy. Table 4 presents the comparison of speed performance.

Table 4 evidently displays that existing GA-PID (Guentri et al., 2021) and MHS (Al-Dhaifallah et al., 2021) reach a speed of 84 km/h and 87 km/h, separately, whereas the IHBA obtains a superior value of 91 km/h that is much farther than the remaining approaches.

4.2 Discussion

An Improved Honey Badger algorithm (IHBA) is suggested in this study to integrate SGs with solar panels, an EV parking lot, and dynamic loads at the PCC. The suggested IHBA makes use of forecasts of PV generation to optimize the G2V or V2G charging profiles of the EVs through the use of dynamic programming. This algorithm minimizes SG effectiveness and takes user preferences into account while reducing reliance on the grid. The results of the study demonstrate the effectiveness of the Honey Badger approach in resolving problems involving large search spaces. To accomplish a balanced grid load profile, a smart charging algorithm is developed and evaluated in the MATLAB environment to optimize EV charging and discharging. In the result analysis, the proposed IHBA is compared with existing approaches such as SRM (Cheng et al., 2020), RI (Kanimozhi et al., 2022) and ANN-PSO (Nouri et al., 2024) in terms of efficiency and V_THD. The existing SRM (Cheng et al., 2020), RI (Kanimozhi et al., 2022) and ANN-PSO (Nouri et al., 2024) has achieved an efficiency of 92.2%, 96.5% and 97% respectively, while proposed IHBA accomplished higher value of 98.47% with V_THD of 3.12%. The proposed IHBA accomplished a higher speed range of 91 km/h, which is superior over existing GA-PID (Guentri et al., 2021) and MHS (Al-Dhaifallah et al., 2021) obtained 84 km/h and 87 km/h, individually. Even though, all optimization algorithms, does not always provide the best solutions to specific problems. Furthermore, while some optimization techniques do work, more needs to be done to increase their efficacy. To further advance the field of heuristic optimization, new optimization techniques inspired by nature must constantly be developed because the problem of how to speed up an algorithm's convergence is still very challenging.

5 Conclusion

This article has confirmed that exploitation of advanced technologies would permit the adoption of EVs into SG model. In such condition, SG could increase the effectiveness of EV for

assisting the utility grid. After that, this paper has looked into the relationship between the SG and EVs in extensive detail. In this work, a novel EMS for smart grid, PV systems, and EV parking lots was developed. Users of the parking lot could select from four charging modes offered by the management system, and the EV elements that must be taken into account while choosing a charging mode were developed. By efficiently searching the search space while avoiding unacceptable areas, the proposed EMS was assessed by the IHBA to create a balance between exploration and exploitation capabilities. Considering the exact same setup, the IHBA is compared with a number of optimization strategies, such as the WOA and EHO. The findings of this study show that the honey badger algorithm is successful in resolving issues with intricate search spaces. According to obtained results, the IMO controller outperformed the WOA and EHO controllers in terms of total harmonic distortion voltage (3.12%), power loss (0.197 kW) and efficiency (98.47%). Its supremacy in terms of convergence speed and striking a healthy balance among exploration and exploitation are also supported by the empirical study. In order to tackle the large-scale optimization problems, future studies will concentrate on strengthening the IHBA by including chaotic maps as well as binary and multi-objective characteristics.

Data availability statement

The original contributions presented in the study are included in the article/supplementary material, further inquiries can be directed to the corresponding authors.

Author contributions

GS: Investigation, Resources, Writing–original draft. RK: Data curation, Visualization, Writing–original draft. PF-G: Funding acquisition, Validation, Writing–review and editing. PB: Formal Analysis, Supervision, Writing–review and editing. RK: Conceptualization, Software, Writing–review and editing.

Funding

The author(s) declare that no financial support was received for the research, authorship, and/or publication of this article.

Conflict of interest

The authors declare that the research was conducted in the absence of any commercial or financial relationships that could be construed as a potential conflict of interest.

Publisher's note

References

Al-Abri, T., and Albadi, M. (2022). "Impacts of electric vehicles on distribution system planning and operation," in 20th International Conference on Renewable Energies and Power Quality (ICREPQ'22); 2022, Vigo, Spain (Renewable Energy Power Qual. J.), 313–317. doi:10.24084/repqj20.296

Al-Dhaifallah, M., Ali, Z. M., Alanazi, M., Dadfar, S., and Fazaeli, M. H. (2021). An efficient short-term energy management system for a microgrid with renewable power generation and electric vehicles. *Neural. comput. Appl.* 33 (23), 16095–16111. doi:10.1007/s00521-021-06247-5

Bishla, S., and Khosla, A. (2023). Honey badger optimized energy management in grid connected solar PV battery for enhancing the stability and power quality. *Energy Storage* 6. e512. doi:10.1002/est2.512

Bot, Y., Yousfi, A., and Allali, A. (2022). Smart control of the bidirectional energy exchange of electric vehicles with the electrical network. *Int. J. Adv. Stud. Comput. Sci. Eng.* 11 (12), 29–35.

Chen, R.-F., Luo, H., Huang, K.-C., Nguyen, T.-T., and Pan, J.-S. (2022). An improved honey badger algorithm for electric vehicle charge orderly planning. *J. Netw. Intell.* 7 (2), 332–346.

Cheng, H., Wang, Z., Yang, S., Huang, J., and Ge, X. (2020). An integrated SRM powertrain topology for plug-in hybrid electric vehicles with multiple driving and onboard charging capabilities. *IEEE Trans. Transp. Electrif.* 6 (2), 578–591. doi:10.1109/TTE.2020.2987167

Düzenli, T., Onay, F. K., and Aydemir, S. B. (2022). Improved honey badger algorithms for parameter extraction in photovoltaic models. *Optik* 268, 169731. doi:10.1016/j.ijleo.2022.169731

Egbue, O., Uko, C., Aldubaisi, A., and Santi, E. (2022). A unit commitment model for optimal vehicle-to-grid operation in a power system. *Int. J. Electr. Power Energy Syst.* 141, 108094. doi:10.1016/j.ijepes.2022.108094

Fathy, A., Rezk, H., Ferahtia, S., Ghoniem, R. M., and Alkanhel, R. (2023). An efficient honey badger algorithm for scheduling the microgrid energy management. *Energy Rep.* 9, 2058–2074. doi:10.1016/j.egyr.2023.01.028

Gan, W., Wen, J., Yan, M., Zhou, Y., and Yao, W. (2024). Enhancing resilience with electric vehicles charging redispatching and vehicle-to-grid in traffic-electric networks. *IEEE Trans. Ind. Appl.* 60 (1), 953–965. doi:10.1109/TIA.2023.3272870

Grasel, B., Baptista, J., and Tragner, M. (2023). "The impact of V2g charging stations (active power electronics) to the higher frequency grid impedance," in 2023 International Conference on Smart Energy Systems and Technologies (SEST); 2023, Mugla, Turkiye (IEEE), 1–6. doi:10.2139/ssrn.4528053

Guentri, H., Allaoui, T., Mekki, M., and Denai, M. (2021). Power management and control of a photovoltaic system with hybrid battery-supercapacitor energy storage based on heuristics methods. *J. Energy Storage* 39, 102578. doi:10.1016/j.est.2021.102578

Hashim, F. A., Houssein, E. H., Hussain, K., Mabrouk, M. S., and Al-Atabany, W. (2022). Honey Badger Algorithm: new metaheuristic algorithm for solving optimization problems. *Math. Comput. Simul.* 192, 84–110. doi:10.1016/j.matcom.2021.08.013

He, T., Lu, D.D.-C., Wu, M., Yang, Q., Li, T., and Liu, Q. (2021). Four-quadrant operations of bidirectional chargers for electric vehicles in smart car parks: G2V, V2G, and V4G. *Energies* 14, 181. doi:10.3390/en14010181

İnci, M., Savrun, M. M., and Çelik, Ö. (2022). Integrating electric vehicles as virtual power plants: a comprehensive review on vehicle-to-grid (V2G) concepts, interface topologies, marketing and future prospects. *J. Energy Storage* 55 (B), 105579. doi:10.1016/j.est.2022.105579

Ismail, A. A., Mbungu, N. T., Elnady, A., Bansal, R. C., Hamid, A.-K., and AlShabi, M. (2023). Impact of electric vehicles on smart grid and future predictions: a survey. *Int. J. Modell. Simul.* 43 (6), 1041–1057. doi:10.1080/02286203.2022.2148180

Justin, F., Peter, G., Stonier, A. A., and Ganji, V. (2022). Power quality improvement for vehicle-to-grid and grid-to-vehicle technology in a microgrid. *Int. Trans. Electr. Energy Syst.* 2022, 1–17. doi:10.1155/2022/2409188

Kanimozhi, G., Natrayan, L., Angalaeswari, S., and Paramasivam, P. (2022). An effective charger for plug-in hybrid electric vehicles (PHEV) with an enhanced PFC rectifier and ZVS-ZCS DC/DC high-frequency converter. *J. Adv. Transp.* 2022, 1–14. doi:10.1155/2022/7840102

Karoń, G. (2022). Energy in smart urban transportation with systemic use of electric vehicles. *Energies* 15, 5751. doi:10.3390/en15155751

Kumar, M. P., Kumaraswamy, D., Jayanth, R., Rohith, K., Rakesh, G., Teja, S. M., et al. (2022). Vehicle-to-grid technology in a micro-grid using DC fast charging architecture. *J. Eng. Sci.* 13 (07), 291–295.

Kumari, A., Trivedi, M., Tanwar, S., Sharma, G., and Sharma, R. (2022). SV2G-ET: a secure vehicle-to-grid energy trading scheme using deep reinforcement learning. *Int. Trans. Electr. Energy Syst.* 2022, 1–11. doi:10.1155/2022/9761157

Liu, S., Xin, D., Yang, L., Li, J., and Wang, L. (2020). A hierarchical V2G/G2V energy management system for electric-drive-reconstructed onboard converter. *IEEE Access* 8, 198201–198213. doi:10.1109/ACCESS.2020.3034968

Liu, Z., Wu, Y., and Feng, J. (2023). Competition between battery switching and charging in electric vehicle: considering anticipated regret. *Environ. Dev. Sustain*. doi:10.1007/s10668-023-03592-4

Madhavaram, P. R., and Manimozhi, M. (2022). Smart energy management strategy for microgrids powered by heterogeneous energy sources and electric vehicles' storage. *Energies* 15 (20), 7739. doi:10.3390/en15207739

Makeen, P., Ghali, H. A., Memon, S., and Duan, F. (2023). Insightful electric vehicle utility grid aggregator methodology based on the G2V and V2G technologies in Egypt. *Sustainability* 15, 1283. doi:10.3390/su15021283

Mojumder, M. R. H., Ahmed Antara, F., Hasanuzzaman, M., Alamri, B., and Alsharef, M. (2022). Electric vehicle-to-grid (V2G) technologies: impact on the power grid and battery. *Sustainability* 14, 13856. doi:10.3390/su142113856

Nouri, A., Lachheb, A., and El Amraoui, L. (2024). Optimizing efficiency of Vehicle-to-Grid system with intelligent management and ANN-PSO algorithm for battery electric vehicles. *Electr. Power Syst. Res.* 226, 109936. doi:10.1016/j.epsr.2023.109936

Rahman, A., Ali, M., Aamir, M., Mumtaz, M., Khan, H. S., and Waqar, A. (2018). "Design and analysis of efficient battery charging/discharging for V2G and G2V application," in 2018 2nd International Conference on Energy Conservation and Efficiency (ICECE); 2018, Lahore, Pakistan (IEEE), 6–13. doi:10.1109/ECE.2018.8554977

Raju, K., Siraj, S. K. B., Venkatesh, M., Wesley, J. J., Madhu, V., and Srinivasarao, V. V. (2023). Vehicle-to-grid technology in a micro-grid using DC fast charging architecture. *J. Eng. Sci.* 14 (05), 681–688.

Spanoudakis, N. I., Akasiadis, C., Iatrakis, G., and Chalkiadakis, G. (2023). Engineering IoT-based open MAS for large-scale V2G/G2V. *Systems* 11, 157. doi:10.3390/systems11030157

Sureshkumar, V., Mugunthan, S., and Amin, R. (2022). An enhanced mutually authenticated security protocol with key establishment for cloud enabled smart vehicle to grid network. *Appl* 15 (5), 2347–2363. doi:10.1007/s12083-022-01350-3

Thirugnanam, K., Yuen, C., Kumar, P., Ghaoud, T., and Sgouridis, S. (2023). Coordinated control strategy for vehicle-to-grid support at distribution node. *IET Smart Grid* 6 (2), 158–174. doi:10.1049/stg2.12086

Thumati, S., Vadivel, S., and Rao, M. V. G. (2023). Optimal integration of photovoltaic public charging stations in multi-consumer electrical distribution system using improved honey badger algorithm. *Int. J. Intelligent Eng. Syst.* 16 (6), 482–491. doi:10.22266/ijies2023.1231.40

Tirunagari, S., Gu, M., and Meegahapola, L. (2022). Reaping the benefits of smart electric vehicle charging and vehicle-to-grid technologies: regulatory, policy and technical aspects. *IEEE Access* 10, 114657–114672. doi:10.1109/ACCESS.2022.3217525

ur Rehman, U. (2022). A robust vehicle to grid aggregation framework for electric vehicles charging cost minimization and for smart grid regulation. *Int. J. Electr. Power Energy Syst.* 140, 108090. doi:10.1016/j.ijepes.2022.108090

Zhang, L., Sun, C., Cai, G., and Koh, L. H. (2023a). Charging and discharging optimization strategy for electric vehicles considering elasticity demand response. *eTransportation* 18, 100262. doi:10.1016/j.etran.2023.100262

Zhang, L., Yin, Q., Zhu, W., Lyu, L., Jiang, L., Koh, L. H., et al. (2023b). Research on the orderly charging and discharging mechanism of electric vehicles considering travel characteristics and carbon quota. *IEEE Trans. Transp. Electrification*, 1. doi:10.1109/TTE.2023.3296964

frontiers | Frontiers in Energy Research

TYPE Original Research
PUBLISHED 26 April 2024
DOI 10.3389/fenrg.2024.1366465

OPEN ACCESS

EDITED BY
Flah Aymen,
École Nationale d'Ingénieurs de Gabès, Tunisia

REVIEWED BY
Uchenna Diala,
University of Derby, United Kingdom
Nikolaos Manousakis,
University of West Attica, Greece

*CORRESPONDENCE
Tania Gupta,
taniagupta2409@gmail.com
Ch. Rami Reddy,
crreddy229@gmail.com
Wael Mobarak,
w.fawzy@ubt.edu.sa

RECEIVED 06 January 2024
ACCEPTED 01 April 2024
PUBLISHED 26 April 2024

CITATION
Gupta T, Bhatia R, Sharma S, Reddy CR, AboRas KM and Mobarak W (2024), A data-driven ensemble technique for the detection of false data injection attacks in the smart grid framework.
Front. Energy Res. 12:1366465.
doi: 10.3389/fenrg.2024.1366465

A data-driven ensemble technique for the detection of false data injection attacks in the smart grid framework

Tania Gupta[1], Richa Bhatia[2], Sachin Sharma[3], Ch. Rami Reddy[4,5]*, Kareem M. AboRas[6] and Wael Mobarak[7]*

[1]Department of Electronics and Communication, NSUT East Campus (Affiliated to GGSIPU), Delhi, India, [2]Netaji Subhash University of Technology, Delhi, India, [3]Electrical Engineering Department, Graphic Era Deemed to be University, Dehradun, India, [4]Department of Electrical and Electronics Engineering, Joginpally B. R. Engineering College, Hyderabad, India, [5]Applied Science Research Center, Applied Science Private University, Amman, Jordan, [6]Department of Electrical Power and Machines, Faculty of Engineering, Alexandria University, Alexandria, Egypt, [7]College of Engineering, University of Business and Technology, Jeddah, Saudi Arabia

The major component of the smart grid (SG) is the advanced metering infrastructure (AMI), which monitors and controls the existing power system and provides interactive services for invoicing and electricity usage management with the utility. Including a cyber-layer in the metering system allows two-way communication but creates a new opportunity for energy theft, resulting in significant monetary loss. This article proposes an approach to detecting abnormal consumption patterns using energy metering data based on the ensemble technique AdaBoost, a boosting algorithm. Different statistical and descriptive features are retrieved from metering data samples, which account for extreme conditions. The model is trained for malicious and non-malicious data for five different attack scenarios, which are analyzed on the Irish Social Science Data Archive (ISSDA) smart meter dataset. In contrast to prior supervised techniques, it works well even with unbalanced data. The efficacy of the proposed theft detection method has been evaluated by comparing the accuracy, precision, recall, and F1 score with the other well-known approaches in the literature.

KEYWORDS

advanced metering infrastructure, cyber security, false data injection attacks, feature extraction, machine learning, smart meter

1 Introduction

The notable characteristics of the smart grid (SG) that increase the effectiveness of the current power system are indeed the two-way power and information exchange. Energy theft has been a severe challenge in the traditional power grid worldwide. Almost all utilities worldwide suffer significant financial losses due to energy theft, primarily in developing countries (Keping et al., 2015). Based on the most recent published research by Northeast Group, LLC, stealing energy costs the world $89.3 billion/year, among which the world's top 50 emerging-market countries lose $58.7 billion/year (Xia et al., 2019). In contrast to the old grid, which manually collects customer billing information monthly, the new SG measures consumer energy consumption minute by minute for each device installed at user premises

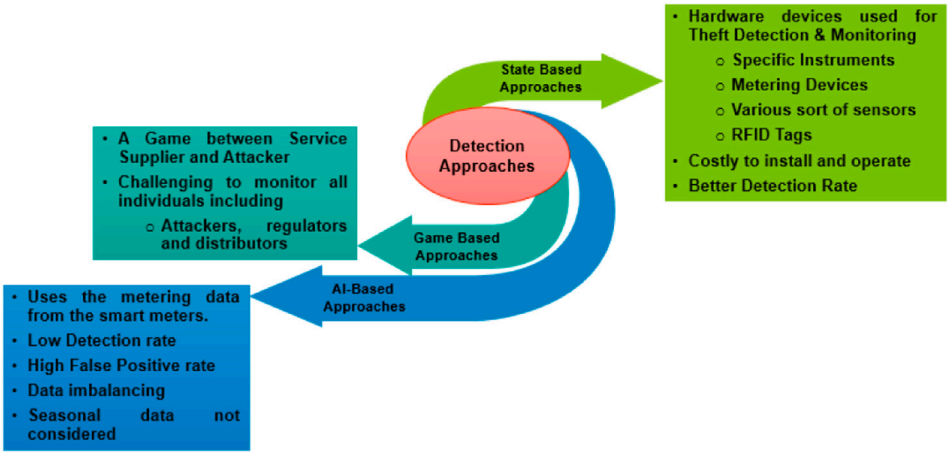

FIGURE 1
Existing energy theft detection approaches.

(Gupta and Bhatia, 2020). This aids the utility in managing loads, providing user billing information, and managing energy utilization (Yu et al., 2021). By providing monitoring capabilities through numerous sensors and accurate readings, the SG claims to lower the risk of energy theft by giving the power utility billing data and price information at a higher frequency, i.e., on an hour-to-hour basis (Zhang et al., 2017).

However, since the SG relies more extensively on information and communication technologies, there are more potential cyber-attack threats, which reduce the SG's reliability and result in significant operational and monetary losses (Attia et al., 2018; Jiang and Li, 2022). There are two entities of electricity losses: technical losses (TLs) and non-technical losses (NTLs) in the SG system. TLs are power losses incurred during electricity generation and transmission. The NTL category includes energy theft, and it states that the most common causes of NTLs include conventional methods such as meter reading bypassing, communication network failures, meter spoofing, and tampering with meter readings using a magnet (Kong et al., 2023). However, due to the introduction of an intelligent digital metering system and the inclusion of an internet layer in the metering system, there are several new entrance points for energy theft in addition to the conventional methods (Sun et al., 2018; Zhang et al., 2021). As a result, it draws the attention of researchers to the SG's cyber security (Jain et al., 2022). Mechanical meters in the old grid can only be adjusted physically. In contrast, advanced metering infrastructure (AMI) metering data open the door for both physical and remote adjustments (Song et al., 2022). Energy theft attacks against the SG could be initiated by malicious users who manipulate their smart meters to claim lower consumption readings to cut their energy bills illegally (Lin et al., 2022). Thus, the need to locate that malicious user and secure the system is of utmost importance (Mrabet et al., 2018; Pengwah et al., 2023).

Historically, to discover irregular energy usage, technicians must examine consumer monthly consumption data collected over an extended period, and after that, they must physically visit each resident community to confirm the condition and connection of each meter (Cheng et al., 2017; Zhang et al., 2023a). Due to research into machine learning (ML) techniques, power utilities now have a new opportunity to identify unusual electricity usage patterns from a variety of energy data (Zhang et al., 2023b; Tan et al., 2023). By identifying anomalous patterns, these techniques can reduce the workload for system operators and increase detection accuracy (Guarda et al., 2023). As per previously available architecture, systems for detecting energy theft are classified into three groups: state-based or power-based, game-based, and artificial intelligence (AI)-based approaches (Jokar et al., 2016), as depicted in Figure 1. In a state-based approach, specific instruments or metering devices were designed to combat energy theft. For instance, a hardware-based method was proposed for identifying fake users (Liu X. et al., 2023; Wang et al., 2024). Various sorts of sensors and radio frequency identification tags are used in this system to identify the malicious user. Additional metrics such as power, voltage, and current are used in the distribution network to detect electricity theft (Wang et al., 2021; Zhang et al., 2024). Despite being costly to install and operate, this system has a good detection rate. Extra devices entail additional expenditures, and such device types are challenging to deploy within the current distribution system (Xiao et al., 2013; Henriques et al., 2014). The game theory-based approach assumes a game between the service supplier and fraudulent users. This strategy was based on sound assumptions. Actual user consumption data are derived from the game equilibrium. This has been theoretically calculated (Amin et al., 2012). However, it must still be solved to articulate the utility function of all stakeholders, including attackers, authorities, suppliers, and alternative solutions (Amin, 2015; Wang et al., 2023).

The third group includes AI-based methods: AMI uses ML algorithms to assess customers' metering data and energy usage patterns to identify those who may be committing electricity theft (Gupta et al., 2022; Liu D. et al., 2023). In this, there are primarily two sorts of schemes: classification-based and clustering-based. Classification approaches often involve analyzing users' past

electricity consumption data with labels to identify odd trends and detect suspected electricity theft behaviors. It needs a dataset with labels (Jiang et al., 2021; Chen Y. et al., 2022). The metering data are utilized for training the classifier, which then identifies dishonest users. In contrast, clustering approaches rely on the information without labels; i.e., by studying the relationship between users, outliers are identified (Jokar et al., 2013; Yang et al., 2016; Sharma et al., 2023). Consumers often follow the same pattern under normal circumstances; hence, deviations from this pattern may indicate the presence of fraud. The classifier is trained using various ML techniques using a metering dataset available widely for research purposes and further used to detect unusual patterns, such as malicious users (Chen B. et al., 2022; Ma and Hu, 2022). The classifier's primary flaw was its poor detection rate and high rate of false positives. Smart meter historical data are the foundation for the clustering models, subject to significant dataset fluctuations that provide a broad range of normal data and low detection rates (Guo and Hu, 2023; Zheng et al., 2023). This makes it very likely that the malicious data that the adversaries introduce will go undetected (Li and Li, 2023; Mo and Yang, 2023). Therefore, there is a requirement for a detection method that overcomes the abovementioned restrictions.

Unbalanced or abnormal data are one of the alarming issues with the current classifier. Real-time samples of normal data are easily available, but fetching theft samples is difficult. On the other hand, theft samples are rare or non-existent for a customer. In addition, algorithms based on classification are susceptible to attacks on the data values, and accepting faulty consumption values by adversaries can contaminate the dataset (Yang et al., 2016). If this factor is not considered properly, it results in a higher false-positive rate. According to what the author has revealed, a false positive will prove expensive because when a malicious user is recognized, a significant amount of procedure is required from the utility. In-person inspection is one of the steps that must be completed before an attack can be considered valid for final verification. Therefore, it is essential to create an adequate model of energy theft detection to overcome these limitations.

This research article introduces a robust energy theft detection system leveraging smart metering data using the AdaBoost ensemble method. The proposed approach addresses the evasion techniques observed in existing classification-based theft detection systems. A comprehensive threat model is presented, accounting for various false data injection (FDI) attack scenarios. The system acknowledges non-malicious elements influencing consumption patterns, including occupant changes, weather variations, and appliance modifications. By incorporating these factors, our method achieves a superior detection rate compared to other available schemes. Experimental assessments were conducted across diverse FDI attack scenarios, benchmarking against state-of-the-art methods such as SVM, LR, KNN, NB, and RFC. The comparative analysis encompassed various performance metrics, demonstrating the effectiveness of our proposed system in enhancing energy theft detection accuracy and resilience against deceptive strategies.

The remainder of this paper is structured as follows: in Section 2, the relevant work on FDI threats is discussed. The system model of an SG monitoring system is discussed in Section 3. The suggested attack detection mechanism is described in Section 4. The performance of the suggested approach is examined and compared to other available methods in Section 5. This paper concludes with Section 6.

2 Related work

This section discusses the studies conducted on the SG's security. We are using smart meter consumption data to identify unethical users. In conventional power networks, analyzing consumer load profiles for indications of energy theft has drawn the interest of experts in the past (Cao et al., 2020; Yang et al., 2023). The majority of recently published works in the literature are devoted to the detection of fraud. AMI daily smart meter readings were used to estimate the consumption pattern of clients using support vector machines (SVMs). The classifier was trained with normal data and thieved sample data from the past. The load profiles of the smart meter malicious user were proposed in a classification-based energy theft detection system. The identifier was educated using historical data from theft and normal sample populations. New samples were categorized based on criteria and SVM outcomes. In a multiclass study, SVM was trained to distinguish between regular and malicious load profile samples. Creating a synthetic dataset addresses and resolves the issue of uneven training datasets (Jokar et al., 2016; Ahmad et al., 2018). It is among the most recent models for detecting power theft (Lyu et al., 2024). It creates a hyperplane to divide the various classes. The XGBoost-supervised technique was proposed to detect the non-malicious user (Buzau et al., 2019). The method based on this ML approach analyzes customer behavior patterns from past kWh consumption data and identifies anomalous activity. A back propagation neural network was constructed and used to analyze SG energy theft (Depuru et al., 2011). The SVM parameters were estimated via a neural network model to reduce the training time of the classifier. Additionally, a data encoding technique was suggested to increase the classifier's effectiveness and speed. However, their system only works to identify energy theft attempts that provide zero-use reports. The metering data are encoded into binary values and transformed at one process phase. As a result, various attack types cannot be detected using the suggested categorization approach. To assess SG power theft, a broad and deep convolutional neural network model was created (Zheng et al., 2018). To investigate the attack path for false data injections against AC-based state estimation in power systems, we presented a new semidefinite programming-based convexification framework that detects globally optimal stealth attacks (Jin et al., 2019). In Alexopoulos et al. (2020), in the case of zero-injection buses, FDI attacks against a PMU linear state estimator based on Cartesian formulation were investigated with the presumption that the attacker would probably attempt to tamper with as few measurements as feasible. A novel hybrid attack (Pei et al., 2020) offered a low-cost attack mechanism that attackers could simply use to target buses with limited connectivity based on state estimation. To achieve observability for the entire system, this algorithm deployed extra-phase measurement units based on a greedy approach

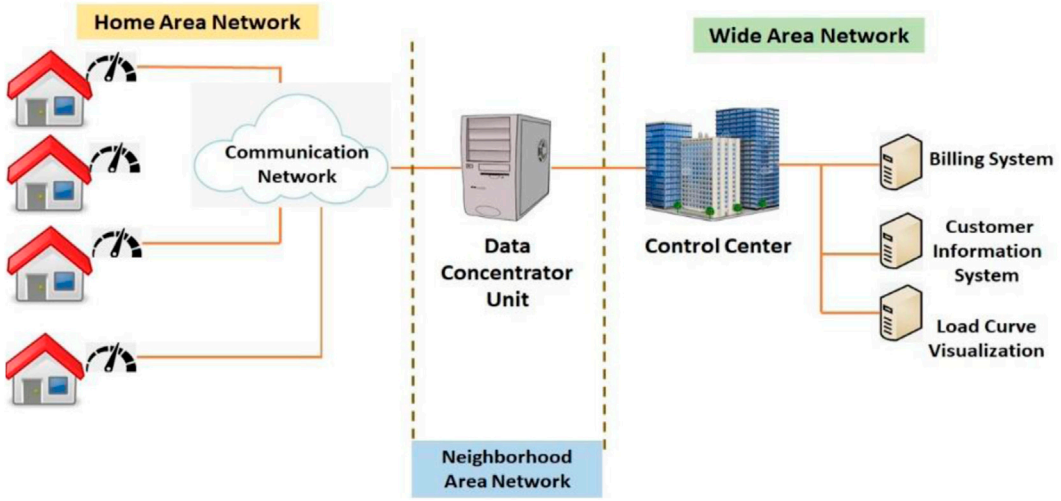

FIGURE 2
Network architecture of the advanced metering infrastructure.

after prioritizing the protection of the most susceptible buses in the first phase. The new energy data sample is categorized using the K-means technique based on the similarity measure. It is one of the simplest methods available (Aziz et al., 2020).

However, many AI-based approaches need more precision for specific reasons. Due to the difficulties in obtaining labeling datasets of electrical thefts, i.e., proper preset thresholds and some external knowledge, the application of classification algorithms is restricted. It makes it harder to achieve in real-time situations, compromising detection accuracy. Unsupervised clustering cannot detect tampered load profiles with standard forms, resulting in low detection precision. Neural networks, for instance, are susceptible to overfitting since they learn the training examples exceptionally well but fail to generalize to new samples. Consequently, an effective system for detecting energy theft is essential to overcome these restrictions. Intending to develop a solution with low computing costs, better accuracy, and fewer false detections, we use the *AdaBoost* method to detect a stealthy attack on smart meter readings in this study. By creating a synthetic attack dataset and assuming that stealing trends are foreseeable, we can solve the issue of unbalanced data. The use of the *AdaBoost* algorithm is motivated by the reasons listed below.

1. Compared to most learning algorithms, the AdaBoost algorithm is less prone to overfitting and corrects misclassifications generated by poor classifiers. The classifiers based on this model have positive performance for anomaly detection problems.
2. Finding relationships between features in large datasets is challenging due to the various feature types. By integrating the weak learners for statistical attributes and descriptive attributes into a strong classifier, the links between these two different types of attributes are managed organically, regardless of any forced conversions between statistical and descriptive features of the dataset.
3. The *AdaBoost* technique is extremely quick when using straightforward, weak classifiers. Considering all the points listed above, we select the ensemble technique. In the proposed design, we put much effort into creating a reliable system that can be installed in the control center and use the data from the smart meter to detect suspicious energy readings and demand data that have been tampered with.

The proposed algorithm is created for various FDI attack scenarios to lessen the chance of the power system experiencing financial loss. The suggested approach was created to effectively anticipate various cyberattacks.

3 System model

This section discusses the AMI network and attack models used in this article.

3.1 Network model

One crucial component of the SG is AMI, which is a network of information and communication, smart meters, and meter data management systems. The home area network (HAN), neighborhood area network (NAN), wide area network (WAN), and utility systems make up the majority of the three significant components that make up the AMI's communication network, as illustrated in Figure 2. Smart meters connected to houses via the HAN are the basis of the AMI. These meters collect current and voltage usage data in real-time and send it across the NAN to a data concentrator. These data are used by the utility for forecasting, demand response (DR), and power billing. WAN links the data concentrator and control center, and smart meters facilitate smooth energy generation and consumption balance. This integration allows for efficient defect detection, real-time customer

TABLE 1 Summary of energy theft attack targeted at AMI systems.

Attack type	Description
Physical attack	• Tampering meter readings illegally
	o By-passing meter readings using a magnet
	o Fake metering
Cyber attack	Eavesdropping on confidential information
	Gaining privileged system access
	Tampering with energy meter storage
Data attack	Targeting the metering values
	Purposely changing consumption to zero
	Revealing the private information of the user

TABLE 2 Mathematical expression of partial reduction-based FDI attack class.

Type	Definition	Attack class
Attack 1 (A_1)	$a_t = \alpha e_t$	Partial reduction of consumption
Attack 2 (A_2)	$a_t = \alpha_t e_t$, where $0.1 < \alpha_t < 0.9$	Partial reduction of consumption

research, and improved smart grid tracking. Overall, smart meters in AMI improve energy management, billing accuracy, and grid responsiveness.

3.2 Attack model

The attacker's approach to attempting an attack is proposed here. The control center gathers information to analyze the consumption patterns of consumers and detect faults. An attacker uses this fine-grained consumption reading and can send false information to utilities to reduce their bill illegally. The primary goal of a consumer stealing electricity is to obtain the expended energy for less money than it is worth. Illegally reporting false bills creates a financial loss to the utility and a disturbance to energy management. A list of the many possible energy attacks against the AMI systems is illustrated in Table 1.

In the proposed threat model, fraudulent data have been introduced into the system at the consumer's location primarily for financial advantage. The paper analyzes the two classes of FDI attacks, as listed in Tables 2, 3, where e_t represents the user's actual energy consumption throughout the time interval t and a_t represents fraudulent energy consumption data collected using the smart meter.

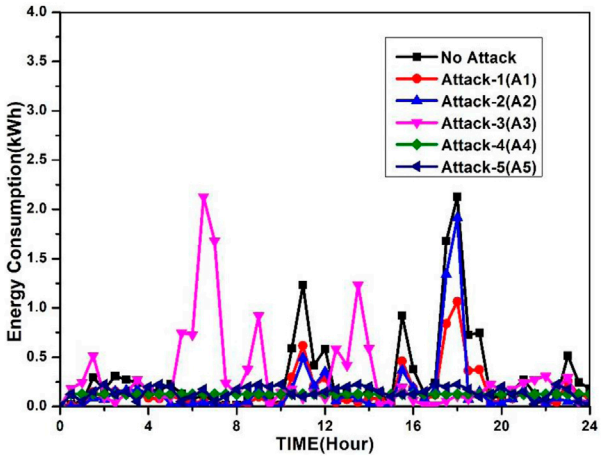

FIGURE 3
An illustration of malicious and non-malicious user's consumption patterns for a day for different attack scenarios.

3.2.1 Partial reduction-based FDI attack class

The primary goal of the user in this kind of FDI attack is to lower the amount of energy used to benefit financially. The attacker can inject the reduced consumption as compared to the actual value for that purpose. The mathematical representation of partial reduction-based FDI attacks is listed in Table 2. The target of each attack is to decrease energy usage by the factor α. The objective of the first attack A_1 is to reduce (e_t) by a flat reduction ratio α, where α is a fixed number from random (0.1, 0.9). In contrast, the objective of attack A_2 is to dynamically reduce consumption by the factor α_t, where α_t varies from $0.1 < \alpha < 0.9$.

3.2.2 Price control-based FDI attack class

In this, the attacker aims to cause financial loss to the utility by changing the energy meter data so that total power consumption will not change but attack the effect financially. These attacks happen when the DR is used, and the price varies throughout the day. The mathematical expressions for the price control attacks A_3, A_4, and A_5 are listed in Table 3. Reversing the day's consumption order is done in A_3. In A_4, the malicious reading of energy consumption a_t is equal to the mean of power readings $\bar{e}_{t-1}$ of the previous day multiplied by a fixed random value α. A_5 multiplies each meter reading with a random value ranging from 0.1 to 0.9 with $\bar{e}_{t-1}$.

Figure 3 is the graphical representation of FDI attacks (A_1–A_5) and no attack scenario for 1 day. Consumption includes all five types of attacks and consumption by the user without attack with respect to the time of 1 day, i.e., 24 hr.

TABLE 3 Mathematical expression of price control-based FDI attack class.

Type	Definition	Attack class
Attack 3 (A_3)	$a_t = e_{24-t}$	Price based
Attack 4 (A_4)	$a_t = \alpha\bar{e}_{t-1}$, where $\bar{e}_{t-1}$ is the mean of previous day i values, α = random (0.1,0.9)	Price based
Attack 5 (A_5)	$a_t = \alpha_t\bar{e}_{t-1}$, where $\bar{e}_{t-1}$ is the mean of previous	Price based

Input: Energy consumption data of N days, with each day having i energy measurement time slots; $E = \begin{bmatrix} e_1^1 & \dots & e_1^i \\ \vdots & \dots & \vdots \\ e_N^1 & \cdots & e_N^i \end{bmatrix}$

Output: The measurement value e_p^c for that selected day p and time slot c denoted as a_i either belongs to the faulty (false) class or non-faulty (true) class

for $e_p^c = 1$ *to* N **do**
  If e_p^c is missed, **then**
  $e_p^c = e_{repeat}{}^{max}$ (filled with the most repeated value)
  End
End
p ← p + 1
Generation of synthetic attack pattern A_b for different attack scenarios
for b = 1 to 5 **do**
  Generation of a synthetic attack pattern for each value of b
  Merging A_b with e_p^c and generating a combined dataset.
Select the combined meter measurement value e_q^c of the latest q days as a training set
  Adaptive Boost Ensemble Method (training dataset)
  Given: $(e_1, a_1), (e_2, a_2), \dots . (e_1, a_1)$, where $e_1 \in \mathcal{E}, a_1 \in \{-1, +1\}$
//Initialization $X_1(i) = \frac{1}{l}$ *for* $i = 1 \dots . l$
  for $(t_1, t_2, t_3, \dots . t_T)$ classifiers **do**
    Train weak learners with the X_t distribution
    get weak hypothesis $h_t = \Re \rightarrow \{-1\,(False), +1\,(true)\}$
    Aim: Select h_t with low weight error:
    $\beta_t = P_{r_i} \sim X_t[h_t(e_i) \neq a_i]$
    Choose $\gamma_t = \frac{1}{2} ln(\frac{1-\beta_t}{\beta_t})$
    Update, **for** l = 1 to i **do**
      $X_{t+1}(l) = \frac{X_t(l) exp(-\gamma_t) a_i h_l(e_i)}{Z_t}$, where Z_t is the normalization factor
    end
  End
  for $e_p^t \epsilon$ testing dataset to **do**
    if $e_p^t \epsilon$ faulty user, **then**
      false class (malicious consumer)
    else
      e_p^t true class (non-malicious consumer)
    end
  End
End

Algorithm 1. Algorithm of the proposed theft detection system, TDS.

4 Proposed energy theft detection model under varying attack scenarios

Our proposed model framework comprises four modules: proposed ensemble modeling technique, data preprocessing, training phase, and testing phase. The first subsection of this section presents a description of the proposed methodology, an ensemble modeling-based *AdaBoost* technique. Then, the subsequent parts cover the remaining three modules of the theft detection approach, which we use to foil attempts on the integrity of our energy meter data. The steps of our proposed approach's framework for detecting electricity theft are presented in Algorithm 1.

4.1 Proposed ensemble modeling technique

AdaBoost is a supervised ML-based boosting algorithm to help classification models perform better. AdaBoost sequentially creates several learning models. The first model is created by conventionally fitting the classifier to the given dataset. The second model is then created by training a second instance of the classifier using the same set of data, with an emphasis on the samples that the previous model incorrectly identified. The third model then uses the weak classifiers from the prior model to train the classifier. By integrating misfit samples of the classifier into a robust classifier or merging weak learners' decision trees from learning models, very accurate predictions may be made to improve the final predictive performance of the system.

Let $t_1, t_2, t_3, \dots . t_T$ represent the collection of generated weak learners of classifiers. Here, the training dataset is represented as e_p^t, where p represents days taken in the training set, with each day having i measurement time slots. $(e_1, a_1), (e_2, a_2), \dots . (e_l, a_l)$, *w*here $e_l \in \mathcal{E}, a_l \in \{-1, +1\}$ is the training set containing l samples, where all e inputs are an element of total set $\mathcal{E}$ and outputs are an element of a set comprising only two values, −1 (false class, i.e., malicious user) and +1 (true class, i.e., non-malicious user). X is the weight of the samples, and i is the ith training sample. $X_1(i) = \frac{1}{l}$ *for* $i = 1 \dots . l$; initialize all the weights of your samples to 1 divided by the number of training samples l. In $\beta_t = P_{r_i \sim X_t}[h_t(e_i) \neq a_i]$, P_{r_i} is the probability, β_t is the minimum misclassification error for the model, and γ_t is the weight of the classifier. Assume that $X_1, X_2, \dots . X_l$ are the weights assigned to dataset samples to show the importance of the data points, where l is the l^{th} training sample. Some of the key points of the AdaBoost-based algorithm for attack detection are summarized below.

- Set weights $X_1(i) = 1/l$ *for* $i = 1 \dots . l$, satisfying Eq. (1).

$$\sum_{i=1}^{c} X_i(1) = 1. \tag{1}$$

- Consider Eq. (1) condition for $(t_1, t_2 \dots . , t_T)$ classifiers.
- Update the weights according to Eq. (2) for $i = 1, 2, \dots . l$.

$$X_{t+1}(i) = \frac{X_t(i)\, exp(-\gamma_t) a_i h_t(e_i)}{Z_t}, \tag{2}$$

where Z_t is a normalization factor and γ_t is the weight of the classifier.

- Choose the generated weak classifier that minimizes the sum of weighted classification errors.
- The classifier's weight is adjusted after each iteration to make it focus on sample points that are challenging to categorize correctly. After an iteration, this is accomplished by updating misclassified sample points with higher weights. In the following iteration, our learning system would pay more attention to these

sample points by assigning them increased weights. In contrast, classifiers would assign less weight to the well-categorized sample points and give less attention in the next iteration. The final prediction is then calculated by summing the weighted predictions from all classifiers.

- It has been demonstrated that using the AdaBoost method, if the misclassification rates of the weak classifiers are less than 50%, then the weighted classification error rate of the strong classifier will converge to zero as the number of iterations increases, i.e., when

$$T \to \infty, \sum_{i=1}^{n} [zwj] X_i I[H(e_i) \neq a_i] \to 0. \quad (3)$$

- The basis of Eq. (3) is that misclassification rates for the weak classifiers are less than 50%.
- By merging the decision trees for the descriptive and statistical aspects of the smart meter into a robust classifier, the linkages between these features are naturally handled. This is the primary reason why our *AdaBoost-based* algorithm achieves good attack detection results.

The decision trees reduce the total of the incorrect classification outputs for true (faulty) and false (non-faulty) samples. The misclassification rates for the selected weak learners are guaranteed to be lower than fifty percent, assuring the algorithm's convergence.

4.2 Data pre-processing

The first step toward training the detection model is data pre-processing, which includes cleaning the raw data, filling in the missing values, and removing extreme values. Our power theft detection model uses energy consumption measurements from a real smart meter dataset of 5,000 customers for training and evaluation purposes (ISSDA, 2020). This dataset comprises energy consumption readings from residential and business users from 2009 to 2010, spanning 533 days. To enhance the financial analysis for a statewide deployment, the main purpose of this study is to assess the impact of user power to find energy theft. Six data sample files containing records of 533 days in each file made up the raw dataset. Each file has three columns: the smart meter identifier, the encoded date and time, and the amount of energy used in kWh. Every document includes 533 days' worth of metering information for every client, captured every half hour, i.e., each user's daily consumption data presented by 48 vector components. All of the consumers' consumption is included in the raw data collection. To prepare the data for our experiment, we divided the raw files by meter ID into many consumption datasets.

Assume $e = [e_1, e_2, e_3 \ldots\ldots, e_{48}]$ as the customer's energy consumption in a day, which is recorded in kWh to the data concentrator unit of AMI for each 30 min. The whole dataset is represented as $E = \begin{bmatrix} e_1^1 & \cdots & e_1^i \\ \vdots & \cdots & \vdots \\ e_N^1 & \cdots & e_N^i \end{bmatrix}$, where N is the total consumption days, with each day having i measuring slots. We use the attack scenarios in Tables 2 and 3 to create attack samples.

TABLE 4 List of features extracted.

Descriptive feature	Statistical feature
Maximum of weekend	Mean of weekend
Minimum of weekend	Mean of week
Total of week	Auto-correlation
Maximum of week	Median of week
Total of weekday	Range
Maximum of weekdays	Entropy
Total of weekend	Quartile 25
Minimum of week	Standard deviation
Minimum of weekdays	Quartile deviation
Minimum of weekend	Coefficient of quartile deviation
	Quartile 75
	Variance of week
	Interquartile range
	Mean of weekday

Missing values are those in which the smart meter cannot record the meter readings for reasons such as an error in transmission, a component break, and a bad connection. When missing values are incorrectly handled, a biased ML model is created, producing unreliable results. The most repeated value imputation method is used to fill in the missing value in the proposed method. The mathematical representation is as follows:

$$C(e_i) = \begin{cases} mode(e_i) & e_i \epsilon NaN \\ e_i & otherwise \end{cases}, \quad (4)$$

where mode (e_i) is the most repeating value of e_i and the value of the data on power usage in one cycle is e_i, indicating NaN as if e_i is not a number value.

4.2.1 Feature extraction

In the second phase of the cleaning process crucial for time-series classification, extreme values are eliminated from the raw dataset. This step is pivotal for accurate classification results. Effective feature extraction is vital for enhanced accuracy and interpretability. The dynamic nature of an individual user's daily consumption pattern necessitates stable features reflecting daily and weekly load patterns. To achieve this, descriptive and statistical features, detailed in Table 4, are extracted monthly for each time slot reading across the entire period. Extreme values, indicative of unusual activities such as vacations or changes in appliances or residences, are removed to ensure data integrity. This refined dataset forms the basis for robust time-series classification.

4.3 Training phase

The next module is used to train a model with the energy meter data readings for the detection of energy theft. For that purpose, we need both benign data and malicious data; otherwise, the classifier will face

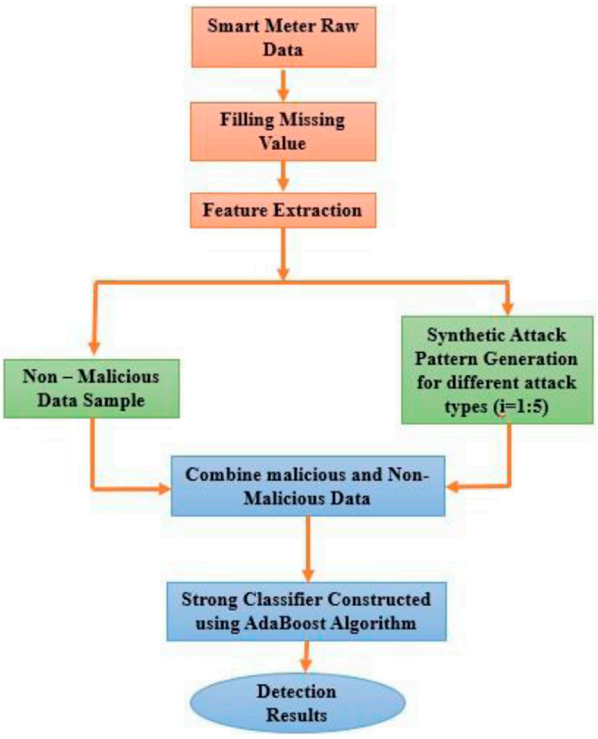

FIGURE 4
Framework of the proposed algorithm.

the problem of data balancing and make the efficiency of the theft detection system low. As the malicious data are not available and it is difficult to gather faulty readings, we propose synthetically generating the malicious dataset for different types of five FDI attack scenarios to address this issue. The attacks in Table 2 are based upon the partial reduction of A_1 and A_2 attacks, and in Table 3, price-based attacks A_3, A_4, and A_5. Energy theft aims to record less usage than the user uses or shift high usage to low-tariff times. Therefore, it is easy to produce malicious samples using benign samples. The suggested ensemble approach is used to detect intruders using meter reading data once the data have been properly formatted. We randomly choose 50% of the data for each user to create five synthetic attack patterns. After generating attack patterns (A_b, where $b = 1: 5$), the non-malicious values are mixed, and the combined dataset is generated. For training the model, we select the historical data (i.e., measurement values) from the most recent m days from the combined dataset. As a result, we have 70% of the data for model training and 30% for model testing. The flow diagram of the proposed algorithm is shown in Figure 4. The model is also trained for existing AI approaches as per the survey, including support vector machine, logistics regression (LR), K- nearest neighbor (KNN), naïve Bayes (NB), and random forest classifier (RFC) to demonstrate the efficacy of the suggested strategy.

4.4 Testing phase

Following the training set, pre-processing and format conversion are performed on each new smart meter reading. Determining whether data are genuine or false, i.e., if testing data belong to the non-malicious or malicious type, enables us to make detection decisions for false data. After introducing a synthetic attack, the *AdaBoost* ensemble technique is applied to a fresh meter reading to assess whether it belongs to the faulty or non-faulty class. The newly created sample is uploaded to the genuine dataset, and the appropriate attack patterns are created and added to the attack dataset. When the fresh sample presented to the classifier identified an assault, the smart meter's suspicious behavior was notified. After that, more data samples of the same meter ID were tested, and suspicious behavior was reported q times, indicating energy theft was discovered. Once energy theft is identified, the required measures, such as an on-site examination, are taken. Repetition is essential so that, for any change (change in an appliance, vacation, or seasonal change), a non-malicious user is not reported, owing to the cost of the on-site inspection. Priority inspection is assigned to a certain region based on the number of customers determined to be defective. If the theft is confirmed, the specific consumer values are included in the attack data values; otherwise, they remain in the authentic dataset. To show the effectiveness of our system, we have implemented experiments as mentioned with other well-known ML techniques and compared them with the proposed method for each attack type, as discussed in detail in Section 5 of this article.

5 Results and discussions

To verify the efficacy of the proposed approach, various supervised algorithms are applied to the data sample described in Section 4. The performance of our scheme was assessed using the metrics accuracy (A_c), precision (P_r), recall (R_e), and F1 score (F_s) given in Eqs (5) and (6).

$$A_c = \frac{T_p + T_n}{T_n + T_p + F_n + F_p} \quad \text{and} \quad P_r = \frac{T_p}{T_p + F_p}, \tag{5}$$

$$F_s = \frac{(2{*}P_r{*}R_e)}{(P_r + R_e)} \quad \text{and} \quad R_e = \frac{T_p}{T_p + F_n}, \tag{6}$$

where T_p is the proportion of attack samples that were classified correctly, F_p is the proportion of attack samples that were mistakenly detected, T_n is the proportion of attack samples that were missed, and F_n user is identified faulty user as a non-faulty user. F_s strikes a compromise between P_r and R_e, measuring the proportion of honest/fraudulent customers that are accurately identified as such.

The model performance is better when Ac is high, whereas F_p is low. The confusion matrix, loaded from the scikit-learn Python package, was used to test our model. In this paper, we use a positive class for the honest customer and a negative class for the dishonest user. The classification method has a problem of prior labeling of the historical dataset, which is resolved by generating synthetic attack patterns for different attack scenarios, as discussed in Section 4. The classifier is trained for all possible types of attack scenarios A_b, where $b = 1: 5$. Experimental analysis for these five types of attacks is discussed in subsequent subsections.

5.1 Experiment no. 1

In the first experiment, different existing AI techniques are applied to the smart meter data for A_1. In our experiment, we

TABLE 5 Performance parameter comparison for A_1.

Technique	Performance comparison			
	A_c	P_r	R_e	F_s
SVM	0.838	0.656	0.836	0.735
LR	0.834	0.671	0.753	0.710
KNN	0.793	0.598	0.712	0.650
NB	0.727	0.496	0.932	0.648
RFC	0.841	0.692	0.740	0.715
Our method	**0.852**	**0.694**	**0.808**	**0.747**

TABLE 6 Performance parameter comparison for A_2.

Technique	Performance comparison			
	A_c	P_r	R_e	F_s
SVM	0.670	0.656	0.836	0.735
LR	0.700	0.682	0.169	0.270
KNN	0.663	0.484	0.337	0.397
NB	0.585	0.439	0.921	0.594
RFC	0.800	0.697	0.697	0.697
Our method	**0.848**	**0.740**	**0.831**	**0.783**

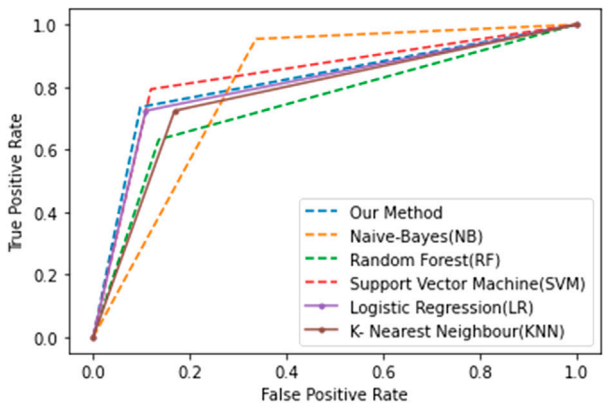

FIGURE 5
Comparison of the ROC curve of the proposed method with existing methods for A_1.

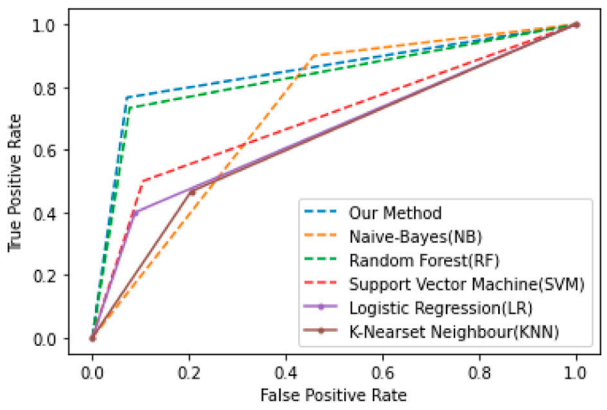

FIGURE 6
Comparison of the ROC curve of the proposed method with existing methods for A_2.

assume the α value is 0.5. A synthetic attack dataset is generated and combined with the non-malicious data, forming a new dataset containing genuine and non-genuine data. In this experiment, we have taken a ratio of 50% for actual data and 50% for synthetic data to create the combined dataset of faulty and non-faulty users. KNN, RFC, SVM, LR, NB, and our method are applied to data samples, and different metrics of the models are evaluated. Performance metrics A_c, P_r, R_e, and F_s are evaluated for each method and compared with the proposed method, as shown in Table 5. For the proposed method, A_c is 85%, whereas for the SVM, it is 83%; for LR, it is 83%; and KNN it is 79%; additionally, for NB, it is 72%; and for RFC, it is 84%. Figure 5 shows the region of convergence (ROC) curve of all the models mentioned on which the experiment is conducted. ROC is the graph between T_p and F_p, representing the performance measurement for the classifier.

5.2 Experiment no. 2

This experiment is conducted for A_2 belonging to the partial reduction FDI attack class, in which a synthetic attack pattern is generated using the definition mentioned in Table 2 and merged with the normal smart meter data. In this, the malicious value a_t is generated by multiplying the real-time energy consumption value e_t of the user with the α factor, whose value is in the dynamic range from 0.1 to 0.9. In the combined dataset, we take the ratio of 70:30% for genuine and non-genuine data. The different evaluation metrics are listed in Table 6 for our method and other compared techniques. For the proposed system, $A_c$is shown as 84%, whereas for the SVM, it is 67%; for LR, it is 70%; for the RFC algorithm, it is 80%; and for KNN, it is 66%. The ROC curve for the differences is compared in Figure 6. As per the result obtained, our method outperforms attack 2 compared to other methods.

5.3 Experiment no. 3

The price control-based FDI attack A_3 was the focus of experiment 3, in which the altered meter reading a_t is the reverse of the day's readings. This assault on the loading mechanism involves changing the price of energy at various times of the day while keeping the overall amount of electricity used constant and reporting used to occur at low-tariff times. The experimental results of this attack by applying our proposed method are listed in Table 7. A comparison of different performance metrics shows that our proposed system achieves an accuracy of 83%, outperforming other

TABLE 7 Performance parameter comparison for A_3.

Technique	Performance comparison			
	A_c	P_r	R_e	F_s
SVM	0.717	0.656	0.836	0.735
LR	0.694	0.682	0.169	0.270
KNN	0.637	0.437	0.972	0.603
NB	0.334	0.294	0.966	0.451
RFC	0.670	0.697	0.697	0.697
Our method	**0.839**	**0.736**	**0.675**	**0.704**

TABLE 8 Performance parameter comparison for A_4.

Technique	Performance comparison			
	A_c	P_r	R_e	F_s
SVM	0.817	0.672	0.773	0.719
LR	0.799	0.718	0.550	0.623
KNN	0.740	0.538	0.740	0.694
NB	0.507	0.378	0.976	0.545
RFC	0.692	0.697	0.697	0.697
Our method	**0.905**	**0.799**	**0.917**	**0.854**

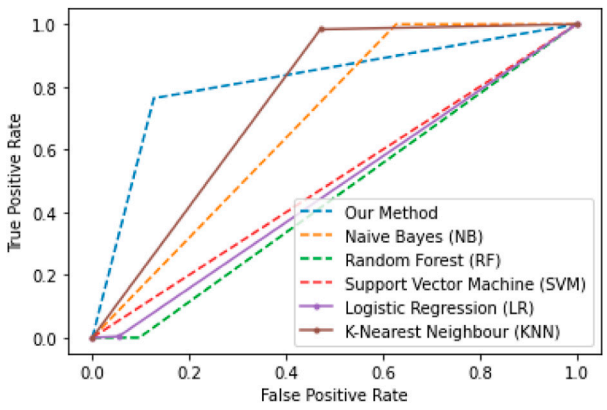

FIGURE 7
Comparison of the ROC curve of the proposed method with existing methods for A_3.

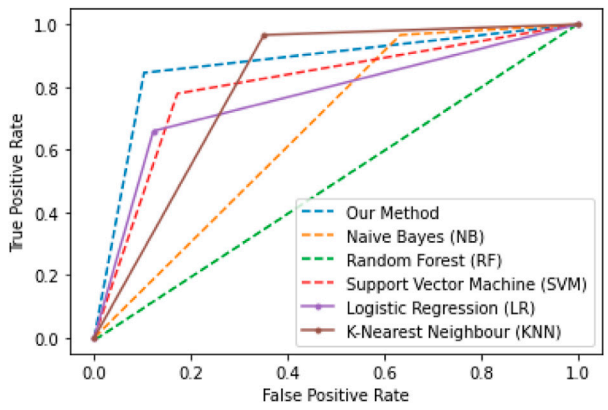

FIGURE 8
Comparison of the ROC curve of the proposed method with existing methods for A_4.

methods such as SVM (71%), LR (69%), RFC algorithm (67%), and KNN (63%). The ROC curve for the different methods is compared in Figure 7.

5.4 Experiment no. 4

Experiment 4 is conducted for A_4 of the price control FDI class, similar to A_3, where fraudulent customers attempt with the same motive. A faulty meter malicious reading is generated by multiplying the mean of the whole day consumption by the random number α, taken as 0.5. Experimental results are listed in Table 8 by applying our theft detection method, and compared with other methods described above, the comparison graph is depicted in Figure 8. The detection accuracy of our system is 90%, which is higher than other techniques.

5.5 Experiment no. 5

A synthetic attack pattern was generated for A_5 in this test. Malicious reading is obtained by multiplying the real meter reading value with a random value α varying from 0.1 to 0.9. Experiment results in comparison are listed in Table 9 by applying our ensemble boosting technique and compared with other existing methods. The detection accuracy comparison graph of our technique with others is shown in Figure 9. A_c of our system is 92% higher than that of other existing techniques. To validate the effectiveness of the proposed approach on unbalanced data, the area under the ROC curve (AUC) has been accessed, showing a comparison of different attack scenarios (A_1–A_5) in Figure 10. The AUC is determined by plotting the receiver characteristics curve, which depicts the relationship between the false-positive and true-positive rates. It serves as a comprehensive measure of classification performance. By leveraging these established metrics, we ensure a thorough demonstration of the proposed scheme's robustness and suitability for handling unbalanced datasets in classification scenarios.

6 Conclusion

In this study, we provide an ensemble *AdaBoost* approach for depicting the relationship between false-positive and true-

TABLE 9 Performance parameter comparison for A_5.

Technique	Performance comparison			
	A_c	P_r	R_e	F_s
SVM	0.710	0.656	0.836	0.735
LR	0.681	0.682	0.169	0.270
KNN	0.665	0.463	0.978	0.629
NB	0.404	0.324	0.977	0.487
RFC	0.70	0.697	0.697	0.697
Our method	**0.923**	**0.817**	**0.945**	**0.877**

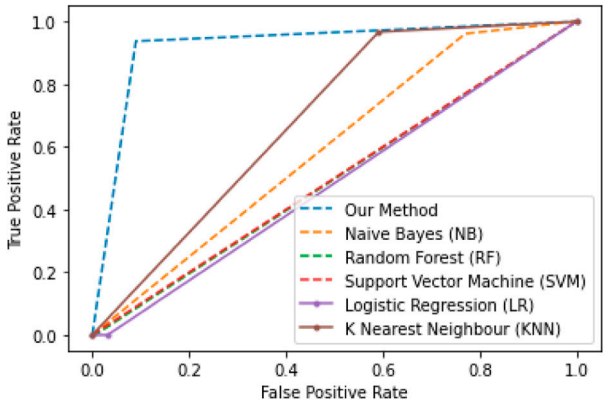

FIGURE 9
Comparison of the ROC curve of the proposed method with existing methods for A_5.

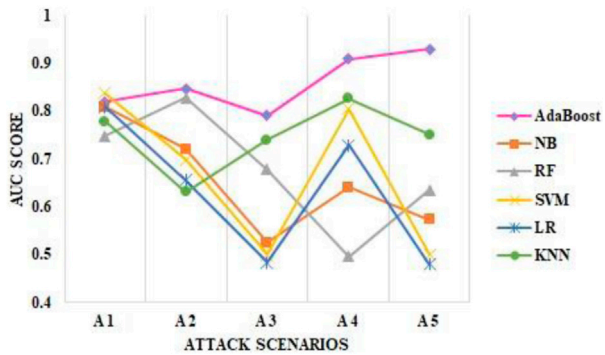

FIGURE 10
Comparison of the AUC score of different attack scenarios (A_1–A_5) for the proposed method with other state-of-the-art methods.

positive rates. It serves as a comprehensive measure of classification performance. By leveraging these established metrics, we ensure a thorough demonstration of the proposed scheme's robustness and suitability for handling unbalanced datasets in classification scenarios or identifying fraudulent users of the SG framework. Numerous models are combined sequentially using the ensemble approach to enhance the ultimate prediction performance. The approach involves providing high weightage to the misclassified user's data samples and iterating again to give better predictions while reducing the false positive rate (F_p). The whole algorithm used in this article does not require a predetermined threshold or any external knowledge. Different statistical and descriptive features are extracted to consider the extreme conditions in data samples, as incorrect identification leads to expensive on-site inspections. The experiment's results demonstrate that the algorithm can more effectively identify faulty data in the AMI through a mix of theoretical analysis and performance simulation, achieving higher detection accuracy than current methods. Similar tests on well-known data analysis algorithms such as SVM, LR, KNN, NB, and RFC were undertaken for performance evaluation. Moreover, the proposed method exhibits a higher detection accuracy of 85.2%–92.3% for attacks 1–5 than that of other state-of-the-art methods, surpassing well-known data analysis algorithms like SVM, LR, KNN, NB, and RFC. The recommended solution uses extensive experimentation on a real-world dataset of 5,000 customers and provides good performance even with a low sample rate, protecting users' privacy.

Data availability statement

The original contributions presented in the study are included in the article/Supplementary Material; further inquiries can be directed to the corresponding authors.

Author contributions

TG: conceptualization, data curation, methodology resources, software, writing–original draft, and writing–review and editing. RB: data curation, methodology, supervision, validation, project administration, and writing–review and editing. SS: conceptualization, data curation, investigation, methodology, project administration, software, supervision, and writing–original draft. CR: investigation, methodology, writing–original draft, and writing–review and editing. KA: conceptualization, investigation, software, and writing–review and editing. WM: data curation, methodology, and writing–review and editing.

Funding

The author(s) declare that no financial support was received for the research, authorship, and/or publication of this article.

Conflict of interest

The authors declare that the research was conducted in the absence of any commercial or financial relationships that could be construed as a potential conflict of interest.

Publisher's note

References

Ahmad, T., Chen, H., Wang, J., and Guo, Y. (2018). Review of various modeling techniques for the detection of electricity theft in smart grid environment. *Renew. Sustain Energy Rev.* 82, 2916–2933. doi:10.1016/j.rser.2017.10.040

Alexopoulos, T. A., Korres, G. N., and Manousakis, N. M. (2020). Complementarity reformulations for false data injection attacks on PMU-only state estimation. *Electr. Power Syst. Res.* 189, 106796. doi:10.1016/j.epsr.2020.106796

Amin, S. (2015). Game-theoretic models of electricity theft detection in smart utility networks: providing new capabilities with advanced metering infrastructure. *IEEE Control Syst.* 35, 66–81. doi:10.1109/MCS.2014.2364711

Amin, S., Schwartz, G. A., and Tembine, H. (2012). *Incentives and security in electricity distribution networks*, 264–280. doi:10.1007/978-3-642-34266-0_16

Attia, M., Senouci, S. M., Sedjelmaci, H., Aglzim, E.-H., and Chrenko, D. (2018). An efficient Intrusion Detection System against cyber-physical attacks in the smart grid. *Comput. Electr. Eng.* 68, 499–512. doi:10.1016/j.compeleceng.2018.05.006

Aziz, S., Hassan Naqvi, S. Z., Khan, M. U., and Aslam, T. (2020). "Electricity theft detection using empirical mode decomposition and K-nearest neighbors," in 2020 Int. Conf. Emerg. Trends Smart Technol., IEEE, Karachi, Pakistan, 26-27 March 2020, 1–5. doi:10.1109/ICETST49965.2020.9080727

Buzau, M. M., Tejedor-Aguilera, J., Cruz-Romero, P., and Gomez-Exposito, A. (2019). Detection of non-technical losses using smart meter data and supervised learning. *IEEE Trans. Smart Grid* 10, 2661–2670. doi:10.1109/TSG.2018.2807925

Cao, B., Zhao, J., Gu, Y., Fan, S., and Yang, P. (2020). Security-aware industrial wireless sensor network deployment optimization. *IEEE Trans. Ind. Inf.* 16, 5309–5316. doi:10.1109/TII.2019.2961340

Chen, B., Hu, J., Zhao, Y., and Ghosh, B. K. (2022b). Finite-time velocity-free rendezvous control of multiple AUV systems with intermittent communication. *IEEE Trans. Syst. Man. Cybern. Syst.* 52, 6618–6629. doi:10.1109/TSMC.2022.3148295

Chen, Y., Zhu, L., Hu, Z., Chen, S., and Zheng, X. (2022a). Risk propagation in multilayer heterogeneous network of coupled system of large engineering Project. *J. Manag. Eng.* 38. doi:10.1061/(ASCE)ME.1943-5479.0001022

Cheng, B., Wang, M., Zhao, S., Zhai, Z., Zhu, D., and Chen, J. (2017). Situation-aware dynamic service coordination in an IoT environment. *IEEE/ACM Trans. Netw.* 25, 2082–2095. doi:10.1109/TNET.2017.2705239

Depuru, SSSR, Wang, L., Devabhaktuni, V., and Nelapati, P. (2011). "A hybrid neural network model and encoding technique for enhanced classification of energy consumption data," in 2011 IEEE Power Energy Soc. Gen. Meet., IEEE, Detroit, Michigan, USA, 24-29 July 2011, 1–8. doi:10.1109/PES.2011.6039050

Guarda, F., Hammerschmitt, B., Capeletti, M., Neto, N., dos Santos, L., Prade, L., et al. (2023). Non-hardware-based non-technical losses detection methods: a review. *Energies* 16, 2054. doi:10.3390/en16042054

Guo, C., and Hu, J. (2023). Time base generator-based practical predefined-time stabilization of high-order systems with unknown disturbance. *IEEE Trans. Circuits Syst. II Express Briefs* 70, 2670–2674. doi:10.1109/TCSII.2023.3242856

Gupta, T., and Bhatia, R. (2020). "Communication technologies in smart grid at different network layers: an overview," in 2020 Int. Conf. Intell. Eng. Manag., IEEE, Singapore, December 14-17, 2020, 177–182. doi:10.1109/ICIEM48762.2020.9160099

Gupta, T., Bhatia, R., and Sharma, R. (2022). False data injection attack detection using machine learning in smart grid: approaches, datasets, and comparative study. *Datasets, Comp. Study*, 1081–1090. doi:10.1007/978-981-19-4364-5_76

Henriques, H. O., Barbero, A. P. L., Ribeiro, R. M., Fortes, M. Z., Zanco, W., Xavier, O. S., et al. (2014). Development of adapted ammeter for fraud detection in low-voltage installations. *Measurement* 56, 1–7. doi:10.1016/j.measurement.2014.06.015

ISSDA (2020). Irish social science data archive. Available at: https://www.ucd.ie/issda/ (Accessed June 24, 2020).

Jain, H., Kumar, M., and Joshi, A. M. (2022). Intelligent energy cyber physical systems (iECPS) for reliable smart grid against energy theft and false data injection. *Electr. Eng.* 104 (4), 331–346. doi:10.1007/s00202-021-01380-9

Jiang, H., Wang, M., Zhao, P., Xiao, Z., and Dustdar, S. (2021). A utility-aware general framework with quantifiable privacy preservation for destination prediction in LBSs. *IEEE/ACM Trans. Netw.* 29, 2228–2241. doi:10.1109/TNET.2021.3084251

Jiang, Y., and Li, X. (2022). Broadband cancellation method in an adaptive co-site interference cancellation system. *Int. J. Electron* 109, 854–874. doi:10.1080/00207217.2021.1941295

Jin, M., Lavaei, J., and Johansson, K. H. (2019). Power grid AC-based state estimation: vulnerability analysis against cyber attacks. *IEEE Trans. Autom. Contr* 64, 1784–1799. doi:10.1109/TAC.2018.2852774

Jokar, P., Arianpoo, N., and Leung, V. C. M. (2013). "Intrusion detection in advanced metering infrastructure based on consumption pattern," in 2013 IEEE Int. Conf. Commun., IEEE, Budapest, Hungary, 13 June 2013, 4472–4476. doi:10.1109/ICC.2013.6655271

Jokar, P., Arianpoo, N., and Leung, V. C. M. (2016). Electricity theft detection in AMI using customers' consumption patterns. *IEEE Trans. Smart Grid* 7, 216–226. doi:10.1109/TSG.2015.2425222

Keping, Yu, Arifuzzaman, M., Zheng, W., Zhang, Di, and Sato, T. (2015). A key management scheme for secure communications of information centric advanced metering infrastructure in smart grid. *IEEE Trans. Instrum. Meas.* 64, 2072–2085. doi:10.1109/TIM.2015.2444238

Kong, J., Jiang, W., Tian, Q., Jiang, M., and Liu, T. (2023). Anomaly detection based on joint spatio-temporal learning for building electricity consumption. *Appl. Energy* 334, 120635. doi:10.1016/j.apenergy.2022.120635

Li, T., and Li, Y. (2023). Artificial intelligence for reducing the carbon emissions of 5G networks in China. *Nat. Sustain* 6, 1522–1523. doi:10.1038/s41893-023-01208-3

Lin, X., Liu, Y., Yu, J., Yu, R., Zhang, J., and Wen, H. (2022). Stability analysis of Three-phase Grid-Connected inverter under the weak grids with asymmetrical grid impedance by LTP theory in time domain. *Int. J. Electr. Power Energy Syst.* 142, 108244. doi:10.1016/j.ijepes.2022.108244

Liu, D., Cao, Z., Jiang, H., Zhou, S., Xiao, Z., and Zeng, F. (2023b). Concurrent low-power listening: a new design paradigm for duty-cycling communication. *ACM Trans. Sens. Netw.* 19, 1–24. doi:10.1145/3517013

Liu, X., Lou, S., and Dai, W. (2023a). Further results on "System identification of nonlinear state-space models.". *Automatica* 148, 110760. doi:10.1016/j.automatica.2022.110760

Lyu, T., Xu, H., Zhang, L., and Han, Z. (2024). Source selection and resource allocation in wireless-powered relay networks: an adaptive dynamic programming-based approach. *IEEE Internet Things J.* 11, 8973–8988. doi:10.1109/JIOT.2023.3321673

Ma, J., and Hu, J. (2022). Safe consensus control of cooperative-competitive multi-agent systems via differential privacy. *Kybernetika*, 426–439. doi:10.14736/kyb-2022-3-0426

Mo, J., and Yang, H. (2023). Sampled value attack detection for busbar differential protection based on a negative selection immune system. *J. Mod. Power Syst. Clean. Energy* 11, 421–433. doi:10.35833/MPCE.2021.000318

Mrabet, Z. El, Kaabouch, N., El, G. H., and El, G. H. (2018). Cyber-security in smart grid: survey and challenges. *Comput. Electr. Eng.* 67, 469–482. doi:10.1016/j.compeleceng.2018.01.015

Pei, C., Xiao, Y., Liang, W., and Han, X. (2020). PMU placement protection against coordinated false data injection attacks in smart grid. *IEEE Trans. Ind. Appl.*, 1. doi:10.1109/TIA.2020.2979793

Pengwah, A. B., Razzaghi, R., and Andrew, L. L. H. (2023). Model-less non-technical loss detection using smart meter data. *IEEE Trans. Power Deliv.* 38, 3469–3479. doi:10.1109/TPWRD.2023.3280551

Sharma, R., Joshi, A. M., Sahu, C., and Nanda, S. J. (2023). Detection of false data injection in smart grid using PCA based unsupervised learning. *Electr. Eng.* 105, 2383–2396. doi:10.1007/s00202-023-01809-3

Song, J., Mingotti, A., Zhang, J., Peretto, L., and Wen, H. (2022). Accurate damping factor and frequency estimation for damped real-valued sinusoidal signals. *IEEE Trans. Instrum. Meas.* 71, 1–4. doi:10.1109/TIM.2022.3220300

Sun, G., Liao, D., Zhao, D., Xu, Z., and Yu, H. (2018). Live migration for multiple correlated virtual machines in cloud-based data centers. *IEEE Trans. Serv. Comput.* 11, 279–291. doi:10.1109/TSC.2015.2477825

Tan, J., Jin, H., Hu, H., Hu, R., Zhang, H., and Zhang, H. (2023). WF-MTD: evolutionary decision method for moving target defense based on wright-Fisher process. *IEEE Trans. Dependable Secur Comput.* 20, 4719–4732. doi:10.1109/TDSC.2022.3232537

Wang, Q., Dai, W., Zhang, C., Zhu, J., and Ma, X. (2024). A compact constraint incremental method for random weight networks and its application. *IEEE Trans. Neural Netw. Learn Syst.*, 1–9. doi:10.1109/TNNLS.2023.3289798

Wang, Y., Jiang, X., Xie, X., Yang, X., and Xiao, X. (2021). Identifying sources of subsynchronous resonance using wide-area phasor measurements. *IEEE Trans. Power Deliv.* 36, 3242–3254. doi:10.1109/TPWRD.2020.3037289

Wang, Y., Yang, H., Xie, X., Yang, X., and Chen, G. (2023). Real-time subsynchronous control interaction monitoring using improved intrinsic time-scale decomposition. *J. Mod. Power Syst. Clean. Energy* 11, 816–826. doi:10.35833/MPCE.2021.000464

Xia, X., Xiao, Y., and Liang, W. (2019). ABSI: an adaptive binary splitting algorithm for malicious meter inspection in smart grid. *IEEE Trans. Inf. Forensics Secur* 14, 445–458. doi:10.1109/TIFS.2018.2854703

Xiao, Z., Yang, X., and Du, D. H.-C. (2013). Non-repudiation in neighborhood area networks for smart grid. *IEEE Commun. Mag.* 51, 18–26. doi:10.1109/MCOM.2013.6400434

Yang, M., Wang, Y., Xiao, X., and Li, Y. (2023). A robust damping control for virtual synchronous generators based on energy reshaping. *IEEE Trans. Energy Convers.* 38, 2146–2159. doi:10.1109/TEC.2023.3260244

Yang, X., Zhang, X., Lin, J., Yu, W., and Zhao, P. (2016). "A Gaussian-mixture model based detection scheme against data integrity attacks in the smart grid," in 2016 25th Int. Conf. Comput. Commun. Networks, IEEE, Waikoloa, Hawaii, USA, 1-4 August 2016, 1–9. doi:10.1109/ICCCN.2016.7568478

Yu, J., Lu, L., Chen, Y., Zhu, Y., and Kong, L. (2021). An indirect eavesdropping attack of keystrokes on touch screen through acoustic sensing. *IEEE Trans. Mob. Comput.* 20, 337–351. doi:10.1109/TMC.2019.2947468

Zhang, H., Li, Y., Gao, D. W., and Zhou, J. (2017). Distributed optimal energy management for energy internet. *IEEE Trans. Ind. Inf.* 13, 3081–3097. doi:10.1109/TII.2017.2714199

Zhang, H., Mi, Y., Fu, Y., Liu, X., Zhang, Y., Wang, J., et al. (2023a). Security defense decision method based on potential differential game for complex networks. *Comput. Secur* 129, 103187. doi:10.1016/j.cose.2023.103187

Zhang, H., Mi, Y., Liu, X., Zhang, Y., Wang, J., and Tan, J. (2023b). A differential game approach for real-time security defense decision in scale-free networks. *Comput. Netw.* 224, 109635. doi:10.1016/j.comnet.2023.109635

Zhang, R., Li, L., Zhang, Q., Zhang, J., Xu, L., Zhang, B., et al. (2024). Differential feature awareness network within antagonistic learning for infrared-visible object detection. *IEEE Trans. Circuits Syst. Video Technol.*, 1. doi:10.1109/TCSVT.2023.3289142

Zhang, X., Wang, Y., Yang, M., and Geng, G. (2021). Toward concurrent video multicast orchestration for caching-assisted mobile networks. *IEEE Trans. Veh. Technol.* 70, 13205–13220. doi:10.1109/TVT.2021.3119429

Zheng, W., Deng, P., Gui, K., and Wu, X. (2023). An Abstract Syntax Tree based static fuzzing mutation for vulnerability evolution analysis. *Inf. Softw. Technol.* 158, 107194. doi:10.1016/j.infsof.2023.107194

Zheng, Z., Yang, Y., Niu, X., Dai, H.-N., and Zhou, Y. (2018). Wide and deep convolutional neural networks for electricity-theft detection to secure smart grids. *IEEE Trans. Ind. Inf.* 14, 1606–1615. doi:10.1109/TII.2017.2785963

frontiers | Frontiers in Energy Research

TYPE Original Research
PUBLISHED 21 May 2024
DOI 10.3389/fenrg.2024.1365735

OPEN ACCESS

EDITED BY
Elżbieta Jasińska,
Wrocław University of Science and Technology, Poland

REVIEWED BY
Minh Quan Duong,
The University of Danang, Vietnam
Matteo Manganelli,
Italian National Agency for New Technologies, Energy and Sustainable Economic Development (ENEA), Italy
Basem Alamri,
Taif University, Saudi Arabia

*CORRESPONDENCE
Mohammed Alghassab,
malghassab@su.edu.sa
Syed Ali Abbas Kazmi,
saakazmi@uspcase.nust.edu.pk

RECEIVED 04 January 2024
ACCEPTED 27 March 2024
PUBLISHED 21 May 2024

CITATION
Raza MK, Alghassab M, Altamimi A, Khan ZA, Abbas Kazmi SA, Ali M and Diala U (2024), Integration of very small modular reactors and renewable energy resources in the microgrid. *Front. Energy Res.* 12:1365735. doi: 10.3389/fenrg.2024.1365735

Integration of very small modular reactors and renewable energy resources in the microgrid

Muhammad Kazim Raza[1], Mohammed Alghassab[2]*, Abdullah Altamimi[3,4], Zafar A. Khan[5,6], Syed Ali Abbas Kazmi[1]*, Majid Ali[1] and Uchenna Diala[7]

[1]U.S.-Pakistan Center for Advanced Studies in Energy (USPCAS-E), National University of Sciences and Technology (NUST), Islamabad, Pakistan, [2]Department of Electrical and Computer Engineering, Shaqra University, Riyadh, Saudi Arabia, [3]Department of Electrical Engineering, College of Engineering, Majmaah University, Al-Majmaah, Saudi Arabia, [4]Engineering and Applied Science Research Center, Majmaah University, Riyadh, Saudi Arabia, [5]School of Computing and Engineering, University of Huddersfield, Huddersfield, United Kingdom, [6]Department of Electrical Engineering, Mirpur University of Science and Technology, New Mirpur City, Pakistan, [7]Department of Electrical and Electronic Engineering, School of Engineering, University of Derby, Derby, United Kingdom

Hybrid microgrids, integrating local energy resources, present a promising but challenging solution, especially in areas with limited or no access to the national grid. Reliable operation of off-grid energy systems necessitates sustainable energy sources, given the intermittent nature of renewables. While fossil fuel diesel generators mitigate risks, they increase carbon emissions. This study assesses the viability of integrating a very small modular renewable energy reactor into a microgrid for replacing conventional diesel generators, substantially curbing greenhouse gas emissions. A comprehensive analysis, including design and economic evaluation, was conducted for an off-grid community microgrid with an annual generation and load of 8.5 GWh and 7.8 GWh, respectively. The proposed microgrid configurations incorporate very small modular reactors, alongside solar, wind, and battery storage systems. MATLAB modeling and simulation across eight cases, accounting for seasonal variations, demonstrate the technical and economic feasibility of case 7. This configuration, integrating modular reactors, photovoltaics, wind turbines, and battery storage, satisfactorily meets load demands. Notably, it boasts a high internal rate of return up to ~31% and a shorter payback period of around 4 years compared to alternative scenarios.

KEYWORDS

photovoltaic, wind turbine, nuclear, battery, microgrid, off-grid

1 Introduction

While fossil fuels still dominate the energy sector, the global demand for energy continues to increase, prompting massive technological advances in the alternative energy industry—including solar, hydropower, nuclear energy, and other renewable sources, as well as advanced energy storage. However, power generation and supply for remote

Abbreviations: ARPA-E, Advanced Research Projects Agency-Energy; BESS, battery energy storage system; DERs, distributed energy resources; DGs, distributed generator; GHGs, greenhouse gases; IRR, internal rate of return; MPPT, maximum power point tracking; MGs, microgrids; SMG, smart microgrid; SPP, simple payback period; NPP, nuclear power plant; NPV, net present value; O&M, operation and maintenance; PV, photovoltaic; P, active power; Q, reactive power; RES, renewable energy sources; SOC, state of charge; vSMR, very small modular Reactors; WT, wind turbine.

communities are still major challenges. The costs of fuel transportation and grid extension are too high for customer-challenging utilities, and there has always been a need to develop a solution for isolated areas to fulfill their energy self-sufficiency with local resources (Lew, 2000). The issue of balancing various competing aspects of power generation, such as capital expenditures, operating costs, emissions, and environmental impact, is a major challenge in realizing this need. To address the global problem of climate change, there has been a growing focus on popular low-carbon energy sources. Renewable energy resources (RER), such as solar photovoltaics and wind power, have low greenhouse gas (GHG) emissions and are also the controlled version of nuclear power plants (Borelli et al., 2016; Bull, 2001). Furthermore, very small modular nuclear reactors (vSMRs) are a new concept for capitalizing power requirements of less than 20 MW, for special applications. The portable version of the smart microgrid (SMG) with vSMRs, and respective inclusion of other energy options, can be used to meet the requirement of off-grid communities (Juan et al., 2024). The compact size and modular design of vSMR make them easily transportable, which makes them suitable for use in microgrid configurations (Juan et al., 2024). Microgrids (MGs) are a new distribution network architecture, based on idea of smart grids that may fully benefit from the integration of a large number of small-scale distributed energy resources and low-voltage power distribution with distributed energy resource (DER) systems (Kuzlu et al., 2017). The MG offers a solution to electrify off-grid areas at a minimal cost rather than adding a traditional cost-intensive infrastructure (Kroposki et al., 2007). Microgrids have two modes—the grid-connected mode, which connects the microgrid to the main grid, and the islanded mode, which isolates the microgrid from the main grid, and in the case of an emergency, it provides a continuous supply of power to the loads (Parhizi et al., 2015). The advantages accredited to MGs include improved power quality and reliability, cost-effectiveness, and carbon emission reduction, particularly using onsite RER (Nwulu and Xia, 2017). The power is supplied to remote area communities by use of photovoltaic (PV), battery energy storage systems (BESS), and a diesel generator, which has been a viable off-grid solution in recent years (Nejabatkhah, 2018).

In MGs, there are different DG units for various RERs, such as solar PV, wind, biomass, fuel cells, and BESS for local loads operating together in harmony, with integrated power electronic controllers and protective devices to feed the load at hand (Meena Agrawal, 2014). The production of RER is highly dependent on local weather and climatic conditions. Non-dispatchable renewable energy's intermittent and stochastic supplies might cause power system instabilities (Denholm and Margolis, 2007; Zahedi, 2011; Khalid and Savkin, 2013; Mahmud and Zahedi, 2016). The RER is a non-controllable and stochastic system and, therefore, requires a BESS, which allows one to store surplus energy during periods when the RER output exceeds the power requirement. The stored power can be reused when the RER is not generating (Roberts and Sandberg, 2011). Storage is predicted to be a critical component of future smart grids (Cosentino et al., 2011; Denholm and Hand, 2011; Roberts and Sandberg, 2011). Therefore, nuclear vSMR can be implemented for clean environments and applications, including those that require both electrical and thermal power sources, since its carbon footprint is very nominal (Iyer et al., 2014).

These reactors may provide baseload energy generation regardless of weather, and they could be linked to a central or distributed grid or run independently. Combining a renewable energy resource (hybridization) with an energy storage system will increase the reliability and stability of the supplied energy. Several articles have discussed the installation of storage, the hybridization of power plants and microgrid power systems at various locations, and their associated components, methods, criteria, and aims. The impact of aging for the entire system is considered, rather than just a single component, which makes the long-term study of an energy system less trustworthy. The simulation process for the operation of the energy system flow and use of optimal component capacity across a year has been conducted for economic evaluations of these systems, aiming at minimizing the payback time. The simulations were run using the average yearly months of meteorological and environmental data. The usage of a supercapacitor module might feed, quickly, peaks in the electrical load, considerably increasing energy self-consumption and self-sufficiency (Hassan, 2020; Ceran et al., 2021; Hassan et al., 2022).

The limitation in previous research is that RERs, such as solar PV and wind, are not better options for running baseload due to their variability and intermittent nature. Fossil fuel-based generators are also used for baseload, which compounds the climate issues. The power delivered to isolated areas via the utility grid is subjected to high financial constraints for transmission lines and infrastructures, which are compounded with high system losses. The population in such isolated areas is dispersed and usually has low income, which makes the recovery of the installed infrastructure very difficult. To handle all these problems, vSMR is the best option to use for base power plants, as it will enable the provision of a sustainable power supply.

The purpose of this study is to formulate and implement RERs, BESS, and vSMR for off-grid communities and evaluate whether the integrated vSMR with renewables in MGs has the technological and economic capacity to replace typical diesel generators, resulting in considerable reductions in GHG emissions. The power generated by these resources are managed well to ensure that reliable power is supplied to the connected loads in an MG. The proposed solution of MGs will also reduce the stress on the transmission grid as well as minimize carbon emissions to the environment.

2 The architecture of the microgrid system

In this study, a typical MG consists of sources such as vSMR, a solar PV system, a wind turbine system (WTS), and a BESS, as shown in Figure 1A. For the simulation of the electric load, wind speed, and solar irradiance, data are available on NREL National Solar Radiation Database (NSRDB) and G. W. Atlas, "Global Wind Atlas" (NREL, 2019; Atlas, 2019). A vSMR, PV, and a wind turbine are used to meet the electrical demand of Nawabshah. The MG is not stable without a BESS to store the electrical energy because RERs are naturally intermittent. The surplus electrical energy will be stored in a BESS to meet the electrical demand and will be discharged as per requirements.

2.1 MATLAB and Simulink model

A microgrid operating at 11 kV is developed in Simulink, as shown in Figure 1B. It is observed that the following units—vSMR, PV, wind, and BESS, are integrated together to achieve the desired system.

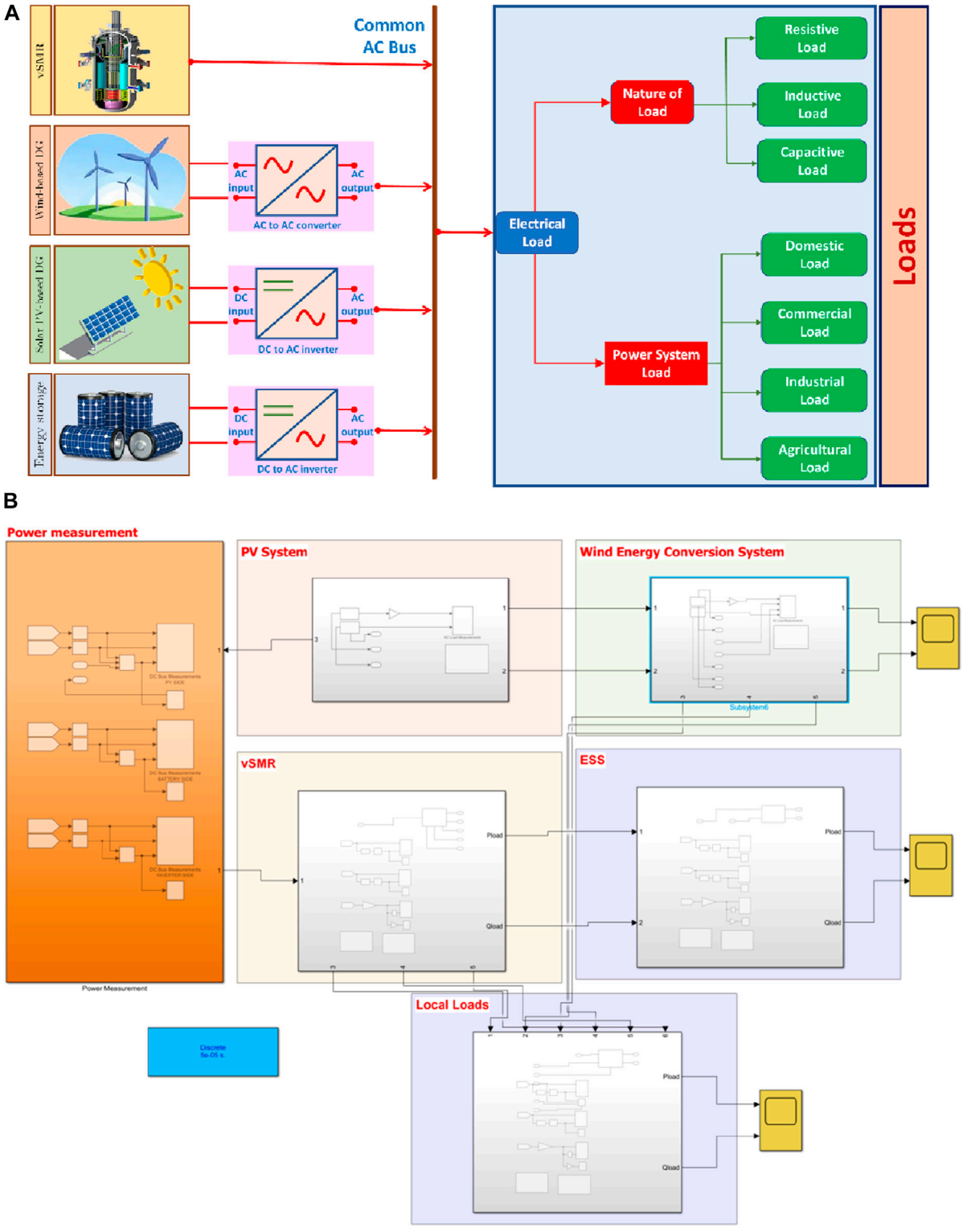

FIGURE 1
(A) System architecture of a vSMR-based MG (Arafat and Van Wyk; Acen et al., 2021; Douglas and Proprietary; incore, 2016). **(B)** MATLAB/Simulink test system with integrated vSMR, PV, and wind turbines.

TABLE 1 Illustration of the test cases.

Case	VSMR	PV	Wind	BESS
0	✓	×	×	×
1	✓	✓	×	×
2	✓	×	✓	×
3	✓	×	×	✓
4	✓	✓	×	✓
5	✓	×	✓	✓
6	✓	✓	✓	×
7	✓	✓	✓	✓

2.2 Illustration of the test cases

In this study, an annual seasonal variation is considered, which includes four seasons—winter, spring, summer, and autumn. Eight cases are developed to simulate the model for different scenarios, as shown in Table 1. Table 1 presents several simulated scenarios used to highlight the vSMR that is used as the baseload, while other resources are turned on and off.

3 System modeling

3.1 System load profile

The load data are collected for Nawabshah in Pakistan. To decrease the computational load, the daily demand profile for each month is considered to be the same. The real-time simulation has 8,760 h in a year. The simulation with 8,760 data points takes approximately 90 times as long as the analysis with 96 data points. Furthermore, the sensitivity analysis performed in this research necessitates running the simulation many times. As a result, each month's hour-by-hour average for each day was used to create the 24 data points for each month and then take the average hour-by-hour for each month of the season. The average for winter is the same as 16 January 2021, the spring average is same as 3 April 2021, and the summer average is the same as 7 June 2021, and that for the autumn season is same as 5 October 2021, resulting in the simulation using 96 data points (4 seasons 1 day/month 24 h/day) rather than 8,760 data points (Ko and Kim, 2019). The daily demand profile (24 data points) for January was the same throughout the month, while the daily load demands for the other three seasons were not the same, as shown in Figure 2.

3.2 Microgrid components

3.2.1 Very small modular reactors (vSMR)

According to the US Energy Department's Advanced Research Projects Agency-Energy (ARPA-E), the vSMR is rated below 10 MWe (World Nuclear Association, 2019). The vSMR can operate in both baseload and load-following modes. At its maximal capacity, the baseload vSMR always offers a constant power level. Load-following vSMR, on the other hand, adjusts its output in response to variations in system demand, over time (Lewis et al., 2016). The following is a list of vSMRs that are still in the developmental stage. The capital cost of vSMRs depends on the amount of generated electricity. The vSMR fuel cost is included in the "fuel cost"; hence, it is not included in the refilling cost. The cost of operation, maintenance, and fuel is unaffected by the amount of power generated. As a result, load-following, which reduces the power output, is not cost-effective (Locatelli et al., 2015). On the other hand, the functioning of a base-load plant is simple; it always

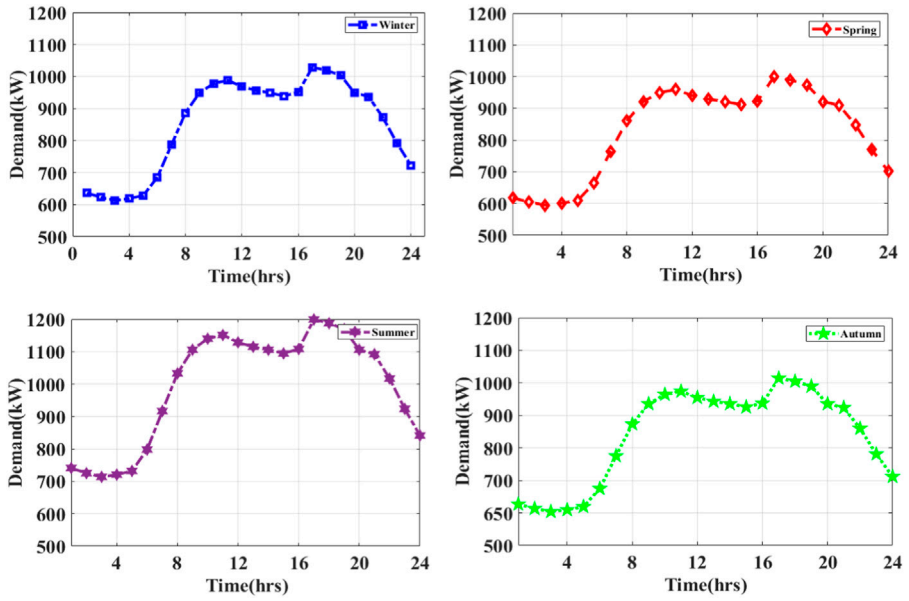

FIGURE 2
Electrical demand for Nawabshah.

TABLE 2 vSMR standard capacities across the globe (Nichol and Desai, 2019).

S#	vSMR model	Capacity (MWe)	Developer
1	eVinci	0.2–5	Westinghouse, United States
2	NuScale micro	1–10	NuScale, United States
3	Aurora	1.5	Oklo, United States
4	SEALER	3–10	LeadCold, Sweden
5	Holos Quad	3–13	HolosGen, United States

supplies the same amount of power during an interval of time. In this study, a vSMR rated at 1 MWe is considered for an MG is shown in Table 2, and specifications are shown in Table 3 (Nichol and Desai, 2019).

3.2.2 Solar power

The seasonal irradiance data are considered for the PV system. Each season's resource data are represented by 24 data points. The hour-by-hour average for each day was used to create the 24 data points for each month, and then the average hour-by-hour for each month of the season was taken. The average for winter was taken on 16 January 2021; for spring, it was taken on 3 April 2021; for summer, it was taken on 7 June 2021; and for autumn, it was taken on 5 October 2021. To get the first data point of January (among 24 data points), the first-hour data point of each day (total of 31 days) was collected and averaged. Similarly, the average of each second-hour data point of each day (total of 31 days) of January was the second resource data point (among 24 data points), as shown in Figure 3A. The amount of solar electricity generated is determined by the surface area of PV panels, solar irradiation, and ambient temperature. The PV panel's capital cost, replacement cost, O&M cost, and lifetime are 1,200 $/kW (Canada Energy Regulator, 2020), 1,000 $/kW (Canada Energy Regulator, 2020), 12 $/kW/Year (IEA, 2020a), and 25 years (Engineering, 2020), respectively.

The total extracted power by solar PV panels is calculated using Eq. 1 (Malik et al., 2020).

$$P_{\mathrm{pv}}(t) = \left[\frac{R_p}{1000}\right] * P_{\mathrm{pv,rated}} * \eta_{pv,MPPT}. \quad (1)$$

Here, R_p denotes perpendicular radiations measured in (W/m^2) at the surface of the PV array, $\eta_{pv,MPPT}$ denotes the efficiency of the PV system's DC/DC converter at maximum power point tracking (MPPT), and $P_{\mathrm{pv,rated}}$ is the rated power of each PV array at R_p = 1000 W/m^2. It is observed in Figure 3A that PV generation is maximum in the spring season, followed by the summer season and the autumn season, and is least during the winter season, across the whole year.

3.2.3 Wind power

For simulation purposes, the resource data of wind speed and the average solar irradiance are considered for each season. The wind speed is used to calculate the mechanical and electrical power, as shown in Eqs 2, 3 (Murty and Kumar, 2020). The WT's capital cost, replacement cost, O&M cost, and lifetime are 1,130 $/kW (Canada Energy Regulator, 2020), 1,130 $/kW, 48$ kW/year (IEA, 2020b), and 25 years (Mone et al., 2015), respectively.

$$\begin{cases} 0 & V < V_{cut,in} \quad V > V_{cut,0} \\ P_W = P_n(V) & V_{cut,in} < V < V_r \\ 1 & V_r < V < V_{\max} \end{cases}. \quad (2)$$

The wind is the primary source of power for wind turbines, and its mechanical power is proportional to the speed and direction of the wind, as shown in Eq. 2. Due to several system component losses, mechanical power cannot be translated completely into electrical power. To account for these losses, mechanical power is multiplied by the generator's efficiency to obtain electrical power, as shown in Eq. 3. The data of wind speed are shown in Figure 3B.

$$P_w(t) = \eta \cdot P_w. \quad (3)$$

3.2.4 BESS

The power of both solar PV systems and wind turbines changes as the weather varies. They will require supplemental resources, such as an auxiliary service, to deal with these variations. The BESS acts as an additional service, modulating active power to manage the frequency and minimize frequency deviation caused by abrupt changes in the RES. Emergency consumption (Ee) in Eq. 6 indicates the unexpected load that was neither scheduled nor controlled by the battery. If a planned load is unexpectedly disconnected, the battery will be charged. Furthermore, battery charging and discharging are stated in Eqs 5, 6 (Murty and Kumar, 2020). The BESS capital cost, replacement cost, operating and maintenance costs, and lifetime are 398 $/kWh, 398 $/kWh, 10 $/kW/Year, and 5 years, correspondingly (Kharel and Shabani, 2018).

The BESS's capability is determined by the electrical demand and supply of energy hours in a day. The battery bank capacity (kWh) is estimated using the following equations (Borhanazad et al., 2014):

TABLE 3 Specifications of the vSMR (Nichol and Desai, 2019).

Parameter	Value	Parameter	Value
Reactor size (kWe)	1,000	Refueling cost of the fuel module ($)	20 million
Plant lifetime (years)	40	Core lifetime (years)	10
Overnight capital cost ($/kWe)	15,000	Decommissioning cost ($/MWh)	5
Fixed O&M cost ($/kWe)	350	Capacity factor (%)	95
Fuel cost ($/MWh)	10	Plant efficiency (%)	40

$$P_{batt} = P_{Load} - (P_{vSMR} + P_{PV} + P_{wind}), \quad (4)$$

$$P_{batt_{ch}} = P_{ch}(t) \quad \text{if} \quad \begin{cases} P_{gen} < P_{load} \\ C_{source}(t) = \min(C_{source}(t)) \end{cases}, \quad (5)$$

$$P_{batt_{ch}} = P_{dis}(t) \quad \text{if} \quad \begin{cases} P_{gen} < P_{load} \\ C_{source}(t) = \min(C_{source}(t)), \\ Ee = 0 \end{cases} \quad (6)$$

$$\text{Subject to } SOC_{\min} < SOC < SOC_{\max}. \quad (7)$$

where $P_{batt_{ch}}$ and $P_{batt_{dis}}$ denote battery charging and discharging, respectively. P_{gen} denotes the total generation of the system, whereas P_{load} denotes the total load of the system. *SOC* stands for the state of charge of the battery which can be determined from the battery shown in Eq. 7.

4 Economic analysis

The financial analysis described in this article is concerned with the evaluation of the vSMR, renewable energy, and BESS installation project, in terms of budget and financial elements, which are used to determine the project's investment viability. In this study, financial analysis is carried out by using the System Advisor Model (SAM) software. The cash flow for year n is represented by C_n, which is the difference between the cash input in year n (C_{in},n) and the cash outflow in year n. According to Eqs 8–10, (C_{out},n) is used to calculate C_n and may be used to determine these cash flows.

$$C_n = C_{in,n} + C_{out,n}, \quad (8)$$

$$C_{out,n} = C_{O\&M} + C_{per} \cdot (1 + r_i)^n, \quad (9)$$

$$C_{in,n} = C_{ener}, \quad (10)$$

where n denotes the debt duration in years and r_i denotes the inflation rate. The yearly cost of operation and maintenance is also indicated as $C_{O\&M}$. C_{per} denotes the monthly expenses, or system credits, whereas *C* denotes the total beginning cost. C_{ener} is the yearly revenue generated by energy savings.

4.1 Simple payback period–SPP

The simple payback period is the time taken for the cash flow to match the total venture capital as given in Eq. 11, where C is the project's capital cost, C_{income} is the income cost, and $C_{O\&M}$ is the operational and maintenance cost.

$$SPP = \frac{C}{C_{income} - C_{cost}} = \frac{C}{C_{ener} - C_{O\&M}}. \quad (11)$$

4.2 Net present value–NPV

A project's net present value is the difference between its discounted. As indicated in the equation 12, it is determined by discounting all cash flows.

$$NPV = \sum_{n=0}^{K} \frac{C_n}{(1+r)^n}, \quad (12)$$

where r is the project's discount rate and Cn is the cash flow after taxes in n years.

4.3 Internal rate of return–IRR

The IRR is the discount rate that results in a zero NPV for the project and is computed by using Eq. 13

$$\sum_{n=0}^{K} \frac{C_n}{(1+IRR)^n} = 0, \quad (13)$$

where C_n denotes the cash flows. The IRR, also known as the economic rate of return, is the rate of return used in capital planning to measure and analyze investment profitability. IRR estimations are frequently used to evaluate the feasibility of investments and projects. The greater the project's IRR, the more likely it is to be completed (Investopedia, 2021).

5 Results and discussion

There are various scenarios simulated in MATLAB. The vSMR is used as a base, and other resources turn on and off. The results of all cases are compared one by one for each season. This study considers 4 months for the winter season—January, February, November, and December. For spring, 2 months, March and April, are considered. For summer, 4 months, May, June, July, and August, are considered. Finally, for the autumn season, 2 months, September and October, are considered.

5.1 Case 0: base case

For the base case, the load demand is supplied by only vSMR, and it supplies constant power to the off-grid communities. Figure 4A shows the load demand curve for different seasons, and the vSMR curve is the total output power of vSMR, during each time interval. The load demand increased from 03:00 to 11:00 and 15:00 to 17:00 in all seasons. The average load demand is highest during the summer season, while the lowest load demand is measured during the spring season.

Figure 4B shows the balance power available after the load demand was fulfilled by vSMR. The maximum surplus power of 96 kW is available in the system, from 01:00 to 06:00, except for the summer season. The maximum power load demand increases to 500 kW, from 07:00 to 22:00, in the summer season. Therefore, the base power cannot meet the load demand as the power supplied to the microgrid is constant.

5.2 Case 1: addition of the renewable resources

In this case, the load demand is fulfilled by vSMR and the solar PV system. The output power of the solar PV varies as it depends on the solar irradiance, while vSMR generates constant power to off-grid communities. Figure 4C shows the load demand requirement

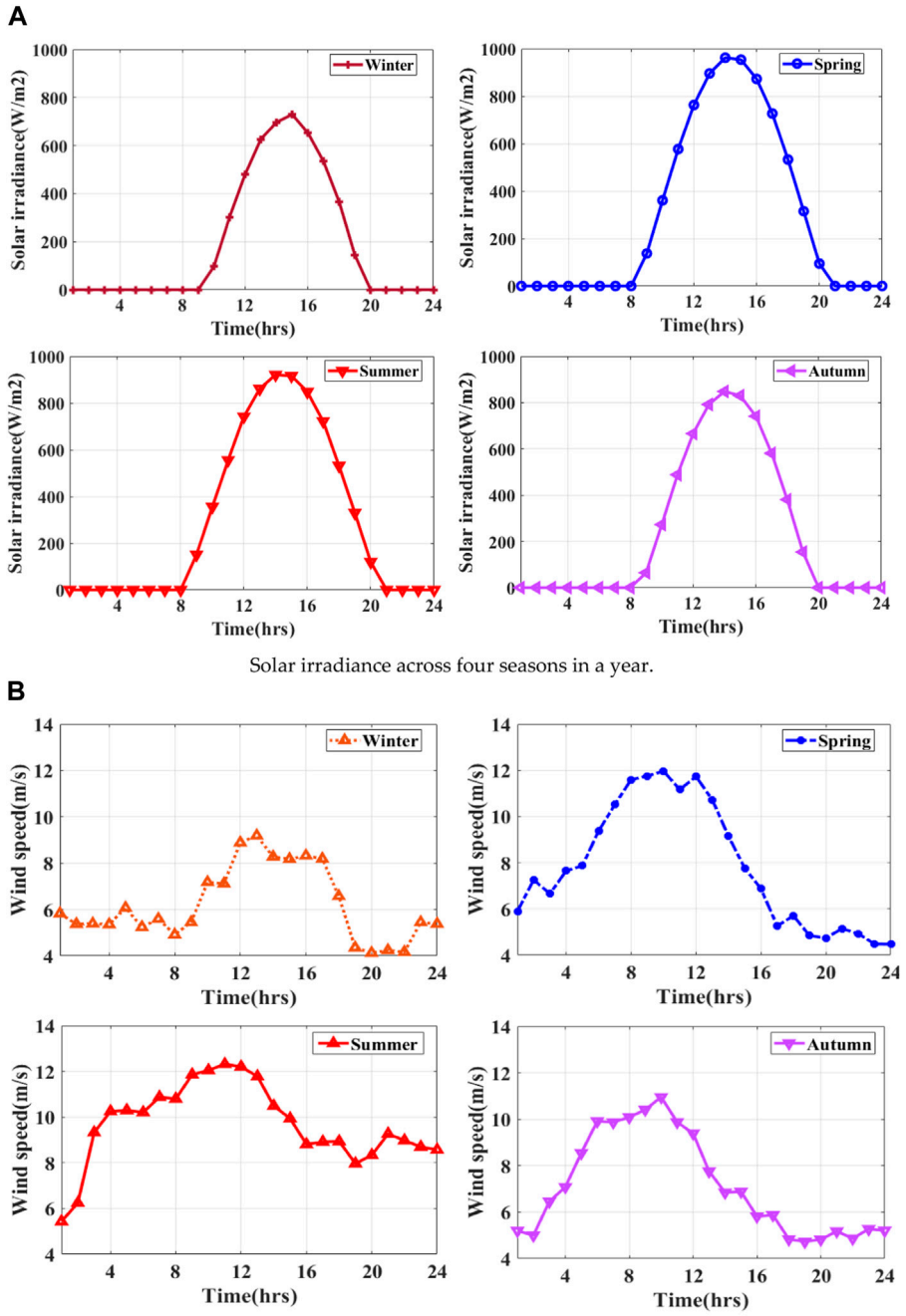

FIGURE 3
(A) Solar irradiance across four seasons in a year. **(B)** Wind speed across four seasons in a year.

for different seasons such as winter, spring, summer, and autumn, while the curve for vSMR and solar PV is the total output power of the system during each time interval. The load demand increased from 03:00 to 11:00 and 15:00 to 17:00 in all seasons. The average load demand is highest during the summer season, while the lowest load demand is measured during the spring season. The output power of solar PV varies from 09:00 to 19:00 as solar irradiance is available during the day. The maximum power extracted from the solar PV system is 568 kW at 15:00 during the spring season.

Figure 4D shows the balance of power available after the load demand was fulfilled by the vSMR and solar PV system. However, when the solar PV is integrated with vSMR, the maximum surplus power of 350 kW is available, from 01:00 to 06:00 and 11:00 to 18:00, during the spring season and the deficit of 390 kW, from 07:00 to 12:00 and 18:00 to 24:00, in the summer season. However, the surplus of 350 kW is due to the solar PV system from 13:00 to 17:00. Moreover, when the solar PV system is injected into the system, the required power is reduced from 500 kW to 350 kW, as compared to case 0.

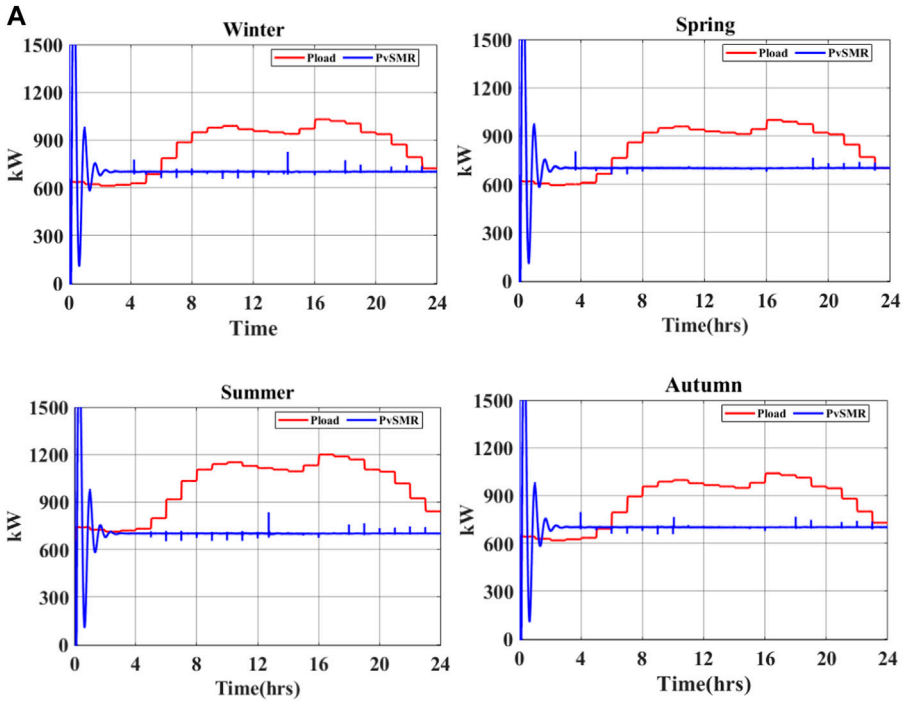

FIGURE 4
(Continued).

5.3 Case 2: vSMR and wind-based renewable resource only

In this case study, the microgrid provides the load demand by integrating vSMR and wind turbines. The output power of wind turbines varies as it depends on wind speed, while the vSMR supplies constant power to off-grid communities. Figure 4E shows the load demand requirement for various seasons and the total individual output power produced by vSMR and wind turbines during each time interval. The load demand increases from 03:00 to 11:00 and 15:00 to 17:00, throughout the year. The average power of a wind turbine is 180 kW, and the maximum power generated by the wind turbine is 243 kW at 13:00 during the summer season.

Figure 4F shows that when vSMR and wind turbine are integrated, the maximum surplus power of 235 kW is available in the system from 01:00 to 06:00 in the winter season, due to less load demand, as industry and markets are closed, while the system faces a shortage of power of 320 kW from 08:00 to 23:00 in the summer season, although the maximum shortage of power in summer is due to the maximum load demand as compared to other seasons. Moreover, when a wind turbine is injected into the system, the

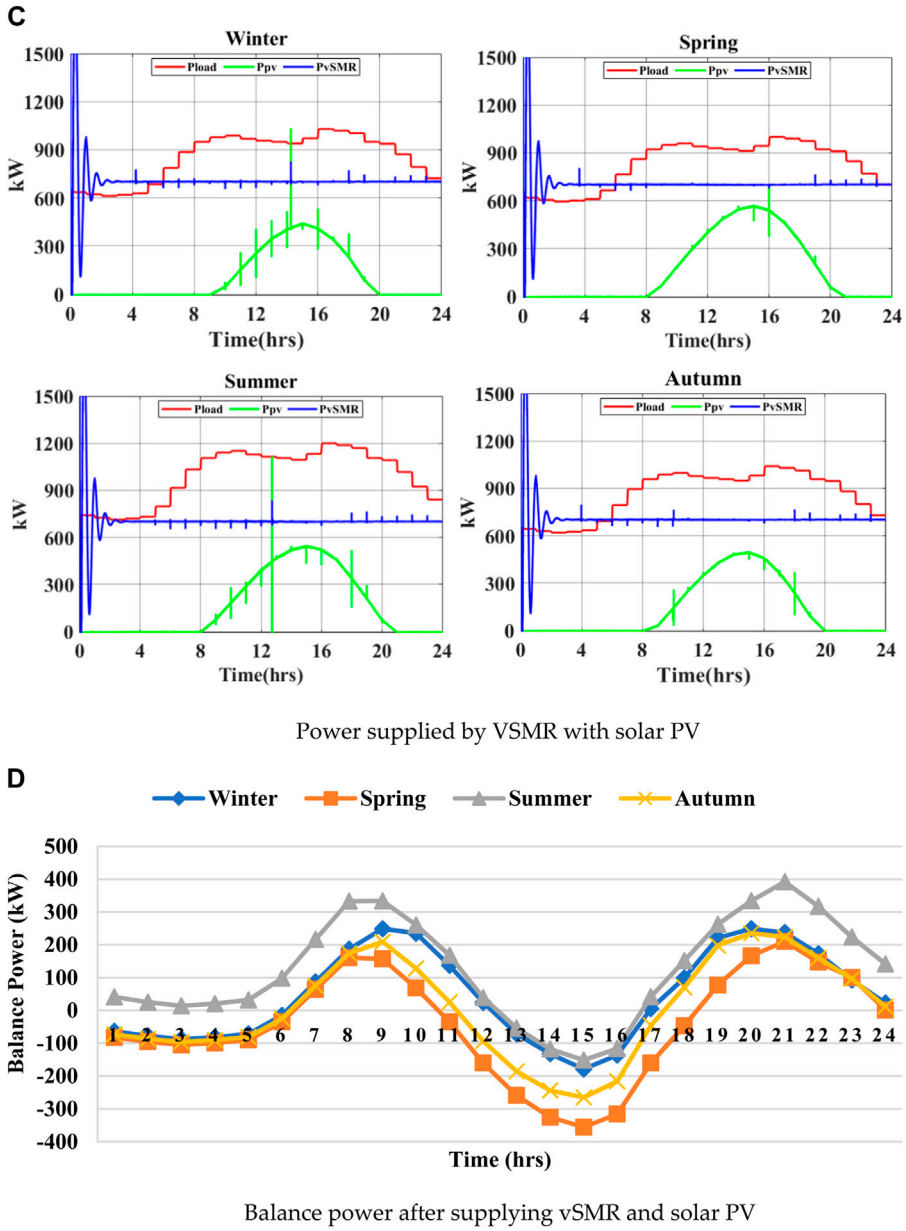

FIGURE 4
(Continued).

trend is the same, but the required power is reduced because the wind speed is available throughout the year. In addition, there is a shortage of power during the winter and summer seasons from 08: 00 to 23:00 and from 09:00 to 23:00 during the spring and autumn seasons.

5.4 Case 3: vSMR and BESS only

In this case, only vSMR with the BESS topology is implemented to meet the load demand, and it provides constant power to off-grid communities. Figure 4G depicts the load demand curve for several seasons, with the curve representing the total output power of vSMR and SOC of BESS for each time interval. In all seasons, the load demand increased from 03:00 to 11:00 and 15:00 to 17:00. The summer season has the highest average load demand, whereas the spring season has the lowest load demand. Except during the summer season, surplus electricity is stored in the BESS from 01:00 to 06:00 and provided to the load from 07:00 to 09:00. Figure 4H depicts the available balance power after the load demand has been met by vSMR with the BESS. However, the shortage of power is during 06:00 to 24:00 in the summer season, 09:00 to 23:00 in the winter season, 09:00 to 23:00 in the autumn season, and 10:00 to 23:00 in the spring season. During the summer season, the maximum power required to fulfill the load demand

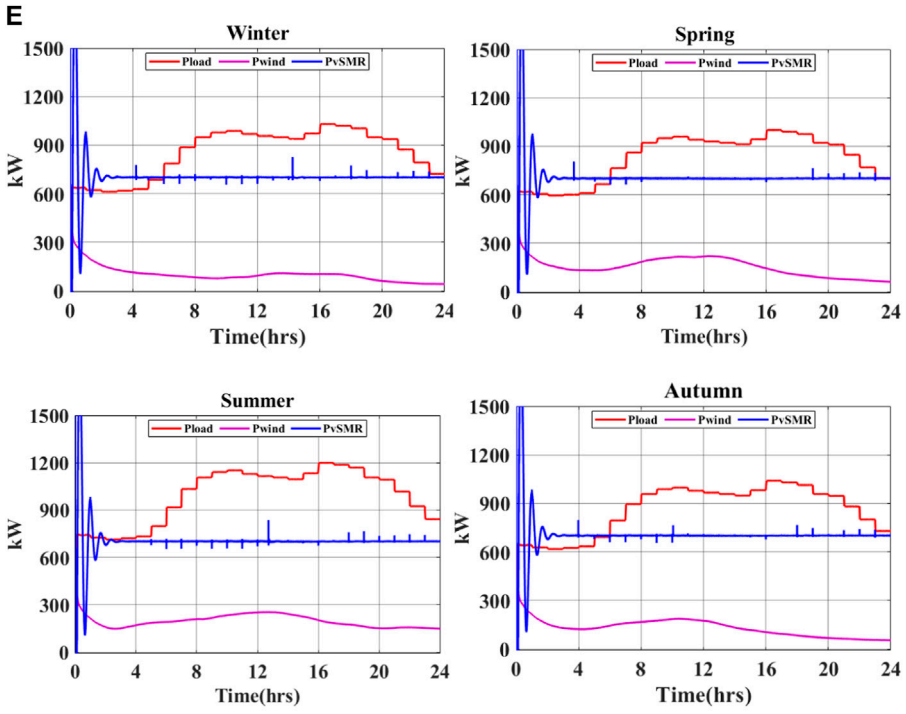

FIGURE 4
(Continued).

is increased to 500 kW from 06:00 to 24:00. Thus, the consistent power supplied to the microgrid's base power with the BESS has been unable to match the load requirement.

5.5 Case 4: vSMR, solar PV, and BESS only

In this case, vSMR and solar PV with BESS topology is implemented to meet the load demand. The solar PV output power varies due to solar irradiation, whereas vSMR provides consistent electricity to off-grid populations. Figure 4I depicts the load demand required for various winter, spring, summer, and fall seasons, with the curve representing the total individual output power of vSMR, solar PV, and BESS at each time interval. In all seasons, load demand increased from 03:00 to 11:00 and 15:00 to 17:00. The summer season has the highest average load demand, whereas the spring season has the lowest load demand. Except for summer, electricity is in excess from 01:00 to 06:00, with the next surplus power in the system when extracted power from solar PV is provided into the system. The excess electricity, on the other hand, is stored in the BESS and used to power the load. The solar PV output power fluctuates from 09:00 to 19:00 according to available solar irradiation

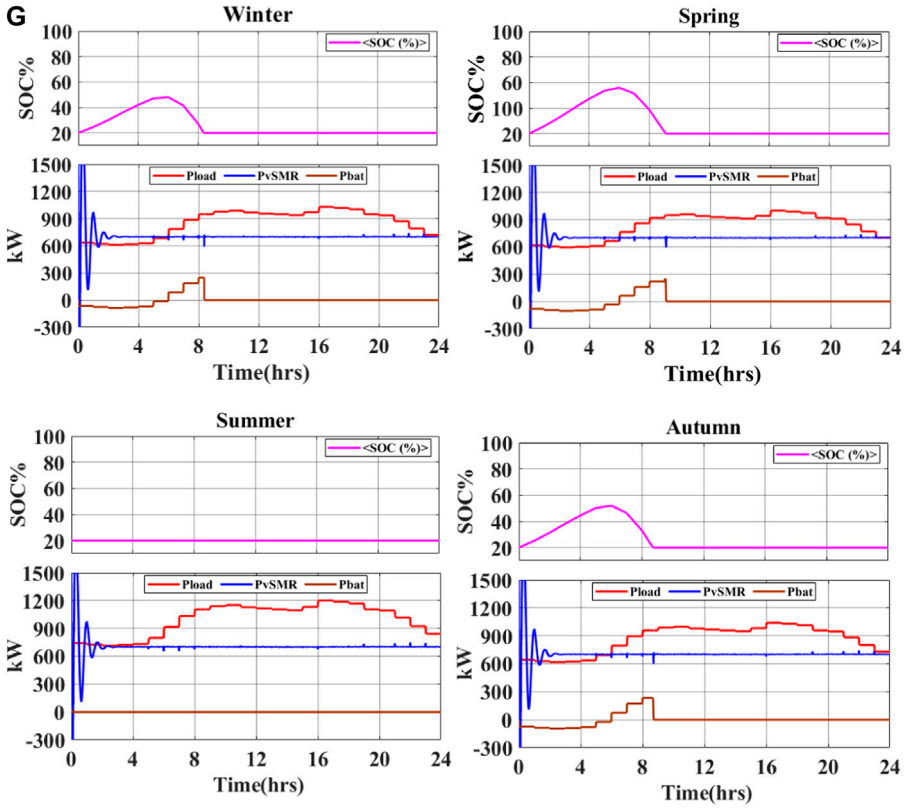

FIGURE 4
(Continued).

during the day. During the spring season, the greatest power extracted from the PV system is 568 kW at 15:00.Furthermore, the BESS stores surplus electricity from 01:00 to 06:00 and 13:00 to 16:00 in the winter season, 01:00 to 06:00 and 11:00 to 14:00 in the spring season, 13:00 to 16:00 in the summer season, and 01:00 to 06:00 and 12:00 to 17:00 in the autumn season. Additionally, during the winter season, BESS is provided to load from 07:00 to 08:00 and 17:00 to 19:00, during the spring season from 07:00 to 10:00 and 19:00 to 24:00, during the summer season from 17:00 to 19:00, and during the fall season from 07:00 to 08:00 and 18:00 to 22:00.

Figure 4J depicts the available balance power after the load demand has been met by the vSMR and solar PV system with BESS, when solar PV and BESS are integrated with vSMR in the microgrid. Despite this, the spring season fulfills the load demand throughout the season and has excess electricity from 15:00 to 18:00. Furthermore, the fall season has excess power from 16:00 to 17:00 but a shortage of electricity from 09:00 to 11:00 and 23:00 to 24:00. Furthermore, while summer and winter have the same surplus and deficit power trends, the duration and quantity of electricity required have changed. Moreover, the shortage of power is during 06:00 to 11:00 and 20:00 to 24:00 during the summer season, with a maximum deficiency power of 390 kW. During the winter season, the shortage of power is during 09:00 to 12:00 and 20:00 to 24:00, with a maximum shortage of over 250 kW.

10.3389/fenrg.2024.1365735

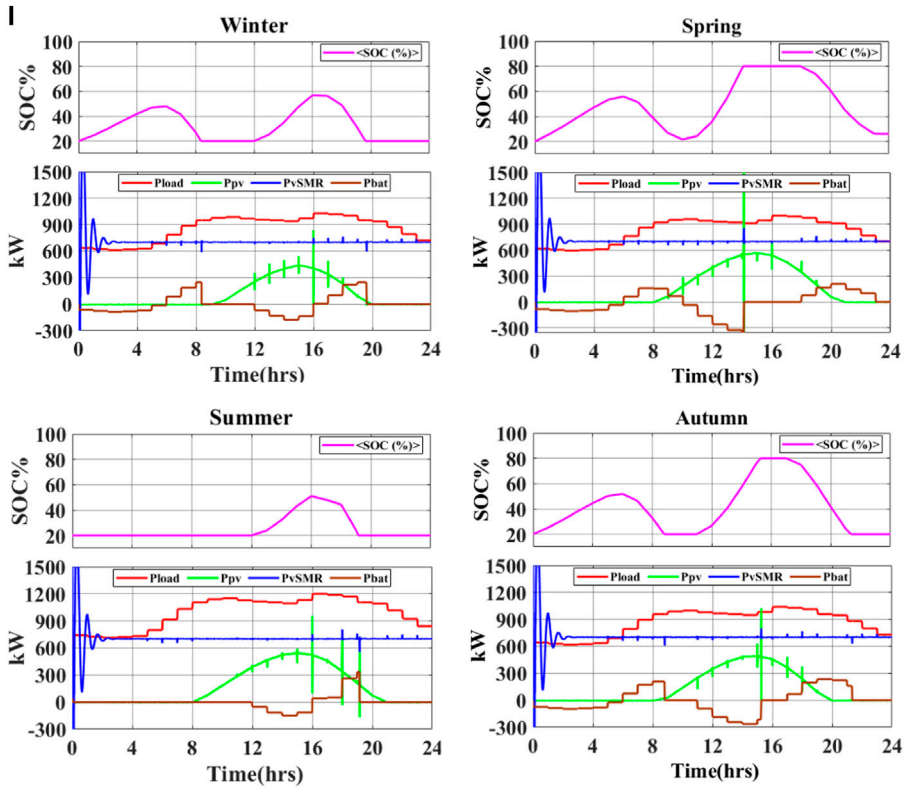

FIGURE 4
(Continued).

5.6 Case 5: vSMR, wind turbine, and BESS only

In this case, vSMR and wind turbines with BESS topology are implemented to meet the load demand. The wind turbine output power varies with wind speed, whereas vSMR provides steady electricity to off-grid populations. Figure 4K depicts the load demand required for various winter, spring, summer, and fall seasons, with the curve representing the total individual output power for the vSMR and wind turbine at each time interval. In all seasons, the load demand increased from 03:00 to 11:00 and 15:00 to 17:00.

The summer season has the highest average load demand, whereas the spring season has the lowest load demand. In addition, during the summer season, the maximum power extracted from the wind turbine is 243 kW at 13:00. Because wind is accessible all year, the output power of wind turbines is available at all times. In addition, during the winter season, BESS reserves surplus electricity from 01:00 to 04:00, during the spring season from 01:00 to 03:00 and 24:00, during the summer season from 01:00 to 06:00, and during the fall season from 01:00 to 04:00 and at 24:00. Furthermore, BESS is provided to load from 07:00 to 11:00 in the winter season, 09:00 to 18:00 in the spring season, 07:00 to 10:00 in the summer season, and 08:00 to 15:00 in the fall season.

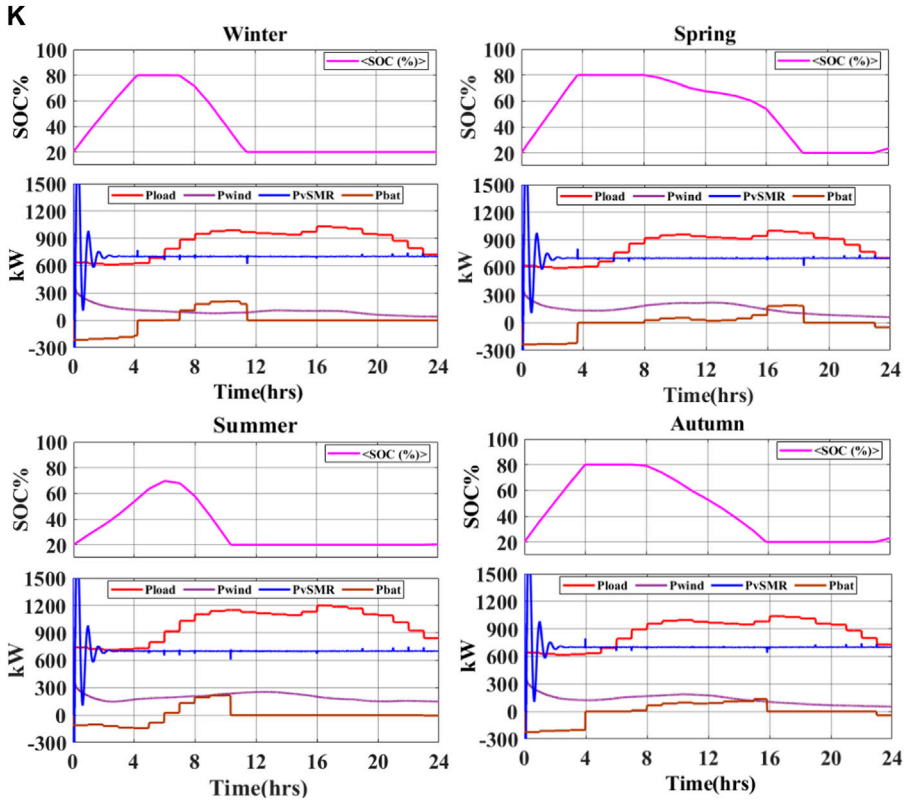

FIGURE 4
(Continued).

Figure 4L depicts the remaining power available after vSMR and wind turbine with BESS have met the load requirement, when the wind turbine and BESS are integrated with vSMR in the microgrid. However, excess electricity is accessible from 05:00 to 06:00 during the winter season, 04:00 to 08:00 during the spring season, and 05:00 to 7:00 during the fall season. Moreover, the system has a power deficit from 12:00 to 23:00 during the winter season, 19:00 to 23:00 during the spring season, 11:00 to 23:00 during the summer season, and 16:00 to 23:00 during the fall season.

5.7 Case 6: vSMR, solar PV, and wind turbines only

In this case, vSMR, solar PV, and wind turbine (WT) topology is implemented to meet the load demand. The solar PV and wind turbine output power varies due to solar irradiation and wind speed, respectively. However, vSMR provides consistent electricity to off-grid populations. Figure 4M depicts the load demand requirements for various seasons such as winter, spring, summer, and fall, whereas the curves for vSMR, solar PV, and

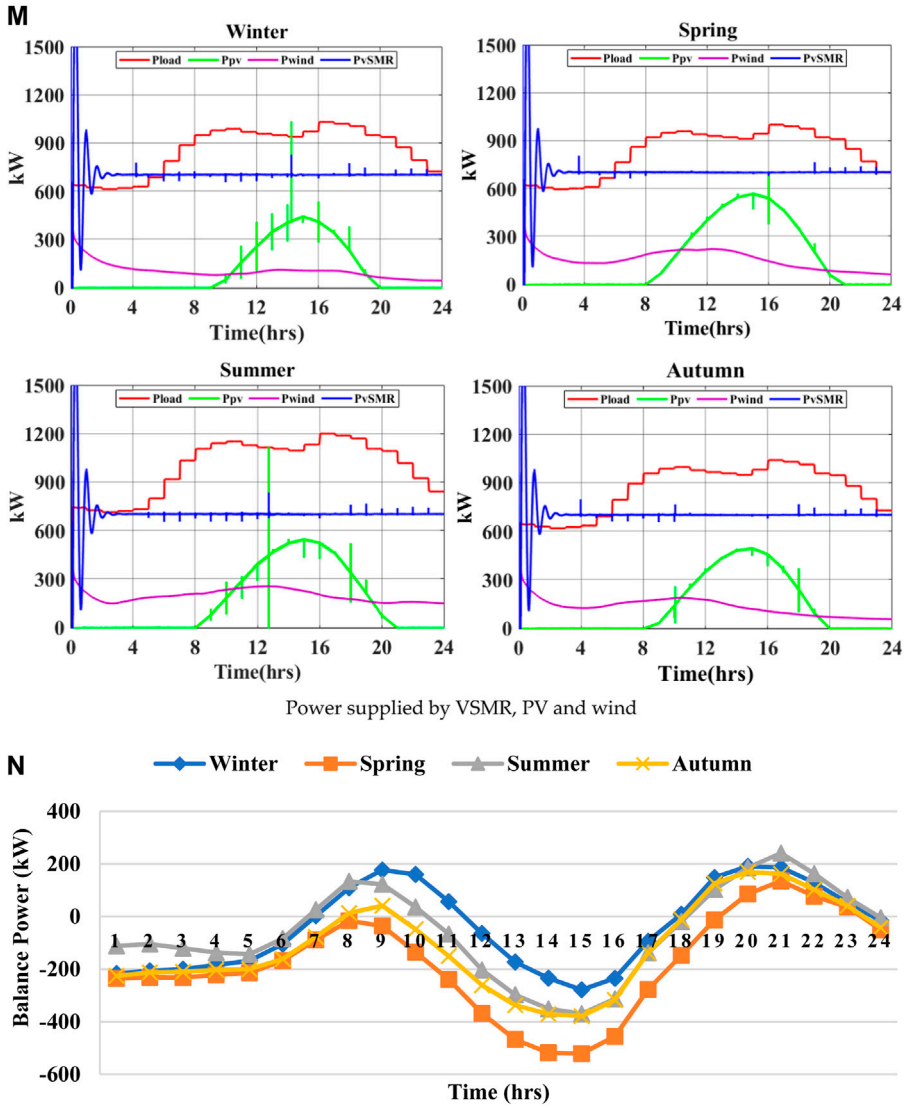

FIGURE 4
(Continued).

wind turbine represent the total output power of the system at each time interval.

In all seasons, the load demand increased from 03:00 to 11:00 and 15:00 to 17:00. The summer season has the highest average load demand, whereas the spring season has the lowest load demand. The output power of solar PV fluctuates from 09:00 to 19:00 because solar irradiance is available throughout the day, but the output power of wind turbines is accessible all year since wind is available. During the summer season, the maximum power taken from the solar PV is 568 kW at 15:00, while the greatest power extracted from the wind turbine is 243 kW at 13:00.

Figure 4N depicts the remaining power after vSMR, solar PV, and wind turbines have met the load requirement. When the solar PV and wind turbine systems are integrated with vSMR, the maximum surplus power of 520 kW is available from 01:00 to 19:00 and at 24:00, during the spring season, and deficit power of 240 kW from 07:00 to 11:00 and 19:00 to 23:00, during the summer season. However, there is a surplus power of 520 kW as a result of the WT and PV systems. Furthermore, when WT and PV systems are fed into the system, the shortage of power drops from 500 kW to 240 kW when compared to the base case.

5.8 Case 7: vSMR, solar PV, and wind turbines with BESS

In this case, the load demand is fulfilled by vSMR, solar PV, and wind turbines with BESS. The solar PV and wind turbine output power varies due to solar irradiation and wind speed. However, vSMR provides consistent electricity to off-grid populations. Figure 4O depicts the load demand requirements for winter, spring, summer, and fall seasons, whereas the curves for vSMR, solar PV, wind turbine,

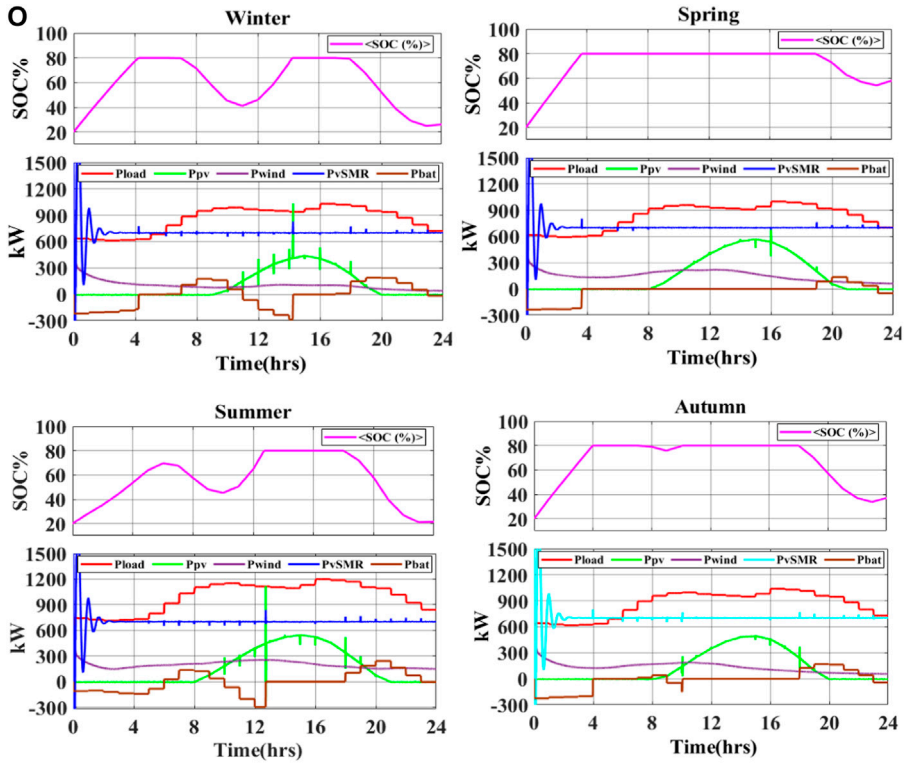

Power supplied by VSMR, solar PV and wind turbine with BESS

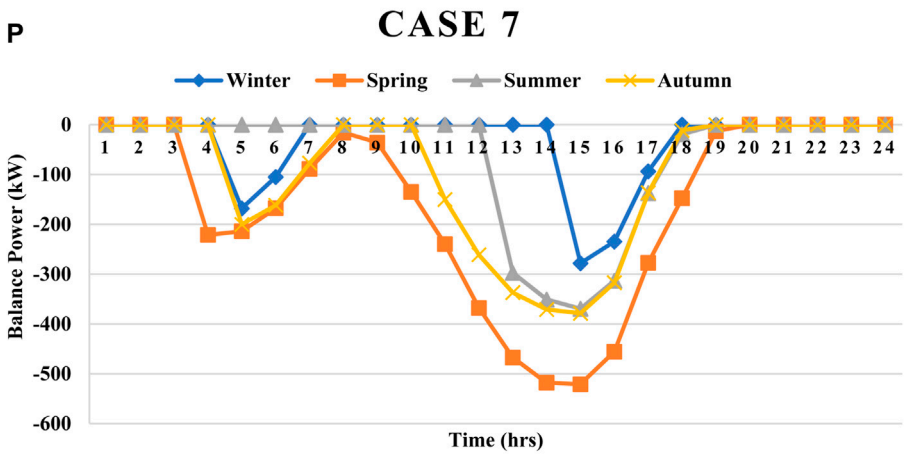

Balance power after supplied by vSMR, solar PV and wind turbine with BESS

FIGURE 4
(Continued).

and BESS represent the total output power of the system at each time interval.

In all seasons, load demand increased from 03:00 to 11:00 and 15:00 to 17:00. Summer has the highest average load demand, whereas spring has the lowest load demand. The output power of solar PV fluctuates from 09:00 to 19:00 because solar irradiance is available throughout the day, but the output power of WT is accessible all year since wind is available. Furthermore, during the summer season, BESS reserves surplus electricity from 01:00 to 04:00 and 20:00 to 23:00 while supplying power to load from 07:00 to 10:00 and 19:00 to 23:00. During the spring season, the maximum power taken from PV is 568 kW at 15:00, while the maximum power extracted from WT is 243 kW at 13:00 during the spring season.

Figure 4P depicts the remaining power available after vSMR, solar PV, and wind turbines have met the load requirement, when solar PV, wind turbines, and BESS are integrated with vSMR in the microgrid. Although it fulfilled the load demand and has excess electricity throughout the year, there is no power shortfall. In addition, the excess electricity is available from 05:00 to 06:00 and 15:00 to 17:00 in the winter season, 04:00 to 19:00 in the spring season, 13:00 to 18:00 in the summer season, and 11 h in the autumn season from 05:00 to 07:00 and 11:00 to 18:00.

10.3389/fenrg.2024.1365735

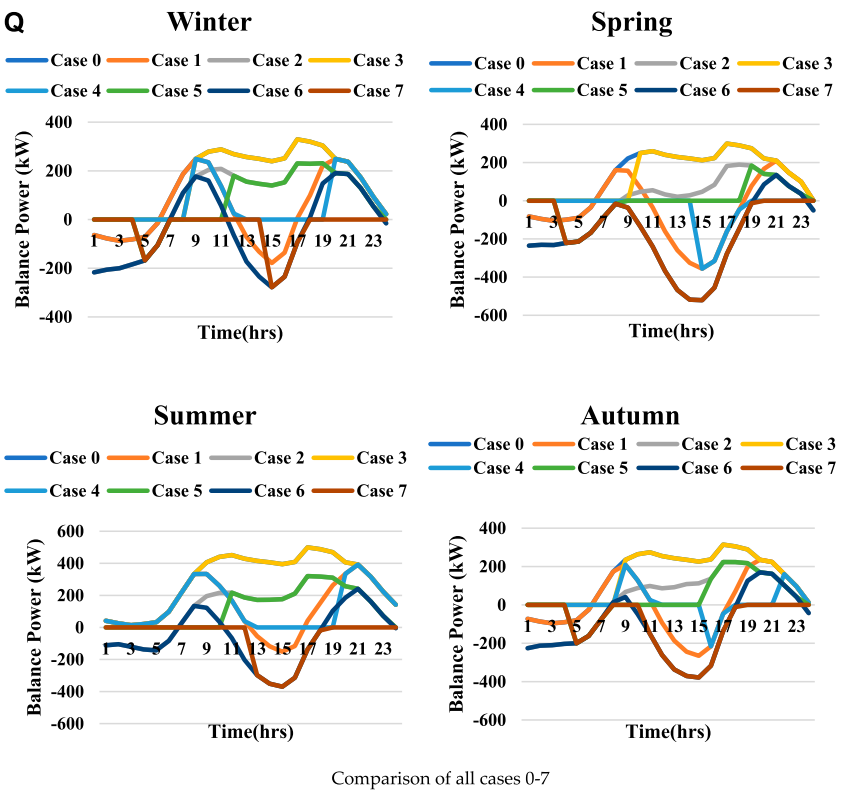

FIGURE 4
(Continued). **(A)** Power supplied by only vSMR. **(B)** Balance power after supplied by only VSMR. **(C)** Power supplied by VSMR with solar PV. **(D)** Balance power after supplied by vSMR and solar PV. **(E)** Power supplied by VSMR and wind turbines. **(F)** Balance power after supplied by vSMR and wind turbines. **(G)** Power supplied by VSMR with BESS. **(H)** Balance power after supplied by vSMR with BESS. **(I)** Power supplied by VSMR and PV. **(J)** Balance power after supplied by vSMR and solar PV with BESS. **(K)** Power supplied by VSMR and wind turbines with BESS. **(L)** Balance power after supplied by vSMR and wind turbines with BESS. **(M)** Power supplied by VSMR, PV, and wind turbines. **(N)** Balance power after supplied by vSMR, PV, and wind turbines. **(O)** Power supplied by VSMR, solar PV, and wind turbines with BESS. **(P)** Balance power after supplied by vSMR, solar PV, and wind turbines with BESS. **(Q)** Comparison of all cases 0–7.

TABLE 4 Comparative performance analysis of different schemes.

Season	Winter		Spring		Summer		Autumn	
Case no.	Total surplus power (kW)	Total deficit power (kW)	Total surplus power (kW)	Total deficit power (kW)	Total surplus power (kW)	Total deficit power (kW)	Total surplus power (kW)	Total deficit power (kW)
0	396	4,082	507	3,626	0	7,067	451	3,854
1	915	2,019	2,165	1,152	438	3,446	1,501	1,607
2	1,095	2,726	1,456	1,288	704	3,387	1,332	1,942
3	0	3,808	0	3,180	0	7,067	0	3,605
4	0	1,420	878	0	0	2,990	261	630
5	273	2,025	707	573	0	2,816	438	1,275
6	2,173	1,223	4,635	334	2,461	1,084	3,342	656
7	879	0	3,886	0	1,487	0	2,401	0

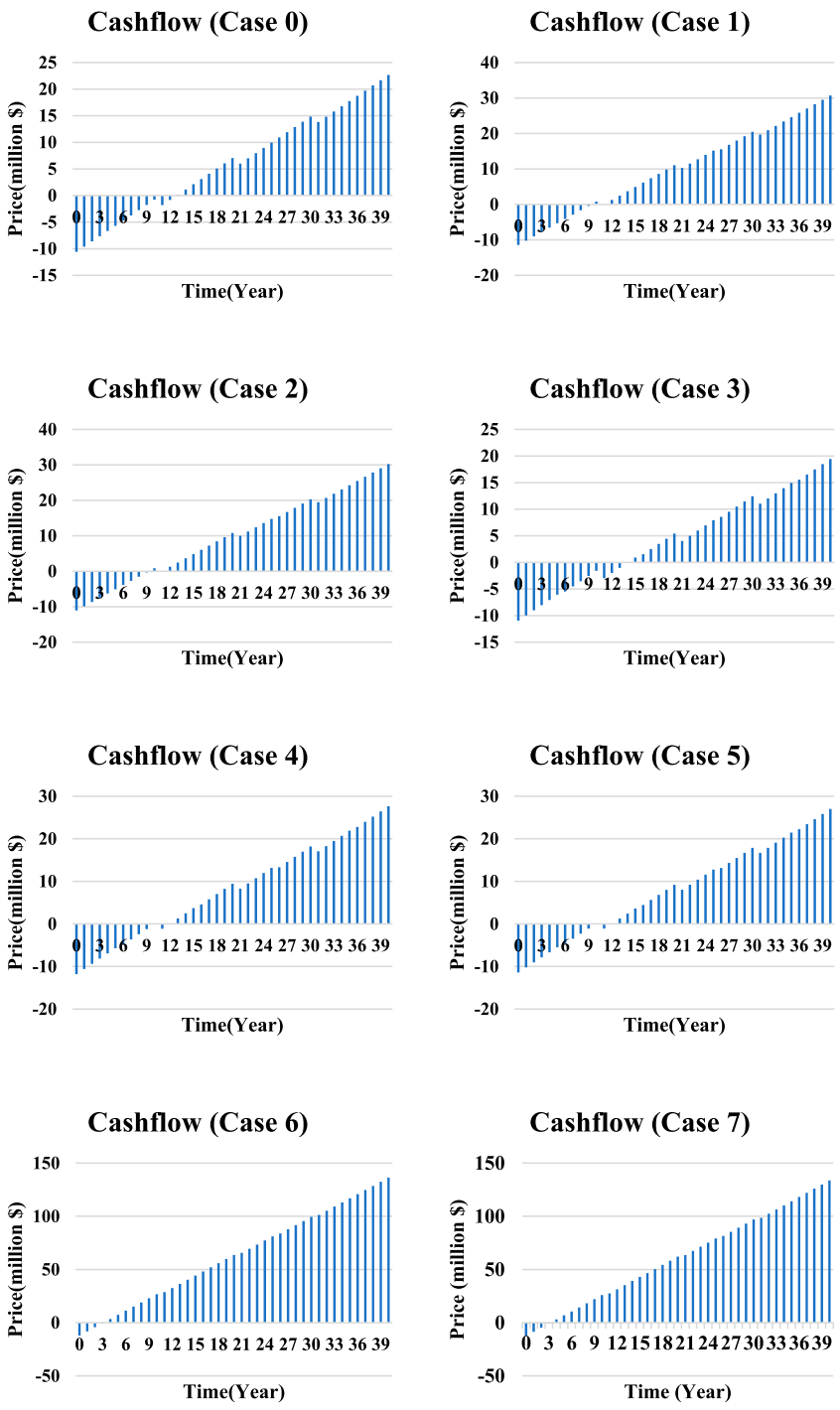

FIGURE 5
Cash flows of cases 0–7 with economic analysis using vSMR, solar PV, and wind turbines with BESS.

5.9 Comparison of cases 0–7

In the comparison of all cases, case 7 is better than the other cases because it integrates vSMR, solar PV, and wind turbines with BESS. It meets the load demand and generates surplus power, while the total surplus power is 8653 kW for the whole year. Case 3 is the worst because there is a power deficit of 17,660 kW throughout the year, as shown in Figure 4Q. The BESS is also used in cases 3, 4, and 5, but they do not meet the load demand.

The comparative performance analysis of different cases is shown in Table 4, based on the total surplus power and total power deficit in all four seasons. As a result, it is observed that case 7 is the best case, as it gives surplus power and no power deficit. On the other hand, all other cases give power lags and deficits which

TABLE 5 Comparison of economic analysis.

Case (#)	Payback (year)	SPP (year)	IRR %	Revenue (end 40 years) (million$)	NPV (million$)
0	12.5	10.69	8	22.6	3.32
1	9.5	9.25	9	30.8	2.20
2	9.3	9.17	9	30.2	2.065
3	13.5	11.16	7	21.7	4.10
4	10	9.61	8	26.16	3.04
5	9.5	9.54	8	27	2.90
6	3.9	3.03	32	136.36	19.08
7	3.99	3.31	31	133.69	18.24

are undesirable. The summary of the performance analysis of the eight cases can be observed and compared easily from Table 4.

Figure 4Q shows that case 7 meets the load demand throughout the year, although other cases have a shortage of power and have not fulfilled the load demand. Moreover, for the winter season, case 7 meets all of the load demand and also surplus power at 05:00, 06:00, 15:00, 16:00, and 17:00. The power values are 168 kW, 105 kW, 278 kW, 234 kW, and 93 kW, respectively. Furthermore, during the spring season, the surplus power is from 03:00 to 19:00, that is, 13 kW–520 kW. Moreover, during the summer season, it meets all of the load demand and also surplus power from 14:00 to 18:00 at 297 kW, 350 kW, 369 kW, 313 kW, 137 kW, and 91 kW. Furthermore, during the autumn season it also meets the load demand from 5:00, 06:00, 07:00 with surplus power 200 kW, 161 kW, and 77 kW, respectively. The surplus power from 11:00 to 18:00 of 11 kW–387 kW varies.

5.10 Economic analysis of vSMR-RER-based microgrid

The study of the economic analysis of different parameters for various scenarios of the system is shown in Table 4. The lifetime period of vSMR, solar PV, WT, and BESS is 40, 25, 25, and 5 years, respectively, and the cash flow of the system and the replacement cost of equipment are shown in Figure 5.

5.10.1 Comparison of economic analysis

The economic comparative performance analysis of different cases is shown in Table 5, based on the net present value, payback period, and revenue, at the end of the system calculated. It shows that if evaluating the NPV and net cash flows of all scenarios, case 7, with the investment, will produce the optimal results for the microgrid. In comparison of all cases, case 7 is better than others because of the power supplied by the integration of vSMR, solar PV, and wind turbines with BESS to meet the load demand. It is clearly shown that the payback periods of case 6 and case 7 are less than those in the other cases. The payback period and NPV of case 6 are 3.9 years and $19.08 million, and those for case 7 is 3.99 years and $18.24 million, respectively. Case 7 used BESS, and case 6 did without BESS. Case 6 has less payback period and more IRR than case 7 but no more difference between them. There is less difference in the cost between them, but case 7 fulfills the requirement of the load demand, as shown in Table 5.

6 Conclusion

This study conducted a comprehensive techno-economic analysis that centered on the combination of vSMR, wind turbines, solar PV, and BESS systems. Diverse scenarios, each having unique combinations of energy sources, were simulated to address the load requirements. The study also considered the temporal variations intrinsic to different seasons. The following conclusions can be drawn from all of the scenarios simulated in this study.

- Seasons affect the output power of solar PV and winds differently as varying solar irradiance and wind profile. The solar irradiance is maximum in the spring season and minimum in the winter season. The wind speed is the highest during the summer season and lowest during the winter season. Thus, seasonal variation plays a significant role in combinations involving wind turbines and solar PV systems.
- The average output power of the system is highest during the summer season and lowest during the winter season. Although the average load is also highest during the summer season and the lowest load demand during the spring season, this is mainly due to the higher generation from both wind turbine and solar PV systems.
- Cases 0, 1, 2, and case 6 without BESS do not meet the load demand effectively. Cases 3, 4, and 5 implemented vSMR and renewable energy sources, with BESS, did not meet the load demand. Thus, having BESS provides good stability and reliability for the MG; however, techno-economic limitation constraints limit the feasibility of such systems. Case 6 is economically feasible but technically not viable; however, case 7 is better than all other cases as it fulfills the load demand.
- Although, the capital cost varied from case 0 to case 7, which is $10.5 million to $12.15 million. The payback period, IRR,

NPV, and revenue, at end of 40 years of case 7, is 3.99, 31%, $18.24 million, and $133.69 million, respectively.

This shows that using vSMR in microgrids is not only technically feasible, but it is economically attractive with a payback period of merely 4 years. This research shows that the future of energy for microgrids can take multiple paths, ranging from hydrogen storage and large-scale batteries to vSMR.

Data availability statement

The original contributions presented in the study are included in the article/Supplementary Material; further inquiries can be directed to the corresponding authors.

Author contributions

MR: formal analysis, investigation, methodology, validation, visualization, and writing–original draft. MoA: conceptualization, funding acquisition, project administration, and writing–review and editing. AA: funding acquisition, methodology, supervision, and writing–review and editing. ZK: conceptualization, methodology, supervision, writing–original draft, and writing–review and editing. SA: conceptualization, formal analysis, investigation, methodology, project administration, writing–original draft, supervision, and writing–review and editing. MaA: conceptualization, supervision, validation, visualization, and writing–review and editing. UD: formal analysis, visualization, and writing–review and editing.

Funding

The author(s) declare that financial support was received for the research, authorship, and/or publication of this article. The authors extend their appreciation to the Deanship of Scientific Research at Shaqra University for funding this research work through the project number (SU-ANN-2023029).

Acknowledgments

The authors extend their appreciation to the Deanship of Scientific Research at Shaqra University for funding this research work through the project number (SU-ANN-2023029).

Conflict of interest

The authors declare that the research was conducted in the absence of any commercial or financial relationships that could be construed as a potential conflict of interest.

Publisher's note

References

Acen, P. M., Time, A. R., Energy, A. C., Renewables, A. M. I., Asian, S., and Hoa, K. (2021). ACEN and AMI to pilot battery energy storage system in Vietnam - SolarQuarter. Available at: https://solarquarter.com/2021/10/18/acen-and-ami-to-pilot-battery-energy-storage-system-in-vietnam/.

Arafat, Y., and Van Wyk, J. *eVinci™ micro reactor*. Pittsburgh, Pennsylvania, United States: Westinghouse.

Atlas, G. W. (2019). Global wind Atlas. Available at: https://globalwindatlas.info/.

Borelli, D., Devia, F., Lo Cascio, E., Schenone, C., and Spoladore, A. (2016). Combined production and conversion of energy in an urban integrated system. *Energies* 9 (10), 817. doi:10.3390/en9100817

Borhanazad, H., Mekhilef, S., Gounder Ganapathy, V., Modiri-Delshad, M., and Mirtaheri, A. (2014). Optimization of micro-grid system using MOPSO. *Renew. Energy* 71, 295–306. doi:10.1016/j.renene.2014.05.006

Bull, S. R. (2001). Renewable energy today and tomorrow. *Proc. IEEE* 89 (8), 1216–1226. doi:10.1109/5.940290

Canada Energy Regulator (2020). Government of Canada, N.E.B. NEB–market snapshot: the cost to install wind and solar power in Canada is projected to significantly fall over the long term. Available at: https://www.cer-rec.gc.ca/nrg/ntgrtd/%0Amrkt/snpsht/2018/11-03cstnstllwnd-eng.html.

Ceran, B., Mielcarek, A., Hassan, Q., Teneta, J., and Jaszczur, M. (2021). Aging effects on modelling and operation of a photovoltaic system with hydrogen storage. *Appl. Energy* 297, 117161. doi:10.1016/j.apenergy.2021.117161

Cosentino, V., Favuzza, S., Graditi, G., Ippolito, M. G., Massaro, F., Riva Sanseverino, E., et al. (2011). "Transition of a distribution system towards an active network. Part II: economical analysis of selected scenario," in 3rd Int. Conf. Clean Electr. Power Renew. Energy Resour. Impact, ICCEP 2011, Ischia, Italy, June, 2011, 15–20.

Denholm, P., and Hand, M. (2011). Grid flexibility and storage required to achieve very high penetration of variable renewable electricity. *Energy Policy* 39 (3), 1817–1830. doi:10.1016/j.enpol.2011.01.019

Denholm, P., and Margolis, R. M. (2007). Evaluating the limits of solar photovoltaics (PV) in electric power systems utilizing energy storage and other enabling technologies. *Energy Policy* 35 (9), 4424–4433. doi:10.1016/j.enpol.2007.03.004

Douglas, M., and Proprietary, C. *Electrical load distribution*, 2.

Engineering (2020). What is the lifespan of a solar panel? Available at: https://www.engineering.com/%0ADesignerEdge/DesignerEdgeArticles/ArticleID/7475/What-Is-the-Lifespan-of-a-Solar-Panel.aspx.

Hassan, Q. (2020). Optimisation of solar-hydrogen power system for household applications. *Int. J. Hydrogen Energy* 45 (58), 33111–33127. doi:10.1016/j.ijhydene.2020.09.103

Hassan, Q., Jaszczur, M., Abdulateef, A. M., Abdulateef, J., Hasan, A., and Mohamad, A. (2022). An analysis of photovoltaic/supercapacitor energy system for improving self-consumption and self-sufficiency. *Energy Rep.* 8, 680–695. doi:10.1016/j.egyr.2021.12.021

IEA (2020a) *Solar panel maintenance costs | solar power maintenance estimates*. Paris, France: IEA.

IEA (2020b) *US wind O&M costs estimated at $48,000/MW; Falling costs create new industrial uses*. Paris, France: IEA|New Energy.

Investopedia (2021). Internal rate of return (IRR) definition and formula. Available at: https://www.investopedia.com/terms/i/irr.asp.

Iyer, G., Hultman, N., Fetter, S., and Kim, S. H. (2014). Implications of small modular reactors for climate change mitigation. *Energy Econ.* 45, 144–154. doi:10.1016/j.eneco.2014.06.023

Juan, A. V., Joseph, G. L., and Charles, J. T. (2024) *Mobile nuclear power plants for ground operations*.

Khalid, M., and Savkin, A. V. (2013). Closure to discussion on 'A method for short-term wind power prediction with multiple observation points. *IEEE Trans. Power Syst.* 28 (2), 1898–1899. doi:10.1109/TPWRS.2013.2255351

Kharel, S., and Shabani, B. (2018). Hydrogen as a long-term large-scale energy storage solution to support renewables. *Energies* 11 (10), 2825. doi:10.3390/en11102825

Ko, W., and Kim, J. (2019). Generation expansion planning model for integrated energy system considering feasible operation region and generation efficiency of combined heat and power. *Energies* 12 (2), 226. doi:10.3390/en12020226

Kroposki, B., Pink, C., Basso, T., and DeBlasio, R. (2007). "Microgrid standards and technology development," in 2007 IEEE Power Eng. Soc. Gen. Meet. PES, Tampa, FL, USA, June, 2007.

Kuzlu, M., Pipattanasompom, M., and Rahman, S. (2017). "A comprehensive review of smart grid related standards and protocols," in ICSG 2017 - 5th Int. Istanbul Smart Grids Cities Congr. Fair, Istanbul, Turkey, April, 2017, 12–16.

Lew, D. J. (2000). Alternatives to coal and candles: wind power in China. *Energy Policy* 28 (4), 271–286. doi:10.1016/S0301-4215(99)00077-4

Lewis, C., MacSweeney, R., Kirschel, M., Josten, W., Roulstone, T., and Locatelli, G. (2016). Small modular reactors: can building nuclear power become more cost-effective. Cumbria, UK: National Nuclear Laboratory. Available at: https://www.researchgate.net/publication/321715136_Small_modular_reactors_Can_building_nuclear_power_become_more_cost-effective.

Locatelli, G., Boarin, S., Pellegrino, F., and Ricotti, M. E. (2015). Load following with Small Modular Reactors (SMR): a real options analysis. *Energy* 80, 41–54. doi:10.1016/j.energy.2014.11.040

Mahmud, N., and Zahedi, A. (2016). Review of control strategies for voltage regulation of the smart distribution network with high penetration of renewable distributed generation. *Renew. Sustain. Energy Rev.* 64, 582–595. doi:10.1016/j.rser.2016.06.030

Malik, M. M., Ali, S., Kazmi, A., Asim, H. W., Ahmed, A. B. I. N., and Shin, D. R. (2020). An intelligent multi-stage optimization approach for community based micro-grid within multi-microgrid paradigm. *IEEE Access* 8, 177228–177244. doi:10.1109/ACCESS.2020.3022411

Meena Agrawal, A. M. (2014). An appraisal of micro-grid project implementations in the east & south-east Asia. *Int. J. Emerg. Trends Engg Dev.* 3 (4).

Mone, C., Hand, M., Bolinger, M., Rand, J., Heimiller, D., and Ho, J. (2017). 2015 cost of wind energy review.

Murty, V. V. S. N., and Kumar, A. (2020). Multi-objective energy management in microgrids with hybrid energy sources and battery energy storage systems. *Prot. Control Mod. Power Syst.* 5 (1), 1–20. doi:10.1186/s41601-019-0147-z

Nejabatkhah, F. (2018). Optimal design and operation of a remote hybrid microgrid. *CPSS Trans. Power Electron. Appl.* 3 (1), 3–13. doi:10.24295/CPSSTPEA.2018.00001

Nichol, M., and Desai, H. (2019). Cost competitiveness of micro-reactors for remote markets. Washington, DC, USA: Nuclear Energy Institute (NEI).

NREL (2019). NREL national solar radiation Database (NSRDB). Available at: https://maps.nrel.gov/nsrdb-viewer/?aL=x8CI3i%255Bv%255D%3Dt%26Jea8x6%255Bv%255D%3Dt%26Jea8x6%255Bd%255D%3D1%26VRLt_G%255Bv%255D%3Dt%26VRLt_G%255Bd%255D%3D2%26mcQtmw%255Bv%255D%3Dt%26mcQtmw%255Bd%255D%3D3&bL=clight&cE=0&lR=0&mC=4.740675384778373%2C22.8515.

Nwulu, N. I., and Xia, X. (2017). Optimal dispatch for a microgrid incorporating renewables and demand response. *Renew. Energy* 101, 16–28. doi:10.1016/j.renene.2016.08.026

Panels, S. *Utility-scale solutions*.

Parhizi, S., Lotfi, H., Khodaei, A., and Bahramirad, S. (2015). State of the art in research on microgrids: a review. *IEEE Access* 3, 890–925. doi:10.1109/ACCESS.2015.2443119

Roberts, B. P., and Sandberg, C. (2011). The role of energy storage in development of smart grids. *Proc. IEEE* 99 (6), 1139–1144. doi:10.1109/JPROC.2011.2116752

incore (2016). Wind turbine cables for wind energy projects - Incore Cables. *Int. Energy Agency – IEA*, 1–7. Available at: https://www.incore-cables.com/wind-turbine-cables/. (Accessed on January 1, 2024)

World Nuclear Association (2019) *Small nuclear power reactors*. London, United Kingdom: World Nuclear Association.

Zahedi, A. (2011). Maximizing solar PV energy penetration using energy storage technology. *Renew. Sustain. Energy Rev.* 15 (1), 866–870. doi:10.1016/j.rser.2010.09.011

frontiers | Frontiers in Energy Research

TYPE Erratum
PUBLISHED 03 July 2024
DOI 10.3389/fenrg.2024.1447781

OPEN ACCESS

APPROVED BY
Frontiers Editorial Office,
Frontiers Media SA, Switzerland

*CORRESPONDENCE
Frontiers Production Office,
production.office@frontiersin.org

RECEIVED 12 June 2024
ACCEPTED 12 June 2024
PUBLISHED 03 July 2024

CITATION
Frontiers Production Office (2024), Erratum: Integration of very small modular reactors and renewable energy resources in the microgrid. *Front. Energy Res.* 12:1447781. doi: 10.3389/fenrg.2024.1447781

Erratum: Integration of very small modular reactors and renewable energy resources in the microgrid

Frontiers Production Office*

Frontiers Media SA, Lausanne, Switzerland

KEYWORDS

photovoltaic, wind turbine, nuclear, battery, microgrid, off-grid

An Erratum on
Integration of very small modular reactors and renewable energy resources in the microgrid

by Raza MK, Alghassab M, Altamimi A, Khan ZA, Abbas Kazmi SA, Ali M and Diala U (2024). Front. Energy Res. 12:1365735. doi: 10.3389/fenrg.2024.1365735

Due to a production error, there was a mistake in Figure 1 as published. Figure 1A was erroneously removed. The corrected Figure 1 appears below.

The publisher apologizes for this mistake. The original version of this article has been updated.

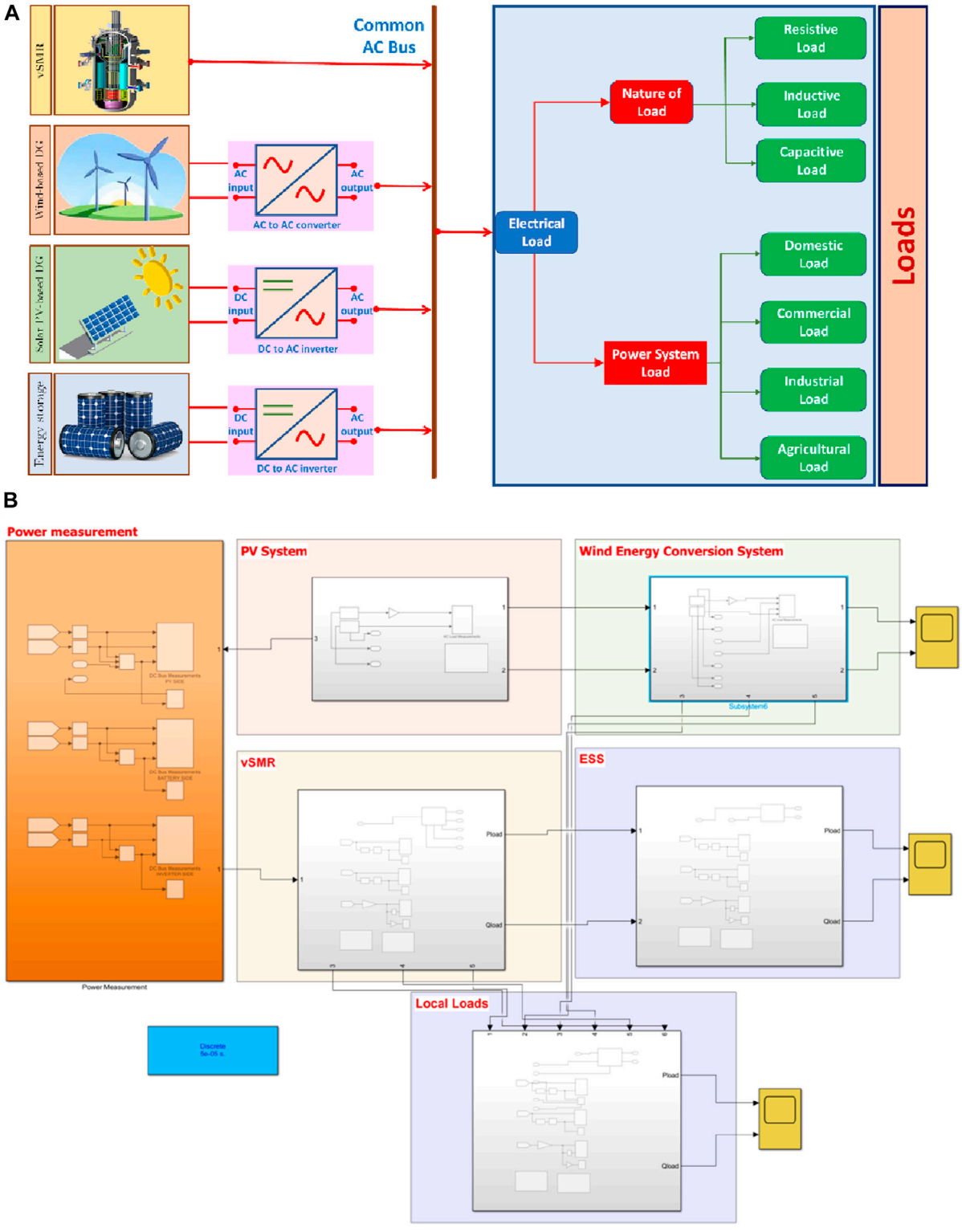

FIGURE 1
(A) System architecture of a vSMR-based MG (Arafat and Van Wyk; Acen et al., 2021; Douglas and Proprietary; incore, 2016). (B) MATLAB/Simulink test system with integrated vSMR, PV, and wind turbines.

frontiers | Frontiers in Energy Research

TYPE Original Research
PUBLISHED 22 May 2024
DOI 10.3389/fenrg.2024.1396899

OPEN ACCESS

EDITED BY
Flah Aymen,
École Nationale d'Ingénieurs de Gabès, Tunisia

REVIEWED BY
Hassan M. Hussein Farh,
Imam Muhammad ibn Saud Islamic University, Saudi Arabia
Yasser Assolami,
Taibah University, Saudi Arabia
Hisham Alharbi,
Taif University, Saudi Arabia

*CORRESPONDENCE
Abdulaziz Almutairi,
ad.almutiri@mu.edu.sa

RECEIVED 06 March 2024
ACCEPTED 26 April 2024
PUBLISHED 22 May 2024

CITATION
Almutairi A, Albagami N, Almesned S, Alrumayh O and Malik H (2024), Optimal management of electric vehicle charging loads for enhanced sustainability in shared residential buildings.
Front. Energy Res. 12:1396899.
doi: 10.3389/fenrg.2024.1396899

Optimal management of electric vehicle charging loads for enhanced sustainability in shared residential buildings

Abdulaziz Almutairi[1]*, Naif Albagami[1], Sultanh Almesned[2], Omar Alrumayh[3] and Hasmat Malik[4,5]

[1]Department of Electrical Engineering, College of Engineering, Majmaah University, Saudi Arabia, [2]Department of Educational Sciences, College of Education, Majmaah University, Saudi Arabia, [3]Department of Electrical Engineering, College of Engineering, Qassim University, Unaizah, Saudi Arabia, [4]Department of Electrical Power Engineering, Faculty of Electrical Engineering, University Technology Malaysia (UTM), Skudai, Malaysia , [5]Department of Electrical Engineering, Graphic Era Deemed to be University, Dehradun, India

Demand management of electric vehicles (EVs) in shared residential parking lots presents challenges for sustainable transportation systems. Especially, in shared parking lots where multiple EVs share the same parking space, such as residential apartments. This is challenging due to involvement of various factors such as limited number of chargers, limited capacity of transformer, and diverse driving behavior of EV owners. To address this issue, this study proposes an optimal demand management framework that addresses limited chargers, transformer capacity, and diverse driving behavior to promote sustainable EV integration. By estimating driving behavior, energy consumption, and utilizing a linear programming-based optimization model, power allocation to EVs is optimized based on multiple factors. A satisfaction index is introduced to measure the satisfaction level of the EV community, further emphasizing user-centric sustainability. Performance analysis includes factors such as power usage, charger utilization, and community satisfaction. The performance of the proposed method is compared with a conventional method and the proposed method increase the satisfaction index of the community by up to 10%. In addition, sensitivity analysis is used to explore the impact of factors like charger availability, EV penetration, and transformer capacity limits. Results show that with 3% EV penetration, satisfaction levels exceed 75%, reaching over 80% with five chargers and 6% EV penetration.

KEYWORDS

electric vehicle charging, demand management, sustainable transportation, shared residential buildings, user satisfaction, resource optimization, integrated sustainability, sustainable communities

1 Introduction

1.1 Motivation

Emissions in transportation represent a critical contributor to global environmental challenges, accounting for a significant portion of greenhouse gas emissions worldwide. It accounts for about a quarter of the total emissions (Vision, 2050), necessitating urgent decarbonization efforts to align with international climate agreements. Electric vehicles

(EVs) are considered a viable option to reduce emissions from the transport sector, especially if they are charged with renewable power (Hussain and Musilek, 2022a). Therefore, the penetration of EVs is increasing day by day. For example, a total of 14% of all new cars sold were electric in 2022, up from around 9% in 2021 and less than 5% in 2020. Over 2.3 million EVs were sold in the first quarter of 2023, about 25% more than in the same period last year. It is expected that about 14 million EVs will be sold by the end of 2023, representing a 35% year-on-year increase (IEA Global EV, 2023). The International Energy Agency (IEA) has also increased the expected share of EVs by 2030 to 35% from 25% in the previous year's outlook report (IEA Global EV, 2023). In addition different issues related to power electronics and their monitoring and control are discussed in (Liu, 2021; Wang et al., 2022). Similarly, the impacts on weak grids is discussed in (Shao et al., 2023) and on low carbon energy economy in (Luo et al., 2024).

However, the transition to EVs as a viable solution for reducing greenhouse gas emissions in the transportation sector presents several challenges for the power sector (Khan et al., 2022; Zhang et al., 2022). For example, at the power system level, accommodating the increased demand necessitates additional power plants to cater to EVs' energy needs and serve as reserves (Heuberger et al., 2020). This heightened demand strains local infrastructure, causing technical issues like voltage fluctuations, network congestion, and phase imbalances, particularly at the distribution level (Hou et al., 2017). Moreover, in residential circuits, the peak EV load coincides with the peak residential load (weekday evenings) and can easily overload the local equipment (Fachrizal et al., 2021; Zhang H. et al., 2023). This is especially challenging for apartment complexes where several EVs are parked and charged together (Hussain and Musilek, 2022b). In addition, the impact of EVs on the air quality in China is assessed in (Lyu et al., 2024) for different cities throughout the lifecycle of EVs. Different types of dispatch strategies are also discussed in the literature such as distributed dispatch (Li et al., 2022) and dynamic dispatch (Duan et al., 2023). Finally, decentralized energy control is discussed in (Shirkhani et al., 2023) and an adaptive lightweight defect detection model is proposed in (Lei et al., 2023).

1.2 Literature review

To address these issues, related to equipment overloading in distribution systems, several studies are conducted in literature. These studies can be broadly divided into two categories. In the first group of studies, system-level measures are suggested to manage the load of EVs. For example (Almutairi and Alyami, 2021), proposes per-unit load estimation of EVs to model and analyze various penetration levels of EVs in different locations (Tran et al., 2019). suggests using home solar panels to charge EVs, aiming to reduce power surges and enhance grid stability (Kong et al., 2022). introduces an optimization model for managing EV charging loads in distribution networks, employing a bi-level programming approach to select charging stations and manage loads. Additionally (Mazhar et al., 2023), evaluates machine learning-based methods for managing EV load in smart cities. Several studies also proposed dynamic pricing as a method to manage EV loads. For instance (Limmer and Rodemann, 2019), proposes dynamic pricing at EV charging stations to reduce peak demand charges and increase operator profits. Similarly (Moghaddam et al., 2019), suggests dynamic pricing to shift loads during evening peaks, aiming to minimize overlaps with residential peak hours and reduce network instability risks. Furthermore (Sayarshad et al., 2021), introduces a dynamic pricing model for urban freight transport involving electric and conventional vehicles, aiming to reduce costs and delays. Different aspects of EVs models such variations in electrical parameters and underlying voltage tracking control are discussed in (Zhang et al., 2021; Zhang X. et al., 2023).

However, several studies report that system-level management and pricing policies alone may not be suitable for effectively managing the load of EVs (Hussain and Musilek, 2021; Geotab, 2023; Hussain and Musilek, 2021; Zhang et al., 2021; Zhang X. et al., 2023; Sayarshad et al., 2021; Moghaddam et al., 2019; Limmer and Rodemann, 2019; Mazhar et al., 2023; Kong et al., 2022; Tran et al., 2019; Almutairi and Alyami, 2021; Lei et al., 2023; Shirkhani et al., 2023; Shirkhani et al., 2023; Duan et al., 2023). This is primarily due to local equipment, especially in distribution systems, often experiencing overload from direct connections of EVs, resulting in technical issues such as voltage fluctuations and network congestion (Geotab, 2023). Moreover, implementing EV charging infrastructure might not universally suit all communities, especially in residential or commercial settings (Almutairi and Alrumayh, 2022). Consequently, a second group of studies has emerged recently, focusing on local demand management of EVs to mitigate local equipment overload, discussed below.

The growing adoption of EVs is discussed in (Tulabing et al., 2018), where localized demand control is proposed to prevent grid congestion. Simulations suggest that a 40% EV participation rate ensures grid resilience despite 100% EV adoption. Additionally (Chen and Chang, 2016), introduces a demand response-based method for EVs, employing cloud-based management to minimize costs. Meanwhile (Hussain et al., 2023), presents a welfare-focused model for realizing Vehicle-to-Vehicle (V2V) communication to manage EV charging stations with multiple EVs (Ahmadi et al., 2023). discusses various approaches for mitigating EV charging costs, including strategies such as solar power connections and V2X approaches. Furthermore, a comprehensive review conducted in (Zhang et al., 2020) focuses on energy management strategies for EVs, highlighting clustered EV demand management as a significant challenge.

1.3 Research gap and contributions

From the literature review, it is evident that numerous studies have explored managing EV load both at the system and local levels. However, most of these studies have concentrated on single homes, analyzing their collective impact on the system. In shared parking stations like residential apartments and commercial centers, EVs can readily overload local equipment, such as transformers. Additionally, allocating power to EVs during system peak load hours poses a complex challenge, involving factors such as customer satisfaction levels, available equipment capacity, and the number of chargers in each locality. The existing literature has not comprehensively considered all these factors together. It is

imperative to consider all these factors collectively to present various options for policymakers aimed at maximizing EV owners' satisfaction. These options may include installing more chargers or upgrading local equipment by the utility. Furthermore, this multi-factor analysis is essential for selecting the optimal number of chargers for a given number/percentage of EVs in any shared parking location.

To address the research gaps identified in the previous paragraphs, a multi-factor EV load management framework is proposed in this study. The aim of this framework is to offer insights into determining the optimal number of chargers and capacity constraints of local equipment (transformers). These insights will assist policymakers and utilities in planning system upgrades and installations suitable for accommodating a specific level of EVs. The framework's implementation involves several steps. The major contributions of this study are as follows:

- EV driver behavior is estimated using the National Household Travel Survey (NHTS) dataset. Subsequently, EV parameters are utilized to determine the daily energy demand of EVs.
- An optimization model is then developed to allocate the available power among EVs within the charging station of a residential apartment complex. This consideration encompasses a shared parking lot accommodating both conventional vehicles and EVs.
- A satisfaction index is proposed to quantitatively measure EV owners' satisfaction levels by comparing the allocated energy demand with the actual demand before their departure time.
- A sensitivity analysis is conducted to assess various parameters, including the number of chargers, EV penetration levels, and transformer capacity limits.

This analysis aims to further enhance the understanding of the framework's performance under different conditions.

The reminder of the paper is organized as follows. Introduction section is followed by modeming of EV demand (Section 2), where vehicle driving parameters and EV parameters are extracted. In section 3, an optimization problem is formulated to allocate power to EVs considering various factors such as number of chargers, number of EVs, and capacity of the distribution equipment such as transformers. The performance of the proposed method is evaluated for a residential apartment complex in Section 4. A sensitivity analysis of various factors, including the number of chargers, the penetration level of EVs, and the limits of the transformer's capacity in conducted in Section 5. Finally, conclusions and future research direction are discussed in Section 6.

2 Demand management of electric vehicles

Managing the demand of EVs in shared parking lots, particularly in residential apartment complexes poses significant challenges. These challenges arise from the limited availability of charging spots and the constraints imposed by local transformers. Consequently, this section begins with the estimation of EV load, followed by strategies for load management specifically focusing on EVs (Section 3).

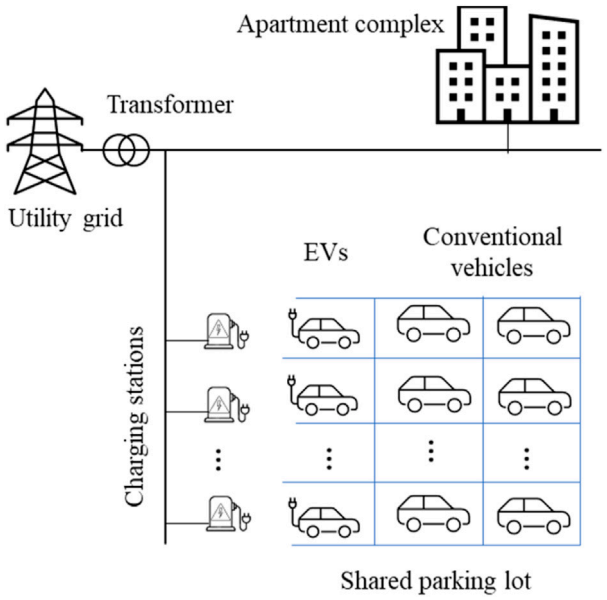

FIGURE 1
Overview of the system configuration.

2.1 System configuration

While the adoption of EVs is increasing worldwide, their penetration levels remain relatively low compared to conventional vehicles. Consequently, most shared parking lots are primarily designated for conventional vehicles, with only a limited number of slots equipped with chargers for EVs. This study considers this prevalent scenario where conventional vehicles dominate the parking spaces. Figure 1 illustrates the system configuration, comprising a residential apartment complex with a shared parking lot. The designated EV spots within the parking lot are equipped with chargers. Both the building and the charging stations are connected to the utility grid via the same transformer. Hence, effective management of the EV load in the charging station becomes crucial since the peak load of residential buildings often coincides with the peak load of EVs. This synchronization occurs because many EV owners tend to park their vehicles and commence charging upon arriving home in the evenings.

2.2 Demand modeling of electric vehicles

Estimating the load of EVs involves several sequential steps. Initially, data pertaining to drivers' travel behavior is required, followed by data related to EVs (Yang et al., 2024). Due to the limited availability of large datasets specifically for EV drivers, conventional vehicle data is commonly utilized, as seen in other studies (NHTS, 2023). The NHTS data is considered reliable and has been utilized by numerous researchers for similar analyses. Therefore, in this study, NHTS data is employed to estimate driver behavior. An overview of the various steps involved is presented in Figure 2. The data is first pre-processed to rectify any erroneous reporting, such as missing fields or unrealistic speeds. Subsequently, vehicle trips are recorded, and daily mileages are computed for each vehicle.

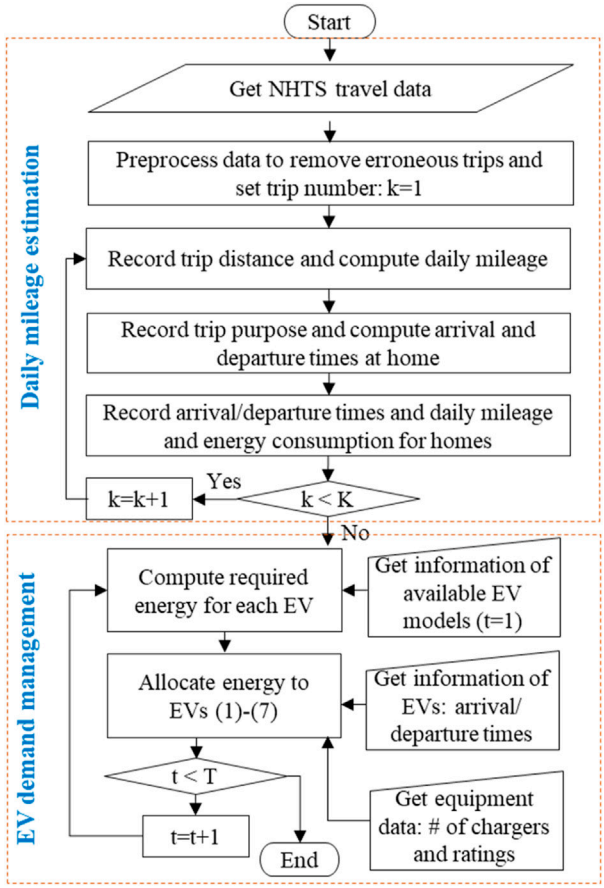

FIGURE 2
EV demand estimation and load management process.

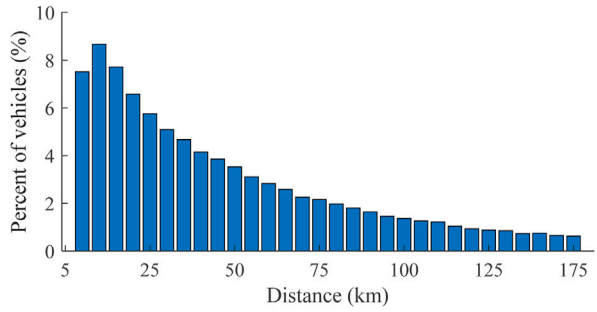

FIGURE 3
Daily mileage of vehicles extracted from the data.

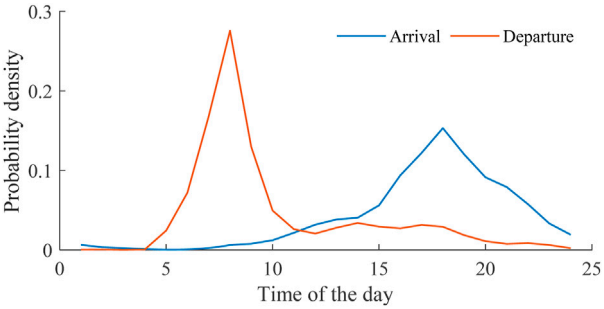

FIGURE 4
Daily arrival and departure times of vehicles.

In this study, stochastic simulation models for PEV deployment are implemented using a data-driven approach that integrates key components such as driver behavior, PEV characteristics, charging infrastructure, grid integration, and policy and market factors. The models utilize historical data and statistical methods to simulate driver behaviors, including trip lengths, frequencies, and charging preferences, based on datasets like the NHTS. The models also consider the need for charging infrastructure and assess the grid impact of PEV charging, taking into account factors like charger placement and capacity. Policy and regulatory analysis are incorporated to evaluate the impact of government policies on EV adoption.

2.2.1 Daily mileage estimation

To estimate the daily mileage of vehicles, each vehicle is assigned an ID and is tracked for each day. Then, the daily mileage is computed based on the total number of trips and distance covered during each trip. The extracted data is shown in Figure 3. It can be observed that most of the vehicles travel under 100 km daily. Details about the estimation process can be found in (Fathy et al., 2023). In this study, home is considered as the test case for EVs. However, it should be noted that the same process can be used to track EVs to different locations such as workplace or any specific location such as commercial centers. The problem formulation remains the same, irrespective of the location.

2.2.2 Arrival and departure time estimation

The study records the origin and destination of each vehicle to ascertain their respective arrival and departure times at home. Notably, a vehicle might have multiple visits to the home, but for this study, the last arrival time and the first departure time are considered. The extracted arrival and departure times of vehicles are depicted in Figure 4, revealing that a majority of vehicles arrive home during the evening hours between 15:00 and 19:00.

2.2.3 Energy demand modeling

Following the estimation of daily mileage for vehicles, the study incorporates technical parameters specific to EVs. The data pertaining to commercially available EVs can be found in (EV Database, 2023). This dataset includes information on the mileage efficiency and useable battery size of various EV models. As per the database, the average energy efficiency across all EVs stands at 195 Wh/km, while the average useable battery size is recorded at 68.9 kWh (as of November 2023). This data serves as the basis for computing the daily energy consumption of EVs. Figure 5 illustrates the daily energy consumption of EVs, revealing that the majority of EVs consume under 25 kWh of energy on a daily basis. This observation aligns reasonably well with the average vehicle mileage of under 100 km per day and an average energy efficiency of 195 Wh/km.

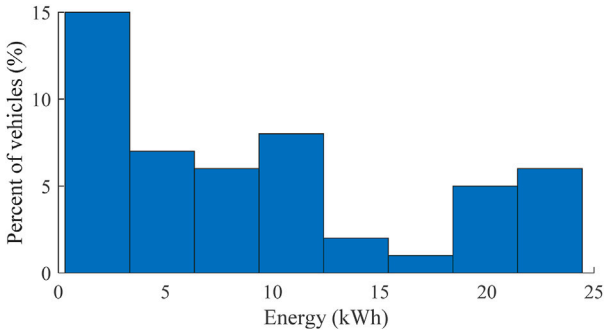

FIGURE 5
Daily energy consumption of EVs.

3 Problem formulation

In this section, an optimization problem is formulated to allocate power to EVs considering various factors such as number of chargers, number of EVs, and capacity of the distribution equipment such as transformers. A linear programming-based model is developed which is guaranteed to be convex and can easily be solved by commercial optimization tools. Due to the convexity of the problem, it can be easily solved in a very short time using commercial software such as CPLEX, making it suitable for real-time applications.

3.1 Objective function

The objective function is designed to minimize the energy difference between the required energy demand (E_i^{dem}) and the allocated energy (E_i^{all}) for EV *i*. In this study, to emulate the real-life behavior of EV consumers, a first-come-first-served approach is implemented. Therefore, the energy gap is penalized based on the difference between the maximum number of intervals (T) and the arrival time of EV *i* (Ta_i). This penalization ensures that the EVs arriving first will occupy the available chargers. It should be noted that E_i^{all} is the decision variable in the objective function while all other factors are parameters.

$$\min \sum_{i \in I} \left(\left(E_i^{dem} - E_i^{all} \right) \cdot \left(T - Ta_i \right) \right) \tag{1}$$

3.2 Constraints

Several constraints are necessary to ensure the equitable allocation of available energy among EVs while adhering to physical constraints such as the availability of chargers and the capacity of the transformer. For instance, Eq. 2 ensures that the total allocated power to any EV (E_i^{all}) should not exceed the required power (E_i^{dem}) for that EV. It is important to note that an EV may not be fully charged within a single time interval '*t*'. Thus, the total allocated power to any EV becomes the accumulation of power allocated to it across all intervals before its departure, mathematically represented as Eq. 3 where $E_{i,t}^{a}$ is the energy allocated to EV *i* at time *t*. Moreover, within each interval '*t*', the maximum chargeable power for any EV is constrained by the charger's rating, as depicted in Eq. 4. Here, R^{ch} denotes the charger's rating in kW, and $B_{i,t}^{ch}$ is a binary variable introduced to monitor the active chargers. For instance, if a charger is in use during any time interval *t* for any EV *i*, the value of $B_{i,t}^{ch}$ will be 1; otherwise, it will be zero. It should be noted that E_i^{all}, $E_{i,t}^{a}$, and $B_{i,t}^{ch}$ are variables in these constraints while all other factors are parameters.

Additional constraints are necessary to ensure that the capacity limits of the transformer are not breached. Eq. 5 stipulates that the total power drawn by all EVs during any time interval '*t*' should be less than or equal to the capacity of the transformer (C_t^{tx}). It is important to note that C_t^{tx} represents the remaining capacity of the transformer after catering to the building's load. Eq. 6 signifies that the sum of chargers utilized by all EVs during any time interval '*t*' should be less than or equal to the number of available chargers (N^{ch}). Furthermore, EVs are only allowed to charge when they are available at the parking station. To enforce this constraint, (7) is introduced. This equation implies that outside of parking intervals, such as before the arrival time (Ta_i) and after the departure time (Td_i), the amount of power allocated to EV *i* should be forced to zero.

$$E_i^{all} \le E_i^{dem} \tag{2}$$

$$E_i^{all} = \sum_{t \in T} E_{i,t}^{a} \tag{3}$$

$$E_{i,t}^{a} \le R^{ch} \cdot B_{i,t}^{ch} \tag{4}$$

$$\sum_{i \in I} E_{i,t}^{a} \le C_t^{tx} \tag{5}$$

$$\sum_{i \in I} B_{i,t}^{ch} \le N^{ch} \tag{6}$$

$$E_{i,t}^{a} = 0 \; if \; t \ge Td_i \| t < Ta_i \tag{7}$$

3.3 Satisfaction index

To evaluate the effectiveness of the proposed allocation scheme and to offer insights to policymakers, this study introduces an index. This index gauges the satisfaction level of EV owners by assessing the allocated power to each EV and comparing it with the required energy. It can be mathematically modeled as

$$SI_i = 100 \cdot \left(1 - \frac{\left(E_i^{dem} - E_i^{all} \right)}{E_i^{dem}} \right) \tag{8}$$

Where E_i^{dem} represents the energy demand, and E_i^{all} signifies the allocated energy to EV *i*. This index is designed to reach a value of 100 when the entire energy demand is met before the departure time. Conversely, it will assume a value of zero when no energy demand is fulfilled, and the departure time has arrived. Operating as a continuous index, it spans values from zero to 100 inclusively, contingent upon the amount of energy received by each EV.

4 Performance evaluation

This section evaluates the performance of the proposed method using a residential apartment complex comprising 320 vehicles. For

10.3389/fenrg.2024.1396899

TABLE 1 Input data of EV fleet used in this section.

EV ID	Load demand (kWh)		Fulfilled (continuous)	Time (h)		
	Original	Fulfilled (proposed)		Arrival	Departure	Parking duration
1	12	12	12	14	19	5
2	12	12	12	15	21	6
3	33	30.4	33	16	0	8
4	35	30.4	35	17	22	5
5	15	15	0	17	1	8
6	30	15.2	0	18	20	2
7	35	30.4	35	18	2	8
8	28	22.8	28	19	2	7
9	13	0	0	20	1	5
10	32	15.2	15.2	21	4	7

this case, the ratio of EVs is approximately 3% (10EVs). Subsequent sections conduct an analysis across different percentage levels. The developed linear programming model is implemented in Python, integrating the optimization tool CPLEX (IBM CPLEX, 2023). This study considers a scheduling horizon of 1 day (T = 24) with a sample period of an hour (t = 1). It should be noted that the performance of the proposed framework is tested for a scheduling horizon of 1 day. However, the formulations are generalized and can be used for any time horizon, such as a week, month, or year. Given the residential nature of the building, most vehicles arrive home in the evening and depart in the morning the following day. Hence, the scheduling horizon spans from 10 a.m. and extends until 10 a.m. the subsequent day. Additionally, most residential buildings utilize level 2 chargers for community charging. Consequently, this study employs level 2 chargers rated at 7.6 kW power.

4.1 Input data

To facilitate visualization, this section focuses on 10 selected EVs, constituting roughly 3% of the total vehicle fleet. Table 1 displays the parameters associated with these selected EVs. The original load demand for each EV is randomly generated within the range of (Liu, 2021; EV Database, 2023) kWh, aligning with the survey data discussed in the previous section. Furthermore, the arrival times of these EVs correspond to the survey data, reflecting the trend of vehicles arriving home mostly during the afternoon and evening hours. Similarly, the departure time of most vehicles is early morning the following day. Therefore, the arrival and departure times for each EV are randomly generated (separately) following a normal distribution. The mean and standard deviation of EV arrival and departure times are based on the NHTS survey data, discussed in the previous section. EVs with both short and long parking durations are selected for this analysis to consider different types of drivers. The parking duration is determined based on the arrival and departure times. In this section, two chargers are considered. Additionally, the transformer's capacity (remaining capacity after serving the building load) is set at 35 kW. The profile of the residential apartment complex on a selected day is shown in Figure 6.

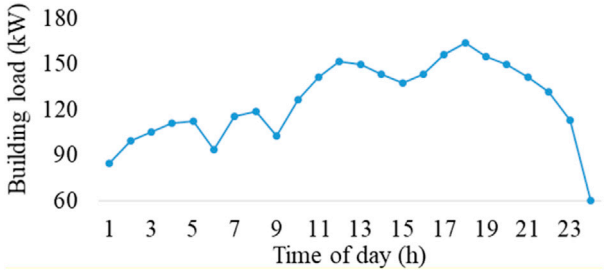

FIGURE 6
Daily energy consumption profile of the building.

4.2 Performance evaluation

This section conducts an analysis of the proposed method's performance using a fleet of 10 EVs based on the parameters outlined in the input data section. The evaluation assesses the performance concerning energy allocation, charger utilization, and driver satisfaction (utilizing the proposed satisfaction index). The performance of the proposed method is compared with conventional method (named as continuous), where once EVs occupies the charger it remains connected until it is fully charged.

4.2.1 Energy allocation

An overview of the original demand for each EV and the total allocated energy before their departure time is depicted in Figure 7. Notably, it is evident that the energy demand of EV1, EV2, and EV5 is entirely satisfied owing to their relatively lower energy demands and medium to high parking durations (refer to Table 1). Furthermore, for EV1 and EV2, the chargers were available since they were the first two EVs to arrive home (Table 1). Interestingly, despite being parked for 5 h, none of the

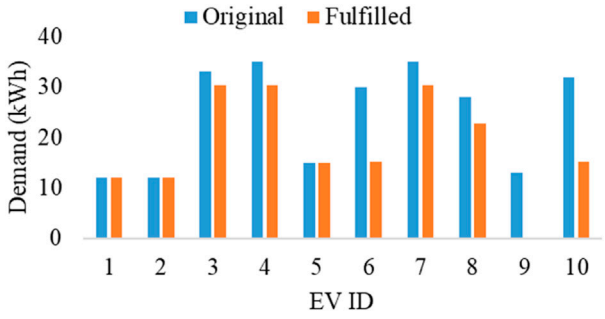

FIGURE 7
Allocate energy to EVs.

energy demands for EV9 are fulfilled. This occurred because both chargers were occupied by other EVs, remaining unavailable before EV9's departure. This observation aligns with the data presented in Table 2, detailing the hourly charging for each EV. For all other EVs, their demand is only partially fulfilled due to various factors such as lower parking durations, higher energy demands, and/or charger unavailability. In the case of the conventional method, the energy demand of EV5, EV6, and EV9 is not fulfilled because both chargers were occupied by EVs that arrived earlier. Details about the charger utilization can be found in Table 3.

4.2.2 Charger utilization

The developed framework ensures that, at any given time interval, no more chargers are utilized than the available count. The binary variable data, employed in the problem formulation to monitor charger usage, has been extracted and visualized in Figure 8. The plot demonstrates that at no point are more than two chargers employed simultaneously. For improved clarity, distinct colors designate different time intervals in the visualization. Moreover, verification from Table 2 reaffirms the usage of a maximum of two chargers throughout any time interval. During intervals 14, 2, and 3, only one charger is in use, attributed to the availability of only one uncharged EV during those periods. Conversely, both chargers are efficiently utilized during the remaining intervals. It is important to note that Table 2 exclusively displays intervals with non-zero values of charging power, rather than representing the entire scheduling horizon.

4.2.3 Driver satisfaction

The evaluation of the proposed satisfaction index for all 10 EVs is illustrated in Figure 9. Notably, the majority of EVs exhibit a satisfaction index exceeding 50%. However, EV9 and EV10 have satisfaction indices below 50%. The average index for the entire community stands at 75%. Contrarily, in case of the continuous method, the satisfaction index of EVs 5, 6, and 9 is zero. In addition, the overall satisfaction index of the community is 65% which is lower than the proposed method.

Improving the index can be achieved through multiple strategies. Firstly, augmenting the number of chargers could notably enhance satisfaction, considering the current limitation of only two chargers available in the building. Additionally, incentivizing EVs to alter their charging and arrival behavior could optimize the utilization of the available chargers, subsequently augmenting the satisfaction index.

5 Discussion and analysis

This section conducts a sensitivity analysis of various factors, including the number of chargers, the penetration level of EVs, and the limits of the transformer's capacity. Detailed discussions regarding each parameter are presented in the subsequent section.

TABLE 2 Interval-wise power allocation to each EV under proposed method.

Interval	EV1	EV2	EV3	EV4	EV5	EV6	EV7	EV8	EV9	EV10
14	7.6	0	0	0	0	0	0	0	0	0
15	4.4	4.4	0	0	0	0	0	0	0	0
16	0	7.6	7.6	0	0	0	0	0	0	0
17	0	0	7.6	7.6	0	0	0	0	0	0
18	0	0	7.6	0	0	7.6	0	0	0	0
19	0	0	0	7.6	0	7.6	0	0	0	0
20	0	0	0	7.6	0	0	0	7.6	0	0
21	0	0	7.6	7.6	0	0	0	0	0	0
22	0	0	0	0	7.4	0	7.6	0	0	0
23	0	0	0	0	7.6	0	7.6	0	0	0
0	0	0	0	0	0	0	7.6	7.6	0	0
1	0	0	0	0	0	0	7.6	7.6	0	0
2	0	0	0	0	0	0	0	0	0	7.6
3	0	0	0	0	0	0	0	0	0	7.6

10.3389/fenrg.2024.1396899

TABLE 3 Interval-wise power allocation to each EV under continuous method.

Interval	EV1	EV2	EV3	EV4	EV5	EV6	EV7	EV8	EV9	EV10
14	7.6	0	0	0	0	0	0	0	0	0
15	4.4	7.6	0	0	0	0	0	0	0	0
16	0	4.4	7.6	0	0	0	0	0	0	0
17	0	0	7.6	7.6	0	0	0	0	0	0
18	0	0	7.6	7.6	0	0	0	0	0	0
19	0	0	7.6	7.6	0	0	0	0	0	0
20	0	0	2.6	7.6	0	0	0	0	0	0
21	0	0	0	4.6	0	0	7.6	0	0	0
22	0	0	0	0	0	0	7.6	7.6	0	0
23	0	0	0	0	0	0	7.6	7.6	0	0
0	0	0	0	0	0	0	7.6	7.6	0	0
1	0	0	0	0	0	0	4.6	5.2	0	0
2	0	0	0	0	0	0	0	0	0	7.6
3	0	0	0	0	0	0	0	0	0	7.6

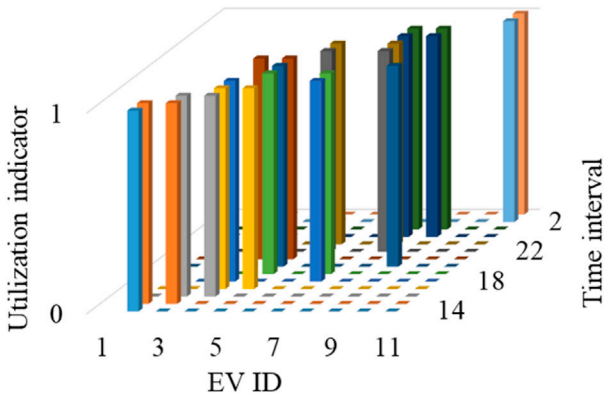

FIGURE 8
Charger usage indictor.

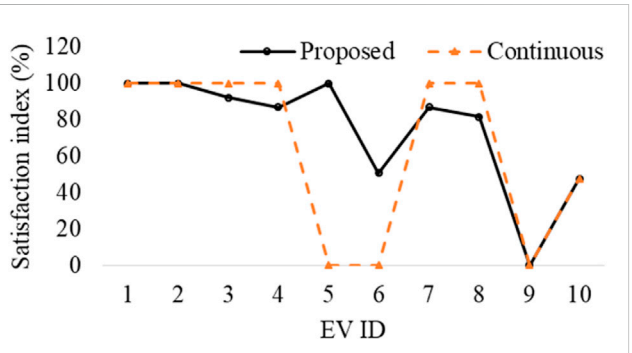

FIGURE 9
Satisfaction index of EV users.

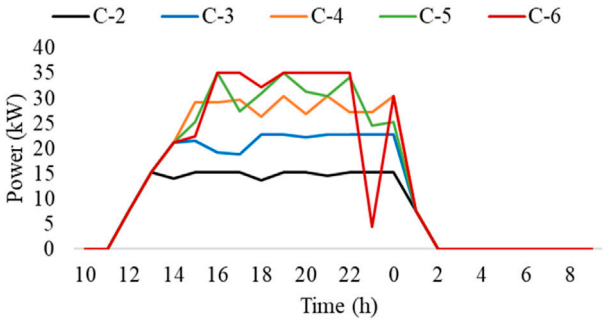

FIGURE 10
Total power consumption of chargers under different number of chargers.

5.1 Number of chargers

In this section, the variation of the number of chargers from 2 to 6 is simulated across five different cases. A fleet of 20 EVs is considered, with a transformer limit set at 35 kW. For each case, computations include the total power consumed by the chargers, the utilization count of chargers in each interval, and the overall satisfaction of the community. The respective results are displayed in Figures 10–12, specifically showcasing intervals with non-zero values of charging power.

Figure 10 demonstrates an anticipated increase in power consumption with the rising number of chargers. Notably, the total power consumption is constrained to 35 kW for specific intervals in the C-5 and C-6 cases, aligning with the

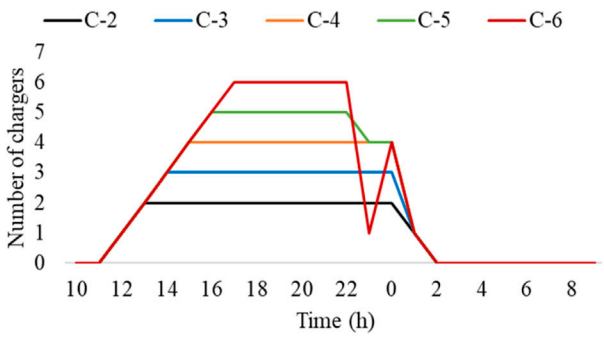

FIGURE 11
Charger utilization under different number of chargers.

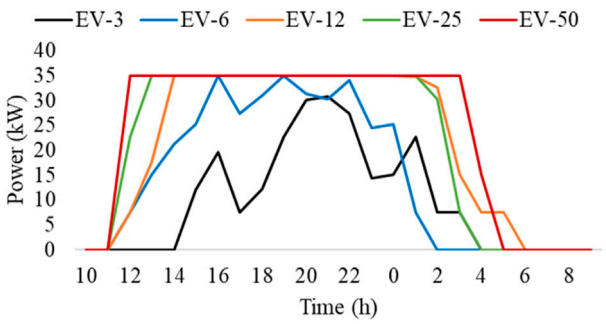

FIGURE 13
Total power consumption under different EV penetration levels.

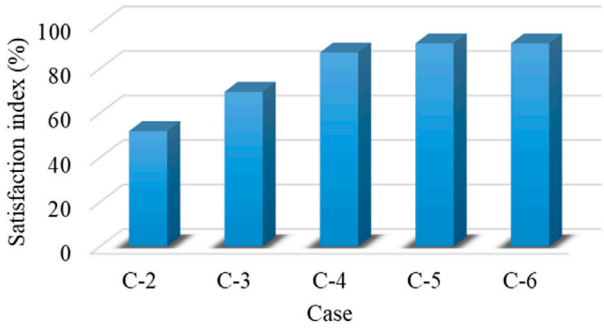

FIGURE 12
Community satisfaction under different number of chargers.

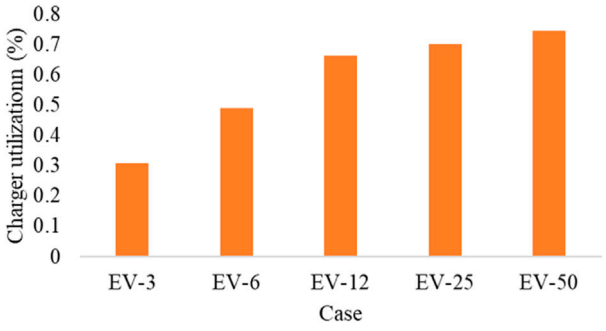

FIGURE 14
Charger utilization under different EV penetration levels.

transformer's available capacity. Figure 11 illustrates that the maximum count of chargers is employed during the evening hours due to the arrival of a higher number of EVs at home. However, it is essential to note that, across each case, the maximum available chargers are utilized.

Examining the satisfaction index in Figure 12 reveals a significant increase in satisfaction levels for the initial three cases, reaching a saturation point in the last two cases. Notably, the satisfaction level for the last two cases remains consistent. This outcome suggests that, considering the fixed transformer capacity and driving behaviors of EV owners, increasing the number of chargers beyond 5 does not notably affect satisfaction. Such results hold vital importance for policymakers to determine the minimum necessary number of chargers for a given EV count.

5.2 Penetration level of EVs

In this section, the share of the EV fleet incrementally increased up to 50% across five simulation cases. Starting from around 3% of the total fleet (320 vehicles), the penetration rate is doubled in each case until it reaches 50% (160 EVs). For consistency, the number of chargers remains fixed at five, and the transformer capacity is set at 35 kW throughout these simulations.

The analysis primarily focuses on the total power consumption of the chargers for each case. Additionally, a charger utilization index is devised to estimate the chargers' utilization under varying penetration rates. The community's satisfaction is also evaluated, and the outcomes are visualized in Figures 13–15. Figure 12 illustrates a proportional increase in charger power consumption with the growing number of EVs, which is an expected outcome. However, the power consumption becomes constrained by the remaining capacity of the transformer (35 kW), notably evident in the last three cases. Consequently, it can be inferred that the current configuration of five chargers and a 35-kW transformer capacity cannot sustain more than a 6% penetration of EVs.

Figure 14 shows the utilization level of chargers during the scheduling horizon (24 h). The utilization is computed using

$$CU = \sum_{t \in T} \sum_{i \in I} \frac{B_{i,t}^{ch}}{T \cdot N^{ch}} \tag{9}$$

Where $B_{i,t}^{ch}$ is the inary varibale indiciating the usage status of the charger, T is the total number of intervals in the scheduling horizon (24 in this case), and N^{ch} is the number of chargers (5 in this case). Figure 14 illustrates that as the EV penetration increases, there's a corresponding rise in charger utilization throughout the scheduling horizon. However, it is evident that there's still some potential to further increase charger utilization in all cases. Nonetheless, this

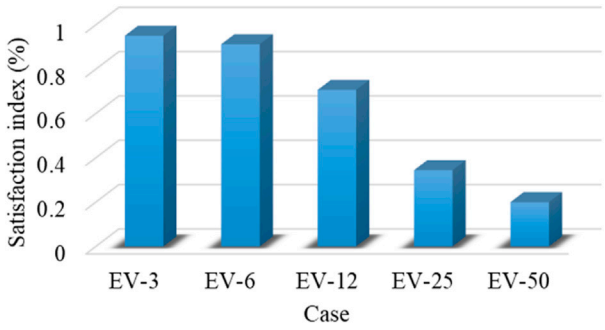

FIGURE 15
Community satisfaction index under different EV penetration levels.

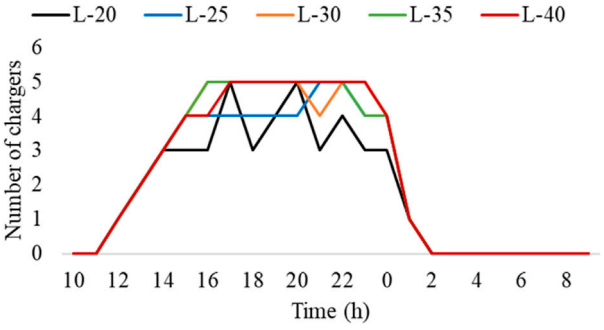

FIGURE 17
Charger utilization under different transformer capacity limits.

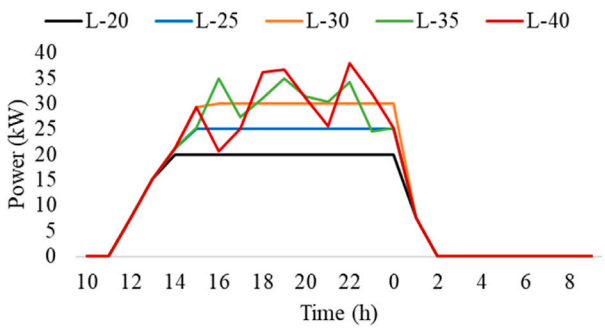

FIGURE 16
Total power consumption under different transformer capacity limits.

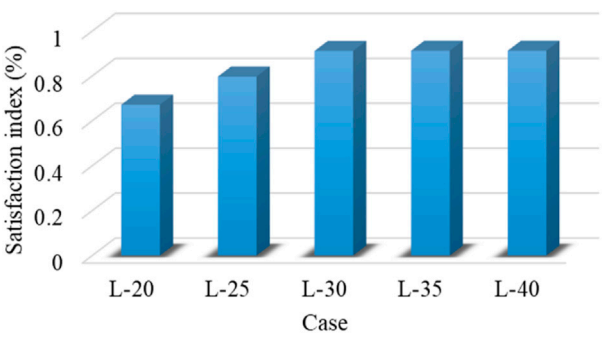

FIGURE 18
Community satisfaction under different transformer capacity limits.

potential expansion is curtailed by the transformer's capacity limitation, as depicted by the power consumption trends in Figure 13.

Examining Figure 15 reveals a decrease in the satisfaction level of the EV community with the escalating EV penetration rates. This decline is directly linked to the transformer's capacity limitations. As the number of EVs increases, more capacity becomes necessary. Consequently, these results suggest that an increasing number of EVs are unable to fulfill their energy demands before their departure times.

This analysis underscores that relying solely on charger utilization as a measure is not sufficient to determine the optimal number of chargers or the EV penetration level. It is imperative to consider both charger utilization and customer satisfaction collectively to determine the most suitable number of chargers for any EV community.

5.3 Impact of transformer capacity

In this section, five simulations are conducted by varying the capacity of the transformer. The analysis includes power consumption, charger utilization, and EV user satisfaction, displayed in Figures 16–18. For these simulations, the number of chargers remains fixed at 5, with 20 EVs considered.

Figure 16 illustrates that the charging power is restricted by the transformer's capacity limits in the initial three cases. However, in the last two cases, the power remains below the capacity limit for most intervals. Additionally, Figure 17 demonstrates that due to these capacity constraints, all chargers are not fully utilized in the first three cases. Conversely, in the last two cases, all five chargers are utilized to maximize consumer satisfaction.

The community satisfaction index in Figure 18 shows an increase during the first three cases and remains stable in the last two cases. This implies that, for this community comprising 20 EVs and 5 chargers, a transformer capacity exceeding 30 kW proves sufficient. Moreover, increasing the transformer capacity beyond this threshold does not significantly impact consumer satisfaction levels. Such insights are crucial for utilities in planning transformer upgrades considering a certain level of EVs and chargers.

5.4 Potential policy implications

Based on the findings of this study, following policy implications can be inferred. Firstly, the study demonstrates the effectiveness of

the proposed framework in efficiently allocating energy and utilizing chargers. The results show that with proper scheduling, EV energy demands can be met while ensuring charger availability and avoiding overloading the transformer. This suggests that policymakers should consider implementing similar optimization strategies in residential areas to manage EV charging effectively.

Secondly, the study highlights the importance of infrastructure planning. The analysis shows that increasing the number of chargers beyond a certain point does not significantly improve user satisfaction. This suggests that policymakers should focus on installing an optimal number of chargers based on factors such as transformer capacity and EV penetration rate. Additionally, the study suggests that increasing transformer capacity can improve user satisfaction up to a certain point, indicating that utilities should consider upgrading transformers in areas with high EV penetration.

Lastly, the study emphasizes the need for incentives to encourage EV owners to adjust their charging behavior. The satisfaction index shows that some EVs are not able to fulfill their energy demands due to charger unavailability. Incentives such as time-of-use pricing or rewards for off-peak charging could help distribute charging load more evenly and improve overall system performance.

6 Conclusion

A framework has been proposed to effectively manage the load of electric vehicles in shared parking lots, considering various critical factors such as the number of chargers, EV penetration levels, and the remaining capacity of the transformer. This framework utilizes a linear programming-based model to simulate diverse scenarios and introduces an index to quantitatively measure the satisfaction level of vehicle owners based on the energy charged before their departure time. Simulation outcomes have revealed that, for a given apartment complex, a consumer satisfaction level exceeding 75% can be achieved when 3% of the total vehicle fleet comprises EVs. Moreover, sensitivity analysis has demonstrated that merely five chargers can elevate the satisfaction level beyond 80% with an EV penetration level of up to 6% (20 EVs). However, the transformer capacity emerges as a pivotal factor in maximizing EV user satisfaction, particularly with higher EV penetration. The findings suggest that the transformer's capacity can become a bottleneck as EV penetration increases. Consequently, it is imperative for policymakers and utilities to collaboratively determine the optimal number of chargers concerning both the transformer's capacity and the expected EV penetration levels. Furthermore, planning equipment upgrades becomes crucial, necessitating considerations of imminent EV and charger penetration levels. Solely increasing the number of chargers is not advantageous under the constraints imposed by the transformer's limited capacity. Thus, a comprehensive approach integrating multiple factors is vital for optimizing EV load management and ensuring consumer satisfaction in shared parking lots.

In this study, the feasibility analysis of managing electric vehicle loads is conducted at a higher level, focusing on overall load management strategies without considering the detailed power flow within the distribution system. The inclusion of power flow analysis would significantly enhance the practicality of this method by providing more detailed insights into how the proposed load management strategies would impact the distribution system's operation and performance. Power flow analysis would allow for a more accurate assessment of potential voltage fluctuations, line losses, and overall system stability, enabling policymakers and utilities to make more informed decisions regarding electric vehicle integration and infrastructure planning.

Data availability statement

The original contributions presented in the study are included in the article/Supplementary material, further inquiries can be directed to the corresponding author.

Author contributions

AA: Conceptualization, Writing–original draft. NA: Methodology, Writing–review and editing. SA: Software, Writing–review and editing. OA: Validation, Writing–review and editing. HM: Formal Analysis, Validation, Writing–original draft.

Funding

The author(s) declare financial support was received for the research, authorship, and/or publication of this article. This research was funded by the Deputyship for Research and Innovation, Ministry of Education in Saudi Arabia, project number (IFP-2022-24).

Acknowledgments

The authors extend their appreciation to the Deputyship for Research and Innovation, Ministry of Education in Saudi Arabia, for funding this research work through project number (IFP-2022-24).

Conflict of interest

The authors declare that the research was conducted in the absence of any commercial or financial relationships that could be construed as a potential conflict of interest.

Publisher's note

References

Ahmadi, M., Sayed, M., Danish, S., Josip, A., Šoli´c, Š., Jakus, D., et al. (2023). Electric vehicle charging station power supply optimization with V2X capabilities based on mixed-integer linear programming. *Sustain* 15, 16073. doi:10.3390/SU152216073

Almutairi, A., and Alrumayh, O. (2022). Optimal charging infrastructure portfolio for minimizing grid impact of plug-in electric vehicles. *IEEE Trans. Ind. Inf.* 18, 5712–5721. doi:10.1109/TII.2022.3146292

Almutairi, A., and Alyami, S. (2021). Load profile modeling of plug-in electric vehicles: realistic and ready-to-use benchmark test data. *IEEE Access* 9, 59637–59648. doi:10.1109/ACCESS.2021.3072982

Chen, Y.-W., and Chang, J. M. (2016). Fair demand response with electric vehicles for the cloud based energy management service. *IEEE Trans. Smart Grid* 9, 458–468. doi:10.1109/TSG.2016.2609738

Duan, Y., Zhao, Y., and Hu, J. (2023). An initialization-free distributed algorithm for dynamic economic dispatch problems in microgrid: modeling, optimization and analysis. *Sustain. Energy, Grids Netw.* 34, 101004. doi:10.1016/J.SEGAN.2023.101004

EV Database (2023). Compare electric vehicles - EV database. Available at: https://ev-database.org/#sort:path~type~order=.rank~number~desc%7Crange-slider-range:prev~next=0~1200%7Crange-slider-acceleration:prev~next=2~23%7Crange-slider-topspeed:prev~next=110~350%7Crange-slider-battery:prev~next=10~200%7Crange-slider-towweight:pre (accessed on November 30, 2023).

Fachrizal, R., Ramadhani, U. H., Munkhammar, J., and Widén, J. (2021). Combined PV–EV hosting capacity assessment for a residential LV distribution grid with smart EV charging and PV curtailment. *Sustain. Energy, Grids Netw.* 26, 100445. doi:10.1016/J.SEGAN.2021.100445

Fathy, A., Al-Shamma', A. A., Farh, H. M. H., Almutairi, A., Albagami, N., Almesned, S., et al. (2023). Electric vehicle load estimation at home and workplace in Saudi Arabia for grid planners and policy makers. *Sustain* 15, 15878. doi:10.3390/SU152215878

Geotab (2023). Charge the north EV case study: EV preparation for fleets | geotab. Available at: https://www.geotab.com/blog/preparing-for-evs/(accessed on November 30, 2023).

Heuberger, C. F., Bains, P. K., and Mac Dowell, N. (2020). The EV-olution of the power system: a spatio-temporal optimisation model to investigate the impact of electric vehicle deployment. *Appl. Energy* 257, 113715. doi:10.1016/J.APENERGY.2019.113715

Hou, M., Zhao, Y., and Ge, X. (2017). Optimal scheduling of the plug-in electric vehicles aggregator energy and regulation services based on grid to vehicle. *Int. Trans. Electr. Energy Syst.* 27, e2364. doi:10.1002/ETEP.2364

Hussain, A., Bui, V. H., and Musilek, P. (2023). Local demand management of charging stations using vehicle-to-vehicle service: a welfare maximization-based soft actor-critic model. *eTransportation* 18, 100280. doi:10.1016/J.ETRAN.2023.100280

Hussain, A., and Musilek, P. (2021). "A game-theoretic approach for charging demand management of electric vehicles during system overload," in 2021 IEEE Electr. Power Energy Conf. EPEC, Toronto, ON, Canada, October, 2021, 353–358.

Hussain, A., and Musilek, P. (2022a). Resilience enhancement strategies for and through electric vehicles. *Sustain. Cities Soc.* 80, 103788. doi:10.1016/j.scs.2022.103788

Hussain, A., and Musilek, P. (2022b). Reliability-as-a-Service usage of electric vehicles: suitability analysis for different types of buildings. *Energies* 15, 665. doi:10.3390/EN15020665

IBM CPLEX (2023). Mathematical program solvers - IBM CPLEX. Available at: https://www.ibm.com/products/ilog-cplex-optimization-studio/cplex-optimizer (accessed on November 30, 2023).

IEA Global EV (2023). Outlook 2023 – analysis - IEA. *Int. Energy Agency*, 1–142.

Khan, Z. A., Imran, M., Altamimi, A., Alvarez-Alvarado, M. S., Sudhakar Babu, T., and Almutairi, A. (2022). Impact assessment of diverse EV charging infrastructures on overall service reliability. *Sustain* 14, 13295. doi:10.3390/SU142013295

Kong, W., Ye, H., Wei, N., Xing, D., and Chen, W. (2022). Dynamic pricing based EV load management in distribution network. *Energy Rep.* 8, 798–805. doi:10.1016/J.EGYR.2022.02.187

Lei, Y., Yanrong, C., Hai, T., Ren, G., and Wenhuan, W. (2023). DGNet: an adaptive lightweight defect detection model for new energy vehicle battery current collector. *IEEE Sens. J.* 23, 29815–29830. doi:10.1109/JSEN.2023.3324441

Li, P., Hu, J., Qiu, L., Zhao, Y., and Ghosh, B. K. (2022). A distributed economic dispatch strategy for power-water networks. *IEEE Trans. Control Netw. Syst.* 9, 356–366. doi:10.1109/TCNS.2021.3104103

Limmer, S., and Rodemann, T. (2019). Peak load reduction through dynamic pricing for electric vehicle charging. *Int. J. Electr. Power Energy Syst.* 113, 117–128. doi:10.1016/J.IJEPES.2019.05.031

Liu, G. (2021). Data collection in MI-assisted wireless powered underground sensor networks: directions, recent advances, and challenges. *IEEE Commun. Mag.* 59, 132–138. doi:10.1109/MCOM.001.2000921

Luo, J., Zhuo, W., Liu, S., and Xu, B. (2024). The optimization of carbon emission prediction in low carbon energy economy under big data. *IEEE Access* 12, 14690–14702. doi:10.1109/ACCESS.2024.3351468

Lyu, W., Hu, Y., Liu, J., Chen, K., Liu, P., Deng, J., et al. (2024). Impact of battery electric vehicle usage on air quality in three Chinese first-tier cities. *Sci. Rep.* 14, 21–13. doi:10.1038/s41598-023-50745-6

Mazhar, T., Asif, R. N., Malik, M. A., Nadeem, M. A., Haq, I., Iqbal, M., et al. (2023). Electric vehicle charging system in the smart grid using different machine learning methods. *Sustain* 15, 2603. doi:10.3390/SU15032603

Moghaddam, Z., Ahmad, I., Habibi, D., and Masoum, M. A. S. (2019). A coordinated dynamic pricing model for electric vehicle charging stations. *IEEE Trans. Transp. Electrif.* 5, 226–238. doi:10.1109/TTE.2019.2897087

NHTS (2023). NHTS datasets. Available at: https://nhts.ornl.gov/download.shtml (accessed on November 30, 2023).

Sayarshad, H. R., Mahmoodian, V., and Bojović, N. (2021). Dynamic inventory routing and pricing problem with a mixed fleet of electric and conventional urban freight vehicles. *Sustain* 13, 6703. doi:10.3390/SU13126703

Shao, B., Xiao, Q., Xiong, L., Wang, L., Yang, Y., Chen, Z., et al. (2023). Power coupling analysis and improved decoupling control for the VSC connected to a weak AC grid. *Int. J. Electr. Power Energy Syst.* 145, 108645. doi:10.1016/J.IJEPES.2022.108645

Shirkhani, M., Tavoosi, J., Danyali, S., Sarvenoee, A. K., Abdali, A., Mohammadzadeh, A., et al. (2023). A review on microgrid decentralized energy/voltage control structures and methods. *Energy Rep.* 10, 368–380. doi:10.1016/J.EGYR.2023.06.022

Tran, V. T., Islam, M. R., Muttaqi, K. M., and Sutanto, D. (2019). An efficient energy management approach for a solar-powered EV battery charging facility to support distribution grids. *IEEE Trans. Ind. Appl.* 55, 6517–6526. doi:10.1109/TIA.2019.2940923

Tulabing, R., James, J., Mitchell, B., Park, H., Boys, J., Salcic, Z., et al. (2018). Mitigation of local grid congestion due to electric vehicles through localized demand control. *Int. Conf. Innov. Smart Grid Technol. ISGT Asia*, 254–259. doi:10.1109/ISGT-ASIA.2018.8467768

Vision (2050). A strategy to decarbonize the global transport sector by mid-century | international council on clean transportation. Available at: https://theicct.org/publication/vision-2050-a-strategy-to-decarbonize-the-global-transport-sector-by-mid-century/(accessed on June 16, 2022).

Wang, Y., Chen, P., Yong, J., Xu, W., Xu, S., and Liu, K. (2022). A comprehensive investigation on the selection of high-pass harmonic filters. *IEEE Trans. Power Deliv.* 37, 4212–4226. doi:10.1109/TPWRD.2022.3147835

Yang, C., Wu, Z., Li, X., and Fars, A. (2024). Risk-constrained stochastic scheduling for energy hub: integrating renewables, demand response, and electric vehicles. *Energy* 288, 129680. doi:10.1016/J.ENERGY.2023.129680

Zhang, F., Wang, L., Coskun, S., Pang, H., Cui, Y., and Xi, J. (2020). Energy management strategies for hybrid electric vehicles: review, classification, comparison, and outlook. *Energies* 13, 3352. doi:10.3390/EN13133352

Zhang, H., Wu, H., Jin, H., and Li, H. (2023a). High-dynamic and low-cost sensorless control method of high-speed brushless DC motor. *IEEE Trans. Ind. Inf.* 19, 5576–5584. doi:10.1109/TII.2022.3196358

Zhang, X., Lu, Z., Yuan, X., Wang, Y., and Shen, X. (2021). L2-Gain adaptive robust control for hybrid energy storage system in electric vehicles. *IEEE Trans. Power Electron.* 36, 7319–7332. doi:10.1109/TPEL.2020.3041653

Zhang, X., Wang, Y., Yuan, X., Shen, Y., and Lu, Z. (2023b). Adaptive dynamic surface control with disturbance observers for battery/supercapacitor-based hybrid energy sources in electric vehicles. *IEEE Trans. Transp. Electrif.* 9, 5165–5181. doi:10.1109/TTE.2022.3194034

Zhang, X., Wang, Z., and Lu, Z. (2022). Multi-objective load dispatch for microgrid with electric vehicles using modified gravitational search and particle swarm optimization algorithm. *Appl. Energy* 306, 118018. doi:10.1016/J.APENERGY.2021.118018

frontiers | Frontiers in Energy Research

TYPE Original Research
PUBLISHED 27 May 2024
DOI 10.3389/fenrg.2024.1413252

OPEN ACCESS

EDITED BY
Flah Aymen,
École Nationale d'Ingénieurs de Gabès, Tunisia

REVIEWED BY
Rajeev Kumar,
KIET Group of Institutions, India
Imane Hammou Ou Ali,
Mohammed V University, Morocco

*CORRESPONDENCE
Abdullah Ali Alhussainy,
aalhussainy0001@stu.kau.edu.sa

RECEIVED 06 April 2024
ACCEPTED 08 May 2024
PUBLISHED 27 May 2024

CITATION
Aifan G. Alsulami A, Alhussainy AA, Allehyani A, Alturki YA, Alghamdi SM, Alruwaili M and Alharthi YZ (2024), A comparison of several maximum power point tracking algorithms for a photovoltaic power system.
Front. Energy Res. 12:1413252.
doi: 10.3389/fenrg.2024.1413252

A comparison of several maximum power point tracking algorithms for a photovoltaic power system

Abdulellah Aifan G. Alsulami[1], Abdullah Ali Alhussainy[1]*, Ahmed Allehyani[2], Yusuf A. Alturki[1,3], Sultan M. Alghamdi[1], Mohammed Alruwaili[4] and Yahya Z. Alharthi[5]

[1]Department of Electrical and Computer Engineering, Faculty of Engineering, King Abdulaziz University, Jeddah, Saudi Arabia, [2]Electrical and Electronic Engineering Department, University of Jeddah, Jeddah, Saudi Arabia, [3]K. A. CARE Energy Research and Innovation Center, King Abdulaziz University, Jeddah, Saudi Arabia, [4]Department of Electrical Engineering, College of Engineering, Northern Border University, Arar, Saudi Arabia, [5]Department of Electrical Engineering, College of Engineering, University of Hafr Albatin, Hafr Al Batin, Saudi Arabia

This paper presents a comparative study between traditional and intelligent Maximum Power Point Tracking (MPPT) algorithms for Photovoltaic (PV) powered DC Shunt Motors. Given the nonlinearity of PV systems, they require nonstandard approaches to harness their full potential. Each PV module has a unique maximum power point on its IV curve due to its nonlinear characteristic nature. Power electronic converters are utilized to enable operation at that point. There are many different algorithms described in the introduction, each with its have their own advantages and drawbacks. Recognizing the potential enhancement of PV system efficiency through effective Maximum Power Point (MPP) tracking, this paper evaluates five MPPT methods under varying DC loads. The five algorithms will be as follows: Incremental Conductance and Perturb and Observe as traditional algorithms. Fuzzy Logic Control, Artificial Neural Networks, and Adaptive Neuro-Fuzzy Inference Systems as Intelligent Algorithms. While traditional algorithms generally produced acceptable results except for Perturb & Observe, intelligent algorithms performed well under rapidly changing solar radiation conditions. Due to inadequate data, intelligent algorithms relying on data training struggled to track the maximum power point when the temperature changed due to inadequate data used for the training. The analysis focuses on the time required by each method to reach peak power under different load conditions, solar irradiance, and temperature variations. The advantages and disadvantages of each MPPT with a shunt DC motor are detailed in the comparative study.

KEYWORDS

photovoltaic (PV), maximum power point (MPP), incremental conductance (INC), perturb and observe (PO), standard test condition (STC), fuzzy logic control (FCL), artificial neural networks (ANN), adaptive neuro fuzzy inference system (ANFIS)

Abbreviations: MPPT, Maximum Power Point Tracking; MMP, Maximum Power Point; PV, Photovoltaic; DC, Direct Current; INC, Incremental Conductance; PO, Perturb and Observe; STC, Standard Test Condition; FCL, Fuzzy Logic Control; ANN, Artificial Neural Networks; ANFIS, Adaptive neuro fuzzy inference system; P Control, Proportional Control; AI, Artificial Intelligence; NB, Negative Big; NM, Negative Medium; NS, Negative Small; PB, Positive Big; ZE, Zero; PM, Positive Medium; G, solar radiation; T, temperature; Vmpp, voltage at maximum power; TL, The load torque.

1 Introduction

Solar power has become a prominent leader in renewable energy due to its reduced cost and ecologically friendly nature, providing a sustainable alternative to fossil fuels (Hasaneen and Mohammed, 2008). The impact of solar energy on this endeavor has been remarkably substantial. The study mentioned in Yang et al. (2024) emphasizes the potential of rural rooftop photovoltaic (PV) systems in addressing regional energy disputes. Additionally, the study mentioned in ang et al. (2024) demonstrates how integrated solar electricity can contribute to sustainable urban growth. In addition, the utilization of solar energy in various systems has been examined in Gao et al. (2024), Yan et al. (2024) through the optimization of hybrid microgrids and renewable-based systems. In addition, the influence of solar energy on the control and dynamic economic dispatch in microgrids has been examined in references (Duan et al., 2023; Shirkhani et al., 2023). These contribute to the enhancement of our comprehension regarding the influence of solar energy on the formation of future energy environments.

With the increasing popularity of PV systems, their production costs have decreased, although inefficiency continues to be a persistent issue. Both the temperatures of the cells and the intensity of sunlight have a crucial influence in determining the power output of photovoltaic (PV) systems. Due to the reliance of PV energy output on factors such as sun's irradiance, ambient temperature, and load, there is no assurance of consistent energy delivery. MPPT, or Maximum Power Point Tracking, is the method used to identify the optimal operating point for a solar PV cell based on certain environmental conditions. By utilizing the Maximum Power Point Tracking (MPPT) technology, the photovoltaic (PV) module achieves enhanced performance and increased longevity. These tactics are employed to optimize the power output of a photovoltaic (PV) module by enhancing its operational efficiency. Figure 1 illustrates the relationship between output power and voltage, and demonstrates how it varies with different levels of solar irradiation. Figure 1 demonstrates that there is a specific point during operation where the PV module reaches its maximum usable power. At that instant, the system must be operated using a Maximum Power Point Tracking (MPPT) technique. Creating sustainable, efficient, and environmentally-friendly energy sources is a top priority in contemporary science and technology (Hasaneen and Mohammed, 2008). Solar power systems, due to their extensive availability, are leading the way in renewable energy research. Although the cost of photovoltaic systems has decreased, improving efficiency continues to be a difficult task. Both the ambient temperature and sunshine intensity have a considerable impact on the output power of these devices.

Unlike traditional power plants, solar energy production relies heavily on unpredictable factors like sunlight irradiance and temperature. This variability necessitates the use of Maximum Power Point Tracking (MPPT) techniques. MPPT ensures a solar photovoltaic (PV) cell operates at its optimal point for a given set of environmental conditions. This optimization extends the lifespan and improves the overall performance of the PV module. Figure 1 illustrates the relationship between output power, voltage, and varying solar irradiation levels. It clearly demonstrates a specific operating point where the PV module delivers maximum power. MPPT algorithms are crucial for operating the system at this optimal point.

Researchers worldwide are constantly striving to extract the most energy possible from renewable resources, particularly PV panels. Numerous MPPT algorithms have been proposed for both standalone and grid-connected PV systems (Bendib et al., 2015). Selecting the most suitable technique can be challenging as each offers advantages and drawbacks (Bhatnagar and Nema, 2013). Broadly, these methods can be categorized as traditional and intelligent approaches.

Traditional MPPT algorithms, such as Incremental Conductance (INC) and Perturb and Observe (P&O), are widely used due to their simple implementation and minimal sensor requirements (Teulings et al., 1993). The INC algorithm tracks the maximum power point (MPP) by monitoring the incremental and transient conductance of the PV system, efficiently delivering power to the load (Wasynezuk, 1983). Studies have shown that P&O and INC algorithms perform similarly under specific conditions (Sera et al., 2013).

However, with advancements in Artificial Intelligence (AI) and machine learning, researchers are exploring the potential of incorporating AI techniques into PV MPPT algorithms for improved accuracy, efficiency, and adaptability. AI-based MPPT solutions leverage the processing capabilities of AI algorithms to enhance MPP tracking and overcome limitations of conventional methods. AI facilitates modeling and

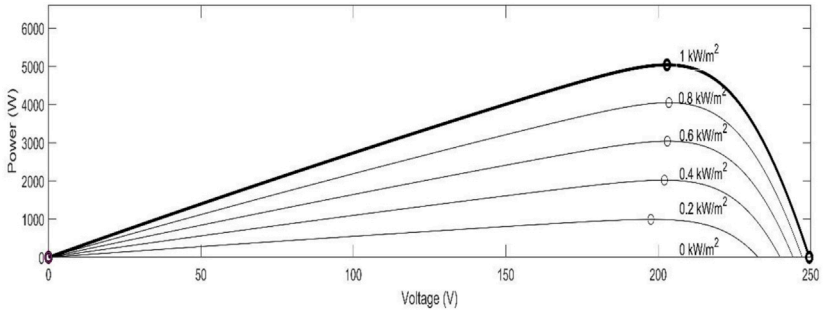

FIGURE 1
The effect of solar radiation variation on the output of PV arrays.

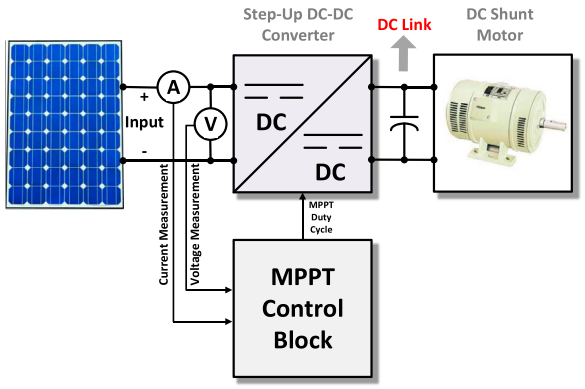

FIGURE 2
The traditional schematic diagram of operating DC shunt motors with solar PV.

understanding the non-linear characteristics of PV panels under various environmental conditions. Algorithms like Fuzzy Logic Control (Dehghani et al., 2021), Artificial Neural Networks (ANN) (Allahabadi et al., 2022), and Adaptive Neuro-Fuzzy Inference System (ANFIS) (Ibrahim et al., 2021) introduce a more dynamic and adaptable MPPT process. As shown in Figure 2, these AI methods offer an alternative approach to reaching the maximum power point by training on a dataset to achieve optimal controller behavior. While AI-based methods provide a promising alternative, they come with limitations such as complexity, cost, and difficulties in handling partially shaded irradiance scenarios.

The pursuit of developing more efficient and reliable Maximum Power Point Tracking (MPPT) algorithms is still ongoing. Bio-inspired algorithms inspired by natural phenomena hold significant promise. Further exploration of bio-inspired approaches, like improved versions of the Moth-Flame Optimizer for handling diverse shading conditions (Zhao et al., 2023), could be a fruitful avenue for future research. Additionally, metaheuristic optimization techniques offer exciting possibilities. Advancements in algorithms like the Novel Marine Predator Inspired Algorithm, focusing on global MPP convergence, warrant further investigation, particularly for complex shading scenarios (Qin et al., 2023). Finally, the potential of hybrid approaches that combine the strengths of traditional and intelligent techniques remains largely untapped. Building upon works like the Hybrid Firefly and Grey Wolf Optimization Algorithm, designed for rapidly changing irradiance, researchers can explore even more sophisticated hybrid models for a wider range of environmental challenges (Babu and Hussain, 2023). These areas of exploration hold the key to unlocking even greater efficiency and adaptability in future solar power systems. Table 1 summarize the key aspect in the literature.

Despite advancements in MPPT algorithms, there remains a significant research gap concerning their performance when interfacing with specific loads, such as the DC shunt motor, which has not been extensively explored in existing literature. Traditional MPPT techniques like Incremental Conductance (INC) and Perturb and Observe (P&O) offer simplicity but may exhibit limitations when connected to dynamic loads like the DC shunt motor, which can introduce complexities due to its varying characteristics and operational dynamics. Conversely, AI-based approaches such as Artificial Neural Networks (ANN) and Adaptive Neuro-Fuzzy Inference Systems (ANFIS) are known for their adaptability but have not been thoroughly investigated in the context of such loads.

This study aims to address this gap by analyzing the performances of various MPPT algorithms (INC, P&O, ANN, ANFIS) specifically when connected to a DC shunt motor load. By focusing on this specific load type, the research aims to provide valuable insights into how different MPPT algorithms perform in real-world scenarios where dynamic loads play a crucial role in system behavior.

The significance of this research lies in its contribution to understanding how MPPT algorithms behave under the influence of a DC shunt motor load, a scenario that has not been extensively studied in the literature. By conducting a comprehensive analysis, this study seeks to identify the strengths and weaknesses of each algorithm in this particular context, thereby guiding the selection of appropriate MPPT techniques for PV systems interfacing with DC shunt motor loads.

The contributions of this research can be summarized as follows:

- Investigating the performance of various MPPT algorithms (INC, P&O, ANN, ANFIS) when connected to a dynamic DC shunt motor load.
- Providing valuable insights into how different MPPT algorithms behave under the influence of a specific load

TABLE 1 Comparative tabular analysis of MPPT algorithms with references.

Algorithm	Advantages	Disadvantages	Suitable for conditions	Reference
Incremental Conductance (INC)	Simple implementation	Requires continuous sensor data	Stable irradiance	Teulings et al. (1993)
Perturb and Observe (P&O)	Simple implementation	Oscillates around MPP	Stable irradiance	Teulings et al. (1993)
Fuzzy Logic Control (FLC)	Adapts to changing conditions	Requires rule base development	Rapidly changing weather	Ansari et al. (2010)
Artificial Neural Network (ANN)	Handles non-linearity	Requires training data	Diverse irradiance and temperature	Allahabadi et al. (2022)
Adaptive Neuro-Fuzzy Inference System (ANFIS)	Combines ANN and FLC benefits	More complex than other methods	Complex operating conditions	Wasynezuk (1983)

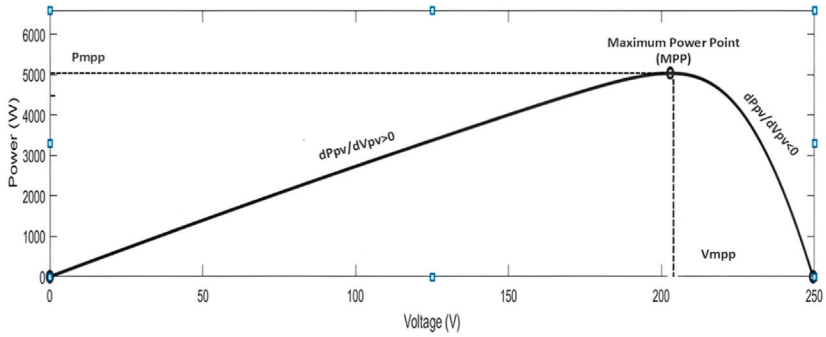

FIGURE 3
The maximum power point of the PV power.

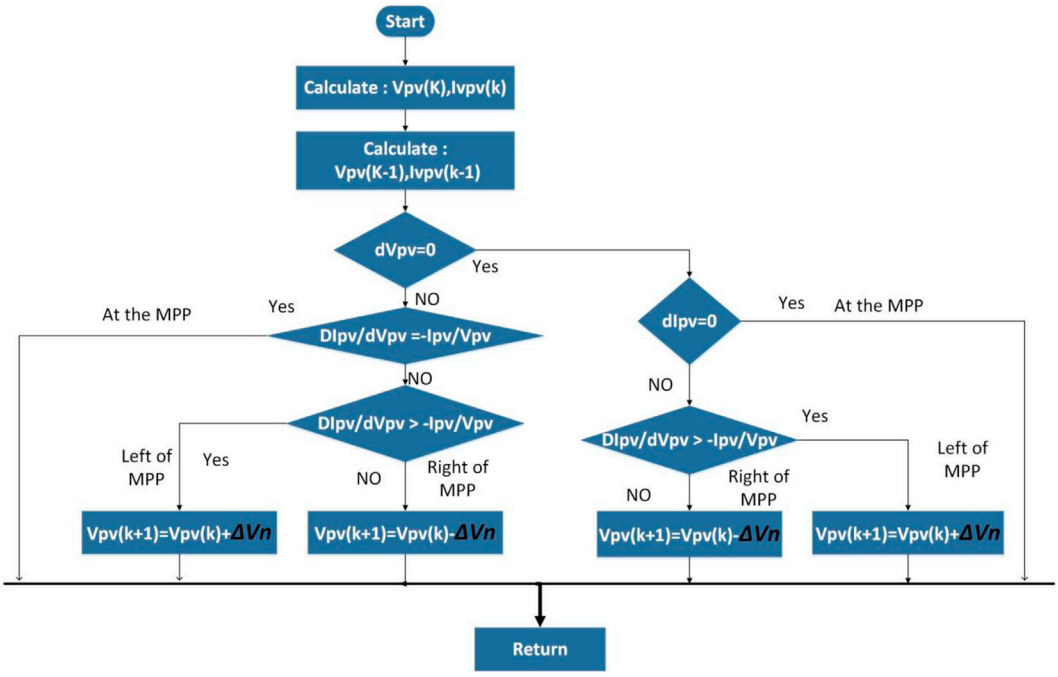

FIGURE 4
The flowchart of the incremental conductance method.

type, facilitating informed decision-making in the selection of MPPT techniques for PV systems.

- Bridging the gap in understanding the behavior of MPPT algorithms in real-world scenarios where dynamic loads like the DC shunt motor are prevalent, thereby contributing to the advancement of MPPT technology in practical applications.

These contributions hold significant implications for the design and optimization of PV systems, particularly in scenarios where dynamic loads play a critical role in system performance and efficiency. By shedding light on the performance of MPPT algorithms with a DC shunt motor load, this research aims to pave the way for further advancements in the field of PV system optimization and control.

The rest of this section will provide a detailed introduction to various Maximum PowerPoint Tracking algorithms, including Incremental Conductance, Perturb and Observe, Fuzzy Logic Control, Artificial Neural Networks, and Adaptive Neuro-Fuzzy Inference System. Section 2 delves into the configuration of the Photovoltaic System, covering modeling, parameters used in this research (Photovoltaic Array, Boost Converter, DC Shunt Motor), and the methodology employed. Section 3 presents the obtained results, analyzes the performance of the system under various weather conditions with each algorithm, and discusses the key takeaways from our research.

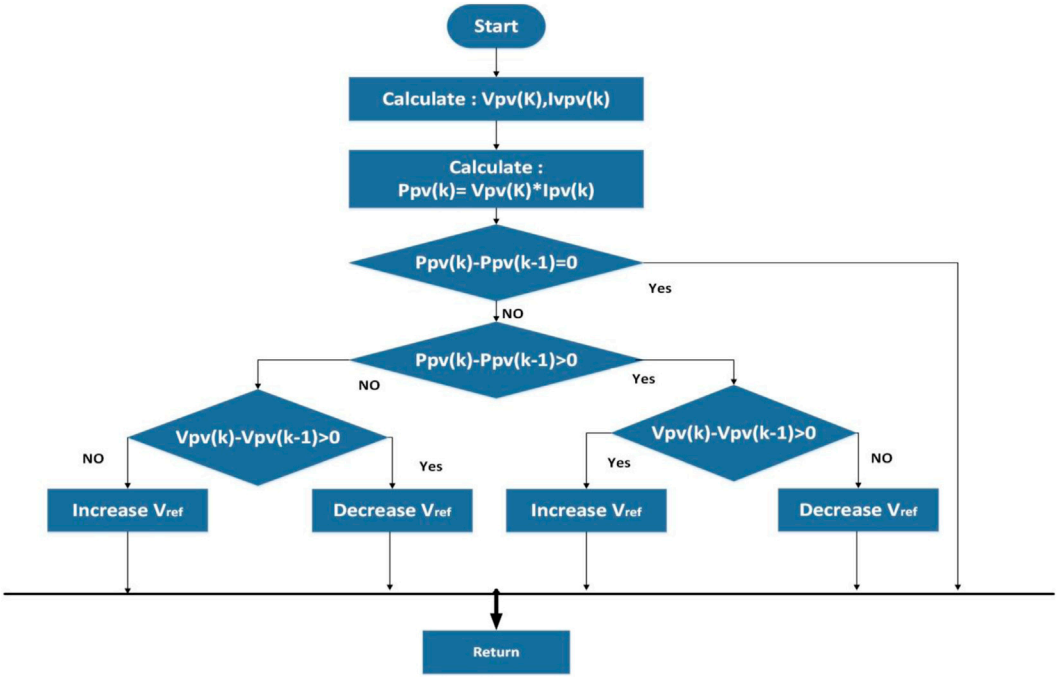

FIGURE 5
The flowchart of the P&O method.

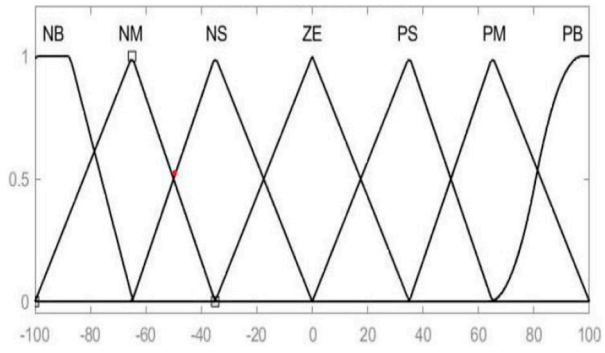

FIGURE 6
Membership function of E(K).

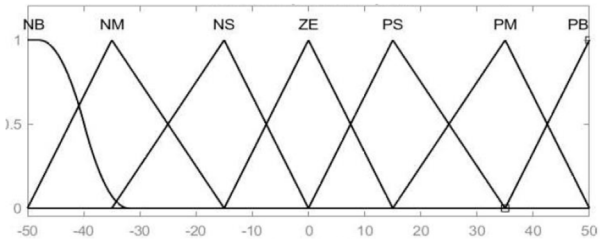

FIGURE 7
Membership function of ΔE(K).

1.1 Incremental conductance method

Many traditional MPPT techniques rely on the principle that the peak power point occurs when the P-V curve's slope is zero (Ibrahim et al., 2021). The rate of change as a measure of "power sensitivity" to voltage adjustments.

- If the power increases with voltage (dP_{pv}/dV_{pv}) > 0, the system is currently left of the optimal point, and raising the voltage drives it closer to the peak.
- Conversely, if the power decreases with voltage (dP_{pv}/dV_{pv}) < 0, the system is to the right of the maximum point, and lowering the voltage steers it in the right direction. This concept is illustrated in Figure 3.

Based on this principle, algorithms like Incremental Conductance (IC) continuously calculate (dP/dV), which represents the "instantaneous conductance" of the system. It then compares this value to the actual "incremental conductance" calculated from voltage and current changes. Figure 4 visualizes the process of adjusting voltage based on this comparison to continuously track the MPP (Elbaset et al., 2020).

1.1.1 Perturb and observe

The system manipulates both current and voltage by adjusting a converter's operating cycle (Ebrahimi, 2017). When power falls below peak efficiency, voltage is boosted. Conversely, if power exceeds its optimum level, voltage is reduced. This "Perturb and Observe" (P&O) approach is favored for its simplicity but suffers

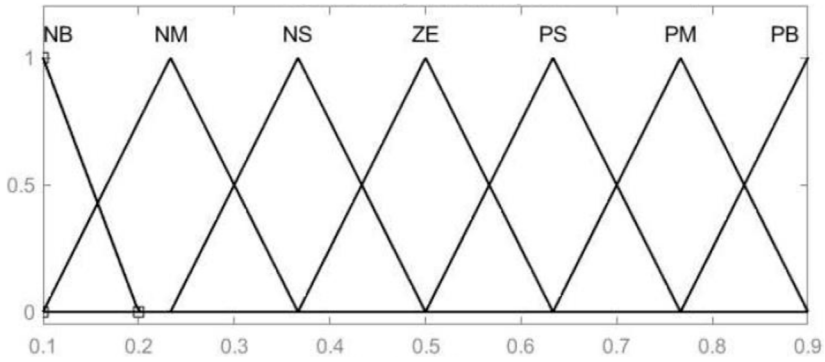

FIGURE 8
Membership function of D(K).

TABLE 2 The fuzzy rules used in the inference engine stage.

E(k)	ΔE(k)						
	NB	NM	NS	ZE	PS	PM	PB
NB	NB	NB	NB	NB	NM	NS	ZE
NM	NB	NB	NB	NM	NS	ZE	PS
NS	NB	NB	NM	NS	ZE	PS	PM
ZE	NB	NM	NS	ZE	PS	PM	PB
PS	NM	NS	ZE	PS	PM	PB	PB
PM	NS	ZE	PS	PM	PB	PB	PB
PB	ZE	PS	PM	PB	PB	PB	PB

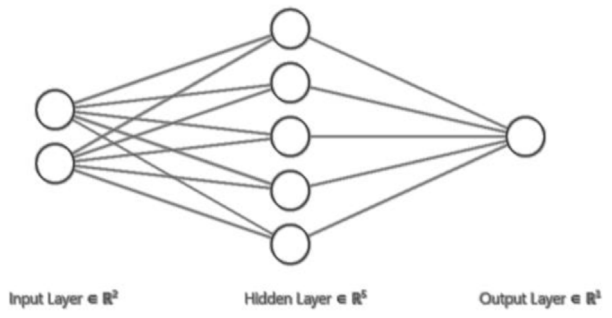

FIGURE 9
The architecture of a simple ANN.

from power fluctuations around the peak point. See Figure 5 for a visual representation of the algorithm (Hart, 2011).

1.2 Fuzzy logic control method

Fuzzy Logic Control (FLC) evaluates the data with varying variables as opposed to explicit logic, which evaluates the data using only true or false. In FLC, we have varying variables between true or false which allows for a more accurate evaluation of the data. The variables in fuzzy logic are converted into linguistic variables to describe the different degrees of the data (Eltamaly, 2020).

FLCs stand out in maximum power point tracking (MPPT) due to their ability to perform effectively without requiring prior knowledge of the photovoltaic (PV) system. This characteristic makes FLCs particularly well-suited for scenarios with rapidly changing weather conditions, where swift adaptation is crucial (Ansari et al., 2010; AzzouziM, 2012).

During MPPT with FLCs, the system's power output undergoes continuous measurement and evaluation. To assess the trend towards the MPP, the rate of change in power with respect to voltage (dP/dV) is calculated. This information, along with the current error (E(k)) and its rate of change (ΔE(k)), forms the input to the FLC, guiding its decision-making process using Eqs 1, 2 as follows (Samosir et al., 2018):

$$\mathrm{E(K)} = \frac{P(k) - P(K-1)}{V(k) - V(K-1)} \tag{1}$$

$$\Delta E(k) = E(k) - E(k-1) \tag{2}$$

Analyzing the error signal, E(k), and its change, ΔE(k), helps understand the location and movement of the MPP on the P-V curve. The error value shows whether the MPP is to the left or right of the present operating point, whereas the change in error reflects the MPP's direction of travel. Using these indications, a control system may make smart modifications to approach the MPP and maximize power generation (Elbaset et al., 2020; Ibrahim et al., 2021).

Fuzzification converts the error E(k) and change of error ΔE(k) into fuzzy inputs using a membership function, such as Negative Big (NB) and Positive Big (PB). The inference engine will use the rule of assessing the input to determine the FLC's suitable linguistic value output. The rules in the inference engine manage the boost converter's duty cycle and monitor power changes. De-fuzzification converts the inference engine's output from linguistic variables to mathematical variables with crisp values, as explained in (Wasynezuk, 1983). Figures 6–8 illustrate the membership functions of E(K), ΔE(k), and the output membership function. Table 2 shows the Fuzzy rules that were

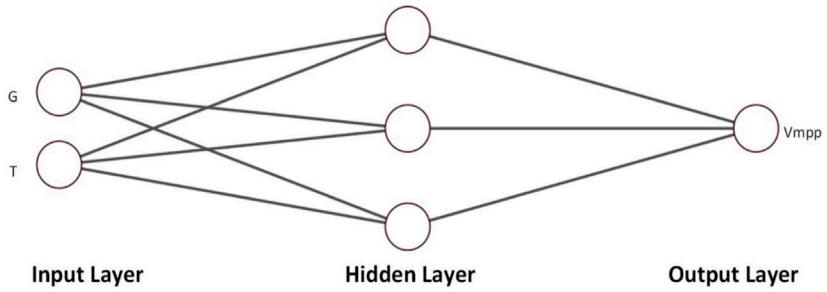

FIGURE 10
The structure of the ANN used in MPPT.

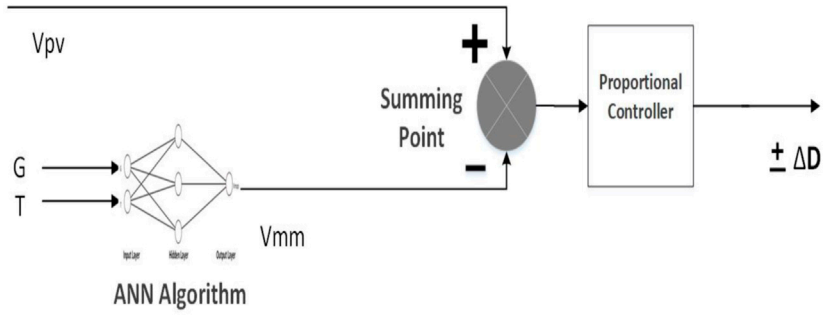

FIGURE 11
The Structure of used ANN in tracking the maximum power.

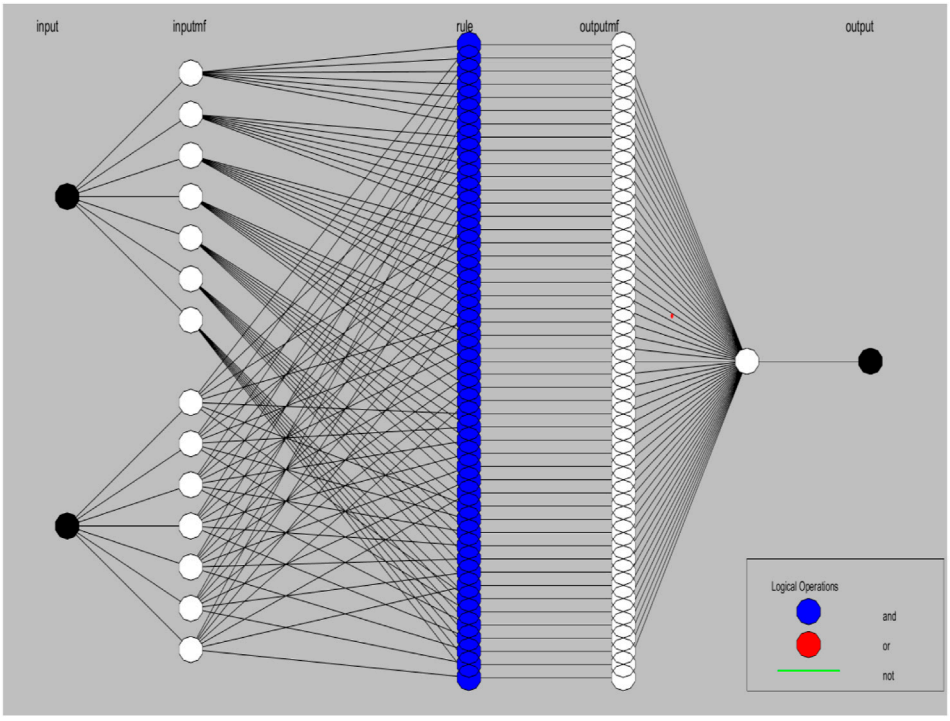

FIGURE 12
The structure of the used ANFIS.

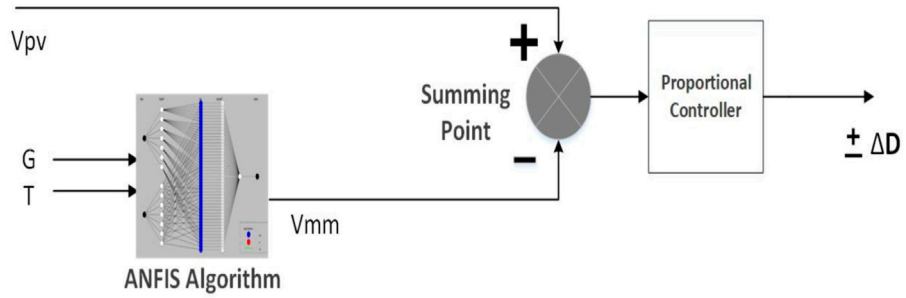

FIGURE 13
The structure of the used ANFIS.

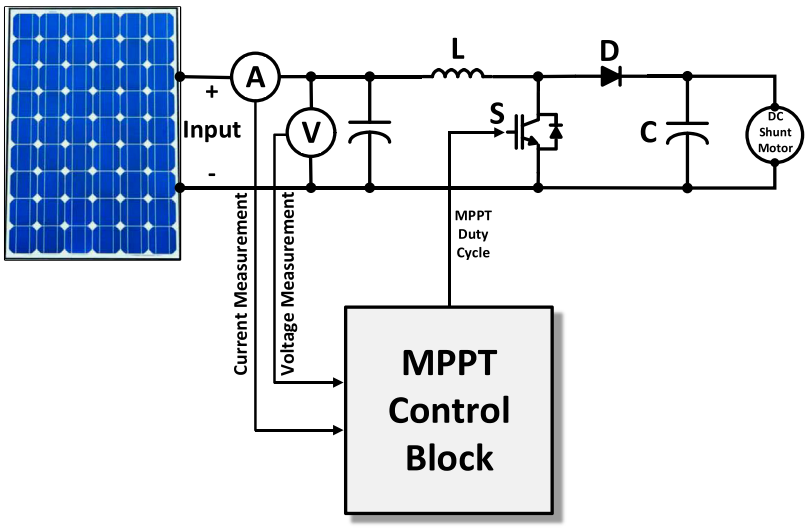

FIGURE 14
PV system, DC boost converter and DC shunt motor circuit schematic.

utilized in the inference engine stage that controlled the input and output variables.

1.3 Artificial neural networks method

Artificial Neural Network (ANN) is an information processing technique inspired by biological neurons to simulate the neurons in human brains. ANN is a type of supervised learning algorithm, which means that it learns by examples. When the ANN is subjected to training sets, it adjusts the weights based on the learning rule (Ebrahimi, 2017). The architecture of a simple ANN is shown in Figure 9.

The simple ANN here consists of an input layer, hidden layer, and output layer connected with the weights. Any layer may consist of many neurons or nodes, as we see here in the hidden layer, which contains five neurons. Multi-hidden layers can also be used in the ANN. Any nonlinear system can be modeled using ANN with suitable representation, making it useful for solving nonlinear systems. Moreover, ANN is very useful for handling incomplete or corrupted data because the ANN does not require any apriori knowledge (Ebrahimi, 2017).

ANN can be used for pattern recognition and classification as well as help in optimization problems, prediction, and control. In power systems we can use ANN in Load forecasting, economic dispatch, security assessment, fault location problems, and power system stability and control (Hart, 2011). As in Eltamaly (2020), the authors recommended using artificial neural networks (ANN) to track the highest power point under various meteorological circumstances. The ANN consists of three layers: the input layer, which includes the irradiance and temperature, the hidden layer, and the output layer, which estimates the voltage at the highest power point, as shown in Figure 10. The temperature range is 25°C–55°C, and the sun radiation range is 0–1,000 W/m^2. The ANN was trained with the error back propagation approach. Figure 11 depicts the structure used to track the MPP, with the inputs being solar radiation (G) and temperature (T), and the controller estimating the voltage at maximum power (Vmpp). Then, the difference is attenuated based on the used system to be the required change in the duty cycle ±ΔD.

10.3389/fenrg.2024.1413252

TABLE 3 The parameter of the PV system including the PV array, dc-dc Boost converter and DC shunt motor.

PV array data	
Parallel strings	4
Series-connected modules per string	6
Maximum Power (W)	209.96
Cells per module (Ncell)	70
Open circuit voltage (V)	41.59
Short-circuit current (A)	7.13
Voltage at maximum power point (V)	33.81
Current at maximum power point (A)	6.21
Voc (%/deg.C)	−0.36529
Isc (%/deg.C)	0.057097
Irradiances (W/m^2)	1,000
Temperature cell (deg.C)	25
Model Parameter	
Light-generated current (A)	7.1824
I_D (A)	2.8024×10^{-10}
Diode ideality factor	0.96937
Rsh (ohms)	55.2029
Rs (ohms)	0.40559
Boost Converter Data	
DC Link Capacitance (mF)	1
Inductance (μH)	24
Outer Capacitance (mF)	5
Switching Frequency (kHz)	20
DC Shunt Motor	
Armature circuit resistance of winding (ohms)	11.2
Field circuit resistance of winding (ohms)	281.3
Inductance of the armature circuit (H)	0.1215
Field circuit inductance (H)	156

1.4 Adaptive neuro fuzzy inference system

Instead of relying solely on human-created rules, the ANFIS enhances performance by leveraging the capabilities of ANNs and FLC. ANFIS employs an ANN to analyze input data, minimize error [E(k)] and rate of change [ΔE(k)], and predict the desired output voltage at the highest power point. This predicted output is supplied to the FLC, which dynamically adjusts the duty cycle of the control parameters to keep the system running at peak efficiency. Using ANN in ANFIS serves two important purposes: first, it decreases error when compared to completely hand-tuned rules, and second, it automates the optimization process, removing the time-consuming trial-and-error approach to rule and membership function creation. Furthermore, FLC's intrinsic tolerance for imperfect inputs improves the overall robustness and efficacy of ANFIS (Wasynezuk, 1983). Figure 12 shows the ANFIS architecture, which processes two input signals [E(k) and ΔE(k)] using seven separate membership functions. The resultant rule activations are then aggregated, and the output membership function calculates the system's maximum power voltage.

The construction of the ANFIS utilized to track the greatest power point is depicted in Figure 13. The controller will estimate the voltage at maximum power (Vmpp) from the inputs of solar radiation (G) and temperature (T). Vmpp is then subtracted from the voltage of the PV array, and the difference is attenuated based on the used system to be the required change in the duty cycle ±ΔD as discussed previously.

2 Configuration of the photovoltaic system

The solar power generation unit, consisting of photovoltaic panels and a controller, will harness the sun's energy and provide direct current electricity. This direct current will be electronically adjusted by a dedicated converter before powering the DC motor (detailed in Figure 14). Let's delve deeper into the intricacies of this solar power generation unit.

2.1 The Photovoltaic array

The PV system is comprised of semiconductor-based solar cells. Solar cells convert solar energy (or sunlight) into electrical energy (Ansari et al., 2010). The PV system's current-voltage relationship is as follows using Eq. 3:

$$I_{pv} = I_D - I_{ph} - I_{sh=}I_{ph} - I_0\left[e^{\frac{q}{A.K.T(V_{Pv}+I_{Pv}+R_s)}-1}\right] - \frac{I_{pv}.R_s + V_{pv}}{R_{sh}} \quad (3)$$

The equation illustrates how many critical elements influence the current output of a photovoltaic (PV) cell. Here's a breakdown of every term:

I_{pv}: The overall electrical current generated by the solar cell, measured in amperes (A).

I_{ph}: The current produced by light shining on the solar cell, also known as the photocurrent (A).

I_D: The current that flows through the built-in diode of the solar cell, typically in the opposite direction of the photocurrent (A).

I_{sh}: The small amount of current that leaks through the solar cell's shunt resistance, usually negligible (A).

I_0: The minute current that flows through the diode, even in the absence of light, is known as the reverse saturation current (A).

K: Boltzmann constant, a fundamental physical constant related to temperature and energy is equal to 1.38×10^{-23} (J/K).

q: The elementary charge of an electron is equal to 1.6×10^{-19} (C).

T: The temperature of the solar cell in kelvins (K).

V_{PV}: The voltage measured across the output terminals of the solar cell (V).

A: A quality factor that accounts for non-idealities in the diode behavior, typically between 1.2 and 1.6 for crystalline silicon solar cells.

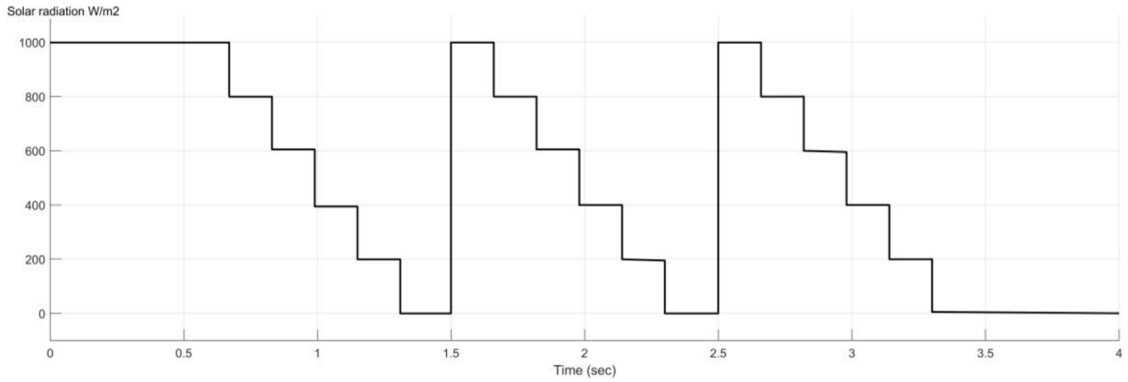

FIGURE 15
Solar radiation in case 2.

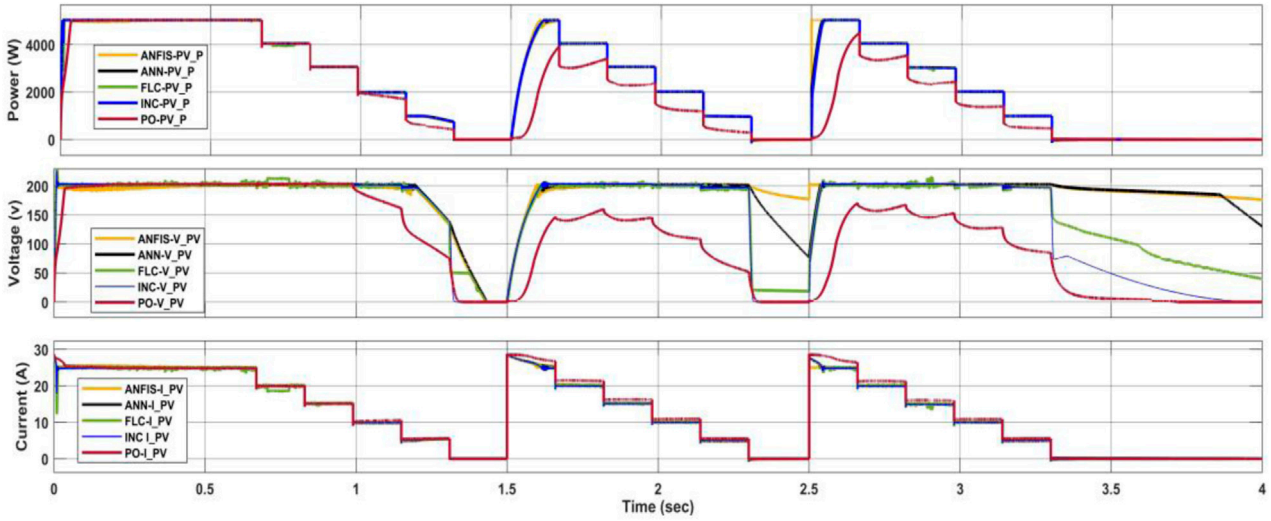

FIGURE 16
PV (P, V, and I) when varying the W/m^2.

R_{sh}: The shunt resistance of the solar cell, a large resistance that allows some current to leak (Ω).

Rs: The series resistance of the solar cell, a small resistance that impedes the flow of current (Ω).

Simply expressed, the equation states that the solar cell's output current (I_{PV}) is controlled by the balance of the light-generated current (I_{ph}) and the currents passing through the diode (I_D) and shunt resistance (I_{sh}). The diode current is determined by the cell's temperature, voltage, and quality factor, whereas the shunt resistance current is often minimal.

2.2 The boost converter

The power output of photovoltaic (PV) panels varies with the amount of sunlight (irradiation). To remedy this, a DC-DC boost converter is used. This device functions as a voltage regulator, generating a constant output voltage regardless of irradiance. This consistent voltage thus permits the use of the maximum power point tracking (MPPT) approach. As previously stated, MPPT optimizes a PV panel's operating point to extract the most power. The boost converter is crucial to this process because it changes both the output voltage and current using the MPPT algorithm. The design of the boost converter requires careful consideration of various elements. These parameters may be computed using existing formulas, as explained in Bendib et al. (2015).

$$C_a = \frac{D.Vpv}{4.\Delta Vpv.f^2.Id}$$

$$D = 1 - \frac{Vpv}{Vdc}$$

$$L_a = \frac{Vpv.(Vdc - Vpv)}{\Delta ILa.f.Vdc}$$

$$\Delta I_{La} = 0.13 * I_{pv} * \frac{Vdc}{Vpv}$$

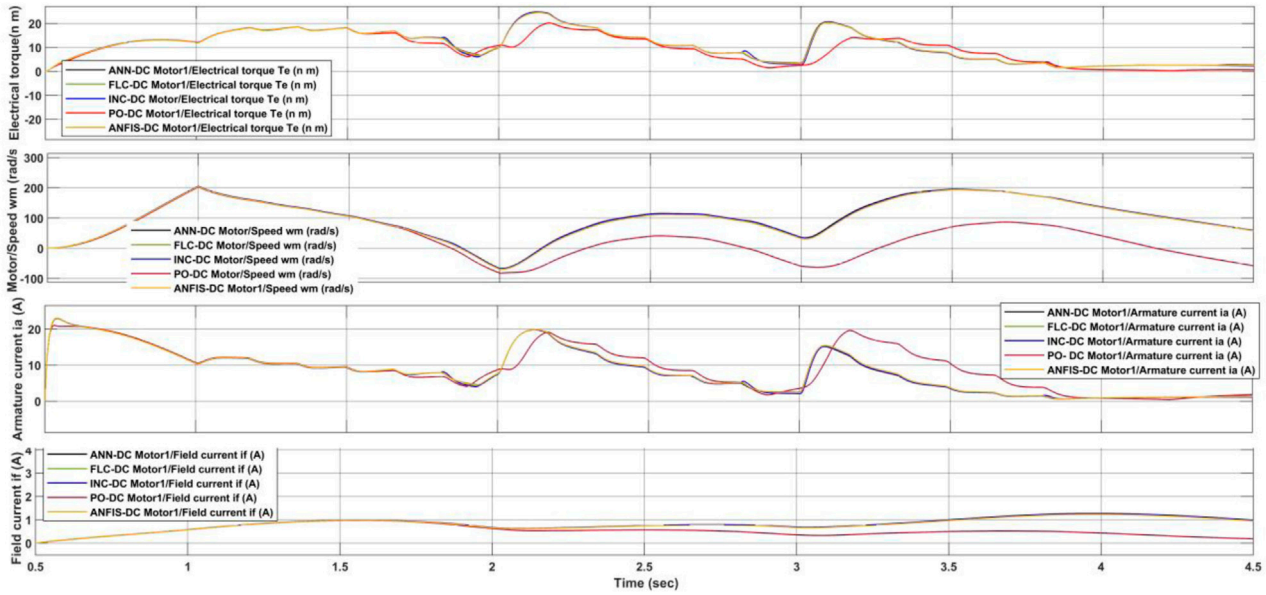

FIGURE 17
Torque, speed, armature current and field current of the DC motor when varying the solar radiation.

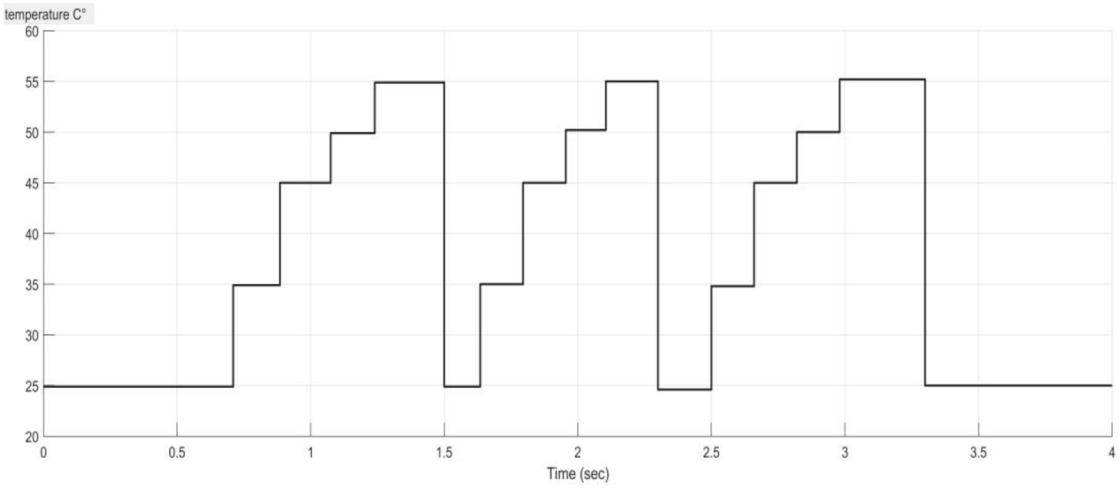

FIGURE 18
Temperature variation in case 3.

$$C1 \geq \frac{Ppv}{\Delta Vo.f.Vdc}$$

where V_{PV} (the input voltage), V_{dc} (the output voltage from the converter), ΔV_{PV} (the change in PV voltage), ΔV_0 (the ripple of the output voltage), I_{PV} (the maximum current of the array A), I_a (the boost converter inductor), ΔI_{La} (the boost inductor's ripple current), P_{PV} (the nominal power of the PV array (W), f_s [the switching frequency (Hz)], Ca (the PV array link capacitance (F), C_1 (the DC link capacitance), and D (the duty cycle of the boost converter that is managed by the MPPT controller).

2.3 DC shunt motor

Instead of directly converting electrical DC power into mechanical energy, this type of motor operates by interacting with magnetic fields. Its unique parallel configuration, featuring an armature winding directly connected to a field winding, enables it to function. The complex behavior of this motor can be mathematically modeled, as detailed in AzzouziM (2012).

$$K\phi = \sum_{n=1}^{7} \alpha\, n\, If^{7-n}$$

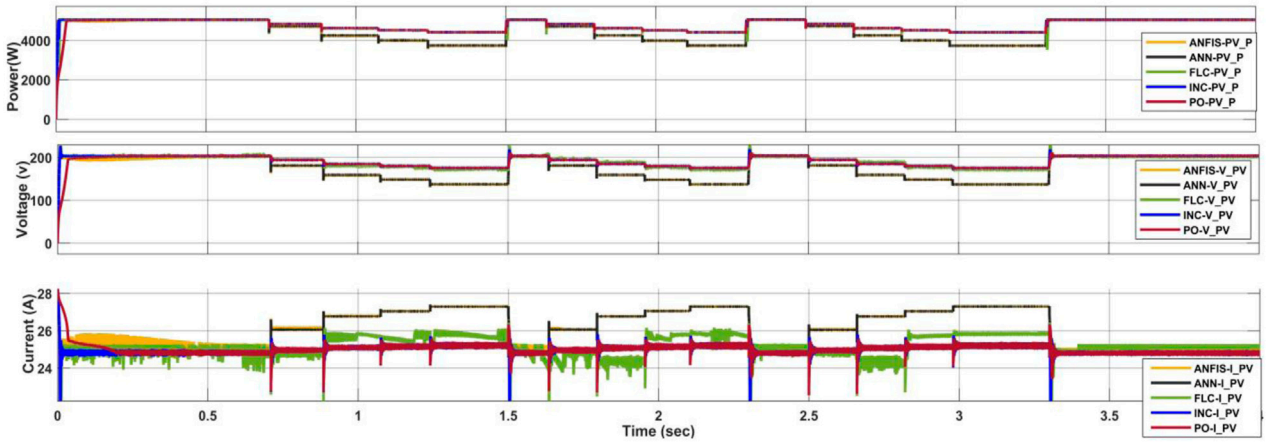

FIGURE 19
PV (P, V, and I) under the C^{o} variation case.

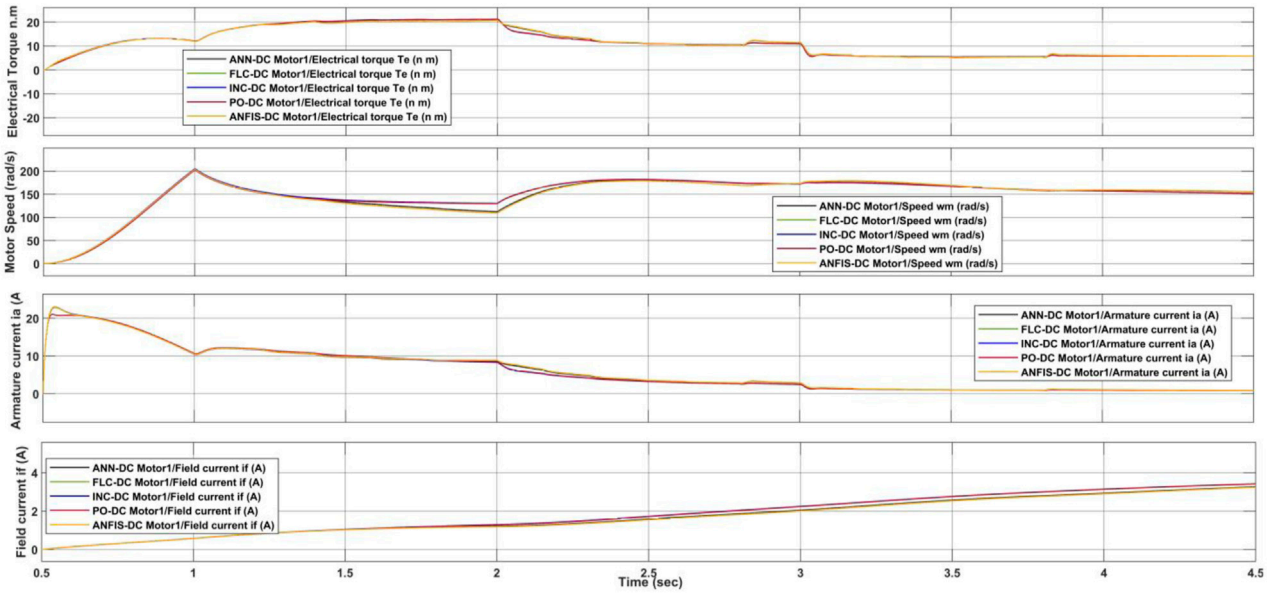

FIGURE 20
Torque, speed, armature current and field current of the DC motor in the temperture variation case.

$$L_f \frac{dif}{dt} = V_f - i_f \left(R_f + R_{adj}\right)$$

$$L_a \frac{dia}{dt} = V_a - i_a R_a - K\phi\,\omega$$

$$J \frac{d\,\omega}{dt} = K\phi\, i_a - T_l$$

Where, L_a represents the armature circuit inductance, I_a represents the armature circuit current, V_a represents the armature circuit voltage, Ra represents the armature circuit winding resistance, L_f represents the field circuit inductance, V_f represents the field voltage, R_f represents the field circuit winding resistance, ω represents the angular speed, K_ϕ represents the DC Shunt motor flux, and T_L represents the motor torque.

The load torque (T_L) would fluctuate in steps from 0 to 4 s. At t = 0 s, the motor works without load, with a maximum speed of 300 rad/sec and a starting current of 42 A. The field current starts at zero and remains constant. At t = 0.5 s, the motor is completely loaded, and the speed drops to around 130 rad/sec rather than 250 rad/sec. In addition, the armature current rises from zero to 7.2 amps. At 1.5 s, the motor is half loaded, and the speed increases to 134 rad/sec due to the decreased load, while the armature current reduces to 3.3 A. At = 2.5 s, the motor is loaded at a fourth of its rated load, and the speed increases to 138 rad/sec while the armature current decreases to 1.6 A. Table 3 lists all of the PV system's parameters, including the PV array, DC-DC Boost Converter, and DC shunt motor.

TABLE 4 Comparison of MPPT algorithms.

Algorithm	Pros	Cons
(P&O)	- Simple implementation	- Slower tracking speed under full load with changing irradiance
	- Good efficiency under full load with constant irradiance	- Fails to track MPP under partial loads and changing irradiance
		- May cause oscillations around MPP
(INC)	- Simple implementation	- Requires continuous sensor data
	- Good efficiency under full load with constant irradiance	- May struggle under rapidly changing irradiance
		- May cause oscillations around MPP
(FLC)	- Adapts well to changing conditions	- Requires development of rule base
	- Fast tracking speed under changing irradiance	- May exhibit larger oscillations in output power
		- Moderate complexity
(ANN)	- Handles non-linearity effectively	- Requires training data
	- Very good efficiency under various conditions (except temperature variations)	- Complex implementation
	- No oscillations	- May struggle under unforeseen operating conditions
(ANFIS)	- Combines ANN and FLC benefits	- Most complex of the presented algorithms
	- Fastest tracking speed, especially under changing irradiance	- Requires training data
	- Very good efficiency (except temperature variations)	- May struggle under unforeseen operating conditions
	- No oscillations	

3 Results and discussion

In this section we will study the performance of the system when utilizing each algorithm under various weather conditions.

3.1 Case_1: solar radiation variation

A study investigated the performance of various algorithms for MPPT in a solar power system under changing solar radiation levels, Figure 15. The system maintained a constant temperature of 25°. The algorithms were evaluated under full, half, and quarter loads of the DC motor.

All algorithms performed well under the full rated load, successfully tracking the maximum power point. However, Figure 16 reveals significant drawbacks for P&O. P&O exhibited slower response times compared to other algorithms. Fuzzy Logic Control (FLC) introduced oscillations in the output power.

The limitations became more pronounced at lower loads. P&O entirely failed to track the maximum power point when the DC motor was loaded at half and a quarter of its capacity. In contrast, Incremental Conductance (IC), Artificial Neural Network (ANN), FLC, and Adaptive Neuro-Fuzzy Inference System (ANFIS) all successfully tracked the (MPP). Notably, ANFIS excelled at rapidly adapting to changing conditions. Under a quarter load with a sudden increase in radiation, ANFIS tracked the MPP within 2.4 s.

Furthermore, Figure 17 highlights the ability of ANN and ANFIS to maintain the desired voltage level during fluctuating radiation. P&O and IC, on the other hand, suffered from voltage drops to minimum levels. All the findings we get in this case study are like the findings of Chatterjee et al. (2008), Esmailian et al. (2014).

3.2 Case_2: temperature variation

A study investigated the performance of various algorithms for a system operating under steady solar radiation of 1,000 W/m^2 (Figure 18). As the motor load decreased from full to a quarter of its rated capacity, the temperature rose from 25°C to 55°C. All algorithms successfully tracked the maximum power point at all load levels. However, P&O, IC, and FLC exhibited superior performance compared to ANN and ANFIS. This advantage is likely due to the limited temperature range (25°C–55°C) used to train the ANN and ANFIS models (Figure 18). Interestingly, P&O, IC, and FLC introduced current oscillations, whereas ANN and ANFIS resulted in smoother current patterns. Electrical torque peaked at roughly 19 N.m at full load and declined with reduced solar radiation for all algorithms. All the findings we get in this case study, like the findings of Fu et al. (2016), Gadalla et al. (2019) as shown in Figures 19, 20. The Results of the comparison will be shown in Table 4 below.

4 Conclusion

This paper investigated the performance of traditional (Incremental Conductance and Perturb & Observe) and intelligent algorithms (Fuzzy Logic Control, Artificial Neural Networks [ANN], and Adaptive Neuro-Fuzzy Inference System [ANFIS]) for maximum power point tracking (MPPT) under rapidly changing environments. Traditional algorithms performed

well under varying solar radiation, but Perturb & Observe struggled at half and quarter loads. Intelligent algorithms excelled under rapid solar radiation changes, with ANFIS achieving the fastest tracking response. However, both ANN and ANFIS suffered limitations due to limited temperature data used for training, hindering their performance under temperature variations. Fuzzy Logic Control (FLC) demonstrated the most consistent and reliable performance across both changing solar radiation and temperature.

This study highlights the importance of considering training data comprehensiveness for intelligent MPPT algorithms. Additionally, the research focused on a DC motor load. Further investigation is required to assess the generalizability of these findings to other load types. The findings presented here hold promise for various applications requiring efficient solar power utilization, particularly those experiencing rapid environmental changes. These include photovoltaic systems integrated into buildings, electric vehicles, and autonomous mobile robots.

Future research should explore methods for incorporating real-time temperature data into the training process for intelligent MPPT algorithms. Additionally, investigating hybrid approaches that combine traditional and intelligent algorithms could leverage the strengths of each for broader applicability.

Data availability statement

The original contributions presented in the study are included in the article/supplementary material, further inquiries can be directed to the corresponding author.

Author contributions

AAG: Conceptualization, Data curation, Formal Analysis, Funding acquisition, Investigation, Methodology, Project administration, Resources, Software, Supervision, Validation, Visualization, Writing–original draft, Writing–review and editing. AAA: Conceptualization, Data curation, Formal Analysis, Funding acquisition, Investigation, Methodology, Project administration, Resources, Software, Supervision, Validation, Visualization, Writing–original draft, Writing–review and editing. AA: Conceptualization, Data curation, Formal Analysis, Funding acquisition, Investigation, Methodology, Project administration, Resources, Software, Supervision, Validation, Visualization, Writing–original draft, Writing–review and editing. YAA: Conceptualization, Data curation, Formal Analysis, Funding acquisition, Investigation, Methodology, Project administration, Resources, Software, Supervision, Validation, Visualization, Writing–original draft, Writing–review and editing. SA: Conceptualization, Data curation, Formal Analysis, Funding acquisition, Investigation, Methodology, Project administration, Resources, Software, Supervision, Validation, Visualization, Writing–original draft, Writing–review and editing. MA: Conceptualization, Data curation, Formal Analysis, Funding acquisition, Investigation, Methodology, Project administration, Resources, Software, Supervision, Validation, Visualization, Writing–original draft, Writing–review and editing.

Funding

The authors declare that no financial support was received for the research, authorship, and/or publication of this article.

Acknowledgments

The authors extend their appreciation to the Deanship of Scientific Research at Northern Border University, Arar, KSA, for funding this research through the project number "NBU-FFR-2024-2124-02." The authors would like to express their profound gratitude to King Abdullah City for Atomic and Renewable Energy (K.A.CARE) for their financial support in accomplishing this work.

Conflict of interest

The authors declare that the research was conducted in the absence of any commercial or financial relationships that could be construed as a potential conflict of interest.

Publisher's note

All claims expressed in this article are solely those of the authors and do not necessarily represent those of their affiliated organizations, or those of the publisher, the editors and the reviewers. Any product that may be evaluated in this article, or claim that may be made by its manufacturer, is not guaranteed or endorsed by the publisher.

References

Allahabadi, S., Iman-Eini, H., and Farhangi, S. (2022). Fast artificial neural network based method for estimation of the global maximum power point in photovoltaic systems. *IEEE Trans. Industrial Electron.* 69 (6), 5879–5888. doi:10.1109/TIE.2021.3094463

ang, C., Kumar Nutakki, T. U., Alghassab, M. A., Alkhalaf, S., Alturise, F., Alharbi, F. S., et al. (2024). Optimized integration of solar energy and liquefied natural gas regasification for sustainable urban development: dynamic modeling, data-driven optimization, and case study. *J. Clean. Prod.* 447, 141405. doi:10.1016/j.jclepro.2024.141405

Ansari, M. F., Chatterji, S., and Iqbal, A. (2010). A fuzzy logic control scheme for a solar photovoltaic system for a maximum power point tracker. *Int. J. Sustain Energ* 29 (4), 245–255. doi:10.1080/14786461003802118

Anurag, A., Bal, S., Sourav, S., and Nanda, M. (2016). A review of maximum power-point tracking techniques for photovoltaic systems. *Int. J. Sustain. Energy* 35, 478–501. doi:10.1080/14786451.2014.918979

AzzouziM (2012). Comparaison between MPPTP&Oand MPPT fuzzy controls in optimizing the photovoltaic generator. *Int. J. Adv. Comput. Sci. Appl.* 3 (12), 57–62. doi:10.14569/IJACSA.2012.031208

Babu, T. S., and Hussain, M. A. (2023). A hybrid firefly and Grey Wolf optimization algorithm for maximum power point tracking of photovoltaic systems under rapidly changing irradiance. *Sustain. Energy Technol. Assessments* 58, 102724.

Bendib, B., Belmili, H., and Krim, F. (2015). A survey of the most used MPPT methods: conventional and advanced algorithms applied for photovoltaic systems. *Renew. Sustain. Energy Rev.* 45, 637–648. doi:10.1016/j.rser.2015.02.009

Bhatnagar, P., and Nema, R. K. (2013). Maximum power point tracking control techniques: state-of-the-art in photovoltaic applications. *Renew. Sustain. Energy Rev.* 23, 224–241. doi:10.1016/j.rser.2013.02.011

Chatterjee, D., et al. (2008). A review of solar MPPT techniques. *Renew. Sustain. Energy Rev.* 12 (4), 1194–1221. doi:10.1016/j.rser.2007.03.005

Dehghani, M., Taghipour, M., Gharehpetian, G. B., and Abedi, M. (2021). Optimized fuzzy controller for MPPT of grid-connected PV systems in rapidly changing atmospheric conditions. *J. Mod. Power Syst. Clean Energy* 9 (2), 376–383. doi:10.35833/MPCE.2019.000086

Duan, Y., Zhao, Y., and Hu, J. (2023). An initialization-free distributed algorithm for dynamic economic dispatch problems in microgrid: modeling, optimization and analysis. *Sustain. Energy, Grids Netw.* 34, 101004. doi:10.1016/j.segan.2023.101004

Ebrahimi, M. J. (2017). "30th power system conference (PSC2015)," in General Overview of Maximum Power Point Tracking Methods for Photovoltaic Power Generation Systems, Tehran, Iran, November, 2017, 228–233.

Elbaset, A. A., Abdelwahab, S. A. M., Ibrahim, H. A., and Eid, M. A. E. (2020) *Performance analysis of photovoltaic systems with energy storage systems*. Berlin, Germany: Springer Nature.

Eltamaly, A. M. (2020) *Modern maximum power point tracking techniques for photovoltaic energy systems*. Berlin, Germany: Springer International Publishing.

Esmailian, A., et al. (2014). A comprehensive review on recent advances in solar photovoltaic maximum power point tracking controllers. *Renew. Sustain. Energy Rev.* 30, 601–616.

Fu, X., Huang, S., Li, R., and Guo, Q. (2016). Thermal load prediction considering solar radiation and weather. *Energy Procedia* 103, 3–8. doi:10.1016/j.egypro.2016.11.240

Gadalla, M., Ghommem, M., Bourantas, G., and Miller, K. (2019). Modeling and thermal analysis of a moving spacecraft subject to solar radiation effect. *Processes* 7, 807. doi:10.3390/pr7110807

Gao, J., Zhang, Y., Li, X., Zhou, X., and J. Kilburn, Z. (2024). Thermodynamic and thermoeconomic analysis and optimization of a renewable-based hybrid system for power, hydrogen, and freshwater production. *Energy* 295, 131002. doi:10.1016/j.energy.2024.131002

Haque, M. T., and Kashtiban, A. M. (2006). Application of neural networks in power systems; A review. *World Acad. Sci. Eng. Technol.*, 53–57.

Hart, D. W. (2011) *Power electronics*. New York, New York, United States: Tata McGraw-Hill Education.

Hasaneen, B. M., and Mohammed, A. A. E. (2008). "Design and simulation of DC/DC boost converter," in Power System Conference, 2008. MEPCON 2008. 12th International Middle East, Aswan, Egypt, March, 2008, 335–340.

Ibrahim, S. A., Nasr, A., and Enany, M. A. (2021). Maximum power point tracking using ANFIS for a reconfigurable PV-based battery charger under non-uniform operating conditions. *IEEE Access* 9, 114457–114467. doi:10.1109/ACCESS.2021.3103039

Ong, C. M. (1998) *Dynamic simulation of electric machinery*. Upper Saddle River, New Jersy 07458: Prentice Hall PTR, 1–220.

Qin, Z., et al. (2023). A Novel marine predator inspired algorithm for maximum power point tracking of photovoltaic systems. *IEEE Trans. Sustain. Energy* 14 (2), 822–833.

Samosir, A. S., Gusmedi, H., Purwiyanti, S., and Komalasari, E. (2018). Modeling and simulation of fuzzy logic based maximum power point tracking (MPPT) for PV application. *Int. J. Electr. Comput. Engineeing* 8, 1315–1323. doi:10.11591/ijece.v8i3.pp1315-1323

Saxena, D., Singh, S. N., and Verma, K. S. S. (2010). Application of computational intelligence in emerging power systems. *Int. J. Eng. Sci. Technol.* 2 (3), 1–7. doi:10.4314/ijest.v2i3.59166

Sedaghati, F., Ali, N., Ali Badamchizadeh, M., Ghaemi, S., and Abedinpour Fallah, M. (2012). PV maximum power-point tracking by using artificial neural network. *Math. Problems Eng.* 2012, 1–10. Article ID 506709, 10 pages. doi:10.1155/2012/506709

Sera, D., Mathe, L., Kerekes, T., Spataru, S. V., and Teodorescu, R. (2013). On the perturb-and-observe and incremental conductance MPPT methods for PV systems. *IEEE J. Photovoltaics* 3 (3), 1070–1078. doi:10.1109/jphotov.2013.2261118

Shirkhani, M., Tavoosi, J., Danyali, S., Sarvenoee, A. K., Abdali, A., Mohammadzadeh, A., et al. (2023). A review on microgrid decentralized energy/voltage control structures and methods. *Energy Rep.* 10, 368–380. doi:10.1016/j.egyr.2023.06.022

Sumathi, S., Ashok Kumar, L., and Surekha, P. (2015) *Solar PV and wind energy conversion systems*. Cham: Springer.

Teulings, W. J. A., Marpinard, J. C., Capel, A., et al. (1993). "A new maximum power point tracking system," in Proc. 24th Annual IEEE PESC, Seattle, WA, USA, June, 1993, 833–838.

Wasynezuk, O. (1983). Dynamic behavior of a class of photovoltaic power systems. *IEEE Trans. Power Appar. Syst.* (9), 3031–3037. doi:10.1109/tpas.1983.318109

Yan, C., Zou, Y., Wu, Z., and Maleki, A. (2024). Effect of various design configurations and operating conditions for optimization of a wind/solar/hydrogen/fuel cell hybrid microgrid system by a bio-inspired algorithm. *Int. J. Hydrogen Energy* 60, 378–391. doi:10.1016/j.ijhydene.2024.02.004

Yang, Y., Si, Z., Jia, L., Wang, P., Huang, L., Zhang, Y., et al. (2024). Whether rural rooftop photovoltaics can effectively fight the power consumption conflicts at the regional scale – a case study of Jiangsu Province. *Energy Build.* 306, 113921. doi:10.1016/j.enbuild.2024.113921

Youssef, A., El Telbany, M., and Zekry, A. (2018). Reconfigurable generic FPGA implementation of fuzzy logic controller for MPPT of PV systems. *Renew. Sustain. Energy Rev.* 82, 1313–1319. doi:10.1016/j.rser.2017.09.093

Zhao, Y., et al. (2023). An improved moth-flame optimizer for maximum power point tracking of photovoltaic systems under partial shading conditions. *IEEE Access* 11, 4722–4734.

frontiers | Frontiers in Energy Research

TYPE Original Research
PUBLISHED 02 September 2024
DOI 10.3389/fenrg.2024.1458115

OPEN ACCESS

EDITED BY
Flah Aymen,
École Nationale d'Ingénieurs de Gabès, Tunisia

REVIEWED BY
Rajeev Kumar,
KIET Group of Institutions, India
Imane Hammou Ou Ali,
Mohammed V University, Morocco

*CORRESPONDENCE
Mohammed Alruwaili,
mohammed.alruwailir@nbu.edu.sa
Sultan Alghamdi,
smalgamdi1@kau.edu.sa

RECEIVED 01 July 2024
ACCEPTED 19 August 2024
PUBLISHED 02 September 2024

CITATION
Hadi H. Awaji H, Alhussainy AA, Alobaidi AH, Alghamdi S, Alghamdi S and Alruwaili M (2024) Real-time energy management simulation for enhanced integration of renewable energy resources in DC microgrids.
Front. Energy Res. 12:1458115.
doi: 10.3389/fenrg.2024.1458115

Real-time energy management simulation for enhanced integration of renewable energy resources in DC microgrids

Hassan Hadi H. Awaji[1], Abdullah Ali Alhussainy[2], Abdulraheem H. Alobaidi[1,3], Sultan Alghamdi[1,3]*, Sami Alghamdi[1,3,4] and Mohammed Alruwaili[5]*

[1]Department of Electrical and Computer Engineering, Faculty of Engineering, King Abdulaziz University, Jeddah, Saudi Arabia, [2]Department of Electrical Engineering, College of Engineering, University of Prince Mugrin, Madinah, Saudi Arabia, [3]Smart Grids Research Group, Center of Research Excellence in Renewable Energy and Power Systems, King Abdulaziz University, Jeddah, Saudi Arabia, [4]K. A. CARE Energy Research and Innovation Center, King Abdulaziz University, Jeddah, Saudi Arabia, [5]Department of Electrical Engineering, College of Engineering, Northern Border University, Arar, Saudi Arabia

The presented work addresses the growing need for efficient and reliable DC microgrids integrating renewable energy sources. However, for the sake of practicality, implementing complex control strategies can increase system complexity. Thus, efficient methodologies are required to provide efficient energy management of microgrids while increasing the integration of renewable energy sources. The primary contribution of this work is to investigate the issues related to operating a DC microgrid with conventional control designed to power DC motors using readily available, non-advanced control strategies with the objective of achieving stable and reliable grid performance without resorting to complex control schemes. The proposed microgrid integrates a combination of uncontrollable renewable distributed generators (DGs) alongside controllable DGs and energy storage systems, including batteries and supercapacitors, connected via DC links. The Incremental Conductance (InCond) algorithm is employed for maximum power point tracking to maximize power output from the PV system. The energy management strategy prioritizes the solar system as the primary source, with the battery and supercapacitor acting as backup power sources to ensure overall system reliability and sustainability. The effectiveness of the microgrid under various operating conditions is evaluated through extensive simulations conducted using MATLAB. These simulations explore different power generation scenarios, including normal operation with varying load levels and operation under Standard Test Conditions (STC). Moreover, fault analysis of the DC microgrid is performed to examine system reliability. The system performance is evaluated using real-time simulation software (OPAL-RT) to validate the effectiveness of the approach under real-time conditions. This comprehensive approach demonstrates the efficacy of operating a DC microgrid with conventional controllers, ensuring grid stability and reliability across various operating conditions and fault scenarios while prioritizing the

use of renewable energy sources. The results illustrated that system efficiency increases with load, but fault tolerance measures, can introduce trade-offs between reliability and peak efficiency.

KEYWORDS

renewable energy sources (RES), battery energy storage (BES), direct current (DC), microgrid (MG), solar photovoltaic (PV)

1 Introduction

The modern power grid is moving toward utilizing distributed energy resources (DERs). The shifting trend from conventional generation based on fossil fuels to dispersed renewable generation aims to reduce greenhouse gas emissions, which have raised many global environmental concerns (Wu et al., 2024). In addition, the shortage and the increasing cost of fossil fuels are causing security concerns regarding the balance between energy supply and demand. In order to meet the need for electrical energy, the utilization of renewable energy sources (RES) is considered a solution to the problem of the deficit of energy supply. The low generation costs and maximum power point tracking (MPPT) capability of solar and wind energy make them the most promising RES technologies (Hossain and Ali, 2016; Kumar et al., 2024). According to the International Renewable Energy Agency (IREA), RES will supply 66% of global energy consumption by 2050 (Gielen et al., 2019). Microgrids (MGs) have recently received significant concentration from many researchers as a promising solution to better utilizing large penetration of RES. Thus, the future distribution grids may consist of a group of microgrids that generate, deliver and store energy. It is an autonomous energy system that serves a particular geographic region. The configuration of the microgrids depends on different types of DERs, such as solar panels, wind turbines, microturbines, and energy storage systems (ESSs), e.g., battery energy systems (BES) and supercapacitors (Marwali et al., 2009; Gowtham et al., 2018). Based on their voltage characteristics, microgrids are categorized into AC microgrids, DC microgrids, or Hybrid AC /DC microgrids. MGs can operate in grid-connected modes, exchanging power with the distribution grid, or operate in islanding modes supplying energy to their local energy demands. In case of catastrophic events, MGs can operate in islanding modes to restore power to some critical loads, hence improving the availability of energy supply. Besides being environmentally friendly, MGs have several advantages, such as providing grid isolation during disturbances, reducing peak load on the grid to prevent failures, and enhancing energy efficiency. However, they face some operational challenges, including maintaining acceptable voltage and frequency, ensuring power quality standards, and difficulty in resynchronization with the utility grid. In islanded green microgrids that consist of only renewable energy sources, the problems related to voltage regulation, power sharing, and battery management are even more severe and require more sophisticated control strategies.

DC microgrids are becoming increasingly popular compared to conventional AC microgrids due to their compatibility with renewable energy sources and electronically controlled loads. DC microgrids offer several advantages, including the absence of conflicts with harmonics or frequencies, eliminating the need for synchronization in islanded mode, and not requiring reactive power control. (Gandhi and Gupta, 2021; Saleh Al-Ismail, 2024). In such a DC microgrid, uncontrollable DGs based on renewable technologies, controllable DGs, and energy storage systems are coupled via DC links. Microgrids with energy storage devices, such as BES and supercapacitors, can enhance system reliability. On the one hand, the stored energy can supply the electric demand during peak hours; on the other hand, the BES and supercapacitors can be recharged during off-peak hours.

An energy management system (EMS) is used to monitor energy usage and control and optimize the generation units of the grid. The EMS generally involves instruments to monitor energy usage, predict future energy demands, control generation assets, and report on the interventions performed. It provides utilities and building management services with real-time data and the ability to tune energy utilization, enabling to minimize energy expenses and promote effectiveness. During periods of peak demands, the EMS may respond to signals from the energy grid to temporarily reduce energy consumption by shedding non-critical loads to stabilize the grid and prevent blackouts. Overall, the EMS aims to ensure optimal energy management of the grid, minimize energy costs, and reduce environmental impact resulting from major power outages.

Several research studies have proposed energy management systems for microgrids in the literature. An effective energy management system for the DC microgrid with PV systems was proposed in (Awaji et al., 2022), which consists of a photovoltaic system with BES to enhance power generation when the power output of the photovoltaic (PV) system is insufficient and a DC shunt motor as a dynamic load. The DC microgrid was studied in three distinct scenarios of weather conditions to analyze the behaviour of the BESS under the variations of power generation and highlight the contributions of BES in stabilizing the system under the stochastic nature of RES and demand variability in the microgrid. The paper (Alarbidi et al., 2023) introduced modelling and control strategies for a fixed-speed wind turbine powered by a permanent magnet synchronous machine (PMSM). Additionally, a case study was conducted to illustrate the impact of wind energy on the short circuit level. The torque-controlled PMSM was regulated using the field orientation approach, which involved the modelling and control approach for the frequency converter on the generator-rotor side. Reference (Rana and Abido, 2017) presented a strategy for energy management of a DC microgrid with PV systems. Here, a model predictive controller (MPC) was proposed to control the power flow between the bidirectional voltage source converter (VSC) and the grid. The implementation of the proposed controller was assessed and compared with that of the classical PI controller, and the results showed that the MPC outperformed the classical PI control. The hybrid ESS's frequency control, consisting of a battery and a supercapacitor, was used in the

microgrid to eliminate frequency power variation by exchanging power with the DC bus. In the study (Rashid et al., 2021), an efficient approach for home energy management of community microgrids was developed. Here, the microgrid considers RES, distributed battery energy systems, one centralized battery storage system, and demand response programs. The results show potential financial returns for residential customers and facilitate sustainable energy generation options in a community. The positive aspects of leveraging RES, BES, and central BES with the proposed optimal power-sharing algorithm were assessed. Reference (Ahmed et al., 2019) presented a control methodology for the DC microgrid energy managing utilizing hybrid ESS. The microgrid comprised RES, variable load, hybrid ESS, and diesel generator. The implementation of the proposed microgrid was validated using simulation, where the voltage level of DC under load variation and intermittent RER never exceeded the allowable tolerance, i.e., ± 5%. A coordinated control methodology for the energy management of a microgrid in a grid-connected mode with solar PV and BES was proposed in (Zhang et al., 2024a). The algorithm coordinated the VSC and bidirectional DC-DC converter relied on the battery's state of charge (SOC). It also compensated for the imaginary power of the load and minimized the unbalanced neutral current. Reference (Alahmed et al., 2019) proposed a dynamic load prioritization methodology built on the artificial neural network (ANN) for microgrid reconfiguration. The proposed method prioritized the microgrid demands relied on the current time, available energy supply, and system reliability factors to provide flexible load restoration under different hours and system conditions. An energy management method using fuzzy logic was applied in (Athira and Pandi, 2017) to ensure generation demand balance in the islanded DC microgrid. The system was evaluated under different load conditions to ensure proper operation of the microgrid with PV panels and a hybrid energy storage system composed of a battery and an ultracapacitor to enhance the battery life. A DC microgrid with a standalone solar PV system was proposed in (El-Shahat and Sumaiya, 2019), aiming to enhance the power conversion efficiency and ensure system permanency. The proposed model reduced the component losses and increased the system efficiency by improving the dynamic response, minimizing the harmonic losses, and obtaining a stable maximum power point value using sum-of-squares optimization for the PV system. Reference (Chahal et al., 2023) developed a model for inverter-based distributed generation technology. Here, a control strategy was employed to enhance disturbance rejection and incorporate an extended range of frequency modes through an analogous internal model. Particle swarm optimization (PSO), focused on minimizing the error in the actual power, was used to discover the best controller parameters. A microgrid operating in grid-connected and autonomous modes was described in (Hussaini et al., 2022) using linear and nonlinear models. An optimization algorithm was proposed for designing various controllers, filters, and power-sharing coefficients. The outcomes validated the efficiency of the suggested PSO approach in tuning the PI regulator, filter, and power-sharing coefficient settings to attain adequate system performance under several disturbances. The microgrid's stability was examined using nonlinear time-domain simulations in a project to construct a nonlinear model of a self-controlled microgrid published in (Wang S. et al., 2024). The PSO methodology was utilized to ascertain the optimal values for the tuned parameters. The outcomes attest to the strength and efficacy of the suggested PSO-based methodology. The real-time digital simulator (RTDS) outcomes validated the suggested controllers' efficacy for the system under consideration under various disturbances and operating situations. In (Hassan et al., 2018), the influence of active load on the microgrid's dynamic stability is investigated. The accompanying controllers are developed for an autonomous microgrid with three DGs based on inverters and an active load. The outcomes showed that the suggested controller has the potential to increase the microgrid's stability and offer effective dampening properties. Additionally, it demonstrated good performance with the autonomous microgrid under consideration having effective damping properties. When used on MG, the study in (Naderi et al., 2023) examined several System of Systems (SOS) control mechanisms. The study concluded that a networked control system allows for improved microgrid control. The (Keerthisinghe and Kirschen, 2020) microgrid concept featured solar systems, a battery, a backup generator, loads, and an electric vehicle charging station with grid connectivity. The performance of the microgrid was evaluated under three operating scenarios: grid-connected mode, islanding mode microgrid using only the battery, and islanding mode microgrid operating using the backup generator. A microgrid constructed by Snohomish PUD in Arlington, Washington, was simulated in real-time using the real-time digital simulator OPAL-RT. Methods for detecting local and remote microgrid islanding were provided in the paper (Rami Reddy et al., 2024). In each class, various detection techniques were investigated, and the benefits and drawbacks of each technique were reviewed based on some assessment indices, such as non-detection zone, detection time, fault detection rate, and power quality indices. The use of signal processing approaches and intelligent classifiers to modify islanding procedures recently was also covered. The control and sharing of real and reactive power outputs of the inverter-based DGs was suggested using an optimal PQ control technique (Ahmad et al., 2023). Here, the study was conducted on two instances of microgrids with various structures, and various disturbances were used to study how well the microgrid performed. The research study found that the dynamic stability of the microgrid was enhanced using the suggested optimal control. A powerful control technique for voltage balancing, grid synchronization, and power management was developed in (Worku et al., 2021) to enhance the stability and dependability of a microgrid based on DERs. The system model and control approach were created in an RTDS. The outcomes demonstrated the efficacy of the suggested control strategy in grid-connected microgrids, islanding microgrids, and microgrid resynchronization.

In short, an energy management system constantly monitors energy use by analyzing real-time data and weather patterns; it predicts future demand and controls generation, including renewables, for efficient power production, as explored in (Lei et al., 2023). Moreover, it provides utilities with valuable data for cost-saving and environmentally friendly grid improvements while integrating renewable energy (Xie et al., 2016). Recent advancements offer promising solutions to microgrid challenges. Research is shifting towards more sophisticated models that capture the dynamic behavior of DERs within the microgrid, as proposed in (Kumar et al., 2024). Additionally, exploring novel control strategies

TABLE 1 Summary of the comparison of microgrid dynamics and control strategies.

Feature	Description	Advantages	Disadvantages	References
Microgrid Dynamics and Control	This study investigates the interplay between Distributed Energy Resources (DERs) inside a microgrid and control systems, with a specific emphasis on maintaining voltage stability, frequency stability, and equitable power distribution to fulfill the total energy requirements	The method enables smooth operation in both grid-connected and islanded modes, while improving power quality and dependability	Increased DER integration can complicate control strategies, and tuning controllers for optimal performance under varying conditions can be challenging	Wu et al. (2024), Kumar et al. (2024), Gandhi and Gupta (2021)
Virtual Inertia Control (VIC)	A software-based method replicates the conventional flywheel effect in generators that use inverters, thereby improving frequency stability, especially in microgrids with a significant amount of renewable energy integration	The proposed method improves the frequency responsiveness in the event of abrupt load increases or power fluctuations, hence enhancing the ability of islanded microgrids to withstand disruptions in the power grid	Precise system modeling is necessary for effective implementation when control algorithms get more complicated	Saleh Al-Ismail (2024), Zhang et al. (2024a)
Advanced Control Strategies	Apply modern methodologies such as Optimal Power Flow Control, Networked Control Systems, and Machine Learning Control to optimize the operation of microgrids and improve their resilience	The system improves the efficiency, dependability, and cost-efficiency of microgrid operation by allowing for immediate adjustment to fluctuations in load and generation patterns	Integrating machine learning algorithms into a system design and implementation might lead to the need for substantial computer resources and increased data complexity	Chahal et al. (2023), Hussaini et al. (2022), Naderi et al. (2023), Ahmad et al. (2023)
Islanding Detection Methods	This paper details the procedure for detecting the disconnection of a microgrid from the primary grid, guaranteeing prompt isolation to avoid any potential safety risks and equipment harm	The system's safety and reliability are improved, while ensuring the protection of utility personnel and equipment	Grid detection technologies are susceptible to noise or sudden changes, thus it is essential to maintain a balance between power supply and demand when operating in islanding mode	Rami Reddy et al. (2024)

using artificial intelligence and machine learning for optimized energy management and enhanced system resilience holds significant potential, moving beyond approaches such as particle swarm optimization (PSO) (Chahal et al., 2023; Hussaini et al., 2022), as demonstrated in research on a DC microgrid energy management system (Awaji et al., 2022). This paper dives deeper into the challenges faced by isolated, renewable-powered microgrids (MGs). To ensure alignment with current research, we comprehensively review recent literature, including microgrid dynamics and control (Gandhi and Gupta, 2021), virtual inertia control for DC microgrids (Saleh Al-Ismail, 2024), advanced control strategies like optimal PQ control and networked control systems for MGs (Naderi et al., 2023; Ahmad et al., 2023), and islanding detection methods (Rami Reddy et al., 2024). Table 1 summarizes the existing work on microgrid dynamics and control strategies.

Several studies on real-time energy management simulations have examined renewable energy integration in microgrids, leading to many approaches to enhancing their efficiency and stability. In (Shirkhani et al., 2023), an extensive survey of decentralized energy management and voltage controls for microgrids is presented and highlights some crucial operational challenges. An online reinforcement learning-based energy management for centrally controlled microgrids is introduced in (Meng et al., 2024), highlighting how adaptive learning can be useful in real-time optimization. Moreover, Ref. (Zhou et al., 2024). proposes a multi-stage adaptive stochastic-robust scheduling approach for hydrogen-based multi-energy microgrids, incorporating stochastic programming and robust optimization to enhance system resilience against uncertainties. Furthermore, (Zhang et al., 2024b), emphasizes embedded DC power flow regulators based on full-bridge modular multilevel converters, which control power flow and improve reliability. Ju et al. (2022) proposes a distributed three-phase power flow for AC/DC hybrid microgrids while considering converter limiting constraints aiming at tackling complexities associated with hybrid AC/DC microgrids.

This presented paper investigates the issues related to operation of a DC microgrid powered by solar and controllable DGs, using readily available batteries and supercapacitor storage connected via DC links. The well-established InCond algorithm has been employed to maximize solar output, while batteries and supercapacitors operate as backups. The energy management strategy for the proposed DC microgrid is based on the system operators' experience, where the solar system is the primary source, while the battery and supercapacitor act as backup power sources. The proposed model will be evaluated through various scenarios, i.e., normal operation and load changes, to ensure effectiveness considering the utilization of the non-advanced controller. All results are tested in a real-time condition using simulation software (OPAL-RT). The combined BES and supercapacitor approach addresses the limitations of BES alone, improving power stability and system efficiency and offering a more comprehensive performance evaluation by considering diverse weather conditions. This demonstrates the feasibility of a reliable and efficient DC microgrid maximizing renewable energy with conventional controls. The contribution of the presented paper can be summarized as follows:

- Analyzing a DC microgrid combining RES and energy storage technologies, such as BES and supercapacitors, to overcome the limitations of battery-based microgrids and leveraging the InCond method for the MPPT of the PV system.

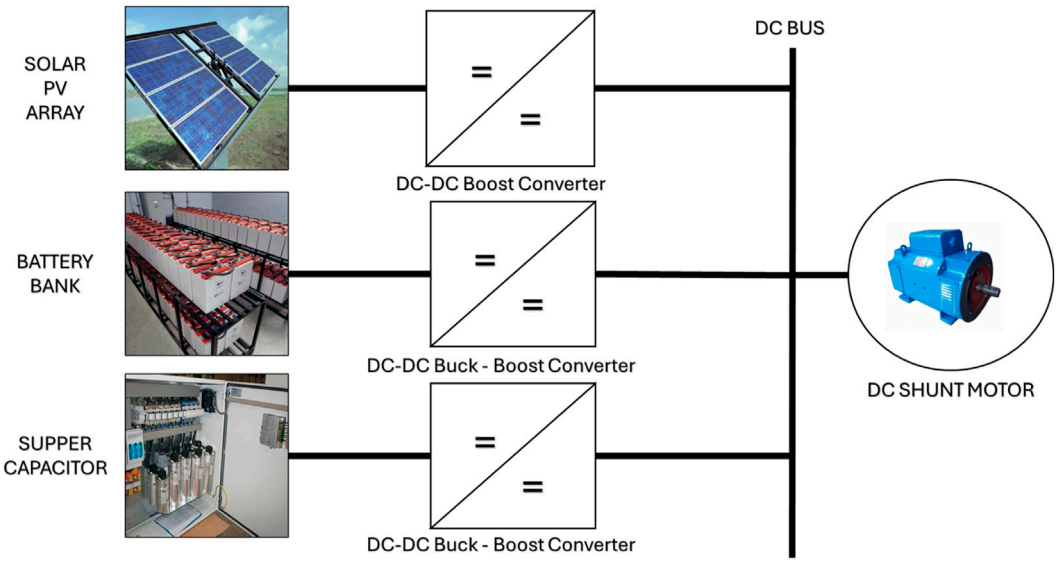

FIGURE 1
Dc microgrid system.

- Evaluating the implementation of the DC microgrid with several practical tests to evaluate the stability of the grid under different operating conditions, including steady-state scenarios, and providing fault analysis on the DC microgrid to assess system reliability.
- Conducting a real-time simulation using the real-time simulator (OPAL-RT) to validate the performance of the suggested DC microgrid.

By addressing these aspects, this paper not only advances the field of energy management in DC microgrids but also offers practical profits like improved energy efficiency, minimized emissions, cost savings, and validation through rigorous simulations. The structure of this article is as follows: Section 2 provides an explanation of the DC Microgrid, while Section 3 contains the system model. Section 4 includes simulation results and a discussion on energy management. Section 5 provides a concise overview of the research findings and explores potential avenues for future research.

2 Microgrid network

A microgrid is a small-scale grid that comprises DGs and ESSs to serve local loads (Dawoud et al., 2021). The microgrid may operate in conjunction with the main grid, referred to as grid-connected mode, or operate independently in an islanded mode, and it can be AC, DC, or hybrid AC-DC based on the voltage characteristics (Fani et al., 2022). The microgrids operating in grid-connected mode can offer ancillary services to the main grid, such as voltage and frequency control, to improve the system's flexibility and reliability by trading energy based on the available energy supply and current energy demands. In this grid-connected mode, DERs operate in an MPPT mode to supply the maximum available power to the grid. The microgrid operating in islanding mode, i.e., isolated from the main grid, can serve its local load from the DERs (Worku et al., 2019). In these microgrid operational modes, the power generation and demand balance is the most critical issue in the energy management of the microgrids. In AC microgrids, DC sources such as PV systems are coupled with the AC system using DC/AC converters. In DC microgrids, DC sources are directly linked to the DC bus, and AC sources are coupled with the DC bus via AC/DC converters. Therefore, DC microgrids have higher system efficiency than AC microgrids due to less power. Converters are required and hence, less investment and operating costs. Hybrid microgrids can supply energy to AC and DC loads; however, they are more complex than DC microgrids. The DC Microgrid can facilitate the utilization of large RES with less complexity and operating costs compared with its counterparts. However, the optimal operation of microgrids should be addressed to ensure efficient performance of both grid-connected and islanding modes and promote sustainable power generation (Jirdehi et al., 2020).

Figure 1 displays the configuration of the DC microgrid. The physical layer is comprised of PV, battery and super capacitor connected to the DC bus through a DC-DC converter to supply a local load. The power production of the photovoltaic (PV) system is influenced by the diurnal cycle, encompassing both day and night periods. Consequently, it has an adverse impact on the DC motor's ability to meet the necessary power demand. Hence, using Battery Energy Storage (BES) in conjunction with the Photovoltaic (PV) system is imperative for a streamlined energy management system to maximize system performance during critical scenarios. The connection in a direct current (DC) system is regarded as simpler compared to an alternating current (AC) system due to the sole requirement of regulating the voltage in a DC bus. In the DC microgrid, distributed generators, ESSs, and local loads are linked via a single DC bus using line regulating converters or are directly connected to the DC bus depending on the operating voltage.

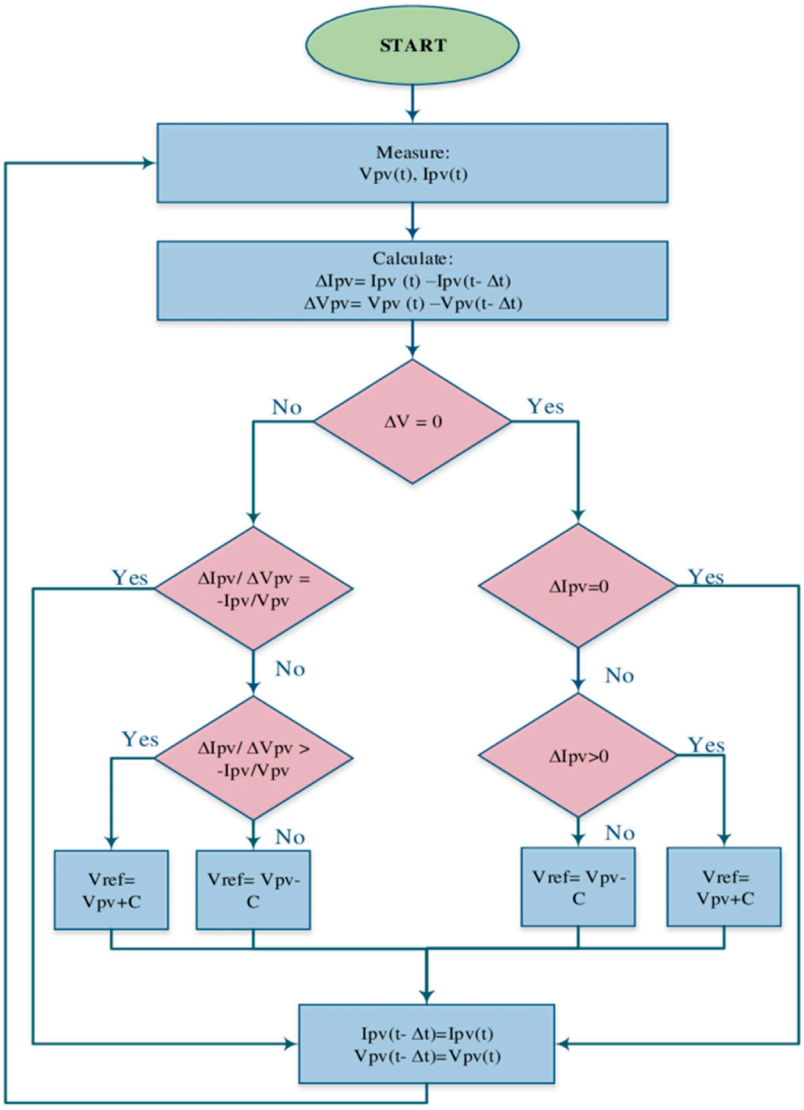

FIGURE 2
Flowchart of InCond Algorithm obtained from (Seyedmahmoudian et al., 2014).

The MPPT algorithm can be employed to maximize the power output of the PV panel by regulating the output voltage and current, considering the variations in irradiance (Elbarbary and Alranini, 2021). Several methods exist to achieve this goal. Among them, the Incremental Conductance (InCond) algorithms are widely used (Seyedmahmoudian et al., 2014). Other approaches for the MPPT of the PV systems leverage heuristic algorithms, such as fuzzy logic control and neural networks. However, these methods provide a local maximum or approximated solution for the MPPT. The V-P curve of the PV panel under normal conditions contains merely one maximum value. However, partial shading of the PV panel may lead to multiple maxima in the curve. The InCond method for the MPPT of the PV system is developed based on the "hill-climbing" principle (Seyedmahmoudian et al., 2014), which involves adjusting the operation point of the PV panel in a direction that can increase the output power of the PV panel. The hill-climbing approach is prevalent for the MPPT of the PV system because of its straightforward implementation and satisfactory performance, particularly during constant solar irradiation. Although this method offers simplicity and requires low computational power, it also has some drawbacks. Oscillations can occur around the MPP, and during rapidly changing weather conditions, the algorithm may fail to track the MPP and move in the wrong direction.

In this paper, the InCond method will be utilized for the MPPT of the PV panels, primarily because of its advantages over other techniques mentioned earlier. The flowchart presented in Figure 2 outlines the process of the InCond MPPT method (Seyedmahmoudian et al., 2014). This method tracks MPP through a simultaneous comparison of InCond ($\Delta V_{pv}/\ \Delta I_{pv}$) and instantaneous conductance ($\Delta V_{pv}/\ \Delta I_{pv}$) (Seyedmahmoudian et al., 2014). Based on the location and PV output characteristic, the controller adjusts the operating point of the PV panel in the direction of the MPP with a step size of C. The speed of the

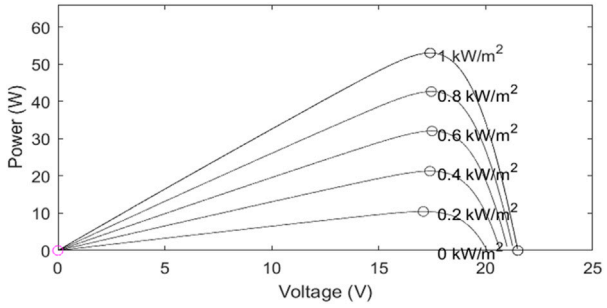

FIGURE 3
Power outputs of PV with different solar radiations.

controller's track mechanism depends on the step size value. A larger step size enables faster MPP tracking but leads to oscillations around the MPP. To address this issue, some researchers have developed a variable step size InCond method. This technique initially uses a large step size to approach the approximate MPP region and then switches to a smaller step size to accurately track the MPP. This enhances the controller's accuracy and prevents oscillations around the MPP (Abdel-Salam et al., 2018). For this study, a regular MPPT technique without advanced control methods was used. The primary goal is to analyse the dynamics of DC microgrids under various conditions.

3 Microgrid system modelling

Herein, the DC microgrid system model is presented. The model comprises a PV system, power converters, BES, supercapacitors, and a DC shunt motor. The following subsections will explain each component in the proposed DC microgrid.

3.1 Photovoltaic array

In the PV system utilizes solar cells composed of semiconductor materials capable of converting solar energy into electrical energy. The photovoltaic (PV) system produces a specific quantity of electrical power determined by the characteristics of voltage (V) and current (I) known as P-V and I-V properties (Zhang et al., 2021). The cells in the PV system are interconnected in either series, parallel, or a hybrid configuration to create a PV array, which is determined by the specific purpose of the system. Equation 1 describes the correlation between the current and voltage of the photovoltaic system.

$$I_{pv} = I_{pc} - I_{diode} - I_{shunt} = I_{pc} - I_{\mathrm{rev}}\left[e^{\frac{q}{A\cdot K\cdot T\left(V_{pv}+I_{pv}+R_{series}\right)}-1}\right] - \frac{V_{pv}+I_{pv}\cdot R_{series}}{R_{shunt}} \quad (1)$$

where I_{pv} denotes the PV cell output current, I_{pc} represents the photocurrent, I_{diode} stands for the current passing through the diode, I_{shunt} depicts the shunt resistance current, K represents the Boltzmann constant which is equal to $1.38 \times 10^{-23}\,(J/K)$, q stands for the charge of electron, I_{rev} denotes the reverse current of the diode, T depicts the cell temperature in kelvin (K), V_{pv} denotes the PV cell output voltage, A stands for the quality factor, R_{shunt} and R_{series} stands for the shunt and series resistances of the equivalent circuit of PV system, respectively. Several reasons, such as the variation of solar radiation and temperature, impact the power output of the PV system. Figure 3 describes the output power of the PV system under variable solar irradiation changes from 0 W/m2 to 1 kW/m2.

3.2 Converter model

In order to compensate for the fluctuation in solar irradiance and maintain a consistent output power, the PV system employs a DC-DC boost converter. This converter is responsible for regulating the output voltage to achieve the desired level, as depicted in Figure 4. In addition, the MPPT algorithm is employed to ascertain the optimal power output of the photovoltaic (PV) system by regulating the voltage and current (Hashim et al., 2018).

There are several techniques to determine the maximum power of the PV system in the literature (Elbarbary and Alranini, 2021; Abdel-Salam et al., 2018). In this paper, the incremental conductance (InCond) for MPPT of the PV system is used. The output DC voltage of the PV system is then stepped-up using power converters to a higher voltage level to match the operating voltage. The choice of switching device is determined by the particular use case, with options including MOSFETs and other semiconductor switching devices. This study utilizes the DC-DC boost converter. The DC-DC boost converter is comprised of two semiconductors, namely a diode and a MOSFET, along with a series inductor and a shunt capacitor. These components are connected to the terminals of the PV system. Upon activation of the MOSFET, the inductor experiences a short circuit, resulting in the accumulation of a substantial charge. This charge is subsequently amplified using the boost DC-DC converter located at the DC bus. Upon deactivation of the MOSFET, the capacitor is connected in parallel with the DC bus in order to maintain a consistent operating voltage. The parameter of the boost DC-DC converter can be approximated using Equations 2–6 as stated in reference (Wang and Zhang, 2023).

$$C_a = \frac{D.V_{pv}}{4.\Delta V_{pv}.f^2.Id} \quad (2)$$

$$D = 1 - \frac{V_{pv}}{V_{dc}} \quad (3)$$

$$L_a = \frac{V_{pv}.\left(V_{dc} - V_{pv}\right)}{\Delta I_{La}.f.V_{dc}} \quad (4)$$

$$\Delta I_{La} = 0.13^{*} I_{pv}{}^{*}\frac{V_{dc}}{V_{pv}} \quad (5)$$

$$C_1 \geq \frac{P_{pv}}{\Delta V_0.f.V_{dc}} \quad (6)$$

where V_{pv} represents the converter's input voltage, V_{dc} denotes the converter's output voltage, ΔV_{pv} depicts the drift in V_{pv}, ΔV_0 represents the output voltage's ripples, I_{pv} denotes PV maximum current, L_a stands for the inductance of the boost converter, ΔI_{La} denotes the inductor ripple current, P_{pv} represents the PV array

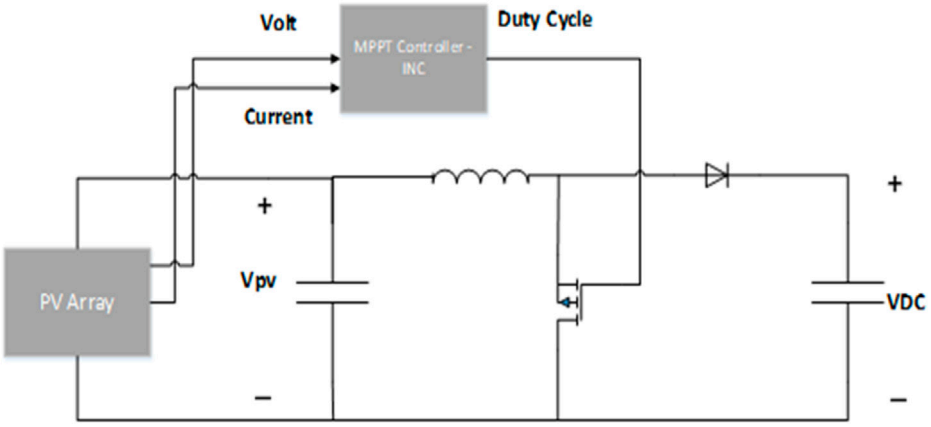

FIGURE 4
DC-DC boost converter.

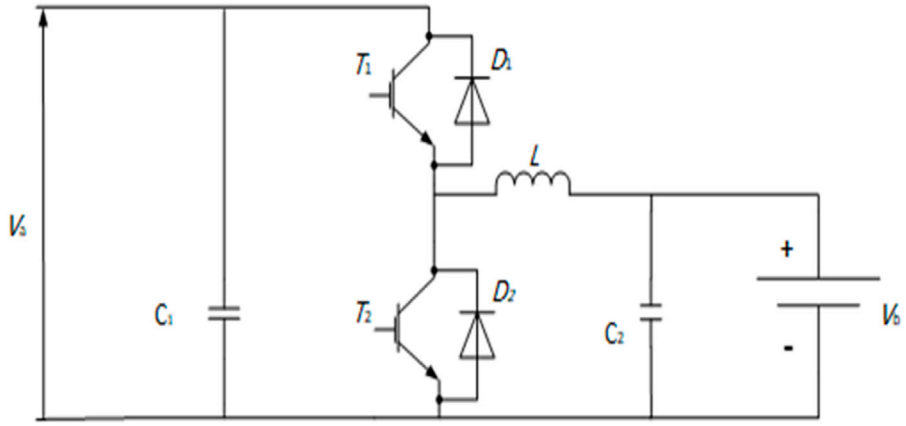

FIGURE 5
Schematic diagram of Bidirectional Buck-Boost Converter.

normal power, f represents the switching frequency, C_a denotes link capacitance of the PV array, C_1 denotes the capacitance of the DC link, and D depicts the converter's duty ratio.

The BES comprises of a battery storage unit, where the size of the battery is calculated according to the size of DC loads, and a bidirectional buck-boost system DC-DC, illustrated in Figure 5. A bidirectional buck-boost converter is utilized to allow a bidirectional power flow of the BES during the charging and discharging modes.

In this setup, the terminals of both the Battery Energy Storage and the supercapacitors are linked to a buck-boost DC-DC converter, which includes a diode connected in series with the load. A parallel connection is made between the switch and the diode using an inductor, while a shunt capacitor is connected to the DC bus. The buck-boost DC-DC converter has the capability to function in either buck mode, where it charges the Battery Energy Storage, or boost mode, where it releases the stored energy from the BES to the grid. During the off period, the buck-boost DC-DC converter produces an output voltage that has a polarity opposite to that of the input voltage. When the switch is activated, an electric current passes through both the switch and the inductor for a specific duration. During this period, the induced voltage has the same polarity as the input voltage, meaning that the rate of change of current over time (di/dt) is positive. When the switch is in the OFF position, the current in the inductor will drop, causing the induced voltage to change polarity. The rate of change of current (di/dt) is negative, resulting in the output voltage having the opposite polarity of the input voltage. The shunt capacitor will ensure a consistent output voltage.

3.3 Battery energy system (BES)

The Battery Energy Storage (BES) system comprises a series of lithium-ion batteries connected to a bidirectional DC-DC buck-boost converter. There are various types of batteries include lithium-

ion, lead-acid, and Ni-Cd batteries. This paper utilizes lithium-ion batteries due to their superior energy density compared to lead-acid and Ni-Cd batteries. In this battery variant, the electrodes are made thicker in order to counterbalance the formation of a passivation film resulting from the interaction between the lithium electrodes and the electrolytes during each cycle of charging and discharging. Nevertheless, due to the presence of denser electrodes, lithium-ion batteries incur higher costs compared to Ni-Cd batteries. This article utilizes Lithium-ion batteries and a bidirectional DC-DC buck-boost converter. The battery capacity is determined based on the DC load. The battery's characteristics, namely the terminal voltage and state of charge (SOC), can be determined using Equations 7, 8 (Akram et al., 2018).

$$V_{bat} = i_{bat} R_{bat} + V_{oc} + V_e^{B\int i_{bat}.dt} - k\,\frac{Ah}{Ah + \int i_{bat}dt} \tag{7}$$

$$\mathrm{SOC} = \left(1 + \frac{\int i_{bat}dt}{Ah}\right)^{*}100 \tag{8}$$

here, the open-circuit voltage has been named V_{oc}, the terminal voltage of the battery has been named V_{bat}, the battery internal resistance has been named R_{bat}, the battery current has been named i_{bat}, the exponential voltage has been named V_e, the polarization voltage has been named k, and the exponential capacity has been named B (Ong, 1997).

During a critical situation, the battery can serve as a contingency. The battery is replenished from the photovoltaic (PV) source when the generated power of the PV system exceeds the power required. The battery can be utilized in discharge mode when the power supply of the microgrid is insufficient, specifically when the PV source is inadequate to meet the load requirement (Mohan et al., 2002) as shown in Equation 9 and Equation 10.

$$E_{batt}(t) = E_{batt}(t-1) + \eta_{batt} \times \sum\left(E_{gen}(t) - E_{load}(t)\right)\ \forall t > 0 \tag{9}$$

$$1 \geq E_{batt}(t) \geq (1 - \mathrm{DOD})\ \forall t > 0 \tag{10}$$

where E_{batt} denotes the battery energy, E_{load} represents the load energy, η_{batt} depicts the BES efficiency, DOD stands for depth of discharge of BES, and E_{gen} denotes the energy supplied from RES.

3.4 Supercapacitor storage

It is imperative that the control, operation, and energy management of the microgrid be carried out in an appropriate manner in order for a smart electrical grid to work efficiently (Sweidan, 2017). The microgrid has a power imbalance, particularly when it is running in the islanded mode, as a result of the considerable integration of intermittent renewable energy sources (RES) and changeable load swings. In the literature, several solutions have been offered to overcome this issue. Some of these options include the support of conventional generation and the sharing of energy amongst smaller microgrids that are located nearby (Wang et al., 2017). The use of energy storage systems is one of the effective methods that can be utilized to lessen the fluctuations in power and improve the stability of microgrids (Zia et al., 2018). In addition, energy storage has the capability of reducing peak demand, enhancing the grid's transient stability, and storing extra energy for use at a later time. A number of different energy storage technologies, such as batteries, supercapacitors, flywheels, and superconducting magnetic energy storage, have been utilized in order to enhance the stability of microgrids. An extremely high-energy density storage solution for long-term energy sources is the combination of supercapacitors and batteries, which is the most promising option (Nazaripouya et al., 2019).

3.5 DC shunt motor

A DC shunt motor is one example of a dynamic load that may be supplied by the DC microgrid. DC shunt motors are able to transform the electrical DC power that is fed into them into the mechanical power that is produced, which can be seen in the motor's speed and torque. The armature winding of the DC shunt motor is connected in parallel with the field winding of the motor that is being used. When the DC power source is applied to the DC shunt motor, a magnetic flux is produced in the stator, which induces the voltage in the armature winding. Advanced controller can be applied to control the DC shunt motor as in (Wang et al., 2024b) to address the current and speed loop. The nonlinear dynamic model of the DC shunt motor can be represented by (Equations 11–14) (Kumar et al., 2022).

$$K_{\varphi} = \sum_{n=1}^{7} \alpha\, n\, {I_f}^{7-n} \tag{11}$$

$$V_f = I_f\left(R_f + R_{\mathrm{con}}\right) + L_f\frac{dI_f}{dt} \tag{12}$$

$$V_{arm} = I_{arm}R_{arm} + K_{\varphi}\,\omega + L_{arm}\,\frac{dI_{arm}}{dt} \tag{13}$$

$$J\frac{d\omega}{dt} = K_{\varphi}\,I_{arm} - T_{Load} \tag{14}$$

here, the rotor armature current has been named I_{arm}, the armature inductance has been named L_{arm}, the armature voltage has been named V_{arm}, the armature winding resistance has been named R_{arm}, the field winding inductance has been named L_{f}, the field voltage has been named V_{f}, the field winding resistance has been named R_{f}, the control resistance of the field has been named R_{con}, the rotor angular velocity has been named ω, the motor torque constant has been named K_{φ}, and the load torque has been named T_{Load}.

4 Results

The performance of the Microgrid is validated by using a real-time simulation (Opal-RT), as shown in Figure 6. The proposed DC microgrid and the proposed algorithms are implemented using MATLAB Simulink. Subsequently, we compiled the algorithmic code in Opal-RT (OP4510) system. The primary objective is to assess the microgrid's dynamic behaviour and evaluate the proposed control strategy's effectiveness under various operating conditions. This research proposes a non-sophisticated control strategy for a DC microgrid powered by solar and controllable DGs, using readily available battery and supercapacitor storage connected via DC links. The control method is based on prioritizing the available sources in

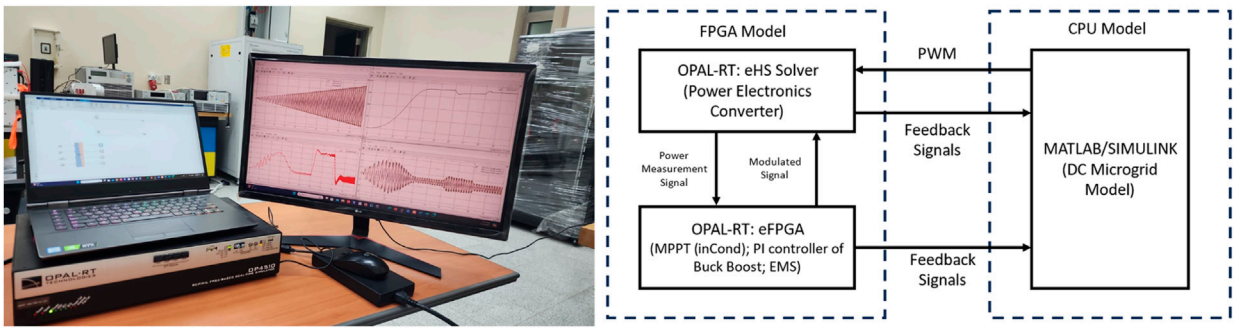

FIGURE 6
Experimental validation setup.

the DC microgrid. The power output of the PV system is of high priority, as it will supply the DC motor and charge the BES. When solar irradiation is low, the BES and supercapacitors will kick in to supply the DC motors. The control signal will be sent by the system operator from the control system that is considered to be a centralized controller who has full access to the available power sources. The well-established InCond algorithm maximizes solar output, while batteries and supercapacitors act as backup. Three main power generation scenarios for the energy management strategy are conducted:

- Full System: Utilizing all available sources - PV system as primary sources, while energy storge system BES and supercapacitors as backup sources.
- Standalone PV: Evaluating system performance solely with the PV system as the primary power source.
- Backup Power Only: Assessing the microgrid's ability to operate solely on BES and supercapacitors, simulating a critical scenario where the PV system is unavailable.

The DC microgrid is tested under these power generation scenarios. Firstly, power sources include the PV system, BES, and supercapacitors used to form the DC microgrid. The second scenario considers a standalone PV microgrid, and the last scenario is the operation of the DC microgrid consisting solely of the backup power sources, i.e., BES and supercapacitors. These different power source scenarios are used to test the dynamics of the microgrid and evaluate the performance of the proposed method under Standard Test Conditions (STC). The following cases are performed to identify the system behaviour under steady-state conditions. Moreover, the case study evaluates the performance of the ESS under different operating conditions. Lastly, the fault analysis on the DC microgrid is performed. It is worth noting that the power rating of the system under study is considered to be 20 kW. These cases have been listed as follows:

1. Steady-State Scenarios:
   - Case 1: Testing under no load to establish baseline performance.
   - Case 2: Testing under full load to evaluate system capability.
2. Fault Scenarios:
   - Case 3: Simulating a PV system fault to assess system response and recovery.

4.1 Steady state operation

It is necessary to do the steady-state analysis of the DC microgrid both with the full load and without any load in order to guarantee the DC microgrid's operation that is both stable and dependable. This analysis aims to identify the system's steady-state behaviour when subjected to different load conditions. To evaluate the steady-state performance, the simulation of the DC microgrid with the full load and no loads are conducted to observe how the system responds over time. The electrical torque values have been chosen in the nominal case with the full load.

4.1.1 Case 1: testing the system under normal conditions with no load

To determine the motor's rotational speed or "no-load speed" and other parameters, this test is conducted by running the motor without any load or external resistance connected to its shaft. The purpose of a no-load test is to evaluate the power flow in the DC microgrid with three power generation scenarios, i.e., the DC microgrid with all power sources, the standalone PV microgrid, and the DC microgrid operating using BES and supercapacitors. Figure 7 shows the torque of the DC motor with no load. Figure 8 shows the output power of the DC microgrid under the three power generation scenarios.

4.1.2 Case 2: testing the system under normal conditions with the full load

This test is similar to Case 1, but the DC microgrid is tested when running the motor with a nominal load. The electrical torque (Te) is constant when the motor's shaft is connected to external resistance and equal to 40 N.m. As shown in Figure 8, the battery and the supercapacitor are charged from the PV system when there is no load in Case 1. In addition, if we sum the power of both the battery and supercapacitor, it will give us

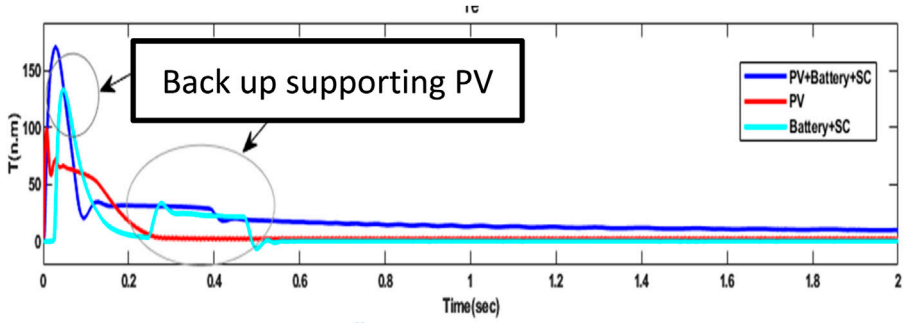

FIGURE 7
Torque of DC motor with no loads.

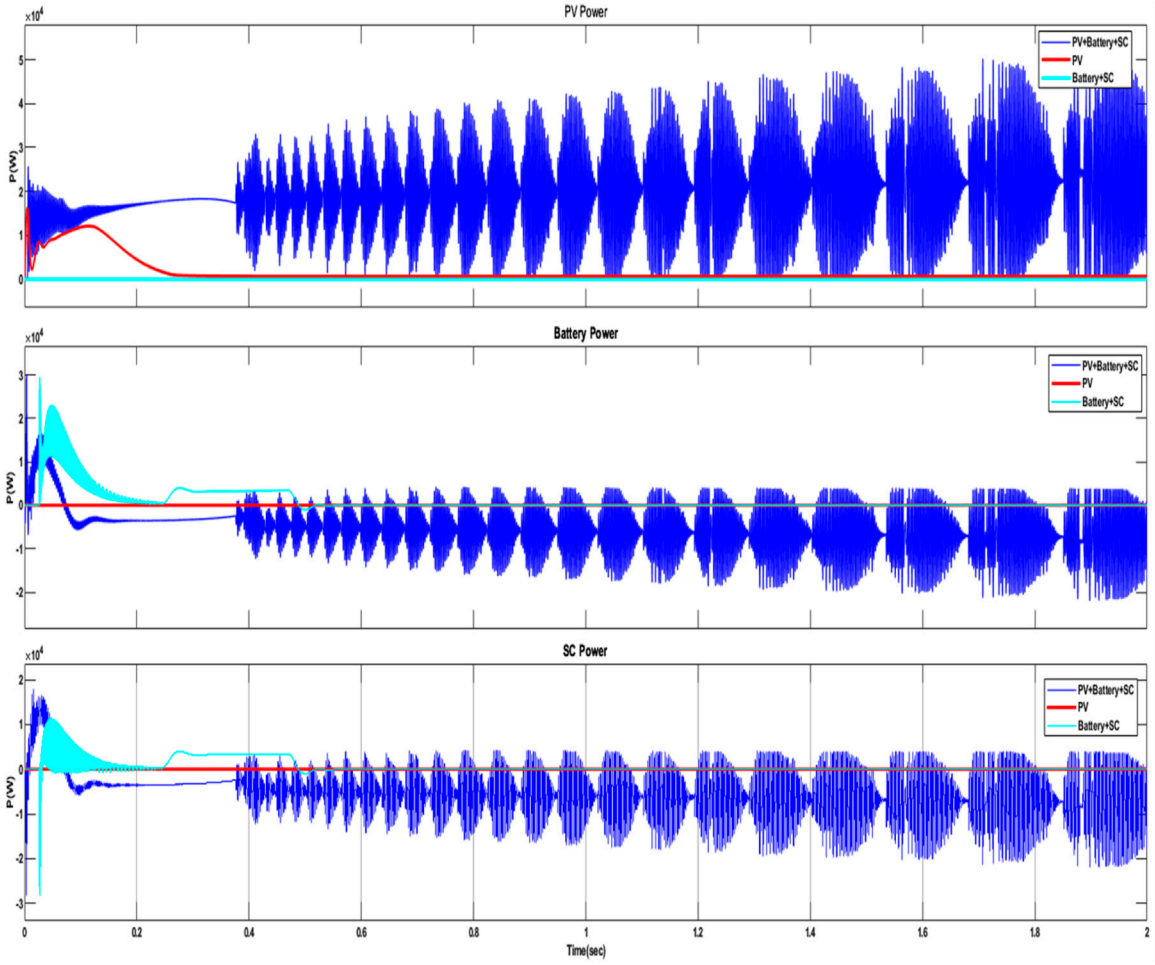

FIGURE 8
PV, BES and S.C of DC Power with no Load.

the PV's power without the motor effective at no load. On the other hand, in Case 2, with the full load, we have a similar behaviour compared with Case 1. The PV system can supply all the load in the DC microgrid and charge the backup sources, and the motor operates more effectively than in Case 1. By comparing the torque of the DC motor in Case1, shown in Figure 7, with Case 2, shown in Figure 9, it can be noticed that the performance of the DC motor in Case 2 is better than in Case 1 due to the presence of the full load in Case 2. Moreover, the comparison reveals that the absence of load initially creates

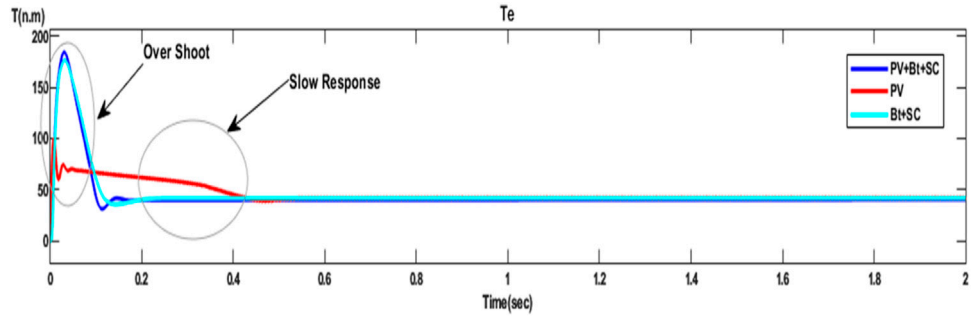

FIGURE 9
Torque of DC motor with Nominal Load.

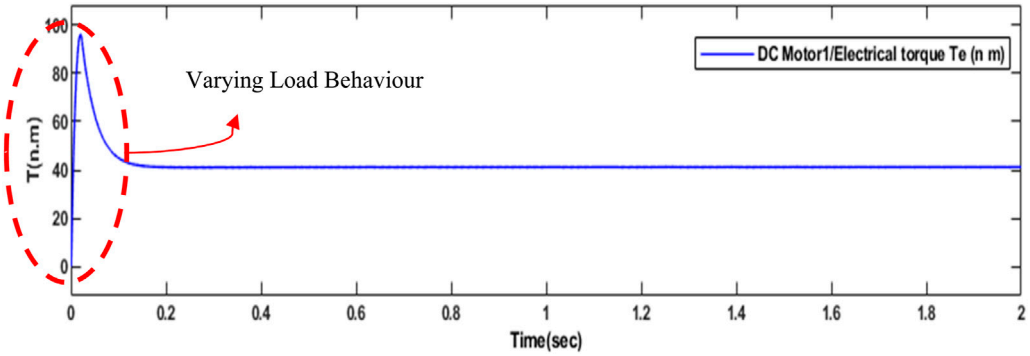

FIGURE 10
Torque of DC motor in PV fault.

instability issues and slow transient responses, as shown in Figure 7.

B. FAULT OPERATION

4.1.3 Case 3: testing the system under PV fault

In the following case, fault analysis is performed to evaluate the reliability of the DC microgrid. In this case, a fault test is applied to the PV system with the short voltage type. Figure 10 shows the DC motor torque, and Figure 11 shows the power output of the power sources during the fault in the PV system. As Figure 11 shows, when the PV fault occurs, the BES supplies the DC motor. It is illustrated that the battery fluctuated in the beginning and then supplied the whole system with the desired output.

Table 2 describes the load/no-load, and fault tolerance on the system efficiency based on the results obtained in the case study. As can be seen, Comparing the load and no-load conditions, the system efficiency in Case 2 is higher efficiency than in Case 1. Hence, operating with the DC microgrid in full load conditions reduces loss, leading to higher system efficiency. Moreover, performing fault analysis Case 3 shows that BES enhances the system's efficiency and ensures uninterrupted power during faults.

5 Discussion

Sever studies have focused on energy management strategies in DC microgrids. Furthermore, all these studies have agreed on efficient power management and system reliability are crucial. However, these studies have employed different in methods as well as areas of focus. While (Li et al., 2023; Duan et al., 2023) utilized optimization focused decision-making process to improve the performance of their systems (Li et al., 2023), relies on using artificial intelligence (AI) whereas bidirectional converters are used by (Duan et al., 2023). Conversely (Luo et al., 2024), focused on using model predictive control for enhanced power flow whereas (Li et al., 2023; Duan et al., 2023) discuss energy losses based on their observation. Nevertheless, these studies serve the same objective of energy management in a DC microgrid. It is obvious that the performance could be slightly different as a result of complex control methodology. The presented paper showed adequate performance with a conventional controller.

For future work, one potential area involves investigating the influence of frequency on the microgrid's behaviour. Additionally, incorporating advanced control systems capable of predicting changes in solar power output and adjusting power supply accordingly could further reduce power fluctuations and enhance stability. Overall, this study provides a valuable foundation for

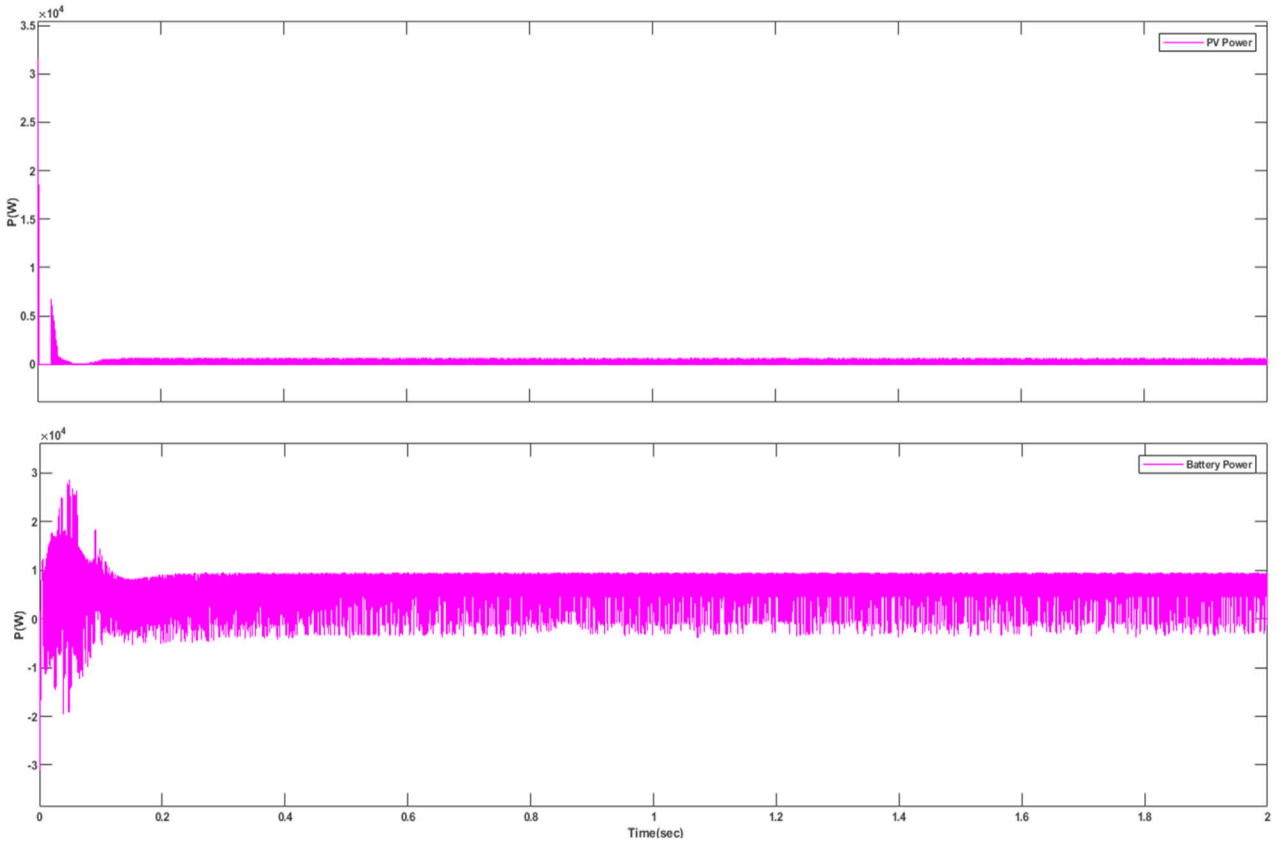

FIGURE 11
PV power and Battery power with PV fault.

TABLE 2 Impact on the system efficiency.

Factor	Description	Impact on efficiency	Cases
Load vs. no-load	Loaded system experiences fewer energy losses, leading to higher efficiency	Operating with a load generally improves efficiency	Cases 1 and 2 (full load vs. no load)
Fault tolerance	BES ensures uninterrupted power during faults, but additional power conversions might decrease efficiency	The trade-off between reliability and peak efficiency	Cases 3 (fault analysis)

developing and optimizing reliable DC microgrids that effectively integrate renewable energy sources like solar power. A valid extension of the presented work is performing an experimental validation.

6 Conclusion

The proposed paper develops an energy management system (EMS) for a DC microgrid, aiming to ensure stable and dependable power delivery for DC motors with conventional control strategies. The microgrid integrates a photovoltaic (PV) system, battery energy storage (BES), and supercapacitors to provide a robust power supply. To optimize PV power generation, the Incremental Conductance (InCond) technique is employed for maximum power point tracking (MPPT). Furthermore, this work investigates the microgrid's performance under various operating scenarios, including diverse power generation conditions and fluctuating solar irradiation. The focus is on maintaining grid stability and reliability. Furthermore, the study examines the performance of the BES in both charging and discharging modes, highlighting its crucial role in power management. Additionally, a fault analysis is conducted to assess the system's response to potential failures and its overall dependability. Further validation of the proposed microgrid is achieved through real-time simulation using OPAL-RT and MATLAB. The results demonstrate that under standard test conditions (1000 W/m^2 solar irradiation and 25°C), the DC motors operate efficiently across various power generation scenarios. The fault analysis emphasizes the importance of the BES in mitigating instability caused by fault conditions. This highlights the BES's role in enhancing the microgrid's overall reliability and ensuring consistent power delivery. The load condition of a system greatly affects its efficiency. This is observable when examining full-load and no-load situations. Conversely, fault tolerance has the potential to affect efficiency

through systems such as BES. Even though BES guarantees the constant supply of power during faults, there are energy conversions needed that might lower overall efficiency. Consequently, this gives rise to a trade-off between the reliability of a system and its peak efficiency thus necessitating careful analysis for specific fault conditions. This research has a few limitations. First, the repeated use of the InCond algorithm might limit adaptability to advanced strategies. Additionally, while the study covers various weather conditions, it does not address extreme events or long-term climate impacts.

Data availability statement

The original contributions presented in the study are included in the article/supplementary material, further inquiries can be directed to the corresponding authors.

Author contributions

HH: Conceptualization, Data curation, Formal Analysis, Investigation, Methodology, Resources, Software, Validation, Visualization, Writing–original draft, Writing–review and editing. AA (2nd author): Conceptualization, Data curation, Formal Analysis, Funding acquisition, Investigation, Methodology, Resources, Software, Validation, Visualization, Writing–original draft, Writing–review and editing. AA (3rd author): Conceptualization, Methodology, Validation, Visualization, Writing–original draft, Writing–review and editing. SuA: Conceptualization, Funding acquisition, Investigation, Methodology, Project administration, Resources, Software, Supervision, Validation, Visualization, Writing–original draft, Writing–review and editing. SaA: Conceptualization, Funding acquisition, Investigation, Project administration, Methodology, Resources, Software, Supervision, Validation, Visualization, Writing–original draft, Writing–review and editing. MA: Conceptualization, Methodology, Validation, Visualization, Writing–original draft, Writing–review and editing.

Funding

The author(s) declare that financial support was received for the research, authorship, and/or publication of this article. The authors would like to express their profound gratitude to King Abdullah City for Atomic and Renewable Energy (K.A.CARE) for their financial support in accomplishing this work. The authors also extend their appreciation to the Deanship of Scientific Research at Northern Border University, Arar, KSA for funding this research work through the project number NBU-FFR-2024-2124-05.

Conflict of interest

The authors declare that the research was conducted in the absence of any commercial or financial relationships that could be construed as a potential conflict of interest.

Publisher's note

All claims expressed in this article are solely those of the authors and do not necessarily represent those of their affiliated organizations, or those of the publisher, the editors and the reviewers. Any product that may be evaluated in this article, or claim that may be made by its manufacturer, is not guaranteed or endorsed by the publisher.

References

Abdel-Salam, M., El-Mohandes, M. T., and Goda, M. (2018). An improved perturb-and-observe based MPPT method for PV systems under varying irradiation levels. *Sol. Energy* 171, 547–561. doi:10.1016/j.solener.2018.06.080

Ahmed, M., Kuriry, S., Shafiullah, M. D., and Abido, M. A. (2019). "DC microgrid energy management with hybrid energy storage systems," in 2019 23rd international conference on mechatronics technology (ICMT) Salerno, Italy, October 23–October 26, 2019 (IEEE), 1–6.

Ahmad, S., Shafiullah, M., Ahmed, C. B., and Alowaifeer, M. (2023). A review of microgrid energy management and control strategies. *IEEE Access* 11, 21729–21757. doi:10.1109/access.2023.3248511

Akram, U., Khalid, M., and Shafiq, S. (2018). Optimal sizing of a wind/solar/battery hybrid grid connected microgrid system. *IET Renew. Power Gener.* 12 (1), 72–80þ. doi:10.1049/iet-rpg.2017.0010

Alahmed, A. S., Taiwo, S. U., Abido, M. A., and Almuhaini, M. M. (2019). "Intelligent flexible priority list for reconfiguration of microgrid demands using deep neural network," in 2019 IEEE innovative smart grid technologies-asia (ISGT asia), Chengdu, China, May 21–May 24, 2019 (IEEE), 3490–3495. doi:10.1109/ISGT-Asia.2019.8881363

Alarbidi, O. M. F., Awaji, H. H. H., Althobiti, A. A., Alhussainy, A. A., Alghamd, A., Abusorrah, A. M., et al. (2023). "Power quality of DQ synchronous frame for wind connected to grid," in 2023 13th International Conference on Power, Energy and Electrical Engineering (CPEEE) Tokyo, Japan, 59–64. doi:10.1109/CPEEE56777.2023.10217705

Athira, G. R., and Pandi, V. R. (2017). "Energy management in islanded DC microgrid using fuzzy controller to improve battery performance," in 2017 international conference on technological advancements in power and energy (TAP energy) Kollam, India, December 21–December 23 2017 (IEEE), 1–6.

Awaji, H. H., Alsulami, A. A. G., Althobiti, A. A., Alhussainy, A. A., Alghamd, A., Milyan, A. H., et al. (2022). "Energy Management System for Direct current (DC) Microgrid," in 2023 13th International Conference on Power, Energy and Electrical Engineering (CPEEE) Tokyo, Japan, 240–245. doi:10.1109/CPEEE56777.2023.10217378

Chahal, M., Tiwari, G., and Saini, S. (2023). Supervisory control of an inverter-based microgrid using PSO algorithm. SONIPAT, India: 2023 9th IEEE India international conference on power electronics (IICPE), 1–6. doi:10.1109/IICPE60303.2023.10474934

Dawoud, N. M., Megahed, T. F., and Kaddah, S. S. (2021). Enhancing the performance of multi-microgrid with high penetration of renewable energy using modified droop control. *Electr. Power Syst. Res.* 201, 107538. doi:10.1016/j.epsr.2021.107538

Duan, Y., Zhao, Y., and Hu, J. (2023). An initialization-free distributed algorithm for dynamic economic dispatch problems in microgrid: modeling, optimization and analysis. *Sustain. Energy, Grids Netw.* 34, 101004. doi:10.1016/j.segan.2023.101004

Elbarbary, Z. M. S., and Alranini, M. A. (2021). Review of maximum power point tracking algorithms of PV system. *Front. Eng. Built Environ.* 1, 68–80. doi:10.1108/febe-03-2021-0019

El-Shahat, A., and Sumaiya, S. (2019). DC-microgrid system design, control, and analysis. *Electronics* 8 (2), 124. doi:10.3390/electronics8020124

Fani, B., Shahgholian, G., Alhelou, H. H., and Siano, P. (2022). "Inverter-based islanded microgrid: a review on technologies and control," in *E-prime-advances in electrical engineering, electronics and energy* 2, 100068. doi:10.1016/j.prime.2022.100068

Gandhi, K., and Gupta, S. K. (2021). Operational strategies and electricity market structure of microgrid: a critical review. *Renew. Energy Focus* 39 (39), 163–171. doi:10.1016/j.ref.2021.09.001

Gielen, D., Gorini, R., Wagner, N., Leme, R., Gutierrez, L., Prakash, G., et al. (2019). *Global energy transformation: a roadmap to 2050*.

Gowtham, K., Sivaramadurai, C. V., Hariprasath, P., and Indurani, B. (2018). "A management of power flow for DC microgrid with solar and wind energy sources," in 2018 international conference on computer communication and informatics (ICCCI) Coimbatore, India, January 04–January 06, 2018 (IEEE), 1–5.

Hashim, N., Salam, Z., Johari, D., and Ismail, N. F. N. (2018). DC-DC boost converter design for fast and accurate MPPT algorithms in stand-alone photovoltaic system. *Int. J. Power Electron. Drive Syst.* 9 (3), 1038. doi:10.11591/ijpeds.v9.i3.pp1038-1050

Hassan, M. A., Worku, M. Y., and Abido, M. A. (2018). Optimal design and real time implementation of autonomous microgrid including active load. *Energies* 11 (5), 1109. doi:10.3390/en11051109

Hossain, M. K., and Ali, M. H. (2016). Transient stability augmentation of PV/DFIG/SG-based hybrid power system by parallel-resonance bridge fault current limiter. *Electr. Power Syst. Res.* 130, 89–102. doi:10.1016/j.epsr.2015.08.016

Hussaini, H., Yang, T., Gao, Y., Wang, C., Bai, Ge, and Bozhko, S. (2022) "Droop coefficient design and optimization using genetic algorithm-A case study of the more electric aircraft DC microgrid," in *Iecon 2022 – 48th annual conference of the*. IEEE Industrial Electronics Society, 1–6.

Jirdehi, M. A., Tabar, V. S., Ghassemzadeh, S., and Tohidi, S. (2020). Different aspects of microgrid management: a comprehensive review. *J. Energy Storage* 30, 101457. doi:10.1016/j.est.2020.101457

Ju, Y., Liu, W., Zhang, Z., and Zhang, R. (2022). Distributed three-phase power flow for AC/DC hybrid networked microgrids considering converter limiting constraints. *IEEE Trans. Smart Grid* 13 (3), 1691–1708. doi:10.1109/TSG.2022.3140212

Keerthisinghe, C., and Kirschen, D. S. (2020). 1 real-time digital simulation of microgrid control strategies. *2020 IEEE power and energy society innovative smart grid technologies conference (ISGT)* (IEEE), 1–5.

Kumar, A., Ibraheem, S., Gupta, R. K., Nguyen, T. A., and Yasin, G. (2022). "Battery-supercapacitor hybrid systems: an introduction," in *Nanotechnology in the automotive industry* (Elsevier), 453–458.

Kumar, K., Kumar, P., and Kar, S. (2024). A review of microgrid protection for addressing challenges and solutions. *Renew. Energy Focus* 49, 100572. doi:10.1016/j.ref.2024.100572

Lei, C., Bu, S., Wang, Q., Chen, Q., Yang, L., and Chi, Y. (2023). Look-ahead rolling economic dispatch approach for wind-thermal-bundled power system considering dynamic ramping and flexible load transfer strategy. *IEEE Trans. Power Syst.* 39, 186–202. doi:10.1109/TPWRS.2023.3238035

Li, B., Wang, J., Nassani, A. A., Binsaeed, R. H., and Li, Z. (2023). The future of Green energy: a panel study on the role of renewable resources in the transition to a Green economy. *Energy Econ.* 127, 107026. doi:10.1016/j.eneco.2023.107026

Luo, J., Zhuo, W., Liu, S., and Xu, B. (2024). The optimization of carbon emission prediction in low carbon energy economy under big data. *IEEE Access* 12, 14690–14702. doi:10.1109/ACCESS.2024.3351468

Marwali, M. N., Keyhani, A., and Dai, M. (2009). *Integration of green and renewable energy in electric power systems*. John Wiley and Sons.

Meng, Q., Hussain, S., Luo, F., Wang, Z., and Jin, X. (2024). An online reinforcement learning-based energy management strategy for microgrids with centralized control. *IEEE Trans. Industry Appl.*, 1–10. doi:10.1109/TIA.2024.3430264

Mohan, N., Undeland, T. M., and Robbins, W. P. (2002). *Power electronics: converters, applications, and design (3rd ed.)*. John Wiley & Sons.

Naderi, M., Khayat, Y., Shafiee, Q., Blaabjerg, F., and Bevrani, H. (2023). Dynamic modeling, stability analysis and control of interconnected microgrids: a review. *Appl. Energy* 334 (2023), 120647. doi:10.1016/j.apenergy.2023.120647

Nazaripouya, H., Chung, Y. W., and Akhil, A. (2019). Nergy storage in microgrids: challenges, applications and research need. *Int. J. Energy Smart Grid* 3 (2), 60–70. doi:10.23884/ijesg.2018.3.2.02

Ong, C. M. (1997). *Dynamic simulation of electric machinery: using MATLAB/SIMULINK*. Prentice Hall.

Rami Reddy, C., Choi, J.-H., Sekhar, O. C., Colak, I., and Khalid, M. (2024). State of the art review of islanding detection methods for integrated distributed generation system. *Electr. Power Components Syst.* 52, 1906–1935. doi:10.1080/15325008.2024.2314197

Rana, M. J., and Abido, M. A. (2017). Energy management in DC microgrid with energy storage and model predictive controlled AC–DC converter. *IET Generation, Transm. and Distribution* 11 (15), 3694–3702. doi:10.1049/iet-gtd.2016.1934

Rashid, M. M. U., Alotaibi, M. A., Chowdhury, A. H., Rahman, M., Alam, M. S., Hossain, M. A., et al. (2021). Home energy management for community microgrids using optimal power sharing algorithm. *Energies* 14 (4), 1060. doi:10.3390/en14041060

Saleh Al-Ismail, F. (2024). A critical review on DC microgrids voltage control and power management. *IEEE Access* 12, 30345–30361. doi:10.1109/access.2024.3369609

Seyedmahmoudian, M., Mohamadi, A., Kumary, S., Oo, A. M. T., and Stojcevski, A. (2014). A comparative study on procedure and state of the art of conventional maximum power point tracking techniques for photovoltaic system. *Int. J. Comput. Electr. Eng.* 6 (5), 402–414. doi:10.17706/ijcee.2014.v6.859

Shirkhani, M., Tavoosi, J., Danyali, S., Sarvenoee, A. K., Abdali, A., Mohammadzadeh, A., et al. (2023). A review on microgrid decentralized energy/voltage control structures and methods. *Energy Rep.* 10, 368–380. doi:10.1016/j.egyr.2023.06.022

Sweidan, T. (2017). Dynamical analysis of DC shunt motor powered by PV generator using perturbation and observation as MPPT tracking technique. *Energy Power Eng.* 9 (1), 55–69. doi:10.4236/epe.2017.91005

Wang, C., Wang, Y., Wang, K., Dong, Y., Yang, Y., and Hanne, T. (2017). An improved hybrid algorithm based on biogeography/complex and metropolis for many-objective optimization. *Math. Problems Eng.* 2017, 2462891. doi:10.1155/2017/2462891

Wang, R., Gu, Q., Lu, S., Tian, J., Yin, Z., Yin, L., et al. (2024b). FI-NPI: exploring optimal control in parallel platform systems. *Electronics* 13 (7), 1168. doi:10.3390/electronics13071168

Wang, R., and Zhang, R. (2023). Techno-economic analysis and optimization of hybrid energy systems based on hydrogen storage for sustainable energy utilization by a biological-inspired optimization algorithm. *J. Energy Storage* 66, 107469. doi:10.1016/j.est.2023.107469

Wang, S., Lu, T., Hao, R., Li, J., Guo, Y., He, X., et al. (2024a). An identification method for anomaly types of active distribution network based on data mining. *IEEE Trans. Power Syst.* 39 (4), 5548–5560. doi:10.1109/TPWRS.2023.3288043

Worku, M. Y., Hassan, M. A., and Abido, M. A. (2019). Real time energy management and control of renewable energy based microgrid in grid connected and island modes. *Energies* 12 (2), 276. Þ. doi:10.3390/en12020276

Worku, M. Y., Hassan, M. A., and Abido, M. A. (2021). Power management, voltage control and grid synchronization of microgrids in real time. *Arabian J. Sci. Eng.* 46, 1411–1429. Þ. doi:10.1007/s13369-020-05062-9

Wu, Y., Cui, J. Z., and Liu, C. (2024). State-of-the-art review on energy management systems, challenges and top trends of renewable energy based microgrids. *EAI Endorsed Trans. Energy Web* 10. doi:10.4108/ew.4124

Xie, K., Dong, J., Singh, C., and Hu, Bo (2016). Optimal capacity and type planning of generating units in a bundled wind–thermal generation system. *Appl. Energy* 164 (2016), 200–210. doi:10.1016/j.apenergy.2015.12.004

Zhang, J., Cho, H., and Mago, P. J. (2021). "Energy conversion systems and energy storage systems," in *Energy services fundamentals and financing*. Editor D. Borge-Diez (Academic Press), 155–179. doi:10.1016/B978-0-12-820592-1.00007-5

Zhang, J., Liu, Y., Zang, J., Liu, Z., Zhou, J., Wang, J., et al. (2024b). An embedded DC power flow controller based on full-bridge modular multilevel converter. *IEEE Trans. Industrial Electron.* 71 (3), 2556–2566. doi:10.1109/TIE.2023.3265041

Zhang, J., Liu, Y., Zhou, J., Zang, J., Shi, G., Wang, J., et al. (2024a). A novel multiport transformer-less unified power flow controller. *IEEE Trans. Power Electron.* 39 (4), 4278–4290. doi:10.1109/TPEL.2023.3347900

Zhou, Y., Zhai, Q., Xu, Z., Wu, L., and Guan, X. (2024). Multi-stage adaptive stochastic-robust scheduling method with affine decision policies for hydrogen-based multi-energy microgrid. *IEEE Trans. Smart Grid* 15 (3), 2738–2750. doi:10.1109/TSG.2023.3340727

Zia, M. F., Elbouchikhi, E., and Benbouzid, M. (2018). Microgrids energy management systems: a critical review on methods, solutions, and prospects. *Appl. energy* 222, 1033–1055. doi:10.1016/j.apenergy.2018.04.103

Nomenclature

Abbreviations

I_{pv}	The PV cell output current
I_{pc}	The photocurrent
I_{pc}	The current passing through the diode
I_{shunt}	The shunt resistance current
K	The Boltzmann constant
q	The charge of electron
I_{rev}	The reverse current of the diode
T	The cell temperature in kelvin (K)
V_{pv}	The PV cell output voltage
A	The quality factor
R_{shunt} and R_{series}	The shunt and series resistances of the equivalent circuit of PV system
V_{pv}	The converter's input voltage
V_{dc}	The converter's output voltage
ΔV_{pv}	Depicts the drift in V_{pv}
ΔV_0	The output voltage's ripples
I_{pv}	PV maximum current
L_a	The in V boost converter
ΔI_{La}	The inductor ripple current
P_{pv}	The PV array normal power
f	The switching frequency
C_a	Link capacitance of the PV array
C_1	The capacitance of the DC link
D	Depicts the converter's duty ratio
V_{oc}	Open-circuit voltage
V_{bat}	The terminal voltage of the battery
R_{bat}	The battery internal resistance
i_{bat}	The battery current
V_e	The exponential voltage
k	The polarization voltage
B	The exponential capacity
E_{batt}	The battery energy
E_{load}	The load energy
η_{batt}	The BES efficiency
DOD	Depth of discharge of BES
E_{gen}	The energy supplied from RES
I_{arm}	The rotor armature current
L_{arm}	The armature inductance
V_{arm}	The armature voltage
R_{arm}	The armature winding resistance
L_{f}	The field winding inductance
V_{f}	The field voltage
R_{f}	The field winding resistance
R_{con}	The control resistance of the field
ω	The rotor angular velocity
K_{φ}	The motor torque constant
T_{Load}	The load torque

frontiers | Frontiers in Energy Research

TYPE Original Research
PUBLISHED 08 October 2024
DOI 10.3389/fenrg.2024.1448046

OPEN ACCESS

EDITED BY
C. H. Rami Reddy,
Chonnam National University, Republic of Korea

REVIEWED BY
Manne Bharathi,
Acharya Nagarjuna University, India
Linfei Yin,
Guangxi University, China
Lefeng Cheng,
Guangzhou University, China

*CORRESPONDENCE
Yongzhi Li,
tuytliyongzhi@163.com

RECEIVED 12 June 2024
ACCEPTED 30 August 2024
PUBLISHED 08 October 2024

CITATION
Xiao J, Zhao W, Li W, Zhao Y, Li Y, Ma X and Liu Y (2024) Active power balance control of wind-photovoltaic-storage power system based on transfer learning double deep Q-network approach.
Front. Energy Res. 12:1448046.
doi: 10.3389/fenrg.2024.1448046

Active power balance control of wind-photovoltaic-storage power system based on transfer learning double deep Q-network approach

Jun Xiao, Wen Zhao, Wei Li, Yankai Zhao, Yongzhi Li*, Xudong Ma and Yuchao Liu

State Grid Shanxi Power Company Lvliang Power Supply Company, Lvliang, China

Introduction: This study addresses the challenge of active power (AP) balance control in wind-photovoltaic-storage (WPS) power systems, particularly in regions with a high proportion of renewable energy (RE) units. The goal is to effectively manage the AP balance to reduce the output of thermal power generators, thereby improving the overall efficiency and sustainability of WPS systems.

Methods: To achieve this objective, we propose the transfer learning double deep Q-network (TLDDQN) method for controlling the energy storage device within WPS power systems. The TLDDQN method leverages the benefits of transfer learning to quickly adapt to new environments, thereby enhancing the training speed of the double deep Q-network (DDQN) algorithm. Additionally, we introduce an adaptive entropy mechanism integrated with the DDQN algorithm, which is further improved to enhance the training capability of agents.

Results: The proposed TLDDQN algorithm was applied to a regional WPS power system for experimental simulation of AP balance control. The results indicate that the TLDDQN algorithm trains agents more rapidly compared to the standard DDQN algorithm. Furthermore, the AP balance control method based on TLDDQN can more accurately manage the storage device, thereby reducing the output of thermal power generators more effectively than the particle swarm optimization-based method.

Discussion: Overall, the TLDDQN algorithm proposed in this study can provide some insights and theoretical references for research in related fields, especially those requiring decision making.

KEYWORDS

wind-photovoltaic-storage power system, renewable energy, active power balance control, double deep Q-Network, transfer learning

1 Introduction

Conventional power generation technologies produce large amounts of greenhouse gases (Russo et al., 2023). To reduce greenhouse gas emissions, various countries have formulated carbon reduction programs. Renewable energy (RE) power generation technology has been widely favored by countries for the advantages of environmental

protection and sustainability (Han et al., 2023). However, the stochastic and fluctuating characteristics of RE generation systems can threaten the reliability of power systems (Guerra et al., 2022). Energy storage (ES) devices can release power to relieve power tension or absorb power to avoid power waste (Dong et al., 2022). Consequently, the stability of the RE power generating system can be enhanced by the RE power plant built by leveraging the complementarity of RE.

When the proportion of RE units in power generation systems is small, the traditional active power (AP) regulation strategy of the RE power generation system can prioritize the consumption of power generated by RE units. The thermal power units cooperate with the RE units to regulate the AP balance of the RE power generation system (Grover et al., 2022). However, when the proportion of RE units in the RE power generation system is large, the RE units need to cooperate with the traditional thermal power units to control the AP balance of the power system (Ye et al., 2023). In this study, the AP balance control problem is considered for a high percentage of RE generation systems.

The AP balance control methods of RE generation systems mainly have two categories: swarm intelligence algorithms and reinforcement learning algorithms. The adaptability of the swarm intelligence algorithm-based AP balance control method is considerable. However, the swarm intelligence algorithm-based AP balance control method has the disadvantages of poor real-time performance and easily falling into local optimization (Moosavian et al., 2024). On the contrary, the AP balance control method based on reinforcement learning has the advantage of high real-time performance (Yin and Wu, 2022).

The swarm intelligence algorithm-based AP balance control method has the advantage of adaptability (Jiang et al., 2022). The AP balance control methods, which are based on hybrid swarm intelligence algorithms comprising Mexican axolotl optimization and the honey badger algorithm, have the potential to reduce carbon emissions, power costs, and peak power consumption in power systems (Revathi et al., 2024). An integrated load scheduling method for RE generation systems based on the Firefly algorithm can reduce the fuel cost of the generation system (Mehmood et al., 2023). Optimal AP scheduling methods for power systems based on hybrid particle swarm optimization and hippocampus optimization algorithms can reduce AP losses in power systems (Hasanien et al., 2024). However, the AP balance control method of wind-photovoltaic-storage (WPS) power system based on swarm intelligence algorithms has the shortcomings of low real-time performance and insufficient regulation accuracy.

The reinforcement learning-based AP balance control method is suitable for AP balance control of power systems in complex environments (Cheng and Yu, 2019). In addition, the AP balance control method for WPS power systems based on reinforcement learning has the advantage of high real-time performance. A decomposed predictive fractional-order proportional-integral-derivative control reinforcement learning algorithm can reduce frequency deviation and improve power quality in integrated energy systems (Yin and Zheng, 2024). The short-term optimal dispatch model framework of the water-wind-photovoltaic multi-energy power system constructed based on the deep Q-network (DQN) algorithm can improve the generation efficiency of multi-energy systems (Jiang et al., 2023). The control strategy of ES devices for energy systems based on improved deep deterministic policy gradient algorithms can integrate the frequency fluctuation of energy systems (Yakout et al., 2023). The energy system optimization control strategy based on the twin delayed deep deterministic policy gradient algorithm can flexibly adjust the components' operation and the ES device's charging strategy according to the output of RE sources and the electricity price (Zhang et al., 2022). The approach of employing electric vehicles as energy storage devices and regulating charging strategies with DQN algorithms is an effective solution to address the security of energy supply issues associated with the future power grid (Hao et al., 2023). A multi-agent game operation strategy consisting of energy retailers, suppliers, and users with integrated demand response is an effective way to alleviate the tension of multi-energy coupling and multi-agent difficulties (Li et al., 2023). N Population multi-strategy evolutionary game theory reveals the long-term equilibrium properties of the long-term bidding problem on the generation side of the power market and provides a theoretical reference to the complex dynamic interactive decision-making problems in related fields (Cheng et al., 2020). However, previous AP balance control methods based on reinforcement learning often need to be relearned when faced with new environments.

This study proposes the transfer learning double deep Q-network (TLDDQN)-based AP balance control method for controlling storage devices in WPS power systems. The proposed TLDDQN combines the advantage of transfer learning that can rapidly adapt to new environments and the advantage of the double deep Q-network (DDQN) algorithm that deals with complex environments. In addition, this study proposes a method to combine the adaptive entropy mechanism to the DDQN algorithm and improve the corresponding adaptive entropy mechanism. Therefore, the TLDDQN method can be effective in training TLDDQN agents and controlling the AP of the WPS power system. The characteristics of the AP balance control method for WPS power systems based on the proposed TLDDQN can be summarized as follows.

(1) This study combines the transfer learning approach and the DDQN to form the TLDDQN algorithm. The proposed TLDDQN algorithm combines the adaptive entropy mechanism to enhance the exploration ability during training and utilizes the transfer learning approach to transfer the generic parameters in the neural network (NN) of the TLDDQN algorithm.
(2) The active probabilistic balance control method for WPS power systems based on the proposed TLDDQN can be applied to control ES devices in WPS power systems.
(3) The active probabilistic balancing control method of the WPS power system based on the TLDDQN algorithm can balance the AP of the WPS power system.

2 Mathematical modeling of renewable energy generators

The devices of the WPS power system are mainly composed of wind power (WP) generation devices, photovoltaic power (PP)

generation devices, and ES devices (Abdelghany et al., 2024). This study analyzes the output characteristics of WP generation devices, PP generation devices, and ES devices to obtain the corresponding mathematical model.

2.1 Mathematical modeling of wind power generation devices

The WP generation devices convert the kinetic energy of the wind into electrical energy (Liu and Wang, 2022). The power generation efficiency of a WP generation device is related to the ambient wind speed (Jung and Schindler, 2023). The output of WP generation devices is expressed as follows (Equation 1).

$$P_{\mathrm{wt}} = \begin{cases} 0, & v < v_{\mathrm{ci}}^{'} \\ a'v^3 + b'v^2 + c'v + d', & v_{\mathrm{ci}}^{'} \le v \le v_{\mathrm{r}}^{'} \\ P_{\mathrm{r}}^{'}, & v_{r}^{'} < v < v_{\mathrm{co}}^{'} \\ 0, & v \le v_{\mathrm{co}}^{'} \end{cases} \tag{1}$$

where, P_{wt} is the output of WP generation devices; $P_{\mathrm{r}}^{'}$ is the rated power of WP generation devices; v is the actual wind speed; $v_{\mathrm{ci}}^{'}$ is the tangential wind speed of WP generation devices; $v_{\mathrm{r}}^{'}$ is the rated wind speed; $v_{\mathrm{co}}^{'}$ is the cut-out wind speed; a', b', c' and d' are the wind speed parameters of WP generation devices.

2.2 Mathematical modeling of photovoltaic power generation devices

The PP generation devices convert solar energy into electrical energy (Bawazir et al., 2023). The power generation efficiency of PP generation devices is related to the light intensity and temperature (Li et al., 2024). The output of power generation devices is expressed as follows (Equation 2).

$$P_{\mathrm{PV}} = P_{\mathrm{STC}} \frac{G_{\mathrm{ING}}}{G_{\mathrm{STC}}} [1 + k(T_C - T_r)] \tag{2}$$

where, P_{PV} is the output of PP generation devices; P_{STC} is the maximum output of the PP generation devices; G_{ING} is the intensity of light; G_{STC} is the standard light intensity; k is the temperature coefficient; T_C is the ambient temperature; T_r is the reference temperature.

2.3 Mathematical modeling of energy storage devices

The ES devices can absorb or release AP. When WP generation devices and PP generation devices generate more power than the load demand, ES devices can absorb power to avoid wasting electricity (Rostamnezhad et al., 2022). When the output power of WP devices and PP devices is less than the load demand, ES devices can release power to relieve the power tension (Song et al., 2023). Batteries are common ES devices. The most widely applied equivalent model for ES plants is the Davignan equivalent model. An ES device can be represented mathematically as follows (Equation 3).

$$SOC(t) = \begin{cases} SOC(t-1) + \dfrac{\eta_{\mathrm{ch}} I_t}{C_N} & \text{Charge} \\ SOC(t) - \dfrac{I_t}{C_N \eta_{dis}} & \text{Discharge} \end{cases} \tag{3}$$

where, $SOC(t)$ is the state of charge at time t; $SOC(t-1)$ is the state of charge of the ES device at time $t-1$; η_{ch} is the charge efficiency; η_{dis} is the discharge efficiency; C_N is the rated power; I_t is the current flows through ES devices.

3 Active power balance control method based on transfer learning double deep Q-network approach

This study proposes a TLDDQN-based AP balance control strategy. This AP balance control strategy based on TLDDQN is applied to cooperate with the traditional thermal generating units for AP balance control of the RE generation system by controlling storage devices in the WPS power system. The transfer learning method is employed to enhance the DDQN, thereby facilitating the formation of the TLDDQN. In addition, this study proposes an improved adaptive entropy mechanism to improve the exploratory ability of agents during the training process. The TLDDQN has the advantage of being able to adapt to different environments and can provide a strategy to maximize the cooperation of the WP and PP systems with the conventional units for the AP balance control of the renewable power system.

3.1 Transfer learning method

Transfer learning achieves the purpose of learning new knowledge quickly through the transfer of similarities (Wang et al., 2023). In contrast to traditional machine learning, transfer learning permits a relaxation of the fundamental assumption that the training data must independently satisfy the same distributional conditions as the test data. When training and test data have different distributions, transfer learning methods allow for fast model building.

The transfer learning approach defines a source domain D_s and a target domain D_t. The source and target domains have different data distributions $P(X_s)$ and $P(X_t)$. The focus of the transfer learning approach is finding the similarities between the source domains and target domains and utilize appropriately.

3.2 Double deep Q-network approach

The DQN employs a combination of deep learning methodologies and Q-learning to address the issue of dimensionality explosion that is inherent to the latter (Yi et al., 2022). The DQN algorithm applies NNs as function approximators to approximate the state-action value. The expression of the objective function of the DQN algorithm is expressed as follows (Equation 4).

$$Y_i^{\mathrm{DQN}} = r + \gamma \max_{a'} Q(s', a'; \theta') \tag{4}$$

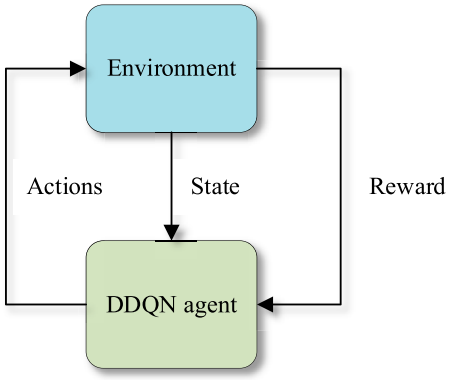

FIGURE 1
Relationship between DDQN agents and environments.

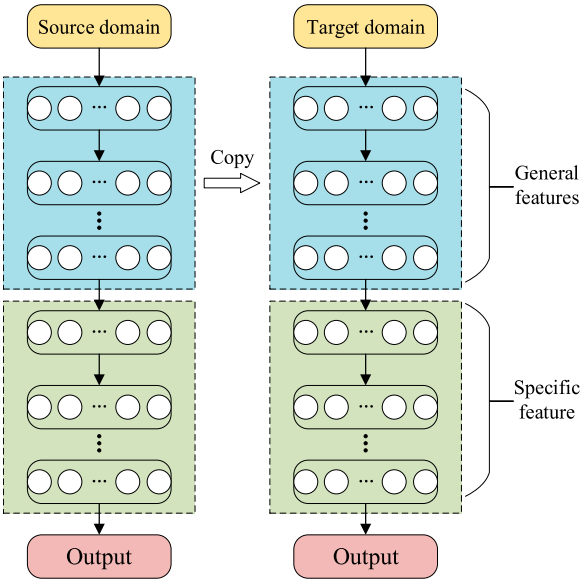

FIGURE 2
Transfer learning methods transfer NNs.

where, r is the reward of actions; γ is the discount factor; (s', a') is the state-action value at the next moment; θ' is the weight of the target network; max is taking the maximum value.

The DQN algorithm is susceptible to overestimation of the Q value. The DDQN algorithm represents an improvement from the original DQN algorithm. The DDQN algorithm separates the action selection and action valuation processes of the DQN algorithm, thus addressing the issue of the DQN algorithm being prone to overestimating the Q value. The optimization function Y_i^{DDQN} of the NN of the DDQN algorithm is expressed as follows (Equation 5).

$$Y_i^{\mathrm{DDQN}} = r + \gamma Q\left(s', \arg\max_{a'} Q(s', a'; \theta^-); \theta'\right) \tag{5}$$

where, the Q-function with weights θ' is applied to select the action behavior; the Q-function with weights θ^- is applied to evaluate the action.

Figure 1 illustrates the relationship between the DDQN agent and environments. The DDQN agent outputs actions to act on environments. The DDQN agent receives the reward value and state of the output actions from environments to update the parameters of agents.

3.3 Improvement of adaptive entropy mechanism

Ordinary reinforcement learning algorithms tend to converge to a local optimum solution in the late stage of training. To solve this problem, some reinforcement learning algorithms combine the entropy maximization method with the reinforcement learning algorithm to obtain stronger algorithmic performance. Reinforcement learning methods that combine the entropy of a policy to maximize the reward also maximize the entropy of the distribution of the actions of policy in each state, rather than just considering maximizing the reward of actions. As a result, compared with ordinary reinforcement learning methods, the reinforcement learning method with the entropy of policies obtains stronger exploration ability and effectively solves the problem of convergence to locally optimal solutions. Accordingly, this study combines the adaptive entropy mechanism into the DDQN algorithm and improves the adaptive entropy mechanism.

The entropy of a strategy is a measure of the uncertainty of a probability distribution. As the distribution becomes more random, the entropy value increases. Reinforcement learning algorithms combining the method of maximizing entropy for the augmentation and generalization of the rewards of agents can be expressed as follows (Equation 6).

$$r(s_t, a_t) = r(s_t, a_t) + \delta H(p) \tag{6}$$

where, $r(s_t, a_t)$ is the reward of the intelligent; δ is the adaptive entropy temperature coefficient; $H(p)$ is the entropy of the strategy.

According to the knowledge of information theory, the entropy of the strategy can be expressed as follows (Equation 7).

$$H(p) = -\sum_i p_i \log(p_i) \tag{7}$$

where, p_i is the state transfer distribution.

In the above process, the value of the adaptive entropy temperature coefficient is very important. Too small an adaptive entropy temperature coefficient will result in the agent easily converging to the local optimal solution; too large an adaptive entropy temperature coefficient will result in the agent generating too much unnecessary exploration. However, previous deep reinforcement learning algorithms do not provide reasonable values for the adaptive entropy temperature coefficient. Therefore, this study proposes improved adaptive entropy temperature coefficients to enhance the rationality of entropy utilization.

This study proposes a method to dynamically adjust the entropy temperature coefficient based on the average reward. If the average reward of an agent is stagnant or decreasing, the entropy value should increase to encourage the exploration of new strategies; on

the contrary, if the average reward continues to increase, the entropy value should decrease to stabilize the currently effective strategies. Therefore, the entropy temperature coefficient proposed in this study can be expressed as follows (Equation 8).

$$\delta' = \begin{cases} \delta'_{\max} \exp(-ite/50)\delta, & if\ (R_t > R_{t-1}) \\ \delta'_{\min}\delta, & else \end{cases} \tag{8}$$

where, δ' is the entropy temperature coefficient proposed in this study; R_t is the average reward of the intelligences; *ite* is the number of iterations in the training process; $\delta'_{\max}$ is the maximum entropy temperature coefficient; $\delta'_{\min}$ is the minimum entropy temperature coefficient; exp is the exponential operator.

3.4 Transfer learning double deep Q-network approach

This study proposes TLDDQN that is formed by the transfer learning approach combined into the DDQN approach. As shown in Figure 2, the NN of the DDQN approach can be split into two parts. One part of the NN is responsible for learning generic features. The other part of the double NN is responsible for learning task-specific features. First, when the deep reinforcement learning agents are under a new environment, the NN in the source domain that is responsible for learning generalized features is directly copied to the target domain. Besides, the corresponding NN parameters are frozen. Then, the transfer learning method randomly initializes the unfrozen NN parameters in the target domain and retrains NN parameters with the data in the target domain.

3.5 Transfer learning double deep Q-network-based active power balance control method for wind-photovoltaic-storage power systems

This study applies the proposed TLDDQN to control ES devices to fully consider the cost factor at the same time as the traditional unit to carry out AP balance control of WPS power systems. Considering the environmentally friendly and renewable advantages of wind and PP generation systems, the AP balance control strategy based on the proposed TLDDQN prioritizes the consumption of power generated by WP and PP generation systems. However, because of the stochastic and fluctuating characteristics of WP and PP generation systems, the power output of the WP-PP systems alone is challenged to match the load consumption. Therefore, the AP balance control strategy in this study applies the proposed TLDDQN method to control ES devices, which are combined with the traditional thermal power generation system for the AP balance control of the WPS power system.

The TLDDQN method is a deep reinforcement learning method that necessitates the definition of the state, action, and reward settings.

The state of an agent is the mathematical representation of the environment in which the agent is located. Therefore, in this study, the state of the agent includes the load power, the power generated by the wind power generator, the power generated by the photovoltaic power generator, and the charge state of the energy storage device at the same moment. Therefore, the state S_t of the agent can be represented as follows (Equation 9).

$$S_t = \{P_{\text{load}}, P_{\text{wt}}, P_{\text{pv}}, soc\} \tag{9}$$

where, P_{load} is the load power; *soc* is the battery status.

The action of the TLDDQN consists of a series of discrete variables. The action a_t is represented as follows (Equation 10).

$$a_t = \left\{ l, l + \frac{h-l}{M}, ..., h \right\} \tag{10}$$

where, l is the lower limit of the action value; h is the upper limit of the action value; M is the dimension of the action space.

The reward setting of the TLDDQN agent mainly takes into account the operational cost of the WPS power system and the discharge power of the ES device. The reward setting *rew* is expressed as follows (Equations 11–17).

$$rew = \alpha r_1(t) + \beta r_2(t) \tag{11}$$

$$r_1(t) = C_f(t) + C_{OM}(t) + C_{DEP}(t) + C_L \tag{12}$$

$$r_2(t) = P_{dis}(t) \tag{13}$$

$$C_f(t) = \sum_{i=1}^{N} C_{fuel} \frac{1}{LHV} \sum_{t=1}^{T} \frac{P_i(t)}{\eta_i(t)} \tag{14}$$

$$C_{OM}(t) = \sum_{i=1}^{N} K_{OM,i} P_i(t) \tag{15}$$

$$C_{DEP}(t) = \sum_{i=1}^{N} \frac{C_{ACC,i}}{8760 P_{ri} f_{cf,i}} P_i(t) \tag{16}$$

$$C_L = C_{\text{bu}} load \tag{17}$$

where, $r_1(t)$ is the WPS power system's operational cost reward; $r_2(t)$ is the ES unit's discharge power reward; α is the operating cost coefficient; β is the discharge power coefficient; N is the times that the AP balance control method is dispatched within a day; $P_{dis}(t)$ is ES unit's discharge power; $C_f(t)$ is the fuel cost consumed; $C_{OM}(t)$ is the maintenance cost; $C_{DEP}(t)$ is the depreciation cost; C_L is the compensation cost for the outage when the load is removed; C_{fuel} is the price of fuel; *LHV* is the low calorific value; $P_i(t)$ is the AP output of the generating unit; $\eta_i(t)$ is the fuel combustion efficiency of the thermal generating unit; $K_{OM,i}$ is the maintenance factor of the generating unit; $C_{ACC,i}$ is the installation cost of the generating unit; P_{ri} is the rated power of the generating unit; $f_{cf,i}$ is the capacity factor; C_{bu} is the compensatory price per unit of electricity; *load* is the excised amount of electricity.

Figure 3 shows the structure of the AP balance control method based on the proposed TLDDQN. The RE unit relies on wind and solar energy to generate electricity. The ES control center receives the power generation information of RE units, the load information, and the charge state information of ES devices. The control method of the ES control center is the AP balance control method based on the TLDDQN. The thermal power unit formulates the thermal power generation strategy based on the power generation situation of the ES device, the power generation situation of RE units, and the load power situation. Figure 4 shows the flowchart of the AP regulation of this study. When the power generated by a RE generator is greater than the load demand, ES device absorb as much of the excess power as possible. When the power generated by the RE

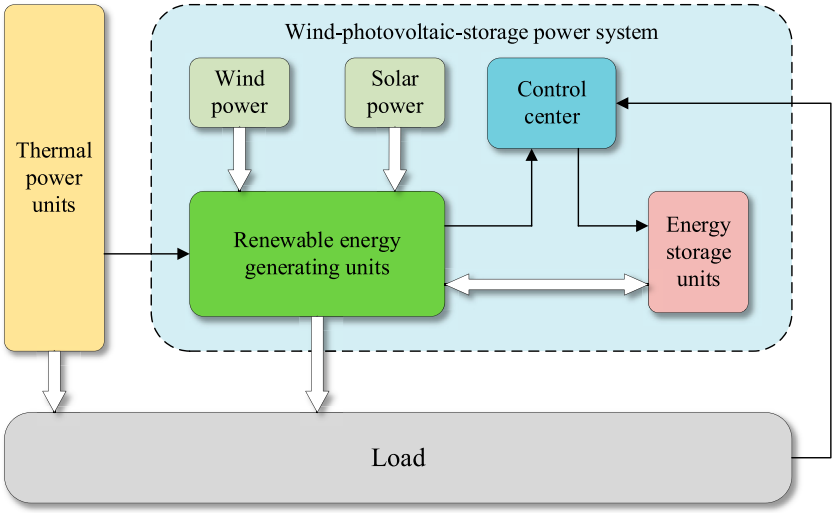

FIGURE 3
Structure of AP balance control method for WPS power system.

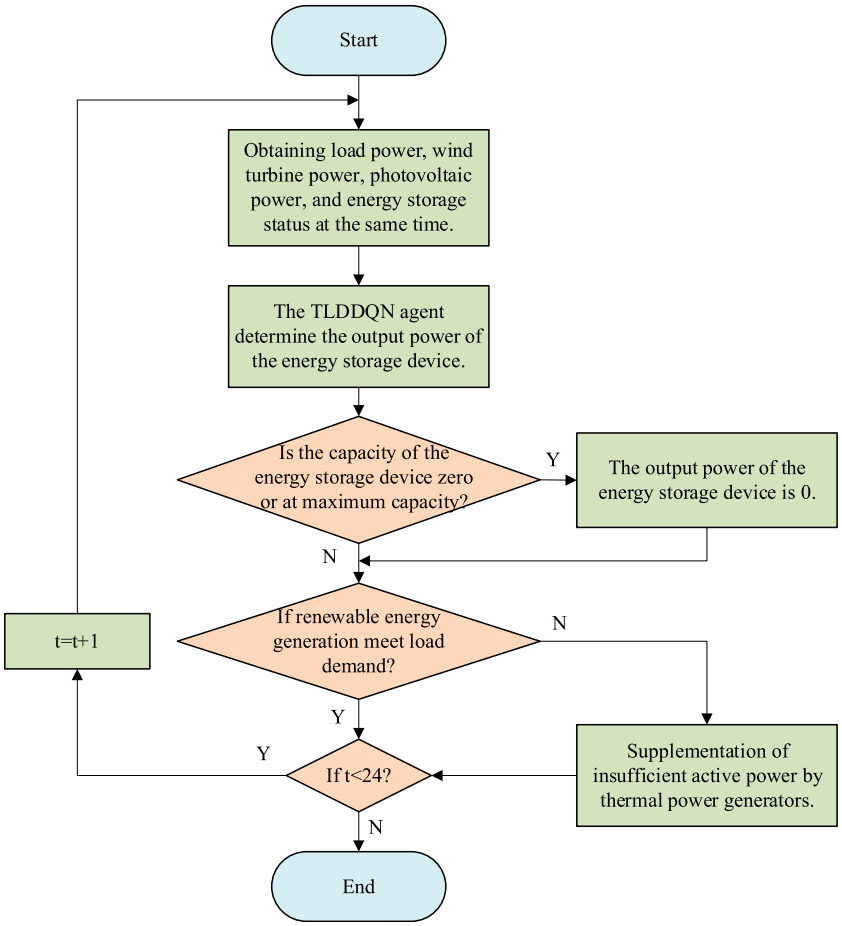

FIGURE 4
AP regulation flowchart.

TABLE 1 Parameters of algorithms.

Algorithm	Paraments	Value
particle swarm optimization	Number of individuals in the population	30
particle swarm optimization	Number of iterations	500
TLDDQN	Greed rate	0.2
TLDDQN	Learning rate	0.05
TLDDQN	Power at the initial moment of the ES device	10
TLDDQN	Maximum capacity of the ES device	20
TLDDQN	Self-discharge rate of ES devices	0.001
TLDDQN	Maintenance costs of ES devices	0.0012
TLDDQN	Maximum output of gas turbines	65

TABLE 2 Load power, wind turbine power, and PP at a site for 24 h.

Time(h)	P_{load} (kW)	P_{wt} (kW)	P_{pv} (kW)
1	62.99	32.76	0
2	57.95	37.8	0
3	55.43	34.57	0
4	51.65	39.06	0
5	50.39	33.28	0
6	62.99	15.12	0
7	81.89	17.64	2.52
8	97.01	21.42	10.08
9	117.17	25.2	16.38
10	127.24	13.12	25.2
11	123.47	7.56	28.98
12	108.35	15.34	30.24
13	99.53	6.3	28.98
14	93.23	7.43	26.46
15	97.01	17.64	21.42
16	109.61	19.42	16.38
17	118.4	31.43	11.34
18	122.21	34.02	2.52
19	129.76	22.68	0
20	136.06	18.9	0
21	125.98	20.16	0
22	105.83	18.57	0
23	89.45	30.24	0
24	66.77	39.06	0

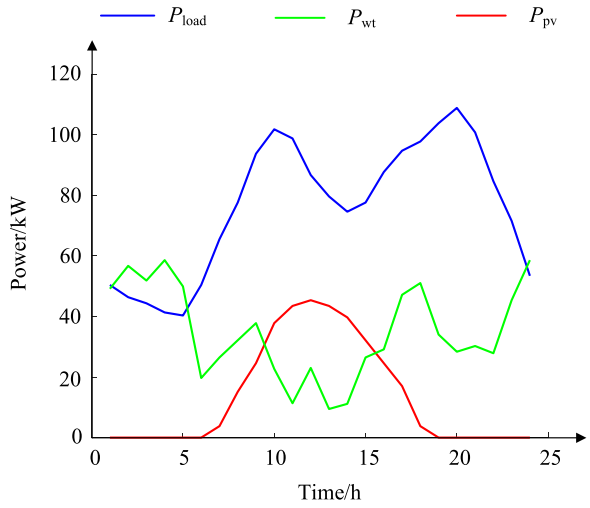

FIGURE 5
Curves of load power, turbine power, and PP at a site.

generator is less than the load demand, the ES device generates active power to reduce the power generated by the thermal generator.

4 Case studies

In this study, experiments are carried out to verify the effectiveness of the AP balance control method based on the TLDDQN proposed in this study based on load power, wind turbine power, and PP data at a site. This study compares the number of iterations required to accomplish convergence between the proposed TLDDQN and DDQN and the output of thermal power generation units by applying the proposed TLDDQN algorithm and particle swarm optimization for AP balance control of WPS power systems.

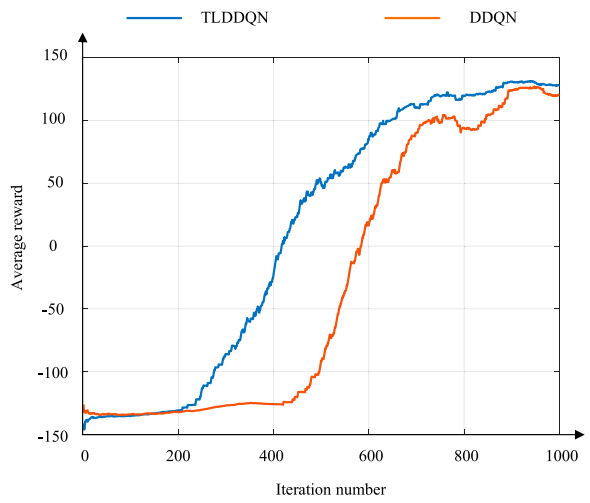

FIGURE 6
Average reward curve during training.

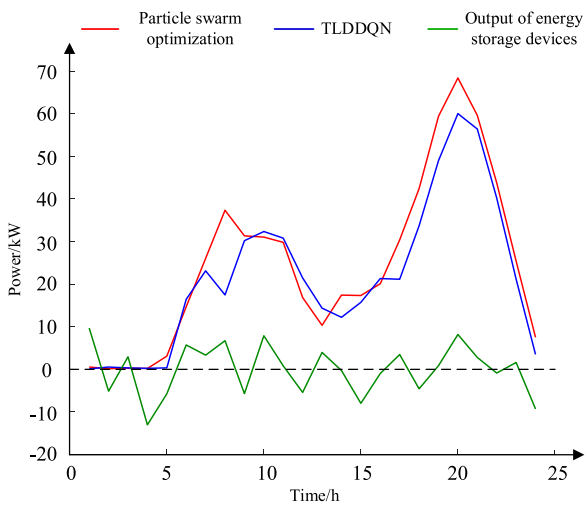

FIGURE 7
Output power of thermal power generators.

4.1 Experimental environment

The simulation software applied in this study is MATLAB R2023a. The simulations in this study were run on a personal computer with the operating system Windows 10, running memory of 16 GB, CPU model AMD R5 3600 (3.6 GHZ), and graphic processing unit model NVIDIA RTX 2070.

Table 1 shows the parameters of the algorithms involved in this study. Table 2 shows the load power, wind turbine power, and PP data updated hourly during a day at a site. Figure 5 shows the graphs of load power, turbine power, and PP obtained from the data in Table 1. Where, P_{load} is load power; P_{wt} is turbine power; P_{pv} is PP. The load power is low at night and high during the day. The wind turbine's power generation shows a large fluctuation during the day. The PP generation unit can only obtain power during the daytime resulting in a pronounced peak in the generation power curve.

4.2 Comparison of training processes

To verify the effectiveness of the TLDDQN algorithm proposed in this study in improving the convergence speed of agents. In this study, TLDDQN algorithm and DDQN algorithm are applied to train agents respectively.

Figure 6 shows the average reward curves of the TLDDQN algorithm and DDQN algorithm. Compared with the traditional DDQN algorithm, the TLDDQN algorithm proposed in this study introduces the adaptive entropy mechanism and makes improvements to the adaptive entropy mechanism. The introduction of the improved adaptive entropy mechanism can improve the exploratory ability of the agents during the training process. In addition, the TLDDQN algorithm proposed in this study introduces the TL method to improve the adaptability of agents. Therefore, compared with the traditional DDQN algorithm, the TLDDQN algorithm proposed in this study has stronger algorithmic performance. In the same environment, the number of iterations required for the TLDDQN agents proposed in this study to reach convergence is about 685. The number of iterations required for the DDQN agents to reach convergence is about 852. Compared to the traditional DDQN algorithm, the TLDDQN method reduces the training time by 19.60%.

In summary, the TLDDQN proposed in this study can converge faster than the traditional DDQN.

4.3 Comparison of adjustment effect

In this study, the AP balance control methods based on the proposed TLDDQN and the particle swarm optimization are applied to control ES devices in the experimental environment shown in Section 4.1, respectively.

The advantageous attributes of our proposed method, characterized by the TLDDQN, are encapsulated in its enhanced capability to modulate energy storage device outputs with precision, effectively addressing the intermittency of renewable energy sources and consequently leading to a substantial reduction in the operational burden on thermal power generation units. Figure 7 shows the thermal power generation power curves of the AP balance control method based on TLDDQN and the thermal power generation power curves of the particle swarm algorithm based on the particle swarm optimization. The AP balance control method based on TLDDQN reduces fossil energy consumption by 12.01% as compared to the particle swarm optimization-based AP balance control method.

In summary, the AP balance control method based on the proposed TLDDQN can solve the cooperation problem between the RE generation system and the traditional thermal generating units.

5 Conclusion

Aiming at the problem that thermal power generation units need to cooperate with RE generation units for the AP

balance control of the WPS power system when the proportion of RE generation devices is high, this study proposes the TLDDQN algorithm-based AP balance control method for the WPS power system. The proposed TLDDQN algorithm-based AP balance control method of the WPS power system can control the ES device of the WPS power system to balance the AP of the regional WPS power system. The features of the proposed AP balance control method for WPS power systems based on the TLDDQN algorithm are summarized as follows.

(1) The AP balance control method for WPS power systems based on the proposed TLDDQN algorithm can reduce the output of thermal power generators compared with the particle swarm optimization.
(2) The AP balance control method of the WPS system based on the proposed TLDDQN combines the advantages of fast learning possessed by transfer learning and the advantages of dealing with complex environments possessed by the DDQN algorithm. In addition, the improved adaptive entropy mechanism can improve the exploratory ability of agents during the training process. Therefore, the AP balance control method of the WPS system based on the proposed TLDDQN can precisely control the AP balance of the WPS system.

In future works, i) more types of RE generation units will be considered; ii) the proposed TLDDQN algorithm will be improved to increase the accuracy of power control.

Data availability statement

The original contributions presented in the study are included in the article/supplementary material, further inquiries can be directed to the corresponding author.

Author contributions

JX: Supervision, Validation, Writing–original draft. WZ: Formal Analysis, Investigation, Writing–original draft. WL: Resources, Visualization, Writing–review and editing. YZ: Validation, Writing–review and editing. YoL: Conceptualization, Software, Writing–original draft. XM: Methodology, Writing–review and editing. YuL: Formal Analysis, Writing–review and editing.

Funding

The author(s) declare that financial support was received for the research, authorship, and/or publication of this article. This research was funded by the State Grid Shanxi Electric Power Company Science and Technology Program, grant number 5205J0230001.

Conflict of interest

Authors JX, WZ, WL, YZ, YoL, XM, and YuL were employed by State Grid Shanxi Power Company Lvliang Power Supply Company.

The authors declare that this study received funding from State Grid Shanxi Electric Power Company. The funder had the following involvement in the study: study design, data collection and analysis, decision to publish, and preparation of the manuscript.

Publisher's note

References

Abdelghany, M. B., Al-Durra, A., Daming, Z., and Gao, F. (2024). Optimal multi-layer economical schedule for coordinated multiple mode operation of wind–solar microgrids with hybrid energy storage systems. *J. Power Sources* 591, 233844. doi:10.1016/j.jpowsour.2023.233844

Bawazir, R. O., Çetin, N. S., and Fadel, W. (2023). Optimum PV distributed generation based on grid and geographical area: a case study of Aden governorate, Yemen. *Energy Convers. Manag.* 297, 117703. doi:10.1016/j.enconman.2023.117703

Cheng, L., Liu, G., Huang, H., Wang, X., Chen, Y., Zhang, J., et al. (2020). Equilibrium analysis of general N-population multi-strategy games for generation-side long-term bidding: an evolutionary game perspective. *J. Clean. Prod.* 276, 124123. doi:10.1016/j.jclepro.2020.124123

Cheng, L., and Yu, T. (2019). A new generation of AI: a review and perspective on machine learning technologies applied to smart energy and electric power systems. *Int. J. Energy Res.* 43 (6), 1928–1973. doi:10.1002/er.4333

Dong, H., Fu, Y., Jia, Q., and Wen, X. (2022). Optimal dispatch of integrated energy microgrid considering hybrid structured electric-thermal energy storage. *Renew. Energy* 199, 628–639. doi:10.1016/j.renene.2022.09.027

Grover, H., Verma, A., and Bhatti, T. S. (2022). DOBC-based frequency and voltage regulation strategy for PV-diesel hybrid microgrid during islanding conditions. *Renew. Energy* 196, 883–900. doi:10.1016/j.renene.2022.06.140

Guerra, K., Haro, P., Gutiérrez, R. E., and Gómez-Barea, A. (2022). Facing the high share of variable renewable energy in the power system: Flexibility and stability requirements. *Appl. Energy* 310, 118561. doi:10.1016/j.apenergy.2022.118561

Han, Y., Liao, Y., Ma, X., Guo, X., Li, G., and Liu, X. (2023). Analysis and prediction of the penetration of renewable energy in power systems using artificial neural network. *Renew. Energy* 215, 118914. doi:10.1016/j.renene.2023.118914

Hao, X., Chen, Y., Wang, H., Wang, H., Meng, Y., and Gu, Q. (2023). A V2G-oriented reinforcement learning framework and empirical study for heterogeneous electric vehicle charging management. *Sustain. Cities Soc.* 89, 104345. doi:10.1016/j.scs.2022.104345

Hasanien, H. M., Alsaleh, I., Tostado-Véliz, M., Zhang, M., Alateeq, A., Jurado, F., et al. (2024). Hybrid particle swarm and sea horse optimization algorithm-based optimal reactive power dispatch of power systems comprising electric vehicles. *Energy* 286, 129583. doi:10.1016/j.energy.2023.129583

Jiang, B., Lei, H., Li, W., and Wang, R. (2022). A novel multi-objective evolutionary algorithm for hybrid renewable energy system design. *Swarm Evol. Comput.* 75, 101186. doi:10.1016/j.swevo.2022.101186

Jiang, W., Liu, Y., Fang, G., and Ding, Z. (2023). Research on short-term optimal scheduling of hydro-wind-solar multi-energy power system based on deep reinforcement learning. *J. Clean. Prod.* 385, 135704. doi:10.1016/j.jclepro.2022.135704

Jung, C., and Schindler, D. (2023). The properties of the global offshore wind turbine fleet. *Renew. Sustain. Energy Rev.* 186, 113667. doi:10.1016/j.rser.2023.113667

Li, K., Ye, N., Li, S., Wang, H., and Zhang, C. (2023). Distributed collaborative operation strategies in multi-agent integrated energy system considering integrated demand response based on game theory. *Energy* 273, 127137. doi:10.1016/j.energy.2023.127137

Li, S., Deng, N., Lee, X., Yan, S., and Chen, C. (2024). Optimal configuration of photovoltaic microgrid with improved ant colony dynamic programming. *J. Energy Storage* 83, 110714. doi:10.1016/j.est.2024.110714

Liu, Y., and Wang, J. (2022). Transfer learning based multi-layer extreme learning machine for probabilistic wind power forecasting. *Appl. Energy* 312, 118729. doi:10.1016/j.apenergy.2022.118729

Mehmood, A., Raja, M. A. Z., and Jalili, M. (2023). Optimization of integrated load dispatch in multi-fueled renewable rich power systems using fractal firefly algorithm. *Energy* 278, 127792. doi:10.1016/j.energy.2023.127792

Moosavian, S. F., Noorollahi, Y., and Shoaei, M. (2024). Renewable energy resources utilization planning for sustainable energy system development on a stand-alone island. *J. Clean. Prod.* 439, 140892. doi:10.1016/j.jclepro.2024.140892

Revathi, R., Senthilnathan, N., and V, K. C. (2024). Hybrid optimization approach for power scheduling with PV-battery system in smart grids. *Energy* 290, 130051. doi:10.1016/j.energy.2023.130051

Rostamnezhad, Z., Mary, N., Dessaint, L. A., and Monfet, D. (2022). Electricity consumption optimization using thermal and battery energy storage systems in buildings. *IEEE Trans. Smart Grid* 14 (1), 251–265. doi:10.1109/tsg.2022.3194815

Russo, M. A., Carvalho, D., Martins, N., and Monteiro, A. (2023). Future perspectives for wind and solar electricity production under high-resolution climate change scenarios. *J. Clean. Prod.* 404, 136997. doi:10.1016/j.jclepro.2023.136997

Song, Y., Mu, H., Li, N., Wang, H., and Kong, X. (2023). Optimal scheduling of zero-carbon integrated energy system considering long-and short-term energy storages, demand response, and uncertainty. *J. Clean. Prod.* 435, 140393. doi:10.1016/j.jclepro.2023.140393

Wang, K., Wang, H., Yang, Z., Feng, J., Li, Y., Yang, J., et al. (2023). A transfer learning method for electric vehicles charging strategy based on deep reinforcement learning. *Appl. Energy* 343, 121186. doi:10.1016/j.apenergy.2023.121186

Yakout, A. H., Hasanien, H. M., Turky, R. A., and Abu-Elanien, A. E. (2023). Improved reinforcement learning strategy of energy storage units for frequency control of hybrid power systems. *J. Energy Storage* 72, 108248. doi:10.1016/j.est.2023.108248

Ye, L., Jin, Y., Wang, K., Chen, W., Wang, F., and Dai, B. (2023). A multi-area intra-day dispatch strategy for power systems under high share of renewable energy with power support capacity assessment. *Appl. Energy* 351, 121866. doi:10.1016/j.apenergy.2023.121866

Yi, Z., Luo, Y., Westover, T., Katikaneni, S., Ponkiya, B., Sah, S., et al. (2022). Deep reinforcement learning based optimization for a tightly coupled nuclear renewable integrated energy system. *Appl. Energy* 328, 120113. doi:10.1016/j.apenergy.2022.120113

Yin, L., and Wu, Y. (2022). Mode-decomposition memory reinforcement network strategy for smart generation control in multi-area power systems containing renewable energy. *Appl. Energy* 307, 118266. doi:10.1016/j.apenergy.2021.118266

Yin, L., and Zheng, D. (2024). Decomposition prediction fractional-order PID reinforcement learning for short-term smart generation control of integrated energy systems. *Appl. Energy* 355, 122246. doi:10.1016/j.apenergy.2023.122246

Zhang, B., Hu, W., Xu, X., Li, T., Zhang, Z., and Chen, Z. (2022). Physical-model-free intelligent energy management for a grid-connected hybrid wind-microturbine-PV-EV energy system via deep reinforcement learning approach. *Renew. Energy* 200, 433–448. doi:10.1016/j.renene.2022.09.125

frontiers | Frontiers in Energy Research

TYPE Original Research
PUBLISHED 21 November 2024
DOI 10.3389/fenrg.2024.1483755

OPEN ACCESS

EDITED BY
Xingshuo Li,
Nanjing Normal University, China

REVIEWED BY
Priya Ranjan Satpathy,
Universiti Tenaga Nasional, Malaysia
Misri Gozan,
University of Indonesia, Indonesia

*CORRESPONDENCE
Salman Habib,
salman.habib@kfupm.edu.sa
Muhammad Khalid,
mkhalid@kfupm.edu.sa

RECEIVED 20 August 2024
ACCEPTED 30 October 2024
PUBLISHED 21 November 2024

CITATION
Habib S, Tamoor M, Gulzar MM, Chauhdary ST, Ahmad H, Alqahtani M and Khalid M (2024) Design, techno-economic evaluation, and experimental testing of grid connected rooftop solar photovoltaic systems for commercial buildings .
Front. Energy Res. 12:1483755.
doi: 10.3389/fenrg.2024.1483755

Design, techno-economic evaluation, and experimental testing of grid connected rooftop solar photovoltaic systems for commercial buildings

Salman Habib[1,2]*, Muhammad Tamoor[3], Muhammad Majid Gulzar[1,4], Sohaib Tahir Chauhdary[5], Hasnain Ahmad[1,6], Mohammed Alqahtani[7] and Muhammad Khalid[4,8]*

[1]Control and Instrumentation Engineering Department, King Fahd University of Petroleum & Minerals, Dhahran, Saudi Arabia, [2]Interdisciplinary Research Center for Smart Mobility and Logistics, King Fahd University of Petroleum & Minerals, Dhahran, Saudi Arabia, [3]Department of Electrical Engineering and Technology, Government College University Faisalabad, Faisalabad, Pakistan, [4]Interdisciplinary Research Center for Sustainable Energy Systems (IRC-SES), King Fahd University of Petroleum & Minerals, Dhahran, Saudi Arabia, [5]Department of Electrical and Computer Engineering, College of Engineering, Dhofar University, Salalah, Oman, [6]Department of Electrical Engineering, Pakistan Institute of Engineering and Applied Sciences (PIEAS), Islamabad, Pakistan, [7]Department of Industrial Engineering and Center for Engineering and Technology Innovations, King Khalid University, Abha, Saudi Arabia, [8]Electrical Engineering Department, King Fahd University of Petroleum & Minerals (KFUPM), Dhahran, Saudi Arabia

This study aims to investigate the potential of rooftop solar photovoltaic systems for commercial buildings. Helio-Scope software is utilized to perform simulations to determine the ideal rooftop area for photovoltaic panels. The efficiency of photovoltaic systems is impacted by the shading effects of photovoltaic modules installed in parallel rows. To enhance energy output, the optimal distance between rows is determined, and it is found that 5-feet inter-row spacing provides the best results. The simulation results indicate that with 5-feet inter-row spacing, photovoltaic system has an energy generation of 371.6 MWh, specific yield of 1508.0 kWh/kWp, performance ratio of 82.1%, solar access rate of 98.9%, total solar resource fraction of 96.3% and a total irradiance of 1655.9 kWh/m^2. The annual nameplate energy is 425.1 MWh, output energy at irradiance levels is 423.1 MWh, optimal DC output is 378.5 MWh, inverter output is 373.5 MWh, and total energy delivered to the national power grid is 371.6 MWh. The average daily DC inverter input power is 158881.5110 W and the average daily AC inverter output power is 152231.6311 W, showing an inverter efficiency of approximately 95.93%. Moreover, detailed testing of the installed PV system is performed on-site to make sure that equipment's performance guarantees are achieved, the system is properly installed and its configuration is suitable for commercial operations. The maximum daily output energy generation of an installed photovoltaic (PV) system is 1.33 MWh, and its average energy generation is 1.09 MWh. The voltage of all strings is within the rated range of the inverter, with a maximum voltage of 835 V and a minimum of 698 V, as tested by PV string open-circuit voltage. The inverter efficiency test is also performed, with a maximum efficiency of 98.83% and fill factors ranging from 81.37% to 82.34%. The payback period of a photovoltaic system is

4.22 years and LCOE is 0.0229$/kWh. PV system saved 215569.818 metric tons of CO_2 in the first year and a total of approximately 5068976.99 metric tons in 25 years.

KEYWORDS

PV system, solar resources, performance analysis, system losses, energy generation, performance ratio, system testing, building solar potential

1 Introduction

With the advancement of industrialization and urbanization, the world's energy consumption continues to increase. Every day more people are migrating to cities, where they live in a society confined to buildings. As a result, the daily energy consumed by buildings grows exponentially and increases the emissions of greenhouse gases (GHG) (Musa et al., 2024). Buildings are among the priorities for climate change mitigation strategies since they account for one-third of the world's final energy consumption and one-fifth of its greenhouse gas (GHG) emissions (Lang et al., 2016). Approximately 74% of the worldwide energy needs are met by fossil fuels (International Energy Agency, 2020). As the main source of energy generation, fossil fuels especially natural gas, coal, and diesel pose significant problems to global warming and GHG. There is an increase in the development and integration of sustainable energy sources to fulfill energy demands in order to lessen these issues (Habib et al., 2023a; Ehsan et al., 2024; Bashir et al., 2024; Habib et al., 2023b).

Photovoltaic (PV) offers a promising technology to achieve this goal because of its significant and prominent environmental benefits as that of a low-carbon energy source and its substantial potential for economic development (Liu et al., 2022; Tamoor et al., 2022a; Nguyen et al., 2024; Bhatti et al., 2024; Wen et al., 2022). After a significant reduction in photovoltaic manufacturing costs due to large-scale deployment, photovoltaics has become economically competitive with alternative energy sources around the world (Zander et al., 2019; Tamoor et al., 2022b; Sinha and Ghosh, 2024; Tamoor et al., 2022c; Tamoor et al., 2020). The main factors behind the constant growth of this technology are its significant cost reduction and the environmental problems associated with fossil fuels. The global cumulative photovoltaic installed capacity has increased exponentially from nearly 0 GW in 1990 to 505.0 GW in 2018 (Appavou et al., 2019). Additionally, 102.4 GW of new PV systems were installed globally in 2018 (Muteri et al., 2020). In contrast to concentrated solar power (CSP) systems, photovoltaic technology can generate energy also in regions with moderate levels of solar irradiance. As a result, this technology has the potential to be utilized (i.e., at the commercial or residential level), and the idea of the solar city has captured the interest of many engineers and researchers (Bouramdane et al., 2021; Tamoor et al., 2021a; Huda et al., 2024; Alshehri et al., 2024; Miran et al., 2022; Tamoor et al., 2021b).

The energy consumption of buildings is increasing rapidly every day in both hot and cold regions (Huang and Zheng, 2018; Kang et al., 2021; Habib et al., 2023c). Office buildings contribute considerably more to this high consumption of energy, consuming 17% of all energy globally (EIA, 2016; EIA, 2006). Energy consumption in Asian countries is extremely high during the summer solstice (Ramli et al., 2017; Liu et al., 2021). The high load during the summer is a result or consequence of the energy required for cooling in both commercial and residential buildings. In the upcoming years, global warming will increase the load even more (Prieto et al., 2018; Van Ruijven et al., 2019). In Asian countries, buildings account for 80.0% of the total energy consumed (Asif, 2016; Shaahid and Elhadidy, 2008), but in European countries, this share is only 40.0% (Machete et al., 2018). In particular for office buildings, photovoltaic installations can be a suitable option to meet the high summer energy demands as the energy generation pattern of photovoltaic systems matches the load pattern of office buildings because primary loads of buildings are high during office time i.e., daytime.

Rooftop PV is an excellent option to integrate renewable energy into the national grid without changing the use of land or adding more distribution or transmission lines (Wiginton et al., 2010; Palmer-Wilson et al., 2019). Rooftops of urban buildings offer potential and suitable sites for photovoltaic (PV) installations. However, an effective approach to harvesting rooftop solar potential by identifying suitable and appropriate roofs to optimize photovoltaic (PV) installations still seems to be challenging (Mohajeri et al., 2018; Mountain and Szuster, 2015). Research on optimizing photovoltaic (PV) installations has started to progress mainly in developed countries in Europe and America, however, there is a shortage of maps showing the potential of solar energy generation for future solar urban planning (Huang et al., 2019). The size of the research area is one of the most crucial factors in assessing the potential of rooftop photovoltaic systems (Schallenberg-Rodríguez, 2013). Applying the same methodologies on a local, regional, or continental scale is often not possible because of the time-consuming procedures, the substantial cost of obtaining the information from various sources, and the lack of diversity in some sections of the data.

Studies investigating PV self-consumption have primarily examined case-specific building types, such as single-family homes (Lang et al., 2015; Chwieduk and Chwieduk, 2021), large-size office buildings (Prajapati and Fernandez, 2019), university campuses (Ali and Alomar, 2022; Tarigan, 2018), or multiple buildings (Ahsan et al., 2020). The utility-scale rooftop photovoltaic system installed in Switzerland was analyzed by Assurin et al. (Assouline et al., 2018) using random forests to determine its generation capability. They proposed a method for calculating roof areas that are available for installing photovoltaic modules and assessed the shading losses brought on by surrounding buildings and trees, without accounting for the losses brought on by mutual shade of the tilted photovoltaic modules. Fina et al. (2020) developed a method to evaluate the economic viability of roof-top photovoltaic systems depending on neighboring energy communities and expanded roof-top photovoltaic potential to analyze the renewable

energy-related policy goals of Austria. Shukla et al. (2016) designed and installed a stand-alone 110-kW photovoltaic system on the flat roof of an Indian hostel. The authors thoroughly examined the technical as well as financial aspects of the proposed photovoltaic system; however, the shading losses were not taken into account. The technical performance of a 5-kW roof-top photovoltaic system was assessed by Yadav and Bajpai (2018). They examined the array efficiency, CUF, average daily energy output, and energy yield of PV systems, but they did not analyze the shading losses. A 200-kW roof-mounted photovoltaic system was studied by Kumar et al. (2019) by using PVSyst simulation software to calculate approximate output energy generation and energy loss and analyze the performance ratio, efficiency of the system, and CUF.

Satpathy et al. (2021a) designed a 19.2 kW grid-connected PV system using PVsyst software, taking into account the site's meteorological data, available components, and numerous loss characteristics for residential buildings. The 3D modeling of the roof is performed in the Sketchup Skelion environment to ensure optimal module placement and prevent unexpected shading during operational hours. The analysis indicates that the estimated system size suggested by both software tools matches closely, with the maximum output of the proposed system estimated at 25 MWh/year. Additionally, the system and maximum array losses are determined to be 0.44 and 0.93 kWh/kWp/day, respectively. Another research examines a comprehensive examination of a 100 kW grid-connected photovoltaic system, including its location, system design, module orientation, selection of components, loss analysis, and energy yield. This research has been utilizing the most efficient PVsyst software for determining acceptable parameters for the optimum planning and designing of a 100 kWp PV system (Satpathy et al., 2021b). In order to determine the prospective benefits of rooftop PV systems, several researchers (Singh, 2020; Mohamed et al., 2024; Tamoor et al., 2023; Al-Amin et al., 2024; Monna et al., 2020; Vargas-Salgado et al., 2024; Yang et al., 2024; Thotakura et al., 2020; Abd Elsadek et al., 2024) utilized simulation software like PVSyst, HelioScope, Homer Pro, Solmetric SunEye, PVGIS, and PV*Sol.

The RETScreen software has been employed to conduct techno-economic, and environmental analyses for a 10.0 MW utility-scale grid-connected PV system across seven cities in Benin. According to the assumptions described in this research, the photovoltaic system generates approximately 13,222 MWh per year of electricity that can be exported to the grid. This results in a PR of approximately 67.3% and a capacity factor of 15.1%. The project produces an LCOE that ranges from 0.110 USD/kWh to 0.125 USD/kWh. In comparison to the utility grid, the utility-scale PV system reduces CO2 emissions by approximately 76.0% (Akpahou et al., 2024). Boruah and Chandel (2024) conducted a technical and economic feasibility study on five commercial grid-connected PV systems with battery energy storage under both net-metering and without net-metering regimes. The Solar Labs and PVSyst software have been used for system design and energy generation calculation, proceeded by HOMER grid software and Excel-based financial simulations for optimization of systems and cost-benefit analysis. The analysis indicated a 200 kWp PV system integrated with a 250 kWh energy storage under net metering as the most optimized solution, with an energy generation cost of 4.21 INR/kWh and a payback period of 6.15 years.

Another research intended to assess the technical, economic, and environmental performances of grid-connected and stand-alone hybrid systems across 21 provinces in seven regions of Turkey, taking into account variations in regional solar irradiations and wind speed. Hybrid systems have been designed and simulated utilizing the HOMER PRO to supply the daily energy demand of 13.2 kWh/day for a home. The results indicated that the most suitable configurations are PV/WT/Grid for a grid-connected hybrid system and PV/WT/DG/BESS for a stand-alone hybrid system. The NPC value ranges from $2,540 to $8,951 for grid-connected and from $23,372 to $40,858 for stand-alone systems (Ayan and Turkay, 2023). This research presents a techno-economic evaluation of grid-connected PV systems in arid regions, focusing on the aspect of peak shaving. The impact of a commissioned 102 kW PV system on peak shaving for the waste-management organization building is evaluated as a practical case. The findings confirm that the installed PV system reduces the peak demand of commercial buildings by an average of 40%–50% during summer afternoons. The results indicated that the proposed project is economically feasible, demonstrating an NPV of €43,671 and an IRR of 34.5% (Mousavi and Bakhshi-Jafarabadi, 2024).

The objective of this research is to examine the potential and assess the optimum methods for installing a grid-connected photovoltaic system on the roof of commercial buildings. This research study comprehensively investigates the constraints/challenges on commercial building rooftops in order to evaluate the utilization of rooftop areas for photovoltaic energy systems. The current research work consequently fills a gap in the scientific literature as it aims to determine the potential of photovoltaic installation on commercial buildings. Commercial buildings vary widely in terms of their sizes and purposes. The shopping plaza is the primary building type covered in this study. The range and intensity of various architectural, structural, and service characteristics that limit the usage of photovoltaics on building rooftops are examined using satellite images. Site visits were also conducted to review and understand the condition of the roof in detail and to verify the results of the assessment procedure based on satellite images. Software such as HelioScope, Aurora Solar, and some standard data are used in the design. For this system, PV modules are mounted on a fixed-mount racking system. The grid-connected photovoltaic system is designed with the HelioScope software. The 3D model is designed and shadow loss is analyzed using Aurora Solar. Building a 3D model with appropriate photovoltaic module configurations, such as azimuth angle, tilt angle and inter-row spacing is challenging when using HelioScope software. In order to optimize solar irradiation, the PV modules are installed at 180° azimuth angle and a 15° tilt angle. To maximize the output energy production of the PV system, we examined different Inter-row spacing.

Although ground-mounted photovoltaic systems are easier to operate and require less maintenance, it is difficult to install PV systems in metropolitan areas due to the cost and availability of land. In contrast, rooftop photovoltaic systems involve no land costs and block solar irradiance from making direct contact with the roof's exterior surface. High temperatures in extremely hot regions, cause building roofs to heat up due to direct sunlight hitting the roof surfaces. In these hot climate regions, solar (PV) modules mounted on building roofs would reduce building cooling

energy requirements due to their ability to shade the roof. Utilizing a grid-connected photovoltaic system reduces the electricity bill because it minimizes the need for a 100% electricity supply from the national grid. The shopping plazas will profit from reduced energy bills, the ability to meet load demand, and be friendly to the environment if the rooftop space of the commercial shopping plazas is utilized efficiently. As a result, it would be highly beneficial to assess the performance of roof-top photovoltaic systems installed on commercial shopping plazas. In summary, the contributions of this research work are as follows.

- Detailed solar resources including solar irradiance (kWh/m^2), wind speed (m/s), ambient temperature (°C), and hourly PV module temperature (°C) for each month have been analyzed.
- A comprehensive analysis has been conducted to study the impact of solar resources on the efficiency and performance of a photovoltaic energy generation system.
- The majority of current research studies assess rooftop photovoltaic systems in a similar way as ground-mounted photovoltaic systems without taking into consideration the mutual shading between parallel arrays of rooftop PV systems. To optimize the inter-row spacing of parallel PV arrays, this research considers and analyzes both rooftop shading and mutual shading between parallel PV arrays.
- Monthly and annual generation (kWh), as well as hourly input power (DC) and output power (AC) at inverters terminal, were used to analyze the performance of the grid-connected photovoltaic system on a commercial shopping plaza over the period of a year.
- Comprehensive assessment of a photovoltaic system's losses, including those caused by irradiance, shading, soiling, reflection, mismatch, temperature, clipping and wiring, etc.
- Detailed testing of the installed PV system is performed including photovoltaic string open-circuit voltage test, photovoltaic string short-circuit current test and other parameters, inverter efficiency tests, and earth resistance and insulation test of DC and power cables.
- Annual energy depreciation of installed photovoltaic system for 25 years as well as actual generation of PV system at 100% load and performance ratio were performed at the site to make sure that the equipment's performance guarantees are met, properly installed, and suitable for commercial operations.
- Finally, indicators related to environmental impact (quantitative information for reducing CO_2 emissions), levelized cost of energy, and payback period were evaluated.

2 Methodology

From a methodological point of view, this research uses an empirical and deductive research design to improve the energy generation performance and efficiency of rooftop photovoltaic systems. From an operational and economic perspective, the ultimate objective of this research is to investigate how different design factors affect a rooftop photovoltaic system's ability to generate energy. These factors such as tilt and azimuth angles, GHI, ambient temperature, and shading from the surrounding obstacles as shown in Table 1.

TABLE 1 Factors influencing PV system performance.

Categories	Factors
Geographical features	Altitude
	Latitude
Weather data	Global horizontal irradiance (GHI) (kWh/m^2)
	Ambient temperature (°C)
PV system componets and installtion	PV module specification
	Inverter specification
	Photovoltaic module size (ft^2)
	The tilt angle of the photovoltaic module
	Azimuth of PV module
Site conditions	Roof type and area
	Surrounding obstacles and shading

2.1 Performance indices

Several indicators were established in accordance with international standards (IEC--61724) used to examine the performance of roof-mounted grid connected PV systems. In this study, the performance indices taken into consideration are the target, actual and specific yields, performance ratio, system efficiency, and losses in the system.

2.1.1 Target AC yield

Equation 1 is used to compute the target AC yield (Alshehri et al., 2024; Malaysia, 2016).

$$Y_{Tar}[kWh] = P(array)_{STC} \times \eta_{sub\_system} \times P_{SH} \times k_{deration} \quad (1)$$

where Y_{Tar} is target AC-yield, $P(array)_{STC}$ is photovoltaic array power at standard test conditions (STC), $\eta_{sub_{system}}$ is efficiency of the sub-system such as PV modules, inverters, etc., P_{SH} is the peak sun-shine hours, $k_{deration}$ is the deration factor of the energy yield and calculated by using Equation 2.

$$k_{deration} = k_{mismatch} \times k_{age} \times k_{soil} \times k_{Temp} \quad (2)$$

where $k_{mismatch}$ is a derating factor caused by the power mismatch between photovoltaic modules, k_{age} is a power derating factor caused by the photovoltaic module aging, and k_{soil} is a derating factor caused by soil or dirt accumulated on photovoltaic modules. k_{temp} is a derating factor of power caused by the cell temperature and calculated by using Equation 3.

$$k_{Temp} = 1 + [\left(\frac{\gamma_{power}}{100\%}\right)\left(T_{avg\_cell} - T_{STC}\right) \quad (3)$$

where T_{STC} is photovoltaic module temperature (°C) under standard test conditions (STC), T_{avg_cell} is average cell temp (°C) under normal

operating condition (NOCT), and γ_{power} is temp coefficient of the power in %/°C (which was obtained from the photovoltaic modules data sheet).

Commonly, target yields are calculated before the installation of grid-connected photovoltaic systems. The target yields are calculated by adding values of P $(array)_{STC}$, η_{sub_system}, $P_{SH,}$ and $k_{deration}$ into Equation 1 and multiplying by the month's total number of days (for example, 31 days in March). It can be observed that while P_{SH} fluctuates each month due to the fluctuating amounts of solar irradiation, values of P $(array)_{STC}$, $\eta_{sub\_system,}$ and $k_{deration}$ are nearly constant. The peak sunshine hours are calculated by using Equation 4 (Alshehri et al., 2024; Malaysia, 2016).

$$P_{SH} = H_{SI}/G_{SI} \tag{4}$$

where H_{SI} is the solar irradiations (kWh/m^2), whereas G_{SI} is solar irradiations under standard test conditions, i.e., 1000 Wh/m^2 (1 kWh/m^2).

2.1.2 Specific yield

Yield is the term used to define how much energy a grid-connected photovoltaic system produces. It is one of the most significant performance indicators for an on-grid PV system because it has direct impact on performance ratio (PR). Equation 5 is used to calculate the measured AC yield produced by a photovoltaic system (Alshehri et al., 2024; Malaysia, 2016).

$$Y_{AC(measured)} = \sum_{t=1}^{N} E_{AC(t)}\,[kWh] \tag{5}$$

where E_{AC} is measured AC output energy in kWh at time "t" (month, day, or hour), and N is the number of observations. Equation 6 is used to calculate the measured DC yield (Alshehri et al., 2024; Malaysia, 2016).

$$Y_{DC(measured)} = \sum_{t=1}^{N} E_{DC(t)}\,[kWh] \tag{6}$$

where E_{DC} is the measured DC output energy in kWh at time "t" (month, day or hour), and N is the number of observations. The quantity of energy produced (AC) by system per-unit capacity is described as the specific yield and calculated by using Equation 7 (Alshehri et al., 2024; Malaysia, 2016).

$$\text{Specific Yield} = \frac{Y_{AC}}{P(array)_{STC}}\,\frac{[kWh]}{[kWp]} \tag{7}$$

2.1.3 Performance ratio

Performance ratio defines an important quality factor that assesses the performance of a photovoltaic system and indicates how close, in practical operations, its performance resembles the ideal performance, regardless of site location, PV module orientation, azimuth angle, tilt angle, and module nominal-rated power capacity. It provides a normalized indicator of the system and contains all design and installation characteristics. The target and measured PR are calculated by using Equation 8 and Equation 9 (Alshehri et al., 2024; Malaysia, 2016).

$$PR_{Tar} = \frac{Y_{Tar}}{P(array)_{STC} \times P_{SH}}\,[\%] \tag{8}$$

$$PR_{measured} = \frac{Y_{measured}}{P(array)_{STC} \times P_{SH}}\,[\%] \tag{9}$$

2.1.4 System efficiencies

The efficiency of the photovoltaic system is divided into three categories: inverter efficiency, photovoltaic array efficiency as well as system efficiency. These efficiencies could be calculated on an annual, monthly, daily, or hourly basis, depending on the available data as well as the desired scale of information. The system efficiency depends on the AC output energy, while the array efficiency depends on the output DC energy. Array efficiency is a measure of the average energy conversion efficiency of photovoltaic arrays and this is the ratio of the daily DC output energy of the array to the product of the daily total solar irradiation in the collector plane and the total surface area of a photovoltaic array. Equation 10 is used for calculating the inverter efficiency (Wittkopf et al., 2012; de Lima et al., 2017).

$$\eta_{INV} = \frac{100 \times E_{AC}}{E_{DC}}\,[\%] \tag{10}$$

The photovoltaic array efficiency and system efficiency of a grid-connected photovoltaic system are calculated by using Equations 11 and 12 (Wittkopf et al., 2012; de Lima et al., 2017). The performance of a complete installed solar (PV) system is represented by overall system efficiency.

$$\eta_{PV\_array} = \frac{100 \times E_{DC}}{H_{col.\,plane} \times A_m}\,[\%] \tag{11}$$

$$\eta_{system} = \frac{100 \times E_{AC}}{H_{col.\,plane} \times A_m}\,[\%] \tag{12}$$

Where E_{AC} is measured AC output energy, E_{DC} is the measured DC output energy, $H_{col.\,plane}$ is total solar irradiation in collector plane (kilowatt-hour/meter^2), and A_m is PV module area (m^2).

2.1.5 Losses analysis

The grid-connected photovoltaic system experiences energy losses in various forms, however, system and array capture losses are those that are most significant. The system losses are caused by the conversions of DC energy into AC energy through PV inverter and calculated by using Equation 13 (Alshehri et al., 2024; Malaysia, 2016; Kymakis et al., 2009):

$$L_{system} = \frac{E_{DC}}{P(array)_{STC}} - \frac{E_{AC}}{P(array)_{STC}} \tag{13}$$

The PV array capture losses are losses associated with array operation that show how PV array is unable to completely utilize the available irradiation. PV array capture losses are calculated by using Equation 14.

$$L_{capture} = P_{SH} - \frac{E_{DC}}{P(array)_{STC}} \tag{14}$$

2.2 Rooftop photovoltaic system description

Photovoltaic modules are installed in parallel rows by connecting them in series to form strings. For impartial and

TABLE 2 Basic information about PV plant.

PV modules	Manufacturer	Longi
	Technology	Mono PERC Half cell
	Power rating	435 Wp
	Product model number	LR4-72HPH 435M
	Total numbers of modules	567
Grid Tie Inverter	Manufacturer	Huawei
	Technology	Transformer less String Inverter
	Power Rating	60 kW
	Product Model Number	SUN 2000-60KTL-M0
	Maximum efficiency	98.7% @380 V/400 V
	Total Numbers of Inverter	04
Outgoing LT Cabinet	Technology	VCB
	Rating	630A
	Total Numbers of Cabinet	01

unbiased research of rooftop photovoltaic systems, the system is designed with high-efficiency photovoltaic modules (Tier 1). To do this, the capacity of the roof photovoltaic system is first calculated for available roof surface area and specific inter-row distance. If the photovoltaic module is facing the sun, a module can get more solar irradiation, which can increase its efficiency. Sun changes its trajectory around the horizon. Trajectories are higher in the summer season and lower in the winter season. The sun's route around the horizon shifts. The path is steep in the summer and low in the winter. To accommodate these seasonal changes in the sun's trajectory, optimal tilt angles of PV arrays are used, at which the photovoltaic system generates maximum energy for each month. In this research, the Longi Solar Mono PERC Half Cell (LR4-72HPH 435 M) photovoltaic module, Huawei (SUN 2000-60KTL-M0), and Outgoing LT Cabinet with 630A rating are used, and Table 2 shows the basic information of PV Plant.

2.3 Testing of installed PV power system

Detailed testing has been performed at the site before commissioning to make sure that the equipment's performance guarantees are met, properly installed, correctly adjusted, and suitable for commercial operations. Different testing of installed PV power systems includes.

1. Photovoltaic string open-circuit voltage test
2. Photovoltaic string short-circuit current test and other parameters
3. Inverter efficiency tests
4. Earth resistance and insulation test of DC and power cables
5. Performance ratio

2.4 Installation site

The building of a commercial shopping plaza is taken as the case study for installation of rooftop on-grid photovoltaic system. There is no specific data on the roof type and roof area of the commercial building; therefore, just one commercial building was chosen. The commercial building is located at 31.4635762 and 73.0816969 in Faisalabad, Pakistan. The satellite view and physical layout of the commercial shopping plaza are shown in Figure 1.

The commercial shopping plaza has a flat roof and two buildings. The total construction area of a commercial shopping plaza is 52,641 square feet, and the total area available for the installation of a photovoltaic system is 37,074 square feet.

- Building 1 (Field Segment 1): The first field segment of the commercial shopping plaza has 27,153.5 square feet of roof area for solar (PV) system installation and a flat roof. The photovoltaic (PV) modules are installed on the flat roof at a fixed tilt angle.
- Building 2 (Field Segment 2): The second field segment of the commercial shopping plaza has 9,920.8 square feet of roof area for solar (PV) system installation and a flat roof. The photovoltaic (PV) modules are installed on the flat roof at a fixed tilt angle.

A survey of the site was conducted and found that there were no noticeable obstructions (like high-rise surrounding buildings and trees) that create shadows on the installed PV modules. The helioScope model was developed taking into consideration the architectural design of a building, specification of the photovoltaic system (module, inverter, etc.), and shading factors. Physical features are modeled in the system, including system size, PV module type (Si-Mono, Si-Poly), tilt angle, azimuth angles, and frame size. The global map can be used to determine the partition and boundaries of the building. The detailed parameters of the photovoltaic system (such as module type and rating, azimuth and tilt angles, module orientation, structure frame size, and spacing, etc.) are imported into the parameter setting bar. Weather data sets are based on local meteorological conditions at a given location.

2.5 Calculation of appropriate roof area

The primary components of photovoltaic power generation systems, which directly transform solar energy into electric energy are photovoltaic modules. Moreover, since sun's energy is irregular/sporadic and fluctuates with time, it is crucial to evaluate how much solar irradiance is effectively converted into electrical energy. Simulation Software makes these evaluations using measurements of surface irradiance or satellite data. Helioscope (Şevik, 2022; Tamoor et al., 2022d; Yar et al., 2022) provides benefits

FIGURE 1
Satellite view and physical layout of a commercial shopping plaza.

like adaptability, sensitivity to the technical aspects of selected PV modules, changeability or modifiability of the orientation and alignment of the photovoltaic modules, and selections of PV inverters and AC/DC wirings. Helioscope simulation software is used for rooftop photovoltaic systems in every field segment. The following Equations 15 –17 are used for each field segment.

$$A_S = N_m \times A_m \tag{15}$$

$$C_S = A_s/A \times 100 \tag{16}$$

$$E_{avg/m} = E \div N_m \tag{17}$$

Where.

- A_s: Suitable area (m^2)
- A_m: Photovoltaic module area (m^2)
- A: Roof area of the building (m^2)
- N_m: Number of photovoltaic modules settled by Helioscope software
- C_S: Suitable area constant (%)
- E: Annual energy generation (MWh/year) of PV system computed by Helioscope
- $E_{avg/m}$: Average annual energy generation per PV panel ((MWh/year)/panel)

2.6 Economic analysis

The financial feasibility of an on-grid roof-mounted photovoltaic system is evaluated by considering indicators such as the payback period and levelized cost of electricity (LCOE). The LCOE is a measurement of the average net present cost of PV energy generation during its lifetime, taking into account the CAPEX of the PV power plants as well as operation and maintenance expenses (OPEX). The payback period and the LCOE are calculated using Equation 18 and Equation 19 (Habib et al., 2023d).

$$\text{Payback period} = \frac{\text{Photovoltaic system's cost (CAPEX)}}{\text{Total annual revenue of PV system}} \tag{18}$$

$$\text{LCOE} = \frac{\text{CAPEX} + \text{OPEX (for 25 years)}}{\text{Energy generations in 25 years}} \frac{(\$)}{(\text{kWh})} \tag{19}$$

2.7 Environmental analysis

An environmental analysis of grid-connected photovoltaic systems was conducted using the quantity of carbon dioxide (CO_2) that can be decreased by the installation of photovoltaic system on the roof of a commercial shopping plaza. The average carbon dioxide factor is 0.58 tCO_2/MWh. Annual CO_2 emission saved in tons is computed by using Equation 20 (Alshehri et al., 2024).

$$(CO_2)_{annual} = 0.58 \times E_{AC} \tag{20}$$

3 Results

3.1 Solar resources

Solar resource data is collected from the Meteonorm (Tamoor et al., 2022e) database. Pakistan has an extremely hot environment; thus, substantial air conditioning is needed in summer. This leads to a very high electric load during this time of year. Peak loads in Pakistan occur in the daytime during the summer solstice due to the substantial cooling loads. As a result, in order to meet high energy demands during the hot summer season, photovoltaic installations could be extremely beneficial. The amount of energy a photovoltaic system produces is directly related to solar irradiance from the sun. The amount of energy produced by photovoltaic modules increases as more solar irradiance is

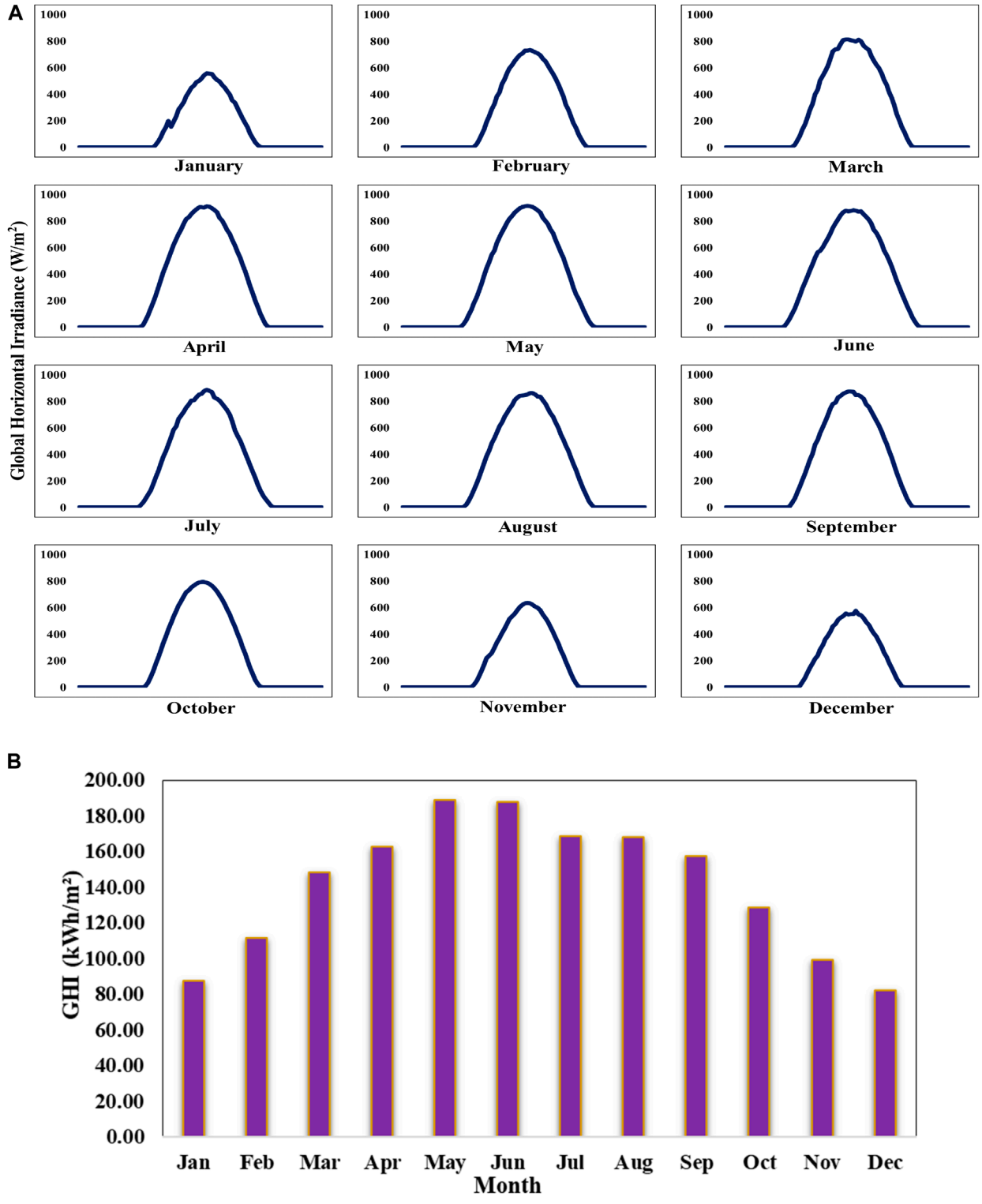

FIGURE 2
(A) Hourly data for global horizontal irradiance for each month **(B)**. Monthly global horizontal irradiance (GHI) at the proposed site.

absorbed by photovoltaic modules (Tamoor et al., 2022e). Solar irradiance, wind speed, ambient temperature, and hourly module temperature have a significant influence on photovoltaic energy generation system's performance. The PV module current has an almost linear relationship with solar irradiance, resulting in an increase in module current with the increase in solar irradiance. The hourly data for global horizontal irradiance (GHI) of the selected site for this research is shown in Figure 2A. According to the Figure, the

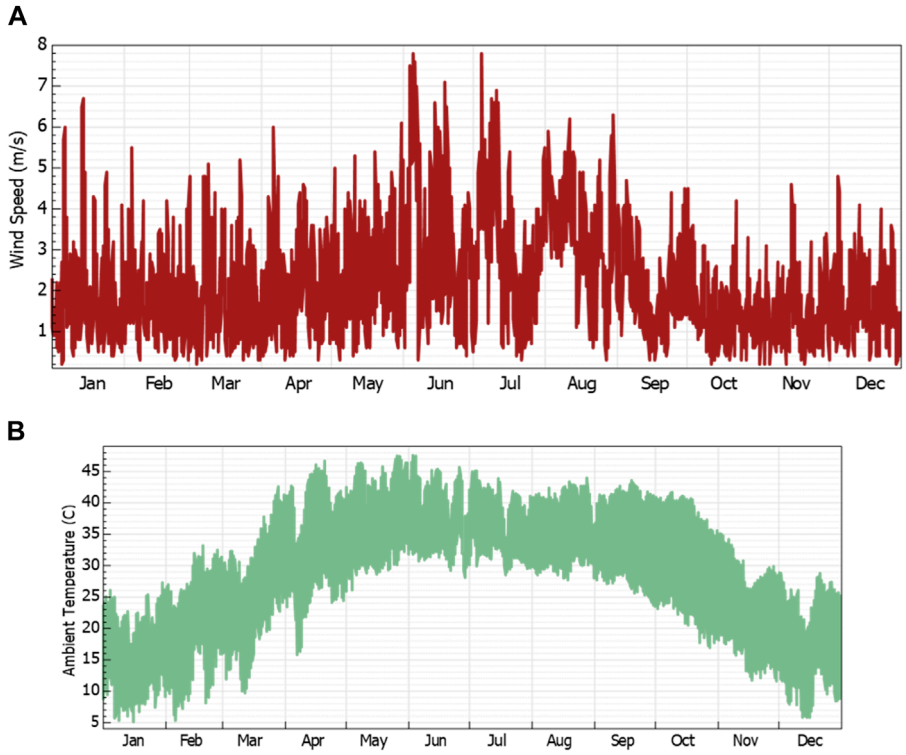

FIGURE 3
(A) Wind speed at the proposed site. **(B)** Ambient temperature at the proposed site.

summer months (April, May, June, July, August, and September) experience the highest levels of global horizontal irradiances. Furthermore, the maximum hourly value of the GHI is 915 W/m^2 in May. From 8:00 a.m. until 12:30 p.m., the solar irradiance started to increase. Thereafter, it started to fall until the end of the day.

Figure 2B indicates the monthly global horizontal irradiation for the selected site. The GHI is measured in May at its highest level (188.8 kWh/m^2) and in December at its lowest level (82.3 kWh/m^2).

Local weather conditions are the main factor affecting wind speed. Particular unusual meteorological conditions such as monsoon season, cyclones, and hurricanes can have an enormous impact on wind speed formation. The wind speed is unstable and variable as can be observed in Figure 3A. The wind speed fluctuates between 0.3 m/s at the lowest point to 7.8 m/s at the highest point. The daily average maximum wind speed is 3.406 m/s, while the average annual wind speed is 2.133 m/s. Since the photovoltaic power generation system does not fully utilize solar irradiance, the remaining is converted to heat, which leads to the overheating of the photovoltaic modules. One of the primary external factors that adversely impact a photovoltaic system's capability to produce power is ambient temperature. Ambient temperatures range from 5.1°C to 47.6°C, while average annual ambient temperature is 28.49°C as shown in Figure 3B. As was to be predicted, the increases in the ambient temperature are followed by increases in the levels of solar irradiance.

The operating temperature of solar cells is reduced by wind flow over photovoltaic modules. The cooling impact of wind on photovoltaic modules makes higher wind speeds beneficial for photovoltaic module operation. The photovoltaic module's surface temperature increases as the ambient temperature rises. Therefore, the PV module's cell temperature will also rise, as a result the operating voltage of the solar cell and output power of the PV system both decrease (Habib et al., 2023e). The maximum hourly operating temperature (°C) of a photovoltaic module is 67.83°C in April, while the minimum hourly operating temperature is 1.22°C in January as shown in Figure 4. Additionally, the average daily maximum operating temperature of a photovoltaic module is 59.70°C, the average daily minimum operating temperature of a solar (PV) module is 4.47°C and the average annual operating temperature of a solar (PV) module is 34.85°C. The daily and annual average module temperature is an average that takes into account both daytime and overnight temperatures. The ambient temperature was consistently lower than PV module temperature, which could be a result of thermal losses that occur during power production.

3.2 Optimization of PV systems and inter-row spacing

In order to identify the optimum inter-row spacing for photovoltaic modules and the potential output energy at the proposed site, a series of experiments have been performed. To maximize output energy production of the PV system, we examined different Inter-row spacing. The simulation experiment is divided

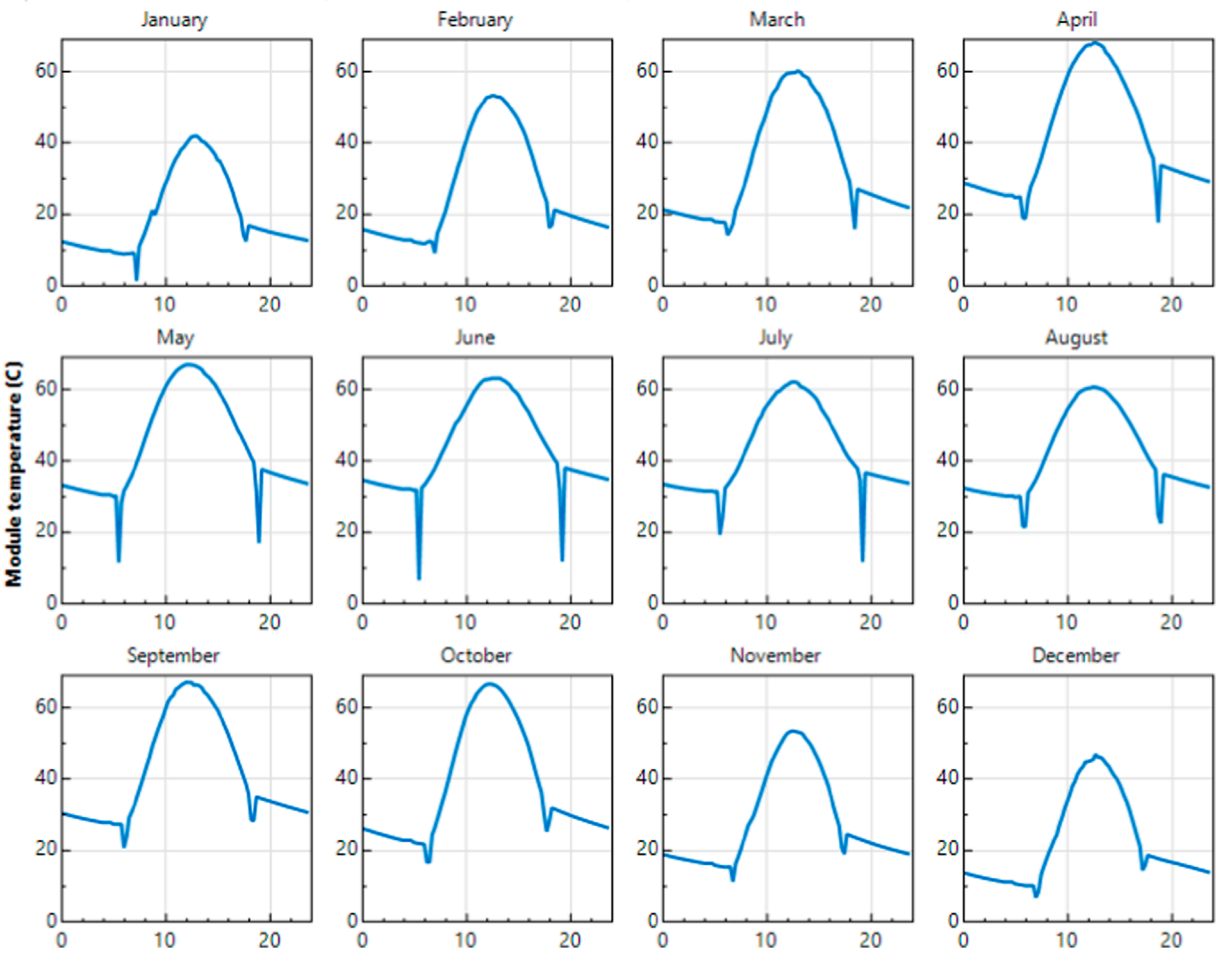

FIGURE 4
Hourly operating temperature of PV module for each month.

TABLE 3 Design Summary of rooftop photovoltaic systems.

Parameters	Inter-row spacing				
	1 foot	2 feet	5 feet	8 feet	11 feet
Number of Photovoltaic modules	860	760	567	450	374
Number of strings	45	40	34	24	21
PV Modules per string	19	19	17/18/15	18	17
Number of inverters	5	5	4	3	3
Frame Size	L2 (1 wide x 2 up)	L2 (1 wide x 2 up)	L2 (1 wide x 2 up)	L2 (1 wide x 2 up)	L2 (1 wide x 2 up)
Module Spacing	0.040 feet	0.040 feet	0.040 feet	0.040 feet	0.040 feet
PV module Orientation	Landscape	Landscape	Landscape	Landscape	Landscape

into five different scenarios. According to research (Habib et al., 2023e), the photovoltaic system generates its maximum energy at a 15° tilt angle and 180° of azimuth in the same city. As a result, in all five scenarios, a 15° tilt angle and 180° azimuth angle are used. In five scenarios, PV module inter-row spacing is 1 foot, 2 feet, 5 feet, 8 feet and 11 feet respectively.

TABLE 4 Performance comparison of a photovoltaic system with different inter-row spacing.

Parameters	Inter-row spacing				
	1 foot	2 feet	5 feet	8 feet	11 feet
Shaded Irradiance (kWh/m^2)	1,712.6	1,766.8	1816.5	1,823.7	1,825.0
Annual Energy Generation	517.9 MWh	481.2 MWh	371.6 MWh	297.5 MWh	246.8 MWh
Performance Ratio	75.3%	79.2%	82.1%	82.7%	82.6%
Specific yield (kWh/kWp)	1,384.3	1,455.4	1,508.0	1,520.0	1,517.0
Tilt and Orientation Factor (TOF) (%)	97.4%	97.4%	97.4%	97.4%	97.4%
Solar Access (%)	93.2%	96.2%	98.9%	99.3%	99.3%
Avg. Total Solar Resource Factor (TSRF) (%)	90.8%	93.7%	96.3%	96.7%	96.8%

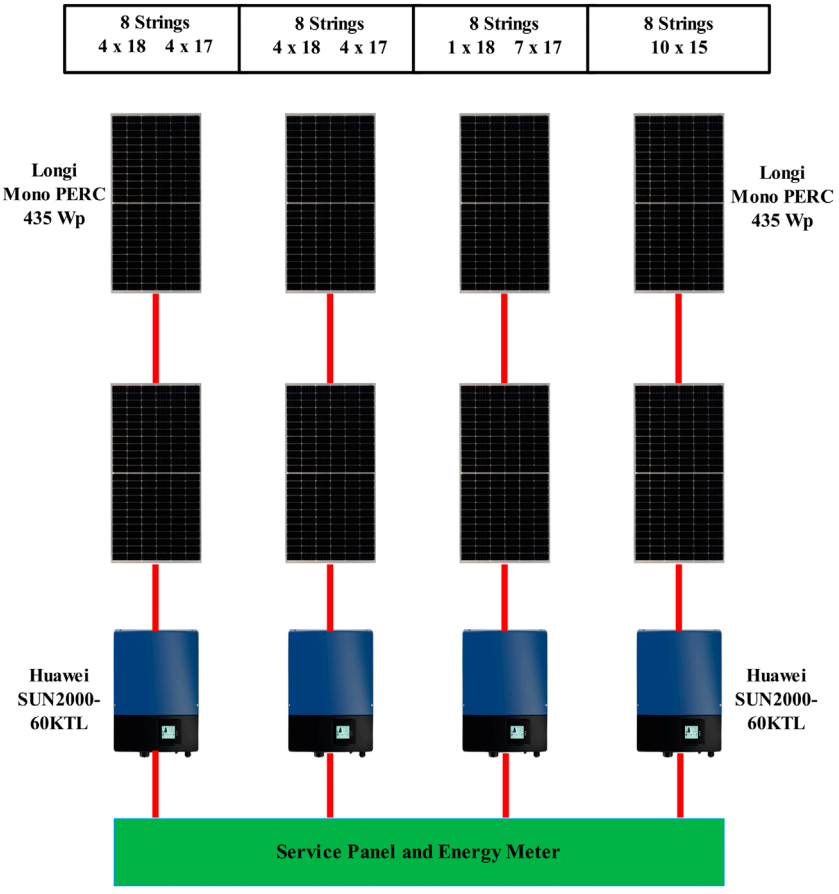

FIGURE 5
Schematic configuration of the connection between photovoltaic modules and inverters.

For the purpose of capturing the most intense solar irradiance, the photovoltaic module is tilted at a specific angle so that it faces direct sunlight for the longest duration of a day. The tilt angle of photovoltaic module creates or leads to mutual shading on parallel rows of a photovoltaic array. It is critical to determine the optimum inter-row spacing for the maximum performance of a photovoltaic system because mutual shading impacts the system's efficiency.

The photovoltaic modules are installed in parallel rows and tested at various inter-row spacings in order to analyze the losses

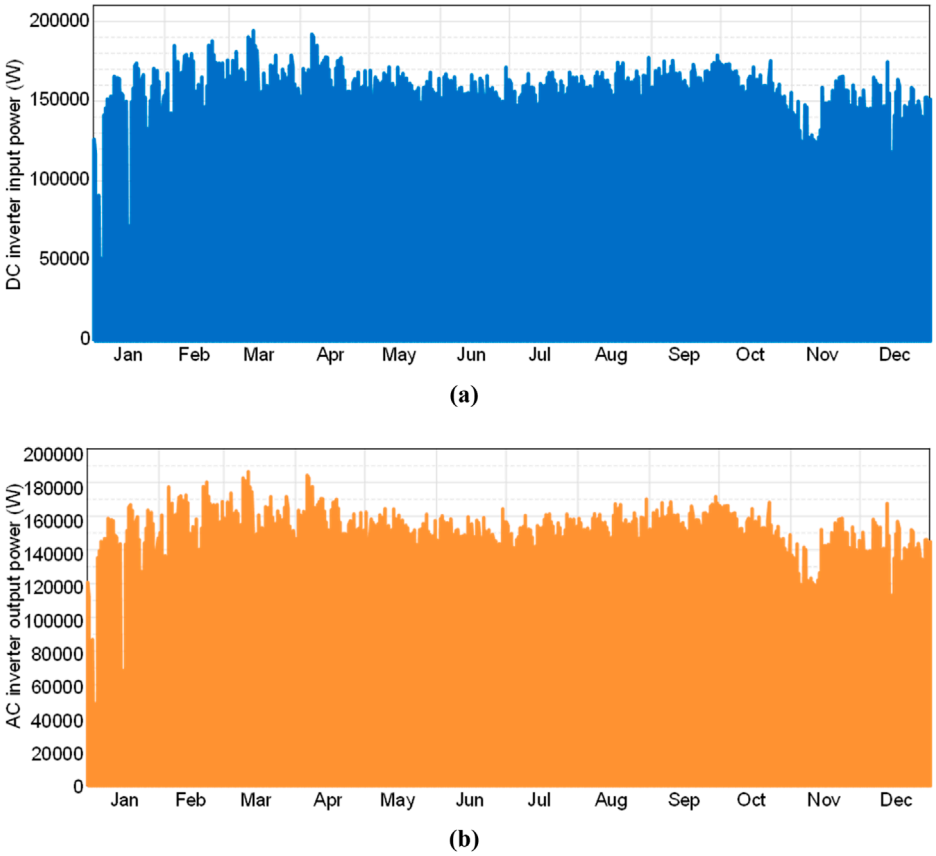

FIGURE 6
Variation in inverter power **(A)** DC input power (W) **(B)** AC output power (W) over a year.

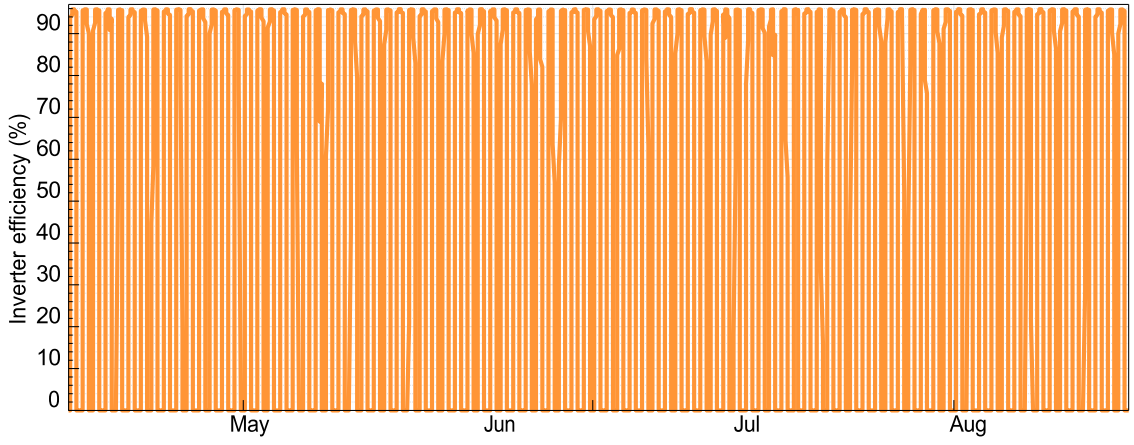

FIGURE 7
Inverter efficiency in the summer season.

caused by mutual shading of photovoltaic arrays. Because of limited roof space, the total number of photovoltaic modules in the planned layout differs, with different inter-row spacing between parallel rows of PV modules. Table 3 presents the design summary of rooftop photovoltaic systems with different Inter-row spacing.

The performance comparison of PV system with different inter-row spacing is shown in Table 4. This comparison includes

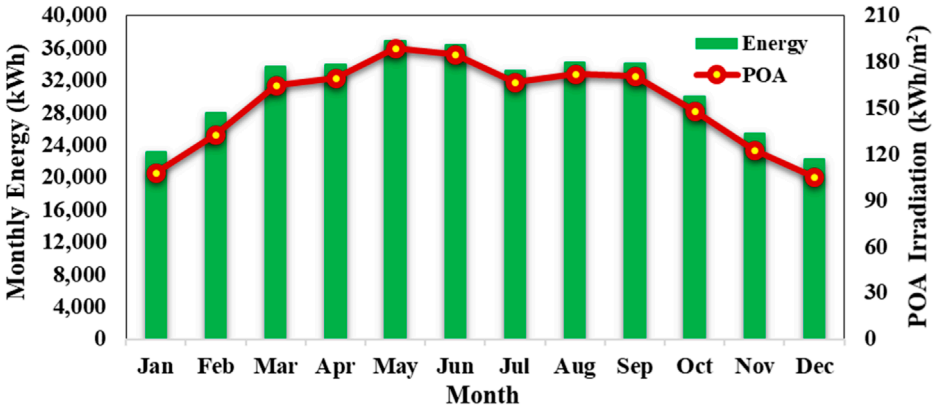

FIGURE 8
Monthly output energy of a PV system and POA irradiation.

TABLE 5 The annual generation of installed system with 5 feet inter-row spacing.

	Description	Output	% Delta
Irradiance (kWh/m^2)	Annual GHI	1691.9	
	POA Irradiance	1837.3	8.6%
	Shaded Irradiance	1816.5	−1.1%
	Irradiance after Reflection	1760.1	−3.1%
	Irradiance after Soiling	1724.9	−2.0%
	Total Irradiance on Collector	1724.9	0.0%
Energy (kWh)	Nameplate	425017.6	
	Output at Irradiance Levels	423121.79	−0.41%
	Output at the Cell Temp Derate	392483.4	−7.2%
	Output After Mismatch	379549.1	−3.3%
	Optimal DC Output	378460.5	−0.3%
	Constrained DC Output	378459.7	0.0%
	Inverter Output	373539.7	−1.3%
	Energy to Grid	371672.1	−0.5%

annually energy generation (MWh), performance ratio of the system at different tilt angle, specific yield (kWh/kWp), solar access (%), TOF, and average total solar resource factor (TSRF).

The photovoltaic energy generation system installed with 1- and 2-feet Inter-row spacing has a maximum number of PV modules but the performance ratio (PR), specific yield (kWh/kWp), solar access and TSRF are low because the efficiency of the system is decreased due to mutual shading effect on photovoltaic modules. In the case of a photovoltaic energy generation system having 8- and 11-feet inter-row spacing, the overall installed capacity of PV system is decreased, but the PR, specific yield (kWh/kWp), solar access, and TSRF are high because there is no mutual shading impact on the photovoltaic modules. Results in Table 4 show that the performance of the rooftop PV system is impacted by inter-row spacing. By increasing inter-row spacing between parallel photovoltaic arrays, the impact of mutual shading on photovoltaic modules is minimized, but the cost of electric wiring and land increases as a result. By comparison analysis, we find that a photovoltaic system installed with 5 feet inter-row spacing is more efficient. With 5 feet inter-row spacing, the results of the simulation indicate that the annual energy generation of the PV system is 371.6 MWh, specific yield (kWh/kWp) is 1,508.0, performance ratio is 82.1%, solar access is 98.9% and TSRF is 96.3%.

3.3 Case study implementation

The building of a commercial shopping plaza is taken as the case study for the installation of a rooftop on-grid photovoltaic system. In accordance with the results discussed in the preceding section, a PV system with a 15° tilt angle and 5 feet inter-row spacing is designed for the commercial shopping plaza. The commercial shopping plaza has a flat roof and two buildings.

3.3.1 Photovoltaic system layout on commercial building

The roof of the commercial shopping plaza has been divided into two segments. The PV system for commercial buildings consists of monocrystalline modules mounted with an L2 structure (2 up x 1 wide) at a 15° tilt angle and 180° azimuth angle. This is because the roof of the building is flat. The photovoltaic module is installed in landscape orientation. The interrow spacing is considered to be 5 feet, a setback is 2.0 feet, and the PV module spacing is 0.040 feet. Photovoltaic modules with a shading rate exceeding 3% have been eliminated.

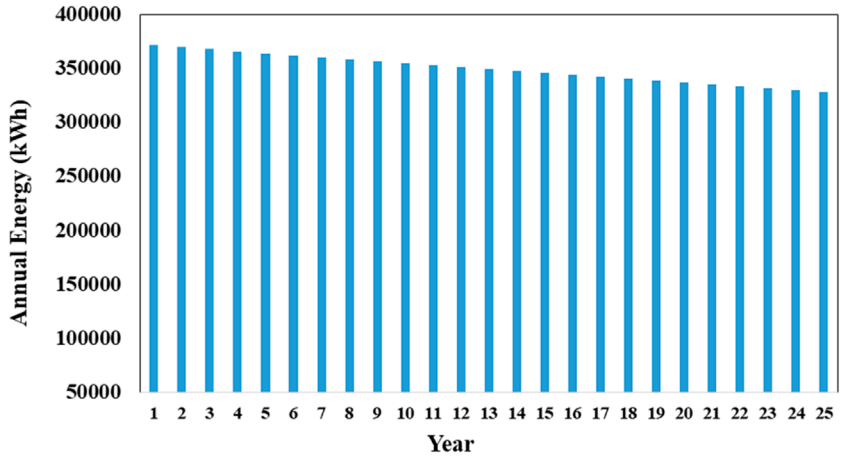

FIGURE 9
Annual energy depreciation of installed photovoltaic system.

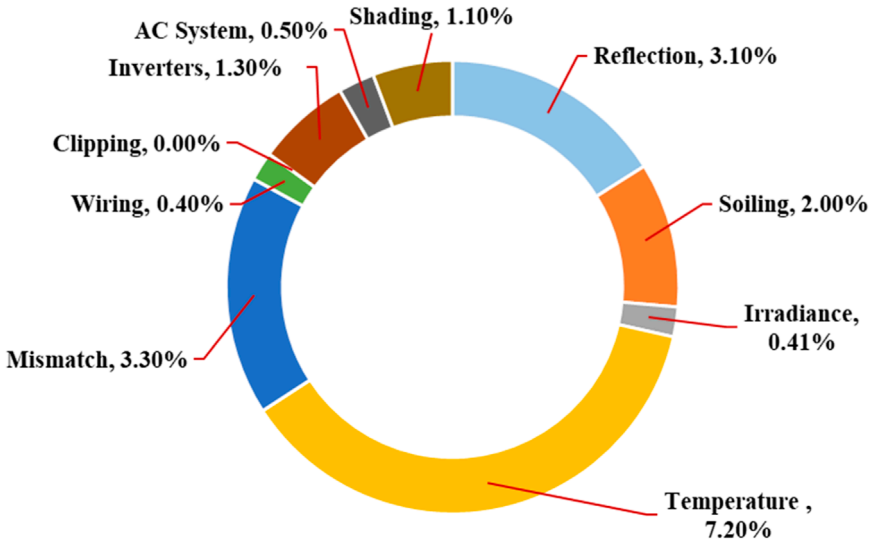

FIGURE 10
Losses of a photovoltaic system installed with 5 feet Inter-row spacing.

The schematic configuration of the connection between photovoltaic modules and inverter shows that the 34 photovoltaic strings are connected to 4 Huawei inverters (SUN 2000-125KTL-JPH0). The first two inverters (1 and 2) are each connected to eight strings, the first four strings consist of 18 photovoltaic modules each, while the four remaining strings consist of 17 photovoltaic modules each. The third inverter is connected to eight strings, each string consisting of 17 photovoltaic modules, except one string which has 18 photovoltaic modules. Similarly, ten photovoltaic module strings are connected to the inverter 4, and each string consists of 15 photovoltaic modules. The schematic configuration of the connection between photovoltaic modules and inverters is shown in Figure 5. The system employs two distinct types of disconnectors: DC breaker (2-pole) is used for each PV string and these breakers are installed between PV arrays and ongrid string inverters, while the AC breakers (4-pole) are installed between the ongrid string inverters and the utility grid. The service panel is used to connect PV systems and AC energy from the utility grid.

3.3.2 Energy generation

In accordance with the simulation findings, the PV system installed on the roof of a commercial shopping plaza has a DC nameplate capacity of 246.645 kW, and the AC nameplate capacity of the inverter is 240 kW with a 1.02 load ratio. The photovoltaic system installed on the commercial shopping plaza has an annual energy generation of 371.4 MWh, a specific power generation (kWh/kWp) of 1,508.4, and a performance ratio (PR) of 82.1%. Figure 6 shows the variation in DC input power (W) and AC output power (W) of all four inverters over the period of a year. The ongrid string

10.3389/fenrg.2024.1483755

TABLE 6 Monitoring and inspection of Installed PV Power System.

Monitoring and inspection of PV module installation					
Inverter #	String #	Tightness	Row to row spacing	Module to module Grounding	Module to frame Grounding
1	1–8	Ok	5 Feet	Ok	Ok
2	1–8	Ok	5 Feet	Ok	Ok
3	1–8	Ok	5 Feet	Ok	Ok
4	1–10	Ok	5 Feet	Ok	Ok

Monitoring and inspection of inverter installation				
Inspection	Inverter No. 1	Inverter No. 2	Inverter No. 3	Inverter No. 4
AC side Connection Configuration	Red/Yellow/Blue/Black	Red/Yellow/Blue/Black	Red/Yellow/Blue/Black	Red/Yellow/Blue/Black
AC Side Connection Tightness	Ok	Ok	Ok	Ok
DC Side Connection	Red/Black	Red/Black	Red/Black	Red/Black
Configurations	Ok	Ok	Ok	Ok
DC Side Connection Tightness	Ok	Ok	Ok	Ok
Communication Wire	Ok	Ok	Ok	Ok
Connection	0.31-meter	0.31-meter	0.31-meter	0.31-meter
Levelness	5-Feet	5-Feet	5-Feet	5-Feet
Inverter to Inverter Spacing	Yes	Yes	Yes	Yes
Inverter Clearance to Floor	Yes	Yes	Yes	Yes
Inverter Body Ground	Yes	Yes	Yes	Yes
Inverter Fixing to Wall	Yes	Yes	Yes	Yes
Iron Duct Installation for PV Cable	Yes	Yes	Yes	Yes
Iron Duct Installation for AC Cables	Yes	Yes	Yes	Yes
The distance between the two inverters is 0.6 m				

Monitoring and inspection of LT cabinet			
Item	Incoming Cabinet 1	Outgoing Cabinet	Metering Cabinet
Placement	Wall Mount	Ground Mount	Wall Mount
Electrical Connections	Ok	Ok	Ok
Communication Wire Connection	Ok	Ok	Ok
Vertical Levelness	Ok	Ok	Ok
Horizontal Straightness	Ok	Ok	Ok
Panel Appearance	Ok	Ok	Ok
Grounding Connection	Ok	Ok	Ok

FIGURE 11
Installed PV system.

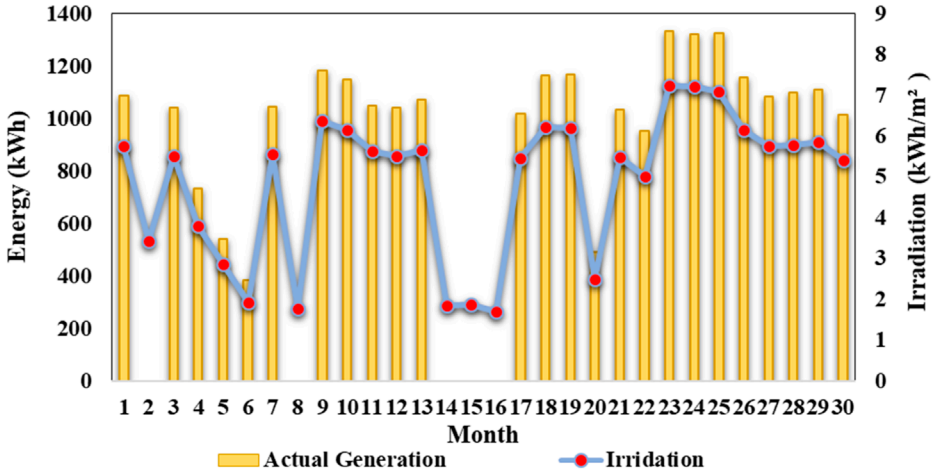

FIGURE 12
The daily actual generation of installed PV system and irradiation level.

inverter transforms input DC power to output AC power with high efficiency, as can be seen by comparing Figures 6A, B. The output power is barely less than input power from PV arrays, showing an inverter efficiency of approximately 95.93%. The maximum daily DC inverter input power is 194614.7417 W, and the average daily DC inverter input power is 158881.5110 W. The maximum daily AC inverter output power is 186698.6914 W, whereas the average daily AC inverter output power is 152231.6311 W. The inverter efficiency in the summer season is shown in Figure 7.

The monthly output energy of a PV system installed with 5 feet of inter-row spacing and the measured plane of array (POA) irradiation is presented in Figure 8. The POA irradiation varied between 189.1 kWh/m^2 in May and 105.3 kWh/m^2 in December. The lowest values of POA irradiation occur in the winter season, and the highest values occur in the summer season. The lowest monthly energy generation is 22202.80 kWh in December, while the maximum monthly energy generation is 36960.10 kWh in May. A commercial shopping plaza's roof-mounted photovoltaic system produced 371672.1 kWh during a year, with an average monthly electricity generation of 30972.67 kWh.

As seen in Figure 8 above, the energy generation of a photovoltaic system is maximum in summer season (May–Jun) and the energy generation is minimal in the winter season (Nov–Jan). According to the simulation results, the total irradiance (kWh/m^2) on collector is 1724.9 kWh/m^2. Annual nameplate energy of the system is 425017.6 kWh, the output energy at irradiance levels is 423,121.8 kWh, the optimal DC output is 378460.5 kWh, the energy at inverter output is 373539.7, whereas the total amount of energy that is fed into the national power grid is 371672.1 kWh as can be seen in Table 5.

Due to prolonged field exposure and environmental factors including temperature and humidity, photovoltaic modules are vulnerable to degradation when exposed to outside conditions. The output power of photovoltaic modules decreases due to degradation, which also affects the efficiency of solar photovoltaic systems. Manufacturers of photovoltaic modules provide performance

10.3389/fenrg.2024.1483755

TABLE 7 PV string open circuit voltage test.

Inverter	String No	No of modules	V_{OC} (voltage)	Optimal voltage range
1	1	18	832	(200V–1000 V)/600 V @380 Vac/400
	2	18	831	(200V–1000 V)/600 V @380 Vac/400
	3	18	835	(200V–1000 V)/600 V @380 Vac/400
	4	18	834	(200V–1000 V)/600 V @380 Vac/400
	5	17	784	(200V–1000 V)/600 V @380 Vac/400
	6	17	783	(200V–1000 V)/600 V @380 Vac/400
	7	17	785	(200V–1000 V)/600 V @380 Vac/400
	8	17	784	(200V–1000 V)/600 V @380 Vac/400
2	1	18	834	(200V–1000 V)/600 V @380 Vac/400
	2	18	834	(200V–1000 V)/600 V @380 Vac/400
	3	18	834	(200V–1000 V)/600 V @380 Vac/400
	4	18	833	(200V–1000 V)/600 V @380 Vac/400
	5	17	788	(200V–1000 V)/600 V @380 Vac/400
	6	17	788	(200V–1000 V)/600 V @380 Vac/400
	7	17	785	(200V–1000 V)/600 V @380 Vac/400
	8	17	788	(200V–1000 V)/600 V @380 Vac/400
3	1	17	787	(200V–1000 V)/600 V @380 Vac/400
	2	17	784	(200V–1000 V)/600 V @380 Vac/400
	3	17	789	(200V–1000 V)/600 V @380 Vac/400
	4	17	788	(200V–1000 V)/600 V @380 Vac/400
	5	17	787	(200V–1000 V)/600 V @380 Vac/400
	6	17	785	(200V–1000 V)/600 V @380 Vac/400
	7	17	783	(200V–1000 V)/600 V @380 Vac/400
	8	18	835	(200V–1000 V)/600 V @380 Vac/400
4	1	15	695	(200V–1000 V)/600 V @380 Vac/400
	2	15	696	(200V–1000 V)/600 V @380 Vac/400
	3	15	697	(200V–1000 V)/600 V @380 Vac/400
	4	15	696	(200V–1000 V)/600 V @380 Vac/400
	5	15	697	(200V–1000 V)/600 V @380 Vac/400
	6	15	695	(200V–1000 V)/600 V @380 Vac/400
	7	15	698	(200V–1000 V)/600 V @380 Vac/400

(Continued on the following page)

TABLE 7 (*Continued*) PV string open circuit voltage test.

Inverter	String No	No of modules	V_{OC} (voltage)	Optimal voltage range
	8	15	697	(200V–1000 V)/600 V @380 Vac/400
	9	15	696	(200V–1000 V)/600 V @380 Vac/400
	10	15	696	(200V–1000 V)/600 V @380 Vac/400

warranties to ensure the durability and reliability of photovoltaic modules. The photovoltaic module's performance warranty period was 5 years in the 1980s and extended to 10–20 years in the 1990s. Currently, the peak power of photovoltaic modules should not decrease to 80% of the original peak power during the 25-year performance warranty period (Jordan and Kurtz, 2013). This indicates that the power degradation rate should not be more than 0.8% per year. The annual production of roof-mounted PV system installed on a commercial shopping plaza in the first year is 371672.1 kWh, in the second year, the annual production is 369760.1 kWh, while in the twenty-fifth year, the annual production is 328329.1 kWh and total annual production of PV system in 25 years is 8739615.5 kWh as shown in Figure 9. This means that the installed photovoltaic system depreciates energy at a rate of 0.88% per year and falls in the standard warranty rate of 0.8% per year.

The degradation rate calculated in this research study provides better results compared to previous research studies, Malvoni et al. (2020) conducted research in similar conditions and found that the degradation rate is estimated at 0.50%/year and 0.32%/year respectively, after a 50-month operational period. The research study conducted by Daher et al. (2023) indicates that the degradation rates for maximum power are 0.84% per year throughout the operational period of the system. Hasan et al. (2022) demonstrated that the performance of photovoltaic modules degrades as the temperature of the modules increases. Efficiency decreases by 0.03%–0.05% for each 1°C increase in temperature without cooling, and a decline of up to 69% at an operating temperature of 64°C.

3.3.3 Losses in PV system

The efficiency, performance, and output energy of a PV array are significantly impacted by losses in a photovoltaic system. Figure 10 demonstrates various losses of the photovoltaic system installed with 5 feet Inter-row spacing. The temperature, wiring, mismatch, clipping, AC system, inverters, reflection, shading, soiling, and irradiance are some of the system losses shown in this figure. These losses are directly correlated with the output of the PV system. In the designed system installed on a commercial shopping plaza, the system has 7.2% temperature losses, 3.3% mismatch losses, 0.40% wiring losses, 0.0% clipping losses, 0.5% AC system losses, 1.3% inverters losses, 3.1% reflection losses, 1.1% shading losses, 2.0% soiling losses and 0.41% irradiance losses.

3.3.4 Monitoring and inspection of installed PV power system

Detailed testing has been performed at the site before commissioning to make sure that the equipment's performance guarantees are met, properly installed, correctly adjusted, and suitable for commercial operations. All steps of PV module installation, inverter installation as, and cabinet installation as shown in Table 6 have been meticulously checked.

3.3.5 Performance analysis of installed PV system

The on-grid solar (PV) system was installed on a commercial shopping plaza with a 15° tilt angle, 5 feet Inter-row spacing, and 180° azimuth angle as shown in Figure 11.

Test results of the installed photovoltaic system were taken for 30 days to evaluate and investigate the output generated energy (kWh) and performance of the photovoltaic (PV) system. We analyzed the experimental system in May because simulation results indicated that photovoltaic system produced the most energy during that month. Figure 12 displays the daily actual generation of the photovoltaic system and the daily irradiation level. The figure shows that the average amount of irradiation is 4.83 kWh/m^2. The daily maximum output energy generation of installed PV system (1333.676 kWh) was recorded on day 23, and its average energy generation was 1091.56 kWh. Due to a faulty transformer on days 2 and 8, energy production is zero. The system is shut down for diagnostic tests from day 14 to day 16.

3.3.6 Different tests performed during commissioning

1. Photovoltaic string open--circuit voltage test.
2. Photovoltaic string short--circuit current test and other parameters.
3. Inverter efficiency tests.
4. Earth resistance and insulation test of DC and power cables.
5. Performance ratio.

3.3.6.1 PV String open circuit voltage test

The maximum voltage that a solar PV cell can generate is called the open-circuit voltage, or V_{OC}, and it occurs whenever there is no current moving/passing through the cell. Open circuit voltage (V_{OC}) indicates the amount of forward bias of solar cell brought on by junction's bias with the photogenerated current. For each installed inverter, the voltages of all strings are also shown in Table 7. As shown in the table, the open circuit voltages of all strings are within the rated range (MPPT range of the inverter. The maximum V_{OC} for inverter 1 is 835 V, inverter 2 is 834 V, inverter 3 is 835 V and inverter 4 is 698 V. Similarly, maximum V_{OC} for a string consisting of 18 PV modules is 835 V, V_{OC} for a string consisting of 17 PV modules is 789 V and V_{OC} for string consist of 15 PV modules is 698 V.

TABLE 8 Short circuit current test and other parameters for a selected string of all inverters.

Inverter	Short-circuit current test and other parameters		
		Measured	STC Actual
1	Voc	767	768.34
	Isc	9.99	11.02
	Vmp	613	621.91
	Imp	10.1	11.08
	Pmp	6,156	6892.06
	Other Parameters		Measured Value
	Irradiance		927.1 W/m^2
	Cell Temperature		50.62°C
	Ambient Temperature		34.45°C
	Fill Factor		81.37%
	Irradiance Change		0.19%
2		Measured	STC Actual
	Voc	803	813.88
	Isc	10	11.08
	Vmp	650	685.52
	Imp	10.2	11.3
	Pmp	6,641	7443.85
	Other Parameters		Measured Value
	Irradiance		928.2 W/m^2
	Cell Temperature		51.57°C
	Ambient Temperature		34.31°C
	Fill Factor		82.34%
	Irradiance Change		0.56%
3		Measured	STC Actual
	Voc	761	771.68
	Isc	9.81	11.06
	Vmp	620.52	629.22
	Imp	10.09	11.29
	Pmp	6,258	7105.58
	Other Parameters		Measured Value
	Irradiance		897.4 W/m^2
	Cell Temperature		53.32°C
	Ambient Temperature		36.64°C
	Fill Factor		81.4%
	Irradiance Change		0.91%
4		Measured	STC Actual
	Voc	805	814.49
	Isc	10.27	11.04
	Vmp	646.8	654.2
	Imp	10.47	11.25
	Pmp	6770.5	7362.02
	Other Parameters		Measured Value
	Irradiance		922 W/m^2
	Cell Temperature		50.67°C
	Ambient Temperature		33.36°C
	Fill Factor		81.91%
	Irradiance Change		0.13%

(Continued on the following page)

TABLE 8 (*Continued*) Short circuit current test and other parameters for a selected string of all inverters.

3.3.6.2 PV String Short circuit current test and other parameters

The maximum value of current in a PV string is called short circuit current (I_{SC}), which flows when the positive and negative terminals are shorted together. The I_{SC} value is employed to calculate/determine maximum current that a PV module produces when it is connected to an inverter or solar charge controller. It is extremely difficult to determine the correct current rating since current output fluctuates every second as the intensity of the sun (irradiance) on the PV panel varies. No reverse polarity was detected, and each string's earthing continuity was apparent enough to function without difficulty. However short circuit current drop in most of the strings in the different inverters is over 5%. The current drop was probably due to low sunlight during the test time, and the shadow of the surrounding objects was also coming on the different strings. Test results of randomly selected one string of each inverter are shown in Table 8. It can be seen from the table that the short-circuit currents of the selected strings of inverters 1, 2, 3, and 4 are 9.99A, 10.0A, 9.81A, and 10.27A, respectively. The measured fill factor of inverters 1, 2 3, and 4 are 81.37%, 82.34%, 81.40%, and 81.91%, respectively.

3.3.6.3 Inverter efficiency test

The ratio of final output generated AC power to input DC power is known as inverter efficiency. Power level, input voltage, and

TABLE 9 Earth resistance test of DC cables (string cables).

Inverter	String No	Positive to negative (Red + Black)	Positive + ground	Negative + ground
		(GΩ)	(GΩ)	(GΩ)
1	1	1.8	1.9	1.6
	2	1.7	1.6	1.6
	3	1.6	1.8	1.7
	4	1.6	1.9	1.8
	5	1.7	1.6	1.6
	6	1.6	1.6	1.7
	7	1.8	1.7	1.8
	8	1.9	1.8	1.7
2	1	1.6	1.6	1.7
	2	1.8	1.7	1.9
	3	1.9	1.8	1.6
	4	1.6	1.7	1.8
	5	1.6	1.8	1.9
	6	1.7	1.7	1.6
	7	1.8	1.6	1.8
	8	1.6	1.6	1.7
3	1	1.7	1.7	1.6
	2	1.8	1.6	1.8
	3	1.7	1.8	1.7
	4	1.6	1.6	1.9
	5	1.9	1.6	1.6
	6	1.7	1.7	1.9
	7	1.6	1.9	1.6
	8	1.7	1.6	1.7
4	1	1.9	1.7	1.8
	2	1.8	1.8	1.6
	3	1.7	1.8	1.7
	4	1.6	1.6	1.8
	5	1.6	1.7	1.7

(Continued on the following page)

TABLE 9 (*Continued*) Earth resistance test of DC cables (string cables).

Inverter	String No	Positive to negative (Red + Black)	Positive + ground	Negative + ground
		(GΩ)	(GΩ)	(GΩ)
	6	1.7	1.8	1.6
	7	1.9	1.7	1.8
	8	1.6	1.6	1.6
	9	1.7	1.9	1.6
	10	1.8	1.7	1.7

inverter temperature all have an impact on inverter efficiency. At the inverter terminals, the input DC power and output AC power are simultaneously measured to determine efficiency in the field. The input and output power was measured at the inverter terminal and the efficiency of inverter 1 is calculated to be 98.83%, inverter 2 is calculated to be 98.76%, inverter 3 calculated to be 98.80%, and inverter 4 is calculated to be 98.81%. All inverters passed the inverter efficiency tests because their efficiency values were within the range of the rated inverter efficiency (98.7%). Other tests like the AC input connection test, DC input connection test, and communication connection test were conducted results are in the satisfactory range.

3.3.6.4 Earth resistance and insulation test of DC and AC power cables

Megger is used for earth resistance and insulation tests of DC cables (positive to negative and negative to ground & positive to ground) and AC cables or power cables (Red + Ground, Yellow + Ground, Blue + Ground, Red + Neutral, Blue + Neutral and yellow + Neutral).

It has ensured that all wire sequences have good insulation and high resistance among each other and there is not any major breakage in insulation during installation which may cause short circuit faults later on. The values of the earth resistance test of DC cables (string cables) are given in Table 9 and the Insulation test of DC cables (string cables) is given in Table 10. The value of resistance of DC cables (positive to negative and negative to ground & positive to ground) varies between 1.6 GΩ and 1.9 GΩ for all strings. These values show that there is high resistance among each other. The insulation of DC cables is the same for all strings and has a very high value (11 GΩ).

Earth resistance and insulation tests of AC cables for all inverters are shown in Table 11. The highest measured resistance of AC cables for inverter 1 is 3.9 GΩ between Red-Ground and Yellow-Neutral. The lowest measured resistance of AC cables for inverter 1 is 2.8 GΩ between Blue-Ground. The highest measured resistance of AC cables for inverter 2 is 3.8 GΩ, for inverter 3 is 3.8 GΩ and for inverter 4 is 3.9 GΩ. The insulation of AC cables for all inverters is 11 GΩ.

10.3389/fenrg.2024.1483755

TABLE 10 Insulation test of DC cables (string cables).

Inverter	String No	Insulation (GΩ)
1	1	11
	2	11
	3	11
	4	11
	5	11
	6	11
	7	11
	8	11
2	1	11
	2	11
	3	11
	4	11
	5	11
	6	11
	7	11
	8	11
3	1	11
	2	11
	3	11
	4	11
	5	11
	6	11
	7	11
	8	11
4	1	11
	2	11
	3	11
	4	11
	5	11
	6	11
	7	11
	8	11
	9	11
	10	11

(Continued on the following page)

TABLE 10 (*Continued*) Insulation test of DC cables (string cables).

3.3.6.5 Performance ratio

The performance ratio is a measure of the performance of the photovoltaic system, taking into consideration environmental conditions (solar irradiance, temperature, etc.). Table 12 shows PR of installed PV system on 100% load. The average measured irradiation is 4.83 kWh/m^2, the maximum daily energy generation of installed photovoltaic system (1333.676 kWh) was recorded on day 23, and its average energy generation was 1091.56 kWh. The maximum performance ratio (80.90%) was recorded on day 6 and the average daily PR of the installed system was 75.70%.

3.4 LCOE and payback period of PV system

The CAPEX of a PV system installed on the roof of a commercial shopping plaza is 160319.25$ as shown in Table 13, and the total revenue that is generated by the installed PV system is 37910.55$ considering a 0.102 $/kWh grid tariff (Habib et al., 2023d). The payback period of the installed photovoltaic system is 4.22 years and the levelized cost of electricity of the photovoltaic system is 0.0229 $/kWh, these are calculated using Equations 18 and 19. The payback period of this research is lower than that of Boruah and Chandel (2024) which has a payback period of 6.15 years. Similarly, LCOE is also lower than research conducted by Akpahou et al. (2024) with an LCOE ranging from 0.110 USD/kWh to 0.125 USD/kWh.

$$\text{Payback period} = \frac{\text{Photovoltaic system's cost (CAPEX)}}{\text{Total annual revenue of PV system}}$$

$$\text{Payback period} = \frac{160,319.25}{37,910.55}$$

$$\text{Payback period} = 4.22 \text{ years}$$

$$\text{LCOE} = \frac{\text{CAPEX} + \text{OPEX (for 25 years)}}{\text{Energy generations in 25 years}} \frac{(\$)}{(\text{kWh})}$$

OPEX = 1,603.19$ (at 1% CAPEX/year (assumption))

OPEX for 25 years = 40,079.81$

The total annual production of PV systems in 25 years is 8739615.5 kWh with an energy depreciated rate of 0.88% per year as shown in Figure 9.

$$\text{LCOE} = \frac{160,319.25 + 40,079.81}{8,739,615.5}$$

$$\text{LCOE} = 0.0229 \ \$/\text{kWh}$$

TABLE 11 Earth resistance and insulation test of AC cables for all inverters.

AC cable 240 mm 3.5 core testing result				
Inverter	Cable size	Color Coding	Resistance (GΩ)	Insulation (GΩ)
1	240 mm	Red-Ground	3.9	11
		Yellow-Ground	3.6	11
		Blue-Ground	2.8	11
		Red-Neutral	2.9	11
		Blue-Neutral	3.6	11
		Yellow-Neutral	3.9	11
2	240 mm	Red-Ground	3.8	11
		Yellow-Ground	3.7	11
		Blue-Ground	3.6	11
		Red-Neutral	3.4	11
		Blue-Neutral	3.7	11
		Yellow-Neutral	3.6	11
3	240 mm	Red-Ground	3.7	11
		Yellow-Ground	3.8	11
		Blue-Ground	3.7	11
		Red-Neutral	3.6	11
		Blue-Neutral	2.9	11
		Yellow-Neutral	3.7	11
4	240 mm	Red-Ground	3.9	11
		Yellow-Ground	2.8	11
		Blue-Ground	3.7	11
		Red-Neutral	3.6	11
		Blue-Neutral	3.8	11
		Yellow-Neutral	3.7	11

The following section present sensitivity analyses concentrating on potential fluctuations in local energy tariffs and market costs.

3.4.1 Optimistic case

- CAPEX decreases by 15%

Photovoltaic system's cost (CAPEX) = 136271.36$

- Grid tariff increases by 10%

New grid tariff = 0.1122 $/kWh
Annual revenue of PV system = 371672.1 × 0.1122 = 41701.61 $

$$\text{Payback period} = \frac{136,271.36}{41,701.61}$$

$$\text{Payback period} = 3.26\,\text{years}$$

OPEX = 1362.71$ (at 1% CAPEX/year (assumption))
OPEX for 25 years = 34067.84$
The total annual production of PV systems in 25 years is 8739615.5 kWh with an energy depreciated rate of 0.88% per year.

$$\text{LCOE} = \frac{136,271.36 + 34,067.84}{8,739,615.5}$$

$$\text{LCOE} = 0.0194 \ \$/\text{kWh}$$

3.4.2 Pessimistic case

- CAPEX increases by 15%

$$\text{Photovoltaic systems cost (CAPEX)} = 184367.14\$$$

- Grid tariff decreases by 10%

$$\text{New grid tariff} = 0.0918\,\$/\text{kWh}$$

$$\text{Annual revenue of PV system} = 371672.1 \times 0.0918 = 34119.49\,\$$$

$$\text{Payback period} = \frac{184,367.14}{34,119.49}$$

$$\text{Payback period} = 5.40\,\text{years}$$

OPEX = 1843.67$ (at 1% CAPEX/year (assumption))
OPEX for 25 years = 46091.78$
The total annual production of PV systems in 25 years is 8739615.5 kWh with an energy depreciated rate of 0.88% per year.

10.3389/fenrg.2024.1483755

TABLE 12 Measured performance ratio of the installed system.

Statistical time	Installed capacity (kWp)	Total irradiation (kWh/m^2)	Actual generation on 100% load	System PR on 100% load (%)	Actual scenario of site
01/05/2023	246.645	5.764	1089.554	76.0168948	
02/0/2023	246.645	3.436			Transformer Faulty
03/05/2023	246.645	5.517	1043.59	76.069798	
04/05/2023	246.645	3.808	732.906	77.3992363	
05/05/2023	246.645	2.865	540.95	75.9307758	
06/05/2023	246.645	1.913	384.84	80.9003823	
07/05/2023	246.645	5.558	1044.968	75.6083546	
08/05/2023	246.645	1.764			Transformer Faulty
09/05/2023	246.645	6.385	1185.844	74.6882007	
10/05/2023	246.645	6.159	1148.592	74.9964871	
11/05/2023	246.645	5.624	1050.06	75.0851653	
12/05/2023	246.645	5.521	1040.728	75.8062180	
13/05/2023	246.645	5.667	1071.988	76.0715122	
14/05/2023	246.645	1.851			System Off
15/05/2023	246.645	1.863			System Off
16/05/2023	246.645	1.696			System Off
17/05/2023	246.645	5.453	1019.098	75.1563689	
18/05/2023	246.645	6.218	1163.574	75.2538336	
19/05/2023	246.645	6.213	1167.382	75.5608748	
20/05/2023	246.645	2.498	492.388	79.2684496	
21/05/2023	246.645	5.485	1035.892	75.9491968	
22/05/2023	246.645	5.014	952.54	76.3983942	
23/05/2023	246.645	7.251	1333.676	73.9669598	
24/05/2023	246.645	7.229	1323.472	73.6244174	
25/05/2023	246.645	7.095	1325.644	75.1380377	
26/05/2023	246.645	6.157	1157.578	75.6077734	
27/05/2023	246.645	5.757	1085.98	75.8596677	
28/05/2023	246.645	5.791	1099.306	76.3396864	
29/05/2023	246.645	5.854	1110.352	76.2769465	
30/05/2023	246.645	5.407	1014.912	75.4844258	
Average Values	246.645	4.8316667	1091.5567	75.7060738	

TABLE 13 CAPEX and grid tariff.

System size	kWp	246.645
First-year production	kWh	371672.1
CAPEX total	USD Fix	160319.25
Grid tariff	USD/kWh	0.102
Annual revenue of PV system	USD	371672.1 × 0.102 = 37910.55

$$\text{LCOE} = \frac{184,367.14 + 46,091.78}{8,739,615.5}$$

$$\text{LCOE} = 0.0264 \ \ \$/\text{kWh}$$

3.5 Carbon dioxide saving

The photovoltaic system installed on the roof of the commercial shopping plaza produced 371672.1 kWh of energy annually in the first year of installation, with an average monthly electricity generation of 30972.67 kWh. By using Equation 20, the CO_2 in the first year is

$$(CO_2)_{\text{first\_year}} = 0.58 \times 371,672.1$$

$$(CO_2)_{\text{first\_year}} = 215,569.818$$

$$(CO_2)_{\text{avg\_monthly}} = 0.58 \times 30,972.67$$

$$(CO_2)_{\text{avg\_month}} = 17,964.149$$

Approximately 215569.818 metric tons of CO_2 were saved in the first year by considering the annual production (301554.2 kWh) of a photovoltaic system installed on the roof of the commercial shopping plaza. The average monthly electricity generation of the system is 30972.67 kWh and approximately 215569.818 metric tons of CO_2 were saved monthly. The total annual production of PV systems in 25 years is 8739615.5 kWh with an energy depreciated rate of 0.88% per year. Hence, a total of approximately 5068976.99 metric tons of CO_2 were saved by the PV system in 25 years.

$$(CO_2)_{25\_\text{year}} = 0.58 \times 8739615.5$$

$$(CO_2)_{25\_\text{year}} = 5,068,976.99$$

4 Discussion and conclusion

Energy demand rises as a result of economic expansion and urbanization. Pakistan, a high-energy-demand nation, fills the shortfall in its energy supply by importing fossil fuels. Pakistan has to modify its energy policy to emphasize sustainable, clean, and renewable energy resources, like other developed nations. Pakistan has enormous solar potential with a 1691.9 kWh/m^2 annual global horizontal solar irradiance. Pakistan has currently made the transition to sustainable energy and developed new regulations for renewable energy systems, including the installation and commercialization of a rooftop photovoltaic system. Therefore, this requires detailed evaluation to determine the capabilities of the PV system and convince decision-makers. To achieve this goal and calculate the appropriate rooftop area for photovoltaic modules, simulations are carried out using HelioScope software.

The objective of this research is to examine the potential of a rooftop photovoltaic system for commercial buildings. This research examines the effects of different design factors on the efficiency and performance of a rooftop photovoltaic system. These factors such as tilt and azimuth angles, GHI, ambient temperature, and shading from the surrounding obstacles. The summer months experience the highest levels of global horizontal irradiance. Furthermore, the maximum hourly value of the GHI is 915 W/m^2 in May. The GHI is measured in May at its highest level (188.8 kWh/m^2) and in December at its lowest level (82.3 kWh/m^2). The wind speed fluctuates between 0.3 m/s at the lowest point to 7.8 m/s at the highest point. The daily average maximum wind speed is 3.406 m/s, while the average annual wind speed is 2.133 m/s. Ambient temperatures range from 5.1°C to 47.6°C, while average annual ambient temperature is 28.49°C. The maximum hourly operating temperature (°C) of photovoltaic module is 67.83°C in April, while the minimum hourly operating temperature is 1.22°C in January. Additionally, average daily maximum operating temperature of a photovoltaic module is 59.70°C, the average daily minimum operating temperature of a solar (PV) module is 4.47°C and the average annual operating temperature of a solar (PV) module is 34.85°C.

The commercial shopping plaza has a flat roof and two buildings. The photovoltaic module is tilted to capture the most intense solar irradiation. An optimal row-to-row distance is calculated with the aim of maximizing energy yield. By simulation analysis, it is found that a photovoltaic system installed with 5 feet Inter-row spacing is more efficient. With 5 feet inter-row spacing, the results of simulation indicate that annually energy generation of PV system is 371.6 MWh, specific yield (kWh/kWp) is 1508.0, performance ratio is 82.1%, solar access is 98.9% and TSRF is 96.3%. The maximum daily DC inverter input power is 194614.7417 W, and the average daily DC inverter input power is 158881.5110 W. The maximum daily AC inverter output power is 186698.6914 W, whereas the average daily AC inverter output power is 152231.6311 W. The output power (AC) is barely less than the input power from PV arrays, showing an inverter efficiency of approximately 95.93%.

According to the simulation results, the total irradiance (kWh/m^2) on the collector is 1724.9 kWh/m^2. The annual nameplate energy of the system is 425017.6 kWh, the output energy at irradiance levels is 423121.8 kWh, the optimal DC output is 378460.5 kWh, the energy at inverter output is 373539.7,

whereas the total amount of energy that is fed into the national power grid is 371672.1 kWh. The annual production of roof-mounted PV system installed on a commercial shopping plaza in the first year is 371672.1 kWh, in the second year, the annual production is 369760.1 kWh, while in the twenty-fifth year, the annual production is 328329.1 kWh and total annual production of PV system in 25 years is 8739615.5 kWh. This means that the installed photovoltaic system depreciates energy at a rate of 0.88% per year and falls in the standard warranty rate of 0.8% per year. In the designed system installed on a commercial shopping plaza, the system has 7.2% temperature losses, 3.3% mismatch losses, 0.40% wiring losses, 0.0% clipping losses, 0.5% AC system losses, 1.3% inverters losses, 3.1% reflection losses, 1.1% shading losses, 2.0% soiling losses and 0.41% irradiance losses.

After the Simulation study, detailed testing was performed at the site before commissioning to make sure that the equipment's performance guarantees were met, properly installed, correctly adjusted, and suitable for commercial operations. Test results of installed photovoltaic system were taken for 30 days to evaluate and investigate the output generated energy (kWh) and performance of the photovoltaic (PV) system. We analyzed the experimental system in May because simulation results indicated that photovoltaic system produced the most energy during that month. The daily maximum output energy generation of installed PV system (1333.676 kWh) was recorded on day 23, and its average energy generation was 1091.56 kWh. Due to a faulty transformer on days 2 and 8, energy production is zero. The system is shut down for diagnostic tests from day 14 to day 16. By PV string open circuit voltage test, the maximum V_{OC} for inverter 1 is 835 V, inverter 2 is 834 V, inverter 3 is 835 V and inverter 4 is 698 V. Similarly, maximum V_{OC} for a string consisting of 18 PV modules is 835 V, V_{OC} for string consist of 17 PV modules is 789 V and V_{OC} for string consist of 15 PV modules is 698 V. It is found that voltages of all strings are within the rated range. PV String Isc Current Test shows that no reverse Polarity was detected, and each string's earthing continuity was apparent enough to function without difficulty. The short circuit currents of the selected strings of inverters 1, 2, 3, and 4 are 9.99A, 10.0A, 9.81A, and 10.27A, respectively. The measured fill factor of inverters 1, 2 3, and 4 are 81.37%, 82.34%, 81.40%, and 81.91%, respectively.

To perform the inverter efficiency test, the input and output power was measured at the inverter terminal. The efficiency of inverter 1 is calculated to be 98.83%, inverter 2 is calculated to be 98.76%, inverter 3 is calculated to be 98.80%, and inverter 4 is calculated to be 98.81%. All inverters passed the inverter efficiency tests because their efficiency values are within the range of the rated inverter efficiency (98.7%). Megger is used for earth resistance and insulation tests of DC cables (Positive to Negative and negative to ground & positive to ground) and AC cables. The value of resistance of DC cables (positive to negative and negative to ground & positive to ground) varies between 1.6 GΩ and 1.9 GΩ for all strings. These values show that there is high resistance among each other. The insulation of DC cables is the same for all string and have a very high value (11 GΩ). The highest measured resistance of AC cables for inverter 1 is 3.9 GΩ between Red-Ground and Yellow-Neutral. The lowest measured resistance of AC cables for inverter 1 is 2.8 GΩ between Blue-Ground. The highest measured resistance of AC cables for inverter 2 is 3.8 GΩ, for inverter 3 is 3.8 GΩ and for inverter 4 is 3.9 GΩ. The insulation of AC cables for all inverters is 11 GΩ. All wire sequences have good insulation and high resistance among each other and there is not any major breakage in insulation during installation which may cause short circuit faults later on. The maximum performance ratio (80.90%) was recorded on day 6 and the average daily PR of the installed photovoltaic system was 75.70%. The installed PV system operates more efficiently because it has a high-performance ratio. The payback period of a solar (PV) system is 4.22 years and the LCOE of the photovoltaic system is 0.0229 $/kWh. The PV system saved 215569.818 metric tons of CO_2 in the first year and a total of approximately 5068976.99 metric tons in 25 years.

Data availability statement

The original contributions presented in the study are included in the article/supplementary material, further inquiries can be directed to the corresponding authors.

Author contributions

SH: Writing–original draft. MT: Writing–original draft. MG: Writing–review and editing. SC: Writing–review and editing. HA: Writing–review and editing. MA: Writing–review and editing. MK: Writing–review and editing.

Funding

The author(s) declare that financial support was received for the research, authorship, and/or publication of this article. The author MA would like to acknowledge the support by the Deanship of Scientific Research through King Khalid University, Saudi Arabia funded by the Large Group Research Project RGP2/392/45.

Conflict of interest

The authors declare that the research was conducted in the absence of any commercial or financial relationships that could be construed as a potential conflict of interest.

Publisher's note

References

Abd Elsadek, E. M., Kotb, H., Abdel-Khalik, A. S., Aboelmagd, Y., and Abdelbaky Elbatran, A. H. (2024). Experimental and techno-economic analysis of solar PV system for sustainable building and greenhouse gas emission mitigation in harsh climate: a case study of aswan educational building. *Sustainability* 16 (13), 5315. doi:10.3390/su16135315

Ahsan, S. M., Khan, H. A., Hassan, N. U., Arif, S. M., and Lie, T. T. (2020). Optimized power dispatch for solar photovoltaic-storage system with multiple buildings in bilateral contracts. *Appl. Energy* 273, 115253. doi:10.1016/j.apenergy.2020.115253

Akpahou, R., Odoi-Yorke, F., and Osei, L. K. (2024). Techno-economic analysis of a utility-scale grid-tied solar photovoltaic system in Benin republic. *Clean. Eng. Technol.* 13, 100633. doi:10.1016/j.clet.2023.100633

Al-Amin, M., Hassan, M., and Khan, I. (2024). Unveiling mega-prosumers for sustainable electricity generation in a developing country with techno-economic and emission analysis. *J. Clean. Prod.* 437, 140747. doi:10.1016/j.jclepro.2024.140747

Ali, O. M., and Alomar, O. R. (2022). Technical and economic feasibility analysis of a PV grid-connected system installed on a university campus in Iraq. *Environ. Sci. Pollut. Res.* 30, 15145–15157. doi:10.1007/s11356-022-23199-y

Alshehri, A., James, P., and Bahaj, A. (2024). Pathways to the large-scale adoption of residential photovoltaics in Saudi Arabia. *Energies* 17 (13), 3180. doi:10.3390/en17133180

Appavou, F., Brown, A., Epp, B., Murdock, H. E., and Skeen, J. (2019). *Renewables 2019 global status report*. Paris, France: REN21.

Asif, M. (2016). Growth and sustainability trends in the buildings sector in the GCC region with particular reference to the KSA and UAE. *Renew. Sustain. Energy Rev.* 55, 1267–1273. doi:10.1016/j.rser.2015.05.042

Assouline, D., Mohajeri, N., and Scartezzini, J. (2018). Large-scale rooftop solar photovoltaic technical potential estimation using Random Forests. *Appl. Energy* 217, 189–211. doi:10.1016/j.apenergy.2018.02.118

Ayan, O., and Turkay, B. E. (2023). Techno-Economic comparative analysis of grid-connected and islanded hybrid renewable energy systems in 7 climate regions, Turkey. *IEEE Access* 11, 48797–48825. doi:10.1109/access.2023.3276776

Bashir, M. F., Shahbaz, M., Ma, B., and Alam, K. (2024). Evaluating the roles of energy innovation, fossil fuel costs and environmental compliance towards energy transition in advanced industrial economies. *J. Environ. Manag.* 351, 119709. doi:10.1016/j.jenvman.2023.119709

Bhatti, A. R., Tamoor, M., Liaqat, R., Rasool, A., Salam, Z., Ali, A., et al. (2024). Electric vehicle charging stations and the employed energy management schemes: a classification based comparative survey. *Discov. Appl. Sci.* 6 (10), 503. doi:10.1007/s42452-024-06190-9

Boruah, D., and Chandel, S. S. (2024). Techno-economic feasibility analysis of a commercial grid-connected photovoltaic plant with battery energy storage-achieving a net zero energy system. *J. Energy Storage* 77, 109984. doi:10.1016/j.est.2023.109984

Bouramdane, A. A., Tantet, A., and Drobinski, P. (2021). Utility-scale PV-battery versus CSP-thermal storage in Morocco: storage and cost effect under penetration scenarios. *Energies* 14 (15), 4675. doi:10.3390/en14154675

Chwieduk, B., and Chwieduk, D. (2021). Analysis of operation and energy performance of a heat pump driven by a PV system for space heating of a single family house in polish conditions. *Renew. Energy* 165, 117–126. doi:10.1016/j.renene.2020.11.026

Daher, D. H., Aghaei, M., Quansah, D. A., Adaramola, M. S., Parvin, P., and Ménézo, C. (2023). Multi-pronged degradation analysis of a photovoltaic power plant after 9.5 years of operation under hot desert climatic conditions. *Prog. Photovoltaics Res. Appl.* 31 (9), 888–907. doi:10.1002/pip.3694

de Lima, L. C., de Araújo Ferreira, L., and de Lima Morais, F. H. B. (2017). Performance analysis of a grid connected photovoltaic system in northeastern Brazil. *Energy Sustain. Dev.* 37, 79–85. doi:10.1016/j.esd.2017.01.004

Ehsan, F., Habib, S., Gulzar, M. M., Guo, J., Muyeen, S. M., and Kamwa, I. (2024). Assessing policy influence on electric vehicle adoption in China: an in-depth study. *Energy Strategy Rev.* 54, 101471. doi:10.1016/j.esr.2024.101471

EIA (2006). *The annual energy review 2006*. Washington, DC, USA: Energy Information Administration EIA.

EIA (2016). *World energy statistics*. Paris, France: OECD Publishing.

Fina, B., Auer, H., and Friedl, W. (2020). Cost-optimal economic potential of shared rooftop PV in energy communities: evidence from Austria. *Renew. Energy* 152, 217–228. doi:10.1016/j.renene.2020.01.031

Habib, S., Aghakhani, S., Nejati, M. G., Azimian, M., Jia, Y., and Ahmed, E. M. (2023b). Energy management of an intelligent parking lot equipped with hydrogen storage systems and renewable energy sources using the stochastic p-robust optimization approach. *Energy* 278, 127844. doi:10.1016/j.energy.2023.127844

Habib, S., Ahmarinejad, A., and Jia, Y. (2023a). A stochastic model for microgrids planning considering smart prosumers, electric vehicles and energy storages. *J. Energy Storage* 70, 107962. doi:10.1016/j.est.2023.107962

Habib, S., Jia, Y., Tamoor, M., Zaka, M. A., Shi, M., and Dong, Q. (2023d). Modeling, simulation, and experimental analysis of a photovoltaic and biogas hybrid renewable energy system for electrification of rural community. *Energy Technol.* 11, 2300474. doi:10.1002/ente.202300474

Habib, S., Liu, H., Tamoor, M., Zaka, M. A., Jia, Y., Hussien, A. G., et al. (2023c). Technical modelling of solar photovoltaic water pumping system and evaluation of system performance and their socio-economic impact. *Heliyon* 9 (5), e16105. doi:10.1016/j.heliyon.2023.e16105

Habib, S., Tamoor, M., Zaka, M. A., and Jia, Y. (2023e). Assessment and optimization of carport structures for photovoltaic systems: a path to sustainable energy development. *Energy Convers. Manag.* 295, 117617. doi:10.1016/j.enconman.2023.117617

Hasan, K., Yousuf, S. B., Tushar, M. S. H. K., Das, B. K., Das, P., and Islam, M. S. (2022). Effects of different environmental and operational factors on the PV performance: a comprehensive review. *Energy Sci. and Eng.* 10 (2), 656–675. doi:10.1002/ese3.1043

Huang, L., and Zheng, R. (2018). Energy and economic performance of solar cooling systems in the hot-summer and cold-winter zone. *Buildings* 8 (3), 37. doi:10.3390/buildings8030037

Huang, Z., Mendis, T., and Xu, S. (2019). Urban solar utilization potential mapping via deep learning technology: a case study of Wuhan, China. *Appl. Energy* 250, 283–291. doi:10.1016/j.apenergy.2019.04.113

Huda, A., Kurniawan, I., Purba, K. F., Ichwani, R., and Fionasari, R. (2024). Techno-economic assessment of residential and farm-based photovoltaic systems. *Renew. Energy* 222, 119886. doi:10.1016/j.renene.2023.119886

International Energy Agency (2020). Renewables. Available at: https://www.iea.org/fuels-and-technologies/renewables (Accessed January 20, 2024).

Jordan, D. C., and Kurtz, S. R. (2013). Photovoltaic degradation rates—an analytical review. *Prog. photovoltaics Res. Appl.* 21 (1), 12–29. doi:10.1002/pip.1182

Kang, H., An, J., Kim, H., Ji, C., Hong, T., and Lee, S. (2021). Changes in energy consumption according to building use type under COVID-19 pandemic in South Korea. *Renew. Sustain. Energy Rev.* 148, 111294. doi:10.1016/j.rser.2021.111294

Kumar, N. M., Gupta, R. P., Mathew, M., Jayakumar, A., and Singh, N. K. (2019). Performance, energy loss, and degradation prediction of roof-integrated crystalline solar PV system installed in Northern India. *Case Stud. Therm. Eng.* 13, 100409. doi:10.1016/j.csite.2019.100409

Kymakis, E., Kalykakis, S., and Papazoglou, T. M. (2009). Performance analysis of a grid connected photovoltaic park on the island of Crete. *Energy Convers. Manag.* 50 (3), 433–438. doi:10.1016/j.enconman.2008.12.009

Lang, T., Ammann, D., and Girod, B. (2016). Profitability in absence of subsidies: a techno-economic analysis of rooftop photovoltaic self-consumption in residential and commercial buildings. *Renew. Energy* 87, 77–87. doi:10.1016/j.renene.2015.09.059

Lang, T., Gloerfeld, E., and Girod, B. (2015). Don´ t just follow the sun–A global assessment of economic performance for residential building photovoltaics. *Renew. Sustain. Energy Rev.* 42, 932–951. doi:10.1016/j.rser.2014.10.077

Liu, H., Deng, S., Habib, S., and Shen, Bo (2022). Emission reduction constrained optimal strategy for refrigeration field: a case study of Ningbo in China. *J. Clean. Prod.* 379, 134667. doi:10.1016/j.jclepro.2022.134667

Liu, Q., Li, J., Tan, X., Jia, Y., Zhang, Y., and Ji, G. (2021). "Research on the influence of summer temperature on electricity demand," in 2021 4th International Conference on Energy, Electrical and Power Engineering (CEEPE) (IEEE), 1259–1263. doi:10.1109/ceepe51765.2021.9475693

Machete, R., Paula, A., Gomes, M. G., and Moret Rodrigues, A. (2018). The use of 3D GIS to analyse the influence of urban context on buildings' solar energy potential. *Energy Build.* 177, 290–302. doi:10.1016/j.enbuild.2018.07.064

Malaysia, S. E. D. A. (2016). "SEDA Malaysia grid-connected PV system course design," in *SEDA Malaysia*. Malaysia.

Malvoni, M., Kumar, N. M., Chopra, S. S., and Hatziargyriou, N. (2020). Performance and degradation assessment of large-scale grid-connected solar photovoltaic power plant in tropical semi-arid environment of India. *Sol. Energy* 203, 101–113. doi:10.1016/j.solener.2020.04.011

Miran, S., Tamoor, M., Kiren, T., Raza, F., Hussain, M. I., and Kim, J. T. (2022). Optimization of standalone photovoltaic drip irrigation system: a simulation study. *Sustainability* 14 (14), 8515. doi:10.3390/su14148515

Mohajeri, N., Assouline, D., Guiboud, B., Bill, A., Gudmundsson, A., and Scartezzini, J. L. (2018). A city-scale roof shape classification using machine learning for solar energy applications. *Renew. Energy* 121, 81–93. doi:10.1016/j.renene.2017.12.096

Mohamed, K., Shareef, H., Nizam, I., Esan, A. B., and Shareef, A. (2024). Operational performance assessment of rooftop PV systems in the Maldives. *Energy Rep.* 11, 2592–2607. doi:10.1016/j.egyr.2024.02.014

Monna, S., Juaidi, A., Abdallah, R., and Itma, M. (2020). A comparative assessment for the potential energy production from PV installation on residential buildings. *Sustainability* 12 (24), 10344. doi:10.3390/su122410344

Mountain, B., and Szuster, P. S. (2015). Solar, solar everywhere: opportunities and challenges for Australia's rooftop PV systems. *IEEE power energy Mag.* 13 (4), 53–60. doi:10.1109/mpe.2015.2416113

Mousavi, S. M. S., and Bakhshi-Jafarabadi, R. (2024). Techno-economic assessment of grid-connected photovoltaic systems for peak shaving in arid areas based on experimental data. *Energy Rep.* 11, 5492–5503. doi:10.1016/j.egyr.2024.05.035

Musa, M., Gao, Y., Rahman, P., Albattat, A., Ali, M. A. S., and Saha, S. K. (2024). Sustainable development challenges in Bangladesh: an empirical study of economic growth, industrialization, energy consumption, foreign investment, and carbon emissions—using dynamic ARDL model and frequency domain causality approach. *Clean Technol. Environ. Policy* 26 (6), 1799–1823. doi:10.1007/s10098-023-02680-3

Muteri, V., Cellura, M., Curto, D., Franzitta, V., Longo, S., Mistretta, M., et al. (2020). Review on life cycle assessment of solar photovoltaic panels. *Energies* 13 (1), 252. doi:10.3390/en13010252

Nguyen, V. G., Sirohi, R., Tran, M. H., Truong, T. H., Duong, M. T., Pham, M. T., et al. (2024). Renewable energy role in low-carbon economy and net-zero goal: perspectives and prospects. *Energy and Environ.*, 0958305X241253772. doi:10.1177/0958305x241253772

Palmer-Wilson, K., Donald, J., Robertson, B., Lyseng, B., Keller, V., Fowler, M., et al. (2019). Impact of land requirements on electricity system decarbonisation pathways. *Energy Policy* 129, 193–205. doi:10.1016/j.enpol.2019.01.071

Prajapati, S., and Fernandez, E. (2019). "Rooftop solar PV system for commercial office buildings for EV charging load," in *2019 IEEE international conference on smart instrumentation, measurement and application (ICSIMA)* (IEEE), 1–5.

Prieto, A., Knaack, U., Auer, T., and Klein, T. (2018). Passive cooling and climate responsive façade design: exploring the limits of passive cooling strategies to improve the performance of commercial buildings in warm climates. *Energy Build.* 175, 30–47. doi:10.1016/j.enbuild.2018.06.016

Ramli, M. A., Twaha, S., and Alghamdi, A. U. (2017). Energy production potential and economic viability of grid-connected wind/PV systems at Saudi Arabian coastal areas. *J. Renew. Sustain. Energy* 9 (6), 065910. doi:10.1063/1.5005597

Satpathy, P. R., Panda, S., Mahmoud, A., and Sharma, R. (2021b). "Optimal design and performance survey of a 100kW P grid-connected PV plant for installation near the top ranked green city of India," in 2021 1st Odisha International Conference on Electrical Power Engineering, Communication and Computing Technology (ODICON) (IEEE), 1–6. doi:10.1109/odicon50556.2021.9428966

Satpathy, P. R., Sharma, R., and Panda, S. (2021a). "Optimal sizing, placement and shading analysis of a 19.2 kW grid-tied residential roof-top PV system," in 2021 1st Odisha International Conference on Electrical Power Engineering, Communication and Computing Technology (ODICON) (IEEE), 1–6. doi:10.1109/odicon50556.2021.9428927

Schallenberg-Rodríguez, J. (2013). Photovoltaic techno-economical potential on roofs in regions and islands: the case of the Canary Islands. Methodological review and methodology proposal. *Renew. Sustain. Energy Rev.* 20, 219–239. doi:10.1016/j.rser.2012.11.078

Şevik, S. (2022). Techno-economic evaluation of a grid-connected PV-trigeneration-hydrogen production hybrid system on a university campus. *Int. J. Hydrogen Energy* 47 (57), 23935–23956. doi:10.1016/j.ijhydene.2022.05.193

Shaahid, S. M., and Elhadidy, M. A. (2008). Economic analysis of hybrid photovoltaic-diesel-battery power systems for residential loads in hot regions-A step to clean future. *Renew. Sustain. Energy Rev.* 12, 488–503. doi:10.1016/j.rser.2006.07.013

Shukla, A. K., Sudhakar, K., and Baredar, P. (2016). Design, simulation and economic analysis of standalone roof top solar PV system in India. *Sol. Energy* 136, 437–449. doi:10.1016/j.solener.2016.07.009

Singh, R. (2020). Approximate rooftop solar PV potential of Indian cities for high-level renewable power scenario planning. *Sustain. Energy Technol. Assessments* 42, 100850. doi:10.1016/j.seta.2020.100850

Sinha, P., and Ghosh, S. (2024). Resource-efficient manufacturing enables PV supply chain diversity: an industry perspective and case study of CdTe PV manufacturing. *Sol. Energy* 269, 112310. doi:10.1016/j.solener.2024.112310

Tamoor, M., Bhatti, A. R., Butt, A. D., Miran, S., Kiren, T., Farhan, M., et al. (2022c). Optimal sizing of a centralized hybrid photovoltaic system for efficient operation of street lights. *J. Eng. Res.*, 1–15. doi:10.36909/jer.icepe.19563

Tamoor, M., Bhatti, A. R., Farhan, M., and Miran, S. (2022d). Design of on-grid photovoltaic system considering optimized sizing of photovoltaic modules for enhancing output energy. *Eng. Proc.* 19 (1), 2. doi:10.3390/ecp2022-12671

Tamoor, M., Bhatti, A. R., Farhan, M., Miran, S., Raza, F., and Zaka, M. A. (2021a). Designing of a hybrid photovoltaic structure for an energy-efficient street lightning system using PVsyst software. *Eng. Proc.* 12 (1), 45. doi:10.3390/engproc2021012045

Tamoor, M., Bhatti, A. R., Hussain, M. I., Miran, S., Kiren, T., Ali, A., et al. (2023). Optimal sizing and technical assessment of a hybrid renewable energy solution for off-grid community center power. *Front. Energy Res.* 11, 1283586. doi:10.3389/fenrg.2023.1283586

Tamoor, M., Habib, S., Bhatti, A. R., Butt, A. D., Awan, A. B., and Ahmed, E. M. (2022e). Designing and energy estimation of photovoltaic energy generation system and prediction of plant performance with the variation of tilt angle and Inter-row spacing. *Sustainability* 14 (2), 627. doi:10.3390/su14020627

Tamoor, M., Hussain, M. I., Bhatti, A. R., Miran, S., Arif, W., Kiren, T., et al. (2022a). Investigation of dust pollutants and the impact of suspended particulate matter on the performance of photovoltaic systems. *Front. Energy Res.* 10, 1017293. doi:10.3389/fenrg.2022.1017293

Tamoor, M., Tahir, M. A. B., and Zaka, M. A. (2021b). Photovoltaic integrated distributed energy generation system for sustainable energy development considering reliability indices and levelized cost of energy. *Int. J. Adv. Trends Comput. Sci. Eng.* 10 (3), 2540–2549. doi:10.30534/ijatcse/2021/1461032021

Tamoor, M., Tahir, M. A. B., Zaka, M. A., and Iqtidar, E. (2022b). Photovoltaic distributed generation integrated electrical distribution system for development of sustainable energy using reliability assessment indices and levelized cost of electricity. *Environ. Prog. and Sustain. Energy* 41, e13815. doi:10.1002/ep.13815

Tamoor, M., Tahir, M. S., Sagir, M., Tahir, M. B., Iqbal, S., and Nawaz, T. (2020). Design of 3 kW integrated power generation system from solar and biogas. *Int. J. Hydrogen Energy* 45 (23), 12711–12720. doi:10.1016/j.ijhydene.2020.02.207

Tarigan, E. (2018). Simulation and feasibility studies of rooftop PV system for university campus buildings in Surabaya, Indonesia. *Int. J. Renew. Energy Res.* 8 (2), 895–908. doi:10.20508/ijrer.v8i2.7547.g7377

Thotakura, S., Kondamudi, S. C., Xavier, J. F., Quanjin, M., Reddy, G. R., Gangwar, P., et al. (2020). Operational performance of megawatt-scale grid integrated rooftop solar PV system in tropical wet and dry climates of India. *Case Stud. Therm. Eng.* 18, 100602. doi:10.1016/j.csite.2020.100602

Van Ruijven, B. J., De Cian, E., and Sue Wing, I. (2019). Amplification of future energy demand growth due to climate change. *Nat. Commun.* 10 (1). 2762. doi:10.1038/s41467-019-10399-3

Vargas-Salgado, C., Díaz-Bello, D., Alfonso-Solar, D., and Lara-Vargas, F. (2024). Validations of HOMER and SAM tools in predicting energy flows and economic analysis for renewable systems: comparison to a real-world system result. *Sustain. Energy Technol. Assessments* 69, 103896. doi:10.1016/j.seta.2024.103896

Wen, Y., Chen, Y., Wang, P., Rassol, A., and Xu, S. (2022). Photovoltaic–electric vehicles participating in bidding model of power grid that considers carbon emissions. *Energy Rep.* 8, 3847–3855. doi:10.1016/j.egyr.2022.03.010

Wiginton, L. K., Nguyen, H. T., and Pearce, J. M. (2010). Quantifying rooftop solar photovoltaic potential for regional renewable energy policy. *Comput. Environ. Urban Syst.* 34 (4), 345–357. doi:10.1016/j.compenvurbsys.2010.01.001

Wittkopf, S., Valliappan, S., Liu, L., Ang, K. S., and Cheng, S. C. J. (2012). Analytical performance monitoring of a 142.5 kWp grid-connected rooftop BIPV system in Singapore. *Renew. Energy* 47, 9–20. doi:10.1016/j.renene.2012.03.034

Yadav, S. K., and Bajpai, U. (2018). Performance evaluation of a rooftop solar photovoltaic power plant in Northern India. *Energy Sustain. Dev.* 43, 130–138. doi:10.1016/j.esd.2018.01.006

Yang, R. J., Zhao, Y., Jayakumari, S. D. S., Schneider, A., Rajan, S. P., Leloux, J., et al. (2024). Digitalising BIPV energy simulation: a cross tool investigation. *Energy Build.* 318, 114484. doi:10.1016/j.enbuild.2024.114484

Yar, A., Arshad, M. Y., Asghar, F., Amjad, W., Asghar, F., Hussain, M. I., et al. (2022). Machine learning-based relative performance analysis of monocrystalline and polycrystalline grid-tied PV systems. *Int. J. Photoenergy* 2022 (1), 1–18. doi:10.1155/2022/3186378

Zander, K. K., Simpson, G., Mathew, S., Nepal, R., and Garnett, S. T. (2019). Preferences for and potential impacts of financial incentives to install residential rooftop solar photovoltaic systems in Australia. *J. Clean. Prod.* 230, 328–338. doi:10.1016/j.jclepro.2019.05.133

Frontiers in
Energy Research

Advances and innovation in sustainable, reliable and affordable energy

Explores sustainable and environmental developments in energy. It focuses on technological advances supporting Sustainable Development Goal 7: access to affordable, reliable, sustainable and modern energy for all.

Discover the latest Research Topics

See more →

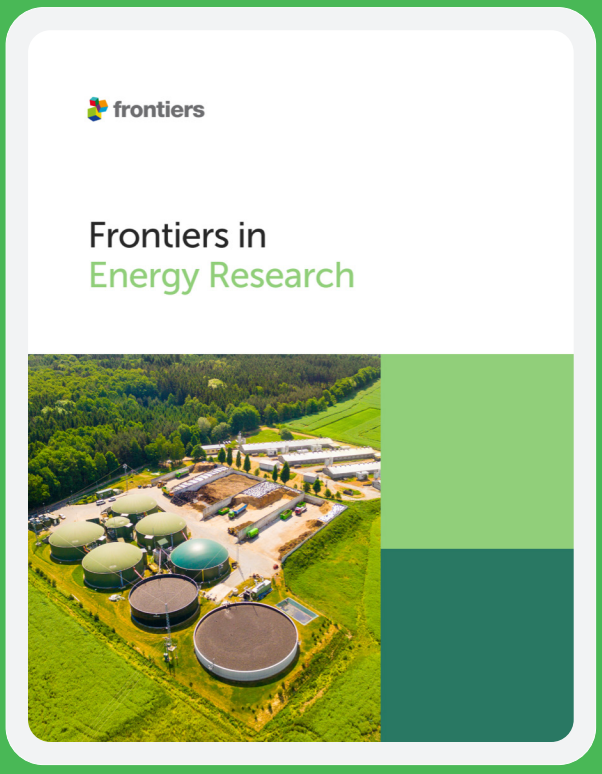

Frontiers

Avenue du Tribunal-Fédéral 34
1005 Lausanne, Switzerland
frontiersin.org

Contact us

+41 (0)21 510 17 00
frontiersin.org/about/contact